



DISSERTATION

Local Electronic Excitations in Extended Systems: a Quantum-Chemistry approach

Ausgeführt zum Zwecke der Erlangung des akademischen Grades eines Doktors
der technischen Wissenschaften unter der Leitung von

O.Univ.-Prof. Dipl.-Phys. Dr.rer.nat. Joachim Burgdörfer
Institut für theoretische Physik, E136

und

O.Prof. Dipl.-Phys. Dr.rer.nat. Ludger Wirtz
Universität Luxembourg

eingereicht an der Technischen Universität Wien
Fakultät für Physik

von

Franz Paul Tiwald

Matrikelnummer 0225097

Mosergasse 14/15

A-1090 Wien

franz.paul.tiwald@tuwien.ac.at

Wien, am

To Martin, Katharina, Edith, Franz, Helene, Josef, and Larisa

Abstract

Real solids and surfaces are not “perfect”. Crystals inevitably contain various defects and surfaces are subject to interactions with ambient particles leading, for example, to oxidation and adsorption. Since such effects are present in everyday devices and applications a deep understanding of the underlying physics is of great importance. In this thesis we study the properties of two very localized imperfections: the F-type color center in alkali-halide crystals and the charge transfer during scattering of an ion from an insulator surface. Both effects have been studied for a long time but a detailed theoretical understanding on the ab-initio level seems to be missing. This thesis provides state-of-the-art ab-initio calculations and addresses open questions. In particular, we present an ab-initio study of the physics underlying the so-called Mollwo–Ivey relation. This relation connects the F-center absorption energies with the crystal lattice constants and has not been fully understood so far. Second, we present the first ab-initio results on the charge-transfer probability during scattering of a proton from a lithium-fluoride surface. This study is based on a non-adiabatic molecular dynamics approach that provides microscopic insight into the charge-transfer process. Both the light absorption by the color center and the charge transfer represent *local* electronic excitations: the F-type color center consists of an electron strongly localized at an anionic vacancy and the electron transferred is strongly localized in close vicinity of the proton. This localization allows for application of the so-called embedded cluster approach in which the extended system is approximated by an embedded finite-sized active cluster. To study the properties of the active clusters we apply high-level quantum chemistry methods solving the electronic Schrödinger equation.

Kurzfassung

Reale Festkörper und Oberflächen sind nicht “perfekt”. Kristalle enthalten eine Vielzahl an Defekten und Oberflächen wechselwirken mit umgebenden Teilchen. Letzteres führt, zum Beispiel, zu Oxidation und Absorption an der Oberfläche. Da solche Effekte tägliche Anwendungen betreffen, ist ein profundes Verständnis ihrer zugrundeliegenden Physik äußerst wichtig. In dieser Arbeit untersuchen wir Eigenschaften zweier sehr lokalisierter Prozesse: Die Absorption von Licht durch das Typ F Farbzentrum in Alkalihalogenidkristallen und den Ladungstransfer bei der Streuung von Ionen an Isolatoroberflächen. Beide Effekte sind seit langem Thema aktueller Forschung und dennoch fehlt bisher eine detaillierte theoretische Beschreibung auf ab initio Niveau. Ziel dieser Arbeit ist es, genau solche ab initio Berechnungen durchzuführen und dadurch offene Fragen zu beantworten. Wir präsentieren im Folgenden eine ab initio Untersuchung der Mollwo Ivey Beziehung, die die Absorptionsenergien der Farbzentren mit den Gitterkonstanten der Alkalihalogenide verbindet. Wir sind dadurch in der Lage erstmals den physikalischen Grund dieser Beziehung zu identifizieren. Weiters präsentieren wir die erste ab initio Berechnung des Elektronentransfers bei der Streuung eines Protons an einer Lithiumfluoridoberfläche. Die Berechnung basiert auf nicht-adiabatischer Molekulardynamik, die eine mikroskopische Beschreibung des Ladungstransfers erlaubt. Beide Prozesse, die Absorption von Licht durch das Farbzentrum und der Ladungstransfer, sind *lokale* elektronische Anregungen. Das Farbzentrum besteht aus einem Elektron, lokalisiert in einer Anionfehlstelle und der Ladungstransfer findet in naher Umgebung des Protons statt. Diese Lokalität erlaubt die Anwendung der Methode der eingebetteten Cluster, in der das Innere und die Oberfläche eines ausgedehnten Kristalls näherungsweise durch einen endlichen, in den Festkörper eingebetteten aktiven Cluster beschrieben wird. Wir studieren die Eigenschaften der eingebetteten Cluster durch das Lösen der elektronischen Schrödingergleichung mit genauen Methoden aus der Quantenchemie.

Contents

1. Introduction	13
2. Introduction to quantum chemistry	19
2.1. The Hartree–Fock approximation	19
2.2. Methods for treating correlations	26
2.2.1. Configuration Interaction with singles and doubles	28
2.2.2. Møller–Plesset perturbation theory of second order	30
2.2.3. Coupled–Cluster methods	32
2.2.4. Multi-configurational self-consistent field	33
2.2.5. Multi-reference configuration interaction with singles and dou- bles (MRCI-SD)	35
2.2.6. Complete active space perturbation theory of second order (CASPT2)	35
2.3. Natural orbitals and the one-particle reduced density matrix	36
3. The F-type color center in lithium fluoride	39
3.1. Previous work	41
3.2. Setting up the calculation: cluster sizes, embedding scheme and basis sets	42
3.3. The Hartree–Fock absorption energy and the F-center orbitals	46
3.4. Beyond Hartree–Fock: absorption energies including correlation	51
3.5. Comparison with experiment	54
3.5.1. Fermi Contact term	54
3.5.2. Relaxation of the ground state - The Franck–Condon absorp- tion energy	55
3.5.3. Line width of the absorption spectrum	56
3.5.4. Electron-phonon coupling	57
3.5.5. Comparison of the theoretical and experimental spectrum	60
3.5.6. Photoluminescence and the relaxed excited state	60
3.6. Solid-state physicist’s and quantum chemist’s approach to the F- center in LiF: a comparison	64

4. The Mollwo–Ivey relation for F-centers in alkali halide crystals	69
4.1. Previous work	70
4.1.1. The point-ion model	70
4.1.2. Relation between the extent of the F-center wave function and its absorption energy	71
4.2. The “box” potential	73
4.3. Scaling with the lattice constant	78
4.3.1. F-center absorption energies in scaled LiF	78
4.3.2. Spatial extent of the F center in scaled LiF	79
4.3.3. Scaled LiF and the Vinti sum rule	81
4.4. Ion-size effects on F centers in real materials	82
4.4.1. Spatial extent of the F center in real alkali-halide crystals . .	84
4.5. F-center absorption energies and the Mollwo–Ivey relation in real alkali-halide crystals	87
5. Non-adiabatic molecular dynamics in a nutshell	91
5.1. The Born–Oppenheimer adiabatic approximation	91
5.2. Beyond the Born–Oppenheimer adiabatic approximation: the non- adiabatic couplings	93
5.3. The diabatic representation	97
5.4. Solution of the time-dependent Schrödinger equation for the nuclear motion	101
5.4.1. Approximate analytic solutions	101
5.4.2. The Tully surface-hopping algorithm	109
5.4.3. Wave-packet propagation	113
5.5. $\text{Si}^{3+} + \text{He}$ charge-transfer cross section	116
6. Charge transfer between a proton and a lithium-fluoride surface	119
6.1. Setting up the calculation: electronic structure of $\text{LiF} + \text{H}^+$ and the embedded cluster approach	122
6.2. Convergence of the electronic structure of embedded LiF clusters . .	124
6.2.1. Dependence of W_{LiF} on quantum-chemistry method and clus- ter size	126
6.2.2. Dependence of $W_{\text{LiF}}^{\text{MS-CASPT2}}$ on basis-set size, embedding, clus- ter shape, and symmetry	130
6.3. The embedded Li_5F_1 cluster	130
6.3.1. Potential energy surfaces of Li_5F_1	131
6.3.2. 1-D dynamics in $\text{Li}_5\text{F}_1 + \text{H}^+$	133
6.3.3. 3-D dynamics in $\text{Li}_5\text{F}_1 + \text{H}^+$	136
6.4. 1-D charge-transfer dynamics in larger clusters	140
6.4.1. Clusters with active F^- ions in the topmost layer only . . .	140
6.4.2. Clusters with active F^- ions in deeper surface layers	144

6.5. 3-D charge-transfer dynamics in $\text{Li}_{20}\text{F}_6\text{-F}_1 + \text{H}^+$	147
6.5.1. The $\text{Li}_{20}\text{F}_6\text{-F}_1 + \text{H}^+$ embedded cluster	147
6.5.2. 1-D and 3-D projectile dynamics	148
6.5.3. Comparison with experiment	151
7. Summary and Outlook	155
A. Appendices	165
A.1. Scaled NaF and LiCl	165
A.2. A refined particle in the box model	167
A.3. Relation between the non-adiabatic vector \vec{F}_{ji} and scalar coupling G_{ji}	168
A.4. Calculation of the non-adiabatic derivative coupling	169
A.5. Total $\text{Si}^{3+} + \text{He}$ charge-transfer cross section within the Landau– Zener approximation	170
A.6. Reflection probability of H^+ from an LiF surface	171
A.7. Extrapolation of the MS-CASPT2 work function	173
A.8. Definition of top-F and top-Li contributions	173
Acknowledgments	175
Bibliography	177

1. Introduction

Pristine, unperturbed crystals and surfaces do not exist in reality: crystals contain various defects and even in ultra-high vacuum chambers there are rest gas atoms interacting with the surface of the sample. In some instances these imperfections cause complications (instability of material), in other instances they are a key feature. Consider, for example, the doping of a silicon crystal with boron and phosphorus to realize a diode within a p-n junction. Complex integrated circuits and nano structures can be patterned onto surfaces using ion-beam lithography [1]. Applications of defects range from the performance enhancement of solar cells [2] to NV-center defects as bits in quantum-computers [3]. In all these cases a deeper understanding of the electronic and structure properties of perturbations of pristine crystals or surfaces is of great importance. In this work we focus on the electronic structure of two local perturbations in ionic alkali halides:

1. the F-type color center defect and its absorption of light and
2. charge transfer to protons impinging on a lithium-fluoride (LiF) surface.

The F-type color center defect in alkali-halide crystals was first observed at the end of the 19th century [4]. Systematic investigations of its properties started in the late 1920s and soon after a basic understanding developed for its structure: the F center consists of a strongly localized electron trapped in an anion vacancy (for reviews see [5–8]). The defect is termed color center since the trapped electron can be excited by absorption of light in the visible range coloring the initially transparent alkali-halide crystal. Despite its seemingly simple electronic structure, ab-initio calculations of the F-center absorption energies remain a challenge and are scarce. In this work we present state-of-the-art ab-initio calculations of the F center in LiF and other alkali halides. We find unprecedented agreement between experimental and theoretical absorption energies and give a detailed picture of the light-absorption process.

In 1931 Mollwo [9] realized that the absorption energies, E_{abs} , of F centers in alkali halides are related to the anion-cation distance, a , of the corresponding crystals by $E_{abs} \propto 1/a^n$. Later, based on a large set of alkali halides, Ivey [10] determined the exponent to be $n = 1.8$. The origin of this exponent has been debated since the Mollwo–Ivey scaling was discovered. The most accepted explanations [11, 12] are based on the scaling of the crystal-Madelung potential. In this interpretation element-specific effects play a minor role. We show in this thesis that the opposite

is true: element-specific effects are responsible for the exponent $n = 1.81$ in the Mollwo–Ivey relation.

In the second topic of this thesis we investigate the charge transfer during scattering of a proton and a lithium-fluoride surface which is a prototypical example for particle-surface scattering. Interactions of heavy particles such as ions, atoms, and molecules with surfaces affect our daily life. Applications range from the radiation damage on satellite surfaces due to solar winds over ion implantation, focused ion-beam techniques applied in semiconductor device fabrication (lithography, nano patterning), to metal finishing (tool steel hardening), and catalytic reactions at surfaces in, e.g., the catalytic converter in cars. A currently important topic is the particle-wall interaction in plasma fusion reactors, in particular, the degradation of the walls confining the plasma. Also in surface analytics methods, such as ion scattering spectroscopy (ISS), low (medium) energy ion spectroscopy (L(M)EIS), secondary ion (neutral) mass spectroscopy (SI(N)MS), Rutherford backscattering spectroscopy (RBS) the physics of particle-surface interactions is exploited.

In 1995 Winter and coworkers found that atoms scattered off alkali-halide surfaces [13, 14] predominantly return as negatively charged ions. This came as a surprise since the charge transfer from alkali-halide surfaces to projectiles was expected to be inefficient since the valence electrons are tightly bound to the anionic sites. The explanation for the high efficiency of the charge transfer invokes the level shift due to the particle-surface interaction [14] that brings the surface-donor and projectile-acceptor level in close resonance. (Quasi-) Resonant charge transfer occurs in many particle-surface combinations [15] but accurate ab-initio descriptions are missing due to the complexity of the system. The charge transfer is induced by the impinging projectile. Electronic and nuclear degrees of freedom are, therefore, coupled and have to be treated simultaneously. Wirtz et al. [16] analyzed ab-initio potential-energy surfaces of electronic states involved in the charge transfer but did not include the motion of the projectile. We extend this work and present in this thesis a time-dependent study of the charge transfer between a proton and a lithium-fluoride surface. In our study electronic and nuclear degrees of freedom are coupled in terms of non-adiabatic molecular dynamics. We provide a detailed microscopic picture of the charge transfer and investigate questions such as how many F^- ions contribute to the charge transfer and how does the charge transfer depend on initial kinematic properties of the proton. We also compare our data on the proton-neutralization probability to (preliminary) experimental data.

The most widely used ab-initio method in solid-state and surface physics is density-functional theory (DFT) in the periodic-boundary implementation. One aspect of this thesis is to explore an alternative approach: we apply quantum-chemistry methods in the framework of the embedded cluster approach (ECA). We use quantum chemistry (QC) since (a) it allows for including correlation effects of localized electrons beyond standard DFT approaches, (b) standard DFT strongly underestimates the band gaps of alkali-halide crystals [17], (c) QC is a powerful tool for calcula-

tion of excited electronic states and the non-adiabatic couplings between them, and (d) DFT as well as time-dependent DFT (TD-DFT) face fundamental difficulties in describing charge-transfer processes [18–21]. The embedded cluster approach is chosen since (a) the Coulomb field of the proton in the charge-transfer problem would require huge supercells or the use of unphysical neutralizing background charges, and (b) periodic boundary implementations of methods beyond Hartree–Fock are very scarce and do not allow for the calculation of excited states (see [22] and references in there). These advantages of quantum chemistry and/or the embedded cluster approach have been used in several studies describing particle-surface interaction and reactions at surfaces. Some of these studies solely use the properties of the potential-energy surfaces to, e.g., extract reaction barriers and identify reaction pathways (see, e.g., [23–27]). Other studies include also the nuclear motion of the particle in front of the surface (see, e.g., [28–31]). So far, however, the coupling of nuclear and electronic degrees of freedom has been treated only in an approximate way. In this thesis we include the nuclear-electronic coupling on an ab-initio level opening the path to an ab-initio description of charge transfer between particle and surface.

The thesis is structured as follows: in chapter 2 we briefly introduce the quantum chemistry methods used throughout the thesis. It is a very “qualitative” introduction and meant for readers only vaguely familiar with standard quantum chemistry. Strengths and weaknesses of various methods are compared and one goal of the chapter is to give the reader an impression of the suitability of a special method for a given system. Chapter 3 and 4 are devoted to the F-type color center defect in alkali-halide crystals. In chapter 3 we focus on the F-center in LiF and study in detail properties such as the absorption energy, the shape of the F-center wave function in its ground and excited state, lattice relaxation, the influence of electron-phonon coupling, the relaxed excited state, and the line width of the absorption. In chapter 4 we extend this investigation to other alkali-halide crystals and present the first ab-initio study of the Mollwo–Ivey relation. In chapter 5 we give an introduction to non-adiabatic dynamics and the methods used to solve the time-dependent Schrödinger equation for coupled nuclear and electronic degrees of freedom, in particular, wave packet propagation on coupled potential energy surfaces and Tully’s semi-classical surface hopping algorithm. We first benchmark these time-dependent approaches by applying them to the charge transfer in ion-atom collisions. Chapter 6 is devoted to the charge transfer during the scattering of a proton from an LiF surface. We present the first ab-initio analysis of the transfer process and determine the neutralization probability of the rescattered projectile. We conclude this thesis with a summary and an outlook 7 in which we point to further particle-surface and particle-solid interaction problems the embedded cluster approach could help to solve.

Publications

Parts of the results discussed in this work have been published in peer-reviewed journals. A list of publications is given below with a reference to the respective chapter of this thesis.

F-type color center in alkali-halide crystals (chapters 3 and 4)

- F Karsai, P Tiwald, R Laskowski, F Tran, D Kollar, S Gräfe, J Burgdörfer, L Wirtz, P Blaha
F center in lithium fluoride revisited: Comparison of solid-state physics and quantum-chemistry approach
Physical Review B **89** 125429, 2014
- P Tiwald, F Karsai, R Laskowski, S Gräfe, P Blaha, J Burgdörfer, L Wirtz
Ab-initio perspective on the Mollwo–Ivey relation for F centers in alkali halides
Physical Review B **92** 144107, 2015

Charge transfer in proton - lithium fluoride scattering (chapter 5)

- P Tiwald, S Gräfe, J Burgdörfer, L Wirtz
Towards an ab-initio description of the charge transfer between a proton and a lithium fluoride surface: A quantum chemistry approach
Nuclear Instruments and Methods in Physics Research Section B Beam Interactions with Materials and Atoms **317** 18, 2012

other topics

- P Tiwald, C Lemell, A Schüller, H Winter, J Burgdörfer
Atomic scattering potentials for an aluminum surface: Test of ab initio calculations
Nuclear Instruments and Methods in Physics Research Section B Beam Interactions with Materials and Atoms **269** 1221, 2011
- P Tiwald, C Lemell, G Wachter, J Burgdörfer
Theory of below-threshold kinetic electron emission
Journal of Physics: Conference Series **257** 012012, 2010

- P Tiwald, A Schüller, H Winter, K Tökesi, F Aigner, S Gräfe, C Lemell, J Burgdörfer
Interaction potentials for fast atoms in front of Al surfaces probed by rainbow scattering
Physical Review B **82** 125453, 2010

2. Introduction to quantum chemistry

The term quantum chemistry denotes all methods and strategies to (approximately) solve the electronic Schrödinger equation of a given atom, molecule, or solid by approximating the correlated many-electron wave functions of ground and excited states. In this sense quantum chemistry has to be distinguished from other methods such as Density Functional Theory (DFT) which approximates the total energy of an electronic system in terms of their reduced one-electron density.

Although the goal of this thesis was not to develop a new quantum chemistry method, this chapter is dedicated to quantum chemistry since it plays a crucial role in the following discussion. This chapter does not feature a complete and detailed review of quantum chemistry but it should introduce the reader in a “qualitative” way to the basics of the methods used and highlight their properties as well as their strengths and weaknesses. This basic knowledge is important to understand and interpret the results shown in the following chapters. Experienced readers might skip this chapter. Readers searching for a more detailed introduction to quantum chemistry are referred to the vast amount of literature on this topic such as the books used to write this chapter [32–34].

This chapter starts out with the definition of the so-called molecular Hamiltonian and the solution of the corresponding Schrödinger equation by the Hartree–Fock approximation which is the starting point for all correlated methods. Afterwards correlated methods ranging from the Multi-Configurational Self-Consistent Field (MCSCF) method up to the Coupled Cluster methods are briefly discussed. Their strategies to include correlation are highlighted and they will be classified in terms of the “kind” of correlation (static and/or dynamic) they account for.

2.1. The Hartree–Fock approximation

The non-relativistic Hamiltonian of a system consisting of N_n nuclei and N_e electrons reads

$$\hat{H}_{\text{tot}} = \hat{T}_n + \hat{T}_e + \hat{V}_{ne} + \hat{V}_{ee} + \hat{V}_{nn}, \quad (2.1)$$

where \hat{T}_n and \hat{T}_e are the kinetic energy operators of nuclei and electrons, respectively. \hat{V}_{nn} , \hat{V}_{ee} , and \hat{V}_{ne} denote the Coulomb interaction between the nuclei (nn), the electrons (ee), and between nuclei and electrons (ne), respectively. After the transformation to the center of mass system and neglecting the center of mass motion as well as the mass-polarization term it can be written as

$$\hat{H}_{\text{tot}} = \hat{T}_n + \hat{H}_e, \quad (2.2)$$

where \hat{H}_e is the electronic Hamilton operator

$$\hat{H}_e = \hat{T}_e + \hat{V}_{ne} + \hat{V}_{ee} + \hat{V}_{nn}. \quad (2.3)$$

In the Born–Oppenheimer or adiabatic approximation the motion of the nuclei \hat{T}_n is neglected and $\hat{H}_{\text{tot}} = \hat{H}_e$. They are “clamped” to certain positions which enter the electronic Hamiltonian via \hat{V}_{ne} and \hat{V}_{nn} as parameters. What happens when the Born–Oppenheimer approximation breaks down is discussed in detail in chapter 5. The stationary electronic Schrödinger equation in the Born–Oppenheimer approximation reads

$$\hat{H}_e \Psi(\vec{r}_1, \vec{r}_2, \dots, \vec{r}_{N_e}; \vec{R}_1, \vec{R}_2, \dots, \vec{R}_{N_n}) = \quad (2.4)$$

$$E_e(\vec{R}_1, \vec{R}_2, \dots, \vec{R}_{N_n}) \Psi(\vec{r}_1, \vec{r}_2, \dots, \vec{r}_{N_e}; \vec{R}_1, \vec{R}_2, \dots, \vec{R}_{N_n}), \quad (2.5)$$

with Ψ the N_e -electron wave function, $\vec{r}_1, \vec{r}_2, \dots, \vec{r}_{N_e}$ the electronic and $\vec{R}_1, \dots, \vec{R}_{N_n}$ the nuclear degrees of freedom, and E_e the total electronic energy, parametrically depending on the nuclear coordinates. \hat{H}_e in its explicit form reads

$$\hat{H}_e = \sum_i^{N_e} \left(-\frac{1}{2} \nabla_i^2\right) - \sum_a^{N_n} \sum_i^{N_e} \frac{Z_a}{|\vec{R}_a - \vec{r}_i|} + \sum_i^{N_e} \sum_{j>i}^{N_e} \frac{1}{|\vec{r}_i - \vec{r}_j|} + \sum_a^{N_n} \sum_{b>a}^{N_n} \frac{Z_a Z_b}{|\vec{R}_a - \vec{R}_b|}. \quad (2.6)$$

Contracting the different operators according to their number of electron indices leads to the more compact form

$$\hat{H}_e = \sum_i^{N_e} \hat{h}_i + \sum_i^{N_e} \sum_{j>i}^{N_e} \hat{g}_{ij} + \hat{V}_{nn}, \quad (2.7)$$

with

$$\begin{aligned}\hat{h}_i &= -\frac{1}{2}\nabla_i^2 - \sum_a^{N_n} \frac{Z_a}{|\vec{R}_a - \vec{r}_i|} \\ \hat{g}_{ij} &= \frac{1}{|\vec{r}_i - \vec{r}_j|},\end{aligned}\tag{2.8}$$

where the one-body operator \hat{h}_i describes the motion of a single electron in the field of all the nuclei and the two-body operator \hat{g}_{ij} accounts for the mutual repulsion between the electrons.

The Hartree approximation states that the total N_e -electron wave function $\Psi_{\text{H}}(\vec{r}_1, \vec{r}_2, \dots, \vec{r}_{N_e})$ can be written as a product of single-particle wave functions $\phi_i(\vec{r})$

$$\Psi_{\text{H}}(\vec{r}_1, \vec{r}_2, \dots, \vec{r}_{N_e}) = \phi_1(\vec{r}) \cdot \phi_2(\vec{r}) \dots \phi_{N_e}(\vec{r}).\tag{2.9}$$

In the Hartree–Fock approximation the total wave function is approximated by a Slater determinant

$$\Psi_{\text{HF}}(\vec{r}_1, \vec{r}_2, \dots, \vec{r}_{N_e}) = \frac{1}{\sqrt{N_e!}} \begin{vmatrix} \phi_1(1) & \phi_2(1) & \cdots & \phi_{N_e}(1) \\ \phi_1(2) & \phi_2(2) & \cdots & \phi_{N_e}(2) \\ \vdots & \vdots & \ddots & \vdots \\ \phi_1(N_e) & \phi_2(N_e) & \cdots & \phi_{N_e}(N_e) \end{vmatrix},\tag{2.10}$$

where we introduce the short hand notation $\phi_i(\vec{r}_j) = \phi_i(j)$. The Slater determinant is anti-symmetric under the interchange of any pair of electron coordinates which accounts for the Pauli principle.

The single-particle wave functions $\phi_i(\vec{r})$ are often called molecular orbitals or spin orbitals and are themselves a product of two components

$$\phi_i(\vec{r}) = \tilde{\phi}_i(\vec{r}) \cdot \xi_i,\tag{2.11}$$

where $\tilde{\phi}_i(\vec{r})$ is the real-space wave function and ξ_i denotes the spin function. Due to the neglect of relativistic effects, spin is introduced ad hoc. Each electron has a spin of $\frac{1}{2}$ with the possible orientations of spin-up and spin-down in, e.g., the z-direction. These two options are represented by $\xi = |\alpha\rangle$ or $\xi = |\beta\rangle$, respectively, where $|\alpha\rangle$ and $|\beta\rangle$ obey the orthonormality conditions

$$\begin{aligned}\langle\alpha|\alpha\rangle &= \langle\beta|\beta\rangle = 1 \\ \langle\alpha|\beta\rangle &= \langle\beta|\alpha\rangle = 0.\end{aligned}\tag{2.12}$$

The Hartree–Fock equations

The energy expectation value of a normalized Hartree–Fock type Slater determinant Ψ_{HF} is given by

$$E_{\text{HF}} = \langle \Psi_{\text{HF}} | \hat{H}_e | \Psi_{\text{HF}} \rangle. \quad (2.13)$$

Inserting $|\Psi_{\text{HF}}\rangle$ of eq. 2.10 and \hat{H}_e of eq. 2.7 leads to [32, 33]

$$E_{\text{HF}} = \sum_i^{N_e} \langle \phi_i | \hat{h}_i | \phi_i \rangle + \frac{1}{2} \sum_i^{N_e} \sum_j^{N_e} \left(\langle \phi_j | \hat{J}_i | \phi_j \rangle - \langle \phi_j | \hat{K}_i | \phi_j \rangle \right) + \hat{V}_{nn}. \quad (2.14)$$

The operators \hat{J}_i and \hat{K}_i are called the Coulomb and exchange operator, respectively and are given by

$$\begin{aligned} \hat{J}_i | \phi_j(2) \rangle &= \langle \phi_i(1) | \hat{g}_{ij} | \phi_i(1) \rangle | \phi_j(2) \rangle \\ \hat{K}_i | \phi_j(2) \rangle &= \langle \phi_i(1) | \hat{g}_{ij} | \phi_j(1) \rangle | \phi_i(2) \rangle. \end{aligned} \quad (2.15)$$

In contrast to the forms of the Hamiltonian in eqs. 2.6 and 2.7 the double sum in eq. 2.14 is allowed to run over all possible values due to the factor $\frac{1}{2}$ and due to the fact that Coulomb and exchange term cancel each other if $i = j$. These two features ensure that double counting of energy contributions as well as the so called self-interaction of an electron with its own charge distribution are properly excluded.

The solution of the stationary Schrödinger equation (eq. 2.4) is equivalent to a variation of the wave function Ψ such that the global minimum of the energy $E_e[\Psi]$ as a functional of the wave function is found. The goal of a Hartree–Fock calculation is to find the optimal set of molecular orbitals $\{\phi_i\}$ such that the wave function Ψ_{HF} corresponds to the minimal energy E_{HF} . For systems with more than a single electron $E_{\text{HF}} > E_{\text{exact}}$ due to the use of an anti-symmetrized product ansatz for Ψ_{HF} . The variation with respect to the molecular orbitals is done under the constraint that the orthonormality of the spin orbitals $\langle \phi_i | \phi_j \rangle$ is not violated. Such a constrained optimization is formulated using Lagrange multipliers and reads

$$\frac{\delta}{\delta \langle \phi_i |} \left[E_{\text{HF}} [\{\phi_k\}_{k=1, \dots, N_e}] - \sum_{l,j}^{N_e} \lambda_{lj} (\langle \phi_l | \phi_j \rangle - \delta_{lj}) \right] = 0. \quad (2.16)$$

This optimization leads to a set of coupled equations [32, 33] called the Hartree–Fock equations

$$\left[\hat{h}_i + \sum_j^{N_e} (\hat{J}_j - \hat{K}_j) \right] \phi_i = \sum_j^{N_e} \lambda_{ij} \phi_j, \quad (2.17)$$

which can be written with the so-called Fock operator $\hat{F}_i = \hat{h}_i + \sum_j^{N_e} (\hat{J}_j - \hat{K}_j)$ as

$$\hat{F}_i \phi_i = \sum_j^{N_e} \lambda_{ij} \phi_j. \quad (2.18)$$

With a unitary transformation that makes the matrix of Lagrange multipliers diagonal, i.e. $\lambda_{ij} = 0$ and $\lambda_{ii} = \epsilon_i$, the HF equations can be simplified to

$$\hat{F}_i \phi_i = \epsilon_i \phi_i. \quad (2.19)$$

The set of orbitals $\{\phi_i\}$ that diagonalizes the Fock operator is called the set of canonical orbitals which we use in the following. Any other set of orbitals $\{\tilde{\phi}_i\}$ that obeys eq. 2.18 but does not diagonalize the Fock operator, leads to different orbital shapes and different diagonal elements of λ_{ij} while leaving the Hartree–Fock approximation to the total energy E_{HF} (eq. 2.14) unchanged. In the canonical form of eq. 2.19 the physical interpretation of the Lagrange multipliers becomes obvious being the energies ϵ_i of the corresponding Hartree–Fock orbitals ϕ_i . According to Koopmans’ theorem (see e.g. [32]), the canonical energies ϵ_i of occupied orbitals ($i \leq N_e$) can be interpreted as the energy needed to remove an electron from the orbital ϕ_i of the N_e -electron system. For unoccupied, i.e. virtual orbitals (see below), ϵ_r ($r > N_e$) is the energy needed or gained by adding an electron to orbital ϕ_j of the N_e -electron system.

Since the Fock operator depends on all the spin orbitals via the Coulomb and the exchange operator this set of equations can only be solved iteratively, i.e., self-consistently. Further the electron–electron repulsion is only treated in an average fashion, i.e., in a mean-field approximation. These two facts lead to the name self-consistent field (SCF) approximation which is equivalently used for the term Hartree–Fock approximation in the field of quantum chemistry.

The total energy of a Hartree–Fock wave function can be written in terms of the spin orbital energies as

$$E_{\text{HF}} = \sum_i^{N_e} \epsilon_i - \frac{1}{2} \sum_{ij}^{N_e} (J_{ij} - K_{ij}) + V_{nn}, \quad (2.20)$$

with

$$\epsilon_i = \langle \phi_i | \hat{F} | \phi_i \rangle = h_i + \sum_j^{N_e} (J_{ij} - K_{ij}), \quad (2.21)$$

and h_i , J_{ij} , and K_{ij} being the matrix elements of the one-body Hamiltonian \hat{h}_i , the Coulomb, and the exchange operator, respectively. The sum over the orbital energies ϵ_i is not the total energy of the Hartree–Fock wave function due to the mean-field character of the Hartree–Fock approximation. ϵ_i includes Coulomb and exchange interaction of the electron ϕ_i with all other occupied electrons, in particular, ϕ_j . Also ϵ_j includes the Coulomb and exchange interactions with all other occupied electrons, in particular, with ϕ_i . The sum $\epsilon_i + \epsilon_j$, therefore, counts the electron–electron interactions twice and makes the subtraction of half the Coulomb and exchange energy in eq. 2.20 necessary.

Restricted and Unrestricted Hartree–Fock

Up to now the Hartree–Fock equations are discussed in their most general form in which every spin orbital is occupied by a single electron. This form is called the Unrestricted Hartree–Fock (UHF) approach since it allows for arbitrary occupation of orbitals with $|\alpha\rangle$ and $|\beta\rangle$ spin. It has, however, the disadvantage of producing a wave function which is not an exact eigenstate of the \hat{S}^2 operator, an effect known as spin contamination.

For singlet, i.e., closed-shell wave functions one can simplify the HF description by forcing the spatial part of the orbitals with $|\alpha\rangle$ and $|\beta\rangle$ spin to be identical. In this case one orbital is occupied by two electrons and the dimension of the matrices in equation 2.24 can be reduced by a factor of two. This procedure comes with the name Restricted Hartree–Fock (RHF) approach which is somewhat misleading since for closed-shell systems (at least in the vicinity of the equilibrium geometry) the results of UHF and RHF are essentially identical.

Treating, however, open-shell systems with identical spatial parts for α and β orbitals is a true restriction. This approach has the name Restricted Open-shell Hartree–Fock (ROHF) and the total energy obtained from such a calculation will always be larger than the one obtained in UHF. While in UHF and RHF canonical orbitals and energies ϵ_i are well defined, it is not possible in ROHF to find a set of orbitals [32, 33] that diagonalizes the matrix of Lagrange multipliers λ_{ij} in equation 2.18. Therefore, orbital shapes and energies are not uniquely defined and cannot be interpreted according to Koopmans’ theorem. Nevertheless, ROHF is routinely used as starting point for correlated methods since it limits the computational costs due to the reduced number of orbitals and results of correlated methods only weakly depend on the choice of ROHF orbitals (see, e.g., [35]).

Solving the Hartree–Fock equations on a computer: Introduction of basis functions

In most quantum chemistry program packages the orbitals are expanded into a total number of N_B , so-called, Gaussian basis functions, $\chi_j(\vec{r})$, localized at the atoms, i.e. sites, of the system

$$\phi_i(\vec{r}) = \sum_j^{N_B} c_{ij} \chi_j(\vec{r}). \quad (2.22)$$

This notation is somewhat simplified since the sum contains both (a) the sum over the atoms and (b) the sum over the basis sets per atom. Further, we dropped the positions \vec{R}_k of the atoms at which the different basis functions are centered. In polar coordinates a basis function located at $\vec{R} = 0$ reads

$$\chi_j(\vec{r}) = \chi_{\zeta,n,l,m}(r, \theta, \varphi) = N Y_{l,m}(\theta, \varphi) r^{2n-2-l} e^{-\zeta r^2}, \quad (2.23)$$

where N is a normalization constant and $Y_{l,m}$ are the spherical harmonics.

Inserting the expansion in eq. 2.22 into the Hartree–Fock equations leads to the so called Hartree–Fock-Roothaan equations which read in matrix form

$$\mathbf{FC} = \mathbf{SC}\epsilon. \quad (2.24)$$

\mathbf{F} is the Fock matrix containing the matrix elements of the Fock operator $\langle \chi_i | \hat{F} | \chi_j \rangle$, \mathbf{C} is the matrix of the expansion coefficients c_{ij} , \mathbf{S} is the so-called overlap matrix $\langle \chi_i | \chi_j \rangle$, and ϵ is a diagonal matrix containing the orbital energies ϵ_i . All matrices are of dimension $N_B \times N_B$. The (self-consistent) solution of the Hartree–Fock-Roothaan equations leads to a spectrum of N_B orbital energies ϵ_i . For a system with N_e electrons, N_e of these orbitals “host” an electron and are, therefore, called *occupied* orbitals. Furthermore, there are $N_{virt} = N_B - N_e$ unoccupied, so-called *virtual* orbitals.

In the following we schematically depict a RHF wave function, i.e., a RHF Slater determinant (fig. 2.1) as follows. When N_B basis functions are used in a calculation the solution of the HF equations leads to N_B orbitals with their corresponding orbital energies. Both are indicated by horizontal bars. For a closed-shell system with N_e electrons $N_e/2$ orbitals are occupied by two electrons, one with spin $|\alpha\rangle$ and one with spin $|\beta\rangle$, respectively. The electrons are depicted by the arrows the direction of which indicate their corresponding spin. “Empty” horizontal lines represent the $N_B - N_e/2$ unoccupied, i.e., virtual orbitals.

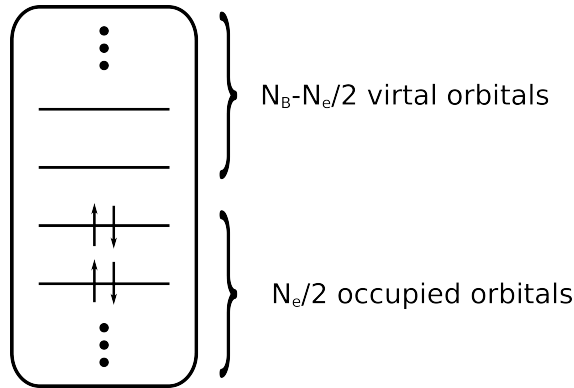


Figure 2.1.: Schematic picture of a closed-shell Hartree–Fock determinant with N_e electrons and, consequently, $N_e/2$ occupied HF orbitals. With a total number of N_B basis functions used, there are $N_B - N_e/2$ virtual, i.e., unoccupied orbitals.

Correlation energy

Due to the product form of a Slater determinant the HF approach treats the interaction between electrons in a mean-field fashion. This becomes manifest in the form of the HF equations 2.19 each of which describes the motion of a single electron in a static potential or “field” created by all the other electrons. Such a single-particle approach neglects the correlated motion of two or more electrons. Therefore, the energy difference between the exact energy of a system, E_{exact} , and the HF energy, E_{HF} , is termed correlation energy E_{corr} . There are, however, different “flavors” of Hartree–Fock namely UHF, ROHF, and RHF and there is no uniform definition as to which flavor E_{HF} refers to. For the remainder of this work we define correlation energy as difference between the exact energy E_{exact} and the HF energy, $E_{\text{HF}} = E_{\text{R(O)HF}}$, corresponding to a restricted (open or closed shell) HF wave function

$$E_{\text{corr}} = E_{\text{exact}} - E_{\text{HF}} = E_{\text{exact}} - E_{\text{R(O)HF}}. \quad (2.25)$$

This choice is made because restricted HF wave functions are the starting points for correlated methods applied in this thesis.

2.2. Methods for treating correlations

There are several ways of dividing the correlation energy into different parts. One can discern, e.g., between inter- and intra-orbital correlation or between Coulomb and Fermi correlation. The latter denotes the correlation between electrons of op-

posite and equal spin, respectively. In the remainder of this thesis we use the quantum-chemistry standard distinction between *dynamic* and *static* correlation. This is not a mathematically rigorous definition and there is no clear border between these two contributions but they are very intuitive and help to group and classify the various quantum chemistry methods. Dynamic correlation denotes the portion of correlation resulting from the mutual Coulomb repulsion between the electrons like, for example, two electrons occupying the same spatial orbital. Static correlation arises from the possibility that the HF wave function can be (nearly) degenerate with excited Slater determinants corresponding to different electronic configurations. Dynamic correlation is present in every physical system containing more than one electron and always needs to be taken into account when a quantitative description of a system is desired. Static correlation is not necessarily of importance for calculating ground state properties. When the ground state energy of a system is energetically well separated from the excited states static correlation can be usually neglected. This is often the case for chemically inert systems close to their equilibrium geometry. A system which belongs to this class of problems is the F-type color center in alkali-halide crystals (chapters 3 and 4). As soon as two or more configurations become energetically nearly degenerate static correlation needs to be included. A prototypical example are charge transfer processes. The ground state of a diatomic LiF molecule at equilibrium inter-nuclear distance has an ionic configuration, the molecule “consists” of an F^- and a Li^+ ion. For large distances between the two particles, however, the ground state corresponds to two neutral atoms. This implies that there is a critical distance at which both configurations $F^- + Li^+$ and $F + Li$ are degenerate. This situation is encountered in chapter 6 where we treat the charge transfer between a proton and a lithium-fluoride crystal. For systems where only dynamic correlation is of importance, the HF wave function typically gives a qualitatively good description and is a good starting point for calculations of dynamic correlation. The most commonly methods used are Configuration Interaction (CI), the Møller–Plesset perturbation theory of second order (MP2), and coupled cluster methods. These three approximations to the correlation energy will be very briefly reviewed in sections 2.2.1, 2.2.2, and 2.2.3, respectively. When static correlation is present the HF wave function is typically not capable of even qualitatively describing the system under consideration and is not suitable as a starting point for correlation calculations. However, static correlation is usually well included by the so called Multi-configurational self-consistent field (MCSCF) method. Dynamic correlation is, however, not accounted for and can be calculated with Multi-Reference CI (MRCI) and Complete active space perturbation theory (CASPT2). Both methods use the MCSCF wave function as starting point which makes them account for both static and dynamic correlation. The MRCI and CASPT2 methods are briefly reviewed in sections 2.2.4, and 2.2.6, respectively.

2.2.1. Configuration Interaction with singles and doubles

The idea of a Configuration Interaction (CI) is to expand the total electronic wave function into the HF wave function and a sum of so-called excited Slater determinants. In an excited Slater determinant one or more orbitals, occupied in the HF determinant, are replaced by orbitals initially belonging to the virtual, i.e., unoccupied space. An equivalent formulation is that one or more electrons are excited from the HF determinant into virtual orbitals. Depending on the number of excited electrons in a given determinant one speaks of a singly, double, triply,... excited determinant when one, two, three,... electrons occupy virtual orbitals, respectively (fig. 2.2).

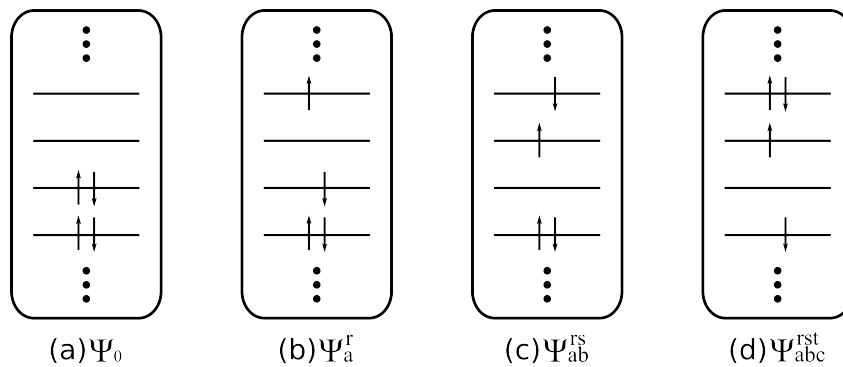


Figure 2.2.: Schematic picture of the Hartree–Fock determinant (a), a singly (b), doubly (c), and triply (d) excited Slater determinant.

We denote the Hartree–Fock wave function by $\Psi_{\text{HF}} = \Psi_0$ and a singly excited determinant by Ψ_a^r . The two indices mean that one electron from an initially occupied orbital a is excited to a virtual orbital r . Doubly and triply excited determinants are, therefore, denoted by Ψ_{ab}^{rs} and Ψ_{abc}^{rst} , respectively. With this notation we can write the exact many-electron wave function as

$$\Psi_{\text{FCI}} = c_0 \Psi_0 + \sum_{ar} c_a^r \Psi_a^r + \sum_{\substack{a<b \\ r<s}} c_{ab}^{rs} \Psi_{ab}^{rs} \quad (2.26)$$

$$+ \sum_{\substack{a<b<c \\ r<s<t}} c_{abc}^{rst} \Psi_{abc}^{rst} + \sum_{\substack{a<b<c<d \\ r<s<t<u}} c_{abcd}^{rstu} \Psi_{abcd}^{rstu} + \dots \quad (2.27)$$

This form is called a full-CI (FCI) expansion since every possible determinant is included. In the limit of a complete basis set this is a numerically exact solution of the many-electron Schrödinger equation. The summation limits ensure that there is no double counting of determinants. The coefficients c_{\dots} are the so-called CI coefficients and their absolute magnitude corresponds to the weight a given determinant contributes to the total wave function. They are optimized in a variational

approach minimizing the energy $E_{\text{FCI}} = \langle \Psi_{\text{FCI}} | \hat{H} | \Psi_{\text{FCI}} \rangle$ corresponding to the FCI wave function.

A full CI calculation includes all types of correlation and its accuracy is solely limited by the basis set size. Unfortunately, an FCI is only feasible for very small systems due to factorially growing number of determinants with atoms/basis sets. In practice one uses truncated CI approaches such as the CI with singles and doubles (CISD) in which only singly and doubly excited determinants are included. The CISD wave function is, therefore, given by

$$\Psi_{\text{CISD}} = c_0 \Psi_0 + \sum_{ar} c_a^r \Psi_a^r + \sum_{\substack{a < b \\ r < s}} c_{ab}^{rs} \Psi_{ab}^{rs}. \quad (2.28)$$

For systems with a single-determinant character, i.e. systems well described by the HF wave function, this is a good approximation. It can be shown that doubly excited determinants account for the major part of correlation energy, larger than the contribution of, e.g., triply and quadruply excited determinants. The CISD wave function is a so-called single-reference wave function, since it contains doubly excited determinants only with respect to the Ψ_{HF} , a single-determinant wave function. Therefore, the CISD is referred to as primarily accounting for dynamic correlation.

A shortcoming of the CISD (actually of all CI expansions, except for a full CI) is the lack of size extensivity: the larger the system, i.e. the number of electrons, gets the smaller is the fraction of correlation energy captured by CISD. Mathematically size extensivity can be expressed as follows [36]. Consider a system of N interacting subsystems A . When the correlation energy E_{corr} determined by a given quantum chemistry method scales with the system size like

$$\lim_{N \rightarrow \infty} \frac{E_{\text{corr}}(N \cdot A)}{N} = \text{const}, \quad (2.29)$$

then the method is size extensive. Lack of size extensivity in CISD is problematic for large systems and when systems of different sizes are compared. In the latter case an error is induced since, effectively, the smaller system is calculated with a higher accuracy although for both the CISD is used.

The reason for this can be explained more intuitively by the related concept of size consistency. Consider two H_2 molecules A and B separated by a large distance. When the CISD energy of each molecule $E(A)$, $E(B)$ is calculated separately, each individual calculation corresponds to a full CI and the total energy is given by $E(A)+E(B)$. When the total energy of the two molecules is determined in a single CISD calculation $E(A+B)$ it does not correspond to an FCI energy. For example, quadruply excited states are not included. Therefore, the CISD calculation of the combined system is effectively of lower quality leading to $E(A+B) \neq E(A)+E(B)$. For

a more detailed discussion of the concepts of size extensivity and size consistency see [36]. The most important properties of the CISD approach (and all other methods accounting for correlation energy) are summarized in table 2.1 at the end of sec. 2.2.

2.2.2. Møller–Plesset perturbation theory of second order

Instead of expanding the total wave function in terms of excited Slater determinants the Møller–Plesset approach is based on the Rayleigh–Schrödinger perturbation theory. The Hamiltonian is split into an unperturbed (solvable) part \hat{H}_0 and a perturbation \hat{V}

$$\hat{H}_e = \hat{H}_0 + \hat{V}. \quad (2.30)$$

In the most common formulation of Møller–Plesset perturbation theory the unperturbed part is given by the sum over the single-particle Fock operators

$$\hat{H}_0 = \sum_i \hat{F}_i = \sum_i [\hat{h}_i + \hat{v}_i^{HF}], \quad (2.31)$$

where $\hat{v}_i^{HF} = \sum_j^{N_e} (\hat{J}_j - \hat{K}_j)$ is the so-called Hartree–Fock potential. The perturbation is given by the electron–electron Coulomb interaction minus the part of electron–electron interaction already included in \hat{H}_0

$$\hat{V} = \sum_{i<j} \frac{1}{|\vec{r}_i - \vec{r}_j|} - \sum_i \hat{v}_i^{HF} = \sum_{i<j} \hat{g}_{ij} - \sum_i \hat{v}_i^{HF}. \quad (2.32)$$

The energy of the system in 0th order approximation is given by

$$E_{\text{MP0}} = E^{(0)} = \langle \Psi_{\text{HF}} | \hat{H}_0 | \Psi_{\text{HF}} \rangle = \sum_i \langle \phi_i | \hat{F}_i | \phi_i \rangle = \sum_i \epsilon_i, \quad (2.33)$$

which is just the sum over all occupied HF-orbital energies. According to Rayleigh–Schrödinger perturbation theory the first order correction is given by

$$\langle \Psi_{\text{HF}} | \hat{V} | \Psi_{\text{HF}} \rangle = -\frac{1}{2} \sum_{i,j} (J_{ij} - K_{ij}). \quad (2.34)$$

The MP1 energy, therefore, is equal to the HF energy since

$$E_{\text{MP1}} = E^0 + E^1 = \sum_i \epsilon_i - \frac{1}{2} \sum_{i,j} (J_{ij} - K_{ij}) = E_{\text{HF}}. \quad (2.35)$$

The first correction to the HF energy comes with the second-order contribution

$$E^{(2)} = \sum_{n \neq \Psi_{\text{HF}}} \frac{|\langle \Psi_{\text{HF}} | \hat{V} | n \rangle|^2}{E_{\text{HF}} - E_n}. \quad (2.36)$$

The index n denotes excited states given by excited Slater determinants. For singly excited determinants the matrix element $\langle \Psi_{\text{HF}} | \hat{V} | n \rangle$ reads

$$\begin{aligned} \langle \Psi_{\text{HF}} | \hat{V} | \Psi_a^r \rangle &= \langle \Psi_{\text{HF}} | \hat{H} | \Psi_a^r \rangle - \langle \Psi_{\text{HF}} | \hat{H}_0 | \Psi_a^r \rangle \\ &= \langle \Psi_{\text{HF}} | \hat{H} | \Psi_a^r \rangle - \langle \Psi_{\text{HF}} | \sum_i \hat{F}_i | \Psi_a^r \rangle \\ &= \langle \Psi_{\text{HF}} | \hat{H} | \Psi_a^r \rangle - \sum_i \epsilon_i \langle \Psi_{\text{HF}} | \Psi_a^r \rangle = 0. \end{aligned} \quad (2.37)$$

Both terms in the last line vanish. The first term is zero due to Brillouin's theorem (see, e.g., [32]) and the second due to the orthogonality of the canonical orbitals. Matrix elements including triply (or higher) excited determinants $\langle \Psi_{\text{HF}} | \hat{V} | \Psi_{abc}^{rst} \rangle$ vanish due to the two-body nature of the operator \hat{V} . Therefore, the matrix element $\langle \Psi_{\text{HF}} | \hat{V} | n \rangle$ is non-zero only for doubly excited determinants Ψ_{ab}^{rs} and eq. 2.36 reduces to

$$E^{(2)} = \sum_{\substack{a < b \\ r < s}} \frac{|\langle \Psi_{\text{HF}} | \hat{V} | \Psi_{ab}^{rs} \rangle|^2}{\epsilon_a + \epsilon_b - \epsilon_r - \epsilon_s} \quad (2.38)$$

$$= \sum_{\substack{a < b \\ r < s}} \frac{|\langle \phi_a(1)\phi_b(2) | \hat{g}_{12} | \phi_r(1)\phi_s(2) \rangle - \langle \phi_a(1)\phi_b(2) | \hat{g}_{12} | \phi_s(1)\phi_r(2) \rangle|^2}{\epsilon_a + \epsilon_b - \epsilon_r - \epsilon_s}, \quad (2.39)$$

leading to a total second-order energy of

$$E_{\text{MP2}} = E_{\text{HF}} + E^{(2)}. \quad (2.40)$$

Since excitations from only a single determinant, the HF wave function, are included the MP2 method primarily accounts for dynamic correlation, too. Obviously the total energy E_{MP2} is not obtained via a variational approach. As a consequence E_{MP2} must not be considered an upper bound for the energy. It is well known that, in many cases, MP2 slightly overestimates the correlation energy and gives too low values for the total energy [33]. Strengths of the MP2 method are its relatively low computational costs and its size extensivity.

2.2.3. Coupled–Cluster methods

One of the most powerful and accurate tools in quantum chemistry are coupled cluster (CC) methods. Their derivation and the underlying formalism is quite lengthy. Therefore, we present only the basic concepts and refer the interested reader to more specialized literature [32–34, 37]. The main idea of coupled cluster methods is to restore or repair the lack of size extensivity of truncated CI expansions. This is done by writing the CC wave function as

$$\Psi_{\text{CC}} = e^{\hat{T}} \Psi_{\text{HF}}, \quad (2.41)$$

where $\hat{T} = \hat{T}_1 + \hat{T}_2 + \hat{T}_3 + \dots$ and \hat{T}_j is a linear combination of all j-type excitations

$$\begin{aligned} \hat{T}_1 \Psi_{\text{HF}} &= \sum_a^{\text{occ}} \sum_r^{\text{virt}} t_a^r \Psi_a^r \\ \hat{T}_2 \Psi_{\text{HF}} &= \sum_{a<b}^{\text{occ}} \sum_{r<s}^{\text{virt}} t_{ab}^{rs} \Psi_{ab}^{rs} \\ &\dots, \end{aligned} \quad (2.42)$$

with $t_a^r, t_{ab}^{rs}, \dots$ are the so-called coupled cluster amplitudes to be determined. Since finding all possible amplitudes is equivalent to a full CI and numerically extremely demanding not all excitations can be included and truncations need to be used. The most common one is CC with singles and doubles (CCSD) with $\hat{T}_{\text{CCSD}} = \hat{T}_1 + \hat{T}_2$ and the coupled cluster wave function

$$\begin{aligned} \Psi_{\text{CCSD}} &= e^{\hat{T}_{\text{CCSD}}} \Psi_{\text{HF}} \\ &= \Psi_{\text{HF}} + \sum_a \sum_r t_a^r \Psi_a^r + \sum_{a<b} \sum_{r<s} t_{ab}^{rs} \Psi_{ab}^{rs} \\ &\quad + \frac{1}{2} \sum_{ab} \sum_{rs} t_a^r t_b^s \Psi_{ab}^{rs} + \frac{1}{2} \sum_{a<b} \sum_{c<d} \sum_{r<s} \sum_{t<u} t_{ab}^{rs} t_{cd}^{tu} \Psi_{abcd}^{rstu} + \dots \end{aligned} \quad (2.43)$$

The form of the wave function makes the advantage of CCSD over CISD in terms of accuracy visible. While the CISD wave function effectively ends after the first three terms in eq. 2.43, the CCSD wave function approximately includes higher excitations (see, e.g., the quadruple excitations in the last term) by estimating their influence in terms of products of lower-excitation amplitudes. These kind of extra terms are called disconnected excitations. The last term in eq. 2.43 corresponds, physically, to the excitation of two non-interacting pairs of interacting electrons. It is explained best by the toy model of two H₂ molecules: for a single H₂ molecule CISD as well as CCSD correspond to a full CI expansion. For two non-interacting,

i.e. well separated, H_2 molecules, however, CISD is not a full CI anymore (triple and quadruple excitations are missing) while CCSD is still equivalent to an FCI. For smaller distances, i.e. when the two H_2 molecules start to interact, also CCSD is not equivalent to an FCI anymore since true, or direct triple and quadruple excitations are missing. The disconnected excitations, however, make coupled-cluster theories size extensive. Even for truncated expansions coupled-cluster total energies cannot be determined variationally due to the large computational effort. Energies are obtained iteratively solving the set of coupled-cluster equations [33] that connect the amplitudes t .

Another acronym appearing in this thesis is CCSD(T) where (T) stands for a perturbative treatment of the contribution of triple excitations. CCSD typically recovers 95% of the correlation energy when large basis sets are used. CCSD(T) reduces the error by another factor of 5 to 10 [38] which makes it one of the most accurate methods still applicable to reasonable system sizes. It is, therefore, often referred to as the “gold standard” of quantum chemistry. Still, CC wave functions account primarily for dynamical correlation since they are based on excitations from Ψ_{HF} .

2.2.4. Multi-configurational self-consistent field

The Multi-configurational self-consistent field (MCSCF) method is quite special since it plays two important roles. First, due to its multi-determinant character it takes into account static correlation between determinants close in energy. Second, it serves as a starting point for the correlation-energy calculation of excited states by providing a new set of orbitals optimized for this purpose.

An MCSCF wave function is, in principle, a truncated CI wave function for which the multi-configuration character is generated as follows. Within the spectrum of HF-orbital energies one defines a so-called active space containing occupied and virtual orbitals (fig. 2.3). Within this space one can allow for, e.g., all possible excitations from occupied to virtual orbitals. This case corresponds to a complete-active space self-consistent field (CASSCF) calculation. One can also restrict the number of excitations by, e.g., defining the maximum occupation number or the maximum number of “holes” of selected orbitals to be one instead of two. This corresponds to a restricted-active space self-consistent field (RASSCF) calculation. The MCSCF wave function is then expanded in terms of the determinants generated by these excitations.

The first conceptual difference between a CISD and an MCSCF lies in the number of excited determinants and in the way they are generated. In a CISD all possible singly and doubly excited determinants are generated with respect to the HF wave function. This produces a large number of determinants which is necessary for the calculation of dynamic correlation. However, all these determinants are at most doubly excited with respect to the HF wave function. In an MCSCF calculation

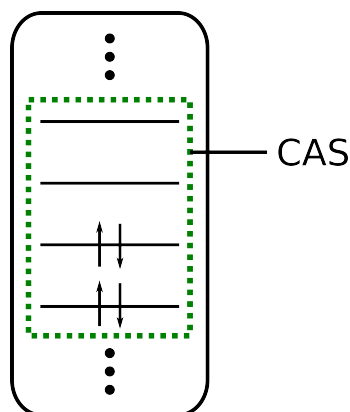


Figure 2.3.: Schematic picture of the Hartree–Fock determinant and the complete-active space (CAS) (green dashed box). The CASSCF (or MCSCF) wave function is a linear combination of all determinants generated by all possible excitations with the CAS.

the number of determinants in the CI expansion is much smaller due to the limited active space. Within this space, however, higher excited Slater determinants are included.

The second conceptual difference makes the MCSCF method suitable for the calculation of excited states. In a CI-type variation of the total energy only the CI coefficients are optimized while the orbitals, generated by a HF calculation, are kept fixed. In an MCSCF calculation, additionally to the CI coefficients, also the orbitals are optimized under the constraint that the sum of ground and excited states of interest $E_0 + E_1 + E_2 + \dots + E_x$ is minimized. This procedure, a so-called state average calculation, produces a set of “average” orbitals corresponding to a better basis for the simultaneous description of ground and excited states and for the calculation of their dynamic correlation in subsequent steps.

The selection of the active space strongly depends on the problem considered. When charge transfer is treated the two (or more) orbitals between which the electron transfer occurs naturally need to be within the active space. Typically, the active space can not be chosen too large since the simultaneous optimization of CI coefficients and orbitals is computationally demanding. Due to the limited active space and the consequently small number of determinants included the MCSCF method is not capable of accounting for dynamic correlation. This deficit can be fixed by applying the methods described in the two following sections. They both rely on MCSCF wave functions as input and use the ideas of CI and perturbation theory, respectively, to include dynamic correlation.

2.2.5. Multi-reference configuration interaction with singles and doubles (MRCI-SD)

The MRCI-SD is a method capable of accounting for both static and dynamic correlation. It does so by combining the ideas of the MCSCF and CISD methods. As input serves the MCSCF wave function with static correlation already included. In order to incorporate dynamic correlation, however, a much larger number of excited determinants is needed. These determinants are generated by forming all possible single and double excitations of all the determinants already contained in the MCSCF wave function. Still the MRCI-SD wave function corresponds to a truncated CI expansion which is not size extensive.

The energy in a MRCI-SD is obtained by optimizing the CI coefficients such that the total energy is minimized separately for each state. The MCSCF orbitals, on which the MRCI-SD is based, are not changed during the energy minimization.

2.2.6. Complete active space perturbation theory of second order (CASPT2)

CASPT2 is a perturbation theory of second order based on a zeroth order wave function MCSCF character [39, 40]. Loosely speaking, it is a combination of the MCSCF and MP2 methods and, indeed, the CASPT2 energy of a HF wave function is equal to its MP2 energy. Static correlation is accounted for by MCSCF and dynamic correlation by MP2 and since both methods are computationally relatively cheap CASPT2 is a very effective tool applicable to quite large systems. Another big advantage of CASPT2 is its size extensivity. Since we compare in the following chapters calculations of large embedded clusters of various sizes CASPT2 is the method of choice for most of the applications discussed in this thesis.

When strong interaction, i.e., a small energy difference between different MCSCF states is present like, for example, in charge transfer problems (see, e.g., chapter 5) the Multi-State CASPT2 (MS-CASPT2) [41] method needs to be applied. In essence, it is an additional, degenerate perturbation theory accounting for this interaction. A second-order effective Hamiltonian for the CASSCF states is constructed leading to second-order off-diagonal matrix elements. The effective Hamiltonian is diagonalized to obtain the final second-order energies. This procedure also leads to new effective zero-th order wave function which are linear combinations of the interacting CASSCF states.

name	type of correlation	energy obtained	size extensive
CISD	dynamic	variationally	no
MP2	dynamic	perturbatively	yes
CCSD	dynamic	perturbatively	yes
MCSCF	static	variationally	yes
MRCI-SD	static + dynamic	variationally	no
CASPT2	static + dynamic	perturbatively	yes

Table 2.1.: Properties of quantum-chemistry methods accounting for correlation energy.

2.3. Natural orbitals and the one-particle reduced density matrix

The probability to find an electron at a given position in space is given by the reduced density function $\rho(\vec{r}_1)$. It can be extracted from the absolute-magnitude squared of the N_e -electron wave function, $\Psi(\vec{r}_1, \vec{r}_2, \dots, \vec{r}_{N_e})$, and subsequent integration over coordinates $\vec{r}_2 \dots \vec{r}_{N_e}$

$$\rho(\vec{r}_1) = N_e \int \Psi(\vec{r}_1, \vec{r}_2, \dots, \vec{r}_{N_e}) \Psi^*(\vec{r}_1, \vec{r}_2, \dots, \vec{r}_{N_e}) d\vec{r}_2 \dots \vec{r}_{N_e}. \quad (2.44)$$

The normalization factor N_e is included so that the integral

$$\int \rho(\vec{r}_1) d\vec{r}_1 = N_e \quad (2.45)$$

equals the total number of electrons. Generalization of the density function $\rho(\vec{r}_1)$ to a density matrix $\rho(\vec{r}_1, \vec{r}_1')$ leads to the definition

$$\rho(\vec{r}_1, \vec{r}_1') = N_e \int \Psi(\vec{r}_1, \vec{r}_2, \dots, \vec{r}_{N_e}) \Psi^*(\vec{r}_1', \vec{r}_2, \dots, \vec{r}_{N_e}) d\vec{r}_2 \dots \vec{r}_{N_e}. \quad (2.46)$$

$\rho(\vec{r}_1, \vec{r}_1')$ is called the one-electron reduced density matrix and depends on two continuous indices. It is connected to the reduced density function via the diagonal of its continuous representation

$$\rho(\vec{r}_1, \vec{r}_1) = \rho(\vec{r}_1) \quad (2.47)$$

and it can be expanded in terms of, e.g., the orthonormal basis of Hartree–Fock orbitals $\{\phi_i\}$ as

$$\rho(\vec{r}_1, \vec{r}'_1) = \sum_{ij} \phi_i(\vec{r}_1) \rho_{ij} \phi_j^*(\vec{r}'_1), \quad (2.48)$$

with

$$\rho_{ij} = \int \phi_i^*(\vec{r}_1) \rho(\vec{r}_1, \vec{r}'_1) \phi_j(\vec{r}'_1) d\vec{r}_1 d\vec{r}'_1. \quad (2.49)$$

For the special case of Ψ being a Hartree–Fock wave function Ψ_{HF} , composed of canonical Hartree–Fock orbitals, the one-electron reduced density matrix turns into

$$\rho^{\text{HF}}(\vec{r}_1, \vec{r}'_1) = \sum_i^{N_e} \phi_i(\vec{r}_1) \phi_i^*(\vec{r}'_1), \quad (2.50)$$

where the sum runs only over occupied orbitals. The discrete form ρ_{ij}^{HF} is a diagonal matrix with ones along the diagonal for indices of occupied orbitals and zeros for indices of unoccupied orbitals

$$\rho_{ij}^{\text{HF}} = \begin{cases} \delta_{ij} & i, j \in \text{occupied} \\ 0 & \text{otherwise.} \end{cases} \quad (2.51)$$

Therefore, the diagonal elements can be interpreted as occupation numbers. For the more general case of Ψ being a wave function including correlation (e.g. a CI expansion of Ψ_{HF}) ρ_{ij} is not diagonal in the basis of the HF orbitals. Since ρ_{ij} is Hermitian, it is, however, possible to find via a unitary transformation a new orthonormal basis set $\{\eta_i\}$

$$\eta_i(\vec{r}) = \sum_k \phi_k(\vec{r}) U_{ki} \quad (2.52)$$

in which ρ_{ij} is diagonal with the continuous representation

$$\rho(\vec{r}_1, \vec{r}'_1) = \sum_i \lambda_i \eta_i(\vec{r}_1) \eta_i(\vec{r}'_1). \quad (2.53)$$

The new orthonormal orbitals $\{\eta_i\}$ are called natural orbitals. In contrast to $\Psi = \Psi_{\text{HF}}$ (eq. 2.50) the sum in the upper equation runs over all orbitals indices and the occupation numbers λ_i vary between 0 and 1. For $i \leq N_e$, occupation numbers are close to one and they are close to zero for $i > N_e$.

Natural orbitals play an important role in speeding up the convergence in CI ex-

pansions. For a given accuracy, the number of determinants formed by natural orbitals needed is smaller than for a determinant formed by any other orthonormal basis. We use natural orbitals in chapter 3 to qualitatively visualize the effect of correlation on localized electrons.

3. The F-type color center in lithium fluoride

Lithium fluoride (LiF) is an ionic alkali-halide crystal consisting of Li^+ and F^- ions arranged in the so-called rock-salt crystal structure with a lattice constant [42] of $d = 7.62$ Bohr corresponding to an anion-cation distance of $a = d/2 = 3.81$ Bohr. Every ion has six neighbor ions of opposite charge located at the vertices of a regular octahedron (fig. 3.1). LiF is an insulator with one of the largest band gaps (14.2 eV, [43]) found in nature. In pristine LiF the size of the band gap makes optical excitations, i.e., the absorption of light in the visible range impossible which renders the material transparent. We encounter almost daily a material with very similar properties which is table salt or, i.e., sodium chloride (NaCl). Already at the end of the 19th century it was realized that after irradiation of ionic crystals with massive particles or gamma radiation the transparent crystals get colored [4]. In the late 1920s (see, e.g., [44]) these findings triggered an enormous effort to understand this effect and find a proper explanation. Exemplary for the huge amount of literature we list here a few books and reviews on this topic [5–8]. Soon it became clear that the radiation causes the formation of a defect created by the removal of an anion, an F^- ion in the case of LiF, the lattice position of which is subsequently occupied by a single electron. This leads to a very localized defect which, in an oversimplified but intuitive picture, can be thought of as an electron in a three-dimensional box [45, 46] with a side length approximately corresponding to the lattice constant. The energy needed to excite this electron trapped in the anion vacancy can be measured by optical absorption spectroscopy and lies, for many alkali-halide crystals, in the optical range. This explains why the defect is termed color-center or F-center where the “F” stands for Farbe, the German word for color. Important to note, however, is the fact that in LiF the F-center absorbs light with an energy of approximately 5 eV which lies above the visible range. Due to the localization of the F-center defect we can employ what is called the embedded-cluster approach (ECA) in the theoretical description. Only a finite fragment of the LiF crystal containing the F^- vacancy, the so-called active cluster, is treated at a high level of theory while the remainder of the extended crystal is essentially approximated by a large matrix of singly charged, positive and negative point charges located at the lattice sites. The electronic structure, i.e., the total, correlated N-electron wave function of the active cluster is then calculated or approximated by methods from quantum chemistry beyond the Hartree–Fock (HF)

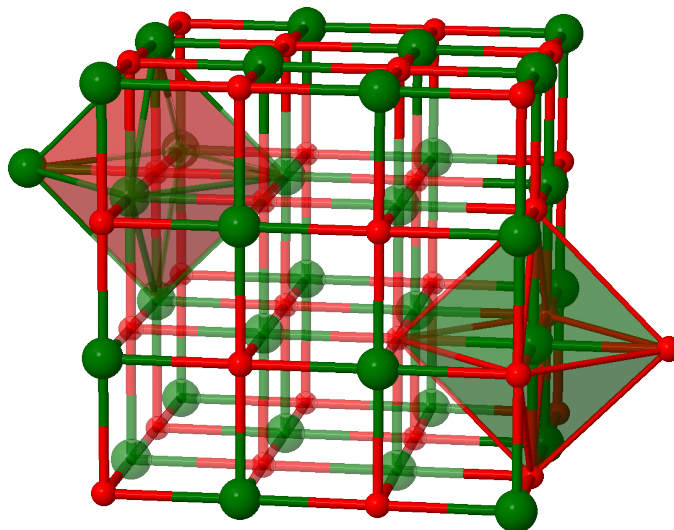


Figure 3.1.: Schematic drawing of the rock-salt crystal structure of a lithium-fluoride crystal. Green-large ions are F^- anions, red-small ions are Li^+ cations. Every ion has six nearest neighbors forming an octahedron.

approximation.

Despite all the previous work related to the F-center in LiF and other materials there are still open questions concerning the extent of the defect-electron wave function and its actual shape in the ground as well as in the so-called relaxed excited state. Another open question is the seemingly non-existent luminescence of the F-center in LiF. Furthermore, all theoretical works determining the absorption energy of the F-center in LiF are so far in unsatisfying agreement with the experimental value. We present here a detailed ab-initio study of the F center and discuss in detail technical aspects, such as embedding, active-cluster size, and basis-set size, as well as the physical aspects, such as geometry relaxation, the Fermi contact term, correlations, and the influence of local and lattice vibrations. While we find very good agreement of the absorption energy with experimental data we reached very quickly computational limits preventing us from completely solving questions concerning the relaxed excited state. Despite this restriction, to our knowledge, the present study is the most detailed performed so far.

The goal of a joint study [47] was to explore both the physics underlying the color center as well as to compare and benchmark results obtained by density functional theory (DFT) and methods beyond, such as GW and the solution of the Bethe-Salpeter equation, against results of the Hartree-Fock (HF) and post-HF approximations. We termed these two strategies the solid-state physicist's and the quantum chemist's approach, respectively. Apart from the solution of the electronic Hamiltonian there is another important difference between these two strategies. While in quantum chemistry the F-center is represented by a finite embedded cluster, the

DFT calculations are carried out in so-called supercells with periodic boundary conditions. Although we focus in this chapter on the quantum chemistry approach and present details of the calculations beyond the ones in the original publication [47] we also compare in sec. 3.6 the quantum chemistry and post-DFT approaches and the results obtained. Readers interested in details of the post-DFT calculations are referred to ref. [47] and the doctoral thesis of Karsai [48].

This chapter is structured as follows. In sec. 3.1 we briefly review and summarize previous work on the F-center in LiF within the framework of the ECA. Sec. 3.2 describes calculation details such as active-cluster and basis-set size as well as the embedding scheme. Hartree–Fock absorption energies and defect-electron wave functions are presented in sec. 3.3. The effect of correlation on the absorption energy and the defect-electron wave functions is studied in sec. 3.4. In sec. 3.5 we discuss further effects to be taken into account to compare our results for the absorption energy to the experimental spectrum. These effects comprise geometry relaxation, the line width of the absorption line and the influence of local and lattice vibrations on the absorption energy. We also compare our results to the experimental spectrum in this section. In sec. 3.6 we compare results from the quantum chemist’s approach with the ones from the solid state physicist’s approach.

3.1. Previous work

The first calculations of the absorption energies of the F-center in alkali halides are single-electron models in which the defect electron is treated as a hydrogenic system embedded either in a matrix of point charges or in a “perfect continuum” [49]. One of the first ab-initio ROHF calculation was done by Murrell and Tennyson [50] using a $\text{Li}_{14}\text{F}_{12}$ active cluster consisting of 14 Li^+ and 12 F^- ions embedded in a point-charge lattice. More advanced studies followed: Kung, Kunz, and Vail [51] performed unrestricted Hartree–Fock (UHF) calculations for the six nearest-neighbor Li^+ ions surrounding the vacancy with additional point charge embedding. Pandey, Seel, and Kunz [52] went beyond HF and combined many-body perturbation theory with UHF calculations for LiF clusters of various sizes up to $\text{Li}_{14}\text{F}_{12}$ but neglected embedding effects completely. Bader and Platts [53] investigated in detail the topology of the F-center ground-state electron density with a $\text{Li}_{14}\text{F}_{12}$ cluster embedded in point charges. For the same cluster size and embedding the most recent and, so far, most detailed ROHF study was presented by Ewig and co-workers [54, 55] including results for the shape of the defect-electron orbital in its ground and excited state.

Common to almost all calculations using pure point charge embedding is the unsatisfying agreement between theory and experiment, or, to be more precise, the underestimation of the absorption energy. The range of values found lies approximately between 3.2 and 4.2 eV while the experimental value is ~ 5 eV. This un-

derestimation is also found in calculations of F-center absorption energies in other alkali halides. In the simple particle-in-the-box model this is due to a box with a too large side length, i.e., a too weak confinement of the defect electron. Indeed, exceptions to the underestimate are those single-electron approaches that, additional to the point-charge embedding, use some kind of confining potential for the defect electron [56, 57]. This clearly indicates that a proper embedding is crucial and needs to go beyond pure point charges. Apart from the improper embedding, sources of errors are the limited active-cluster size, the limited basis-set size, and the neglect of correlation and electron-phonon interactions. In this work we systematically investigate these issues which leads us to much more consistent results than those found so far.

3.2. Setting up the calculation: cluster sizes, embedding scheme and basis sets

The sizes of the active clusters used in this study are $\text{Li}_{14}\text{F}_{12}$, $\text{Li}_{38}\text{F}_{18}$, $\text{Li}_{62}\text{F}_{62}$, and $\text{Li}_{92}\text{F}_{86}$ (fig. 3.2). The distance between cation and anion, a , is set to 3.81 a.u. taken from experimental data [42] and all the ions are, for the time being, located at lattice sites of pristine LiF. The $\text{Li}_{14}\text{F}_{12}$ cluster is a cube with a side length of three ions and the vacancy located at the very center. Adding one F^- ion surrounded by four Li^+ ions on each side of this cube leads to the $\text{Li}_{38}\text{F}_{18}$ cluster. The $\text{Li}_{62}\text{F}_{62}$ cluster is again a cube with a side length of five ions. Finally, the $\text{Li}_{92}\text{F}_{86}$ cluster is composed of the $\text{Li}_{62}\text{F}_{62}$ cube plus four fluoride and five lithium ions on each of its sides.

These clusters are embedded (fig. 3.3) in several layers of the so-called ab-initio model potentials [58, 59] (AIMPs) and, beyond these layers, a large, cubic matrix of positive and negative point charges located at the lattice sites of Li^+ and F^- ions, respectively. AIMPs are all electron potentials which, in contrast to pure point charges, also include exchange terms via a non-local potential. Exchange leads to repulsive forces between electrons of equal spin, or, in this case between the electrons of the active cluster and the “frozen” electrons of the AIMPs. The use of AIMPs is, therefore, important to prevent unphysical excessive polarization of ions at the border of the active cluster. In extreme cases this can lead to so-called charge leakage which denotes the accumulation of charge, i.e., electrons, outside the active cluster. With larger basis sets and without AIMPs we indeed observe charge leakage which becomes manifest in defect-electron orbitals located far away from the active cluster. Only the use of more than one layer of AIMPs leads to defect-electron orbitals localized on the active cluster. For the $\text{Li}_{62}\text{F}_{62}$ cluster we use four layers of AIMPs (2072 in total) and five layers of point charges (9970 in total). Independent of the size of the active cluster we use a cubic point charge

matrix which comprises 23^3 lattice sites and in which charges are arranged as proposed by Evjen [60] with fractional charges of ± 0.5 , 0.25 , 0.125 at faces, edges, and corners, respectively. At the center, the place of the F-center vacancy, this leads to a Madelung constant of 1.747562 in good agreement with the converged value of 1.747565 . The value of our Madelung constant does not change when it is calculated, e.g., for the corner of the $\text{Li}_{62}\text{F}_{62}$ cluster.

Every active ion hosts a local, Gaussian-type basis set. We use Dunning's correlation-consistent polarized valence-only basis sets [61] of double, triple, and quadruple zeta quality abbreviated by cc-pVDZ, cc-pVTZ, and cc-pVQZ, respectively. Additionally to the basis sets localized at the ionic sites we also place a basis set pertinent to an F atom at the vacancy site. This additional basis set, however, has hardly any influence on the results of our calculations. Orbital size, shape, and energy as well as the absorption energy hardly change (the latter by less than 0.01 eV) compared to calculations without the basis set at the vacancy site. This is in line with earlier studies [53, 62, 63] and indicates that the defect electron is well described by basis sets localized on ions surrounding the vacancy. For the $\text{Li}_{62}\text{F}_{62}$ cluster and the cc-pVTZ basis set this gives a total number 3750 Gaussian-type basis functions. This rather large number of basis functions leads to a huge demand for disk space via the two-electron integral file. The so-called Cholesky decomposition option in the quantum chemistry program package MOLCAS [64] approximates the two-electron integrals. It allows for tremendous reduction of disk space needed and, thereby, considerably reduces the computation time due to a reduction of I/O operations. Without the Cholesky decomposition some of the results presented here could not be obtained with computers available. The approximate treatment of the two-electron integrals leads ultimately to an approximation of the total energies determined by the quantum chemistry calculation. The approximation strength is governed by the so-called Cholesky threshold parameter. For vanishing Cholesky threshold the total energies converge to the value of a conventional calculation with exactly evaluated two-electron integrals. In our calculations we use the standard Cholesky threshold of 10^{-4} . Further reduction of the threshold by a factor of 10 leads to a reduction of the absorption energy by approximately 0.03 eV which is below 1% of the experimental value.

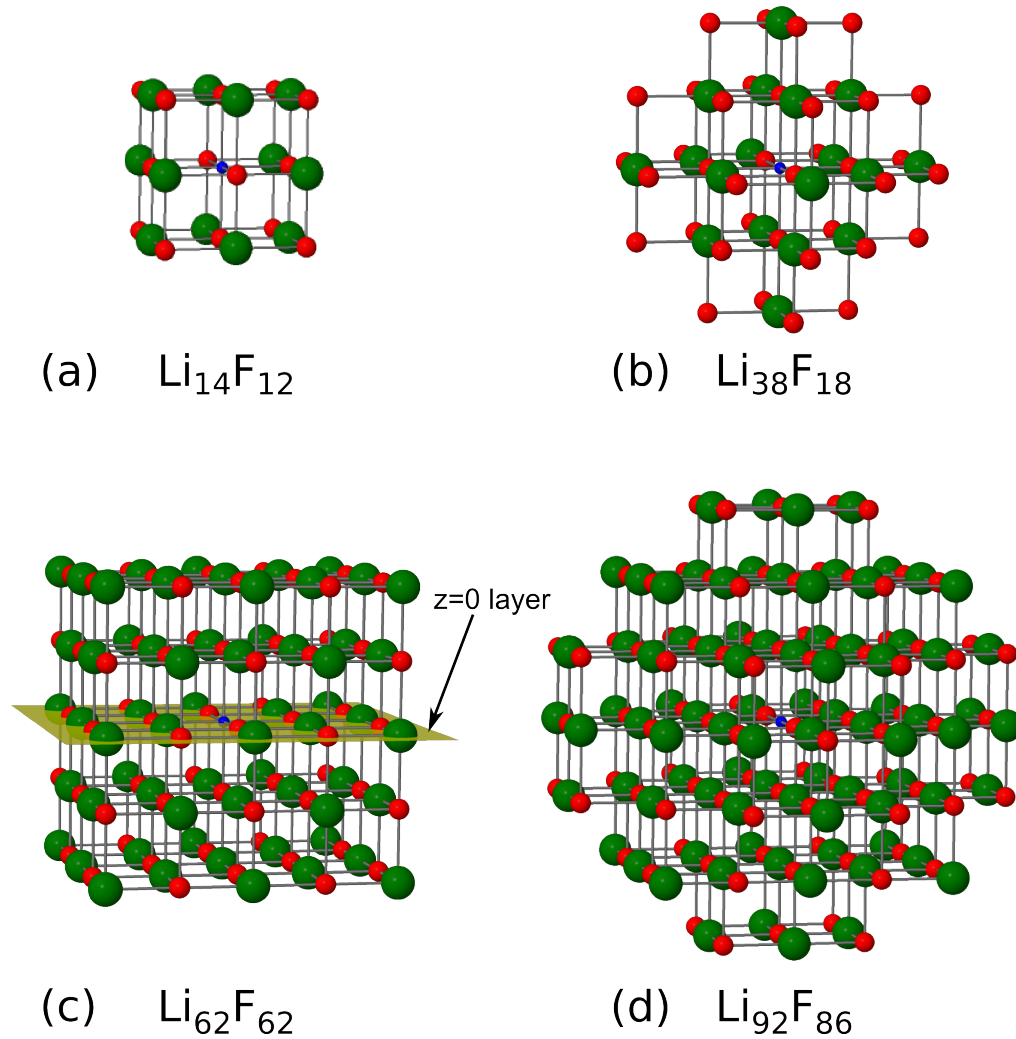


Figure 3.2.: Pictures of active LiF clusters. Red colored Li^+ ions are drawn smaller in contrast to the larger, green F^- ions. The blue spheres in the center of the clusters indicate the place of the anion vacancies. The cluster sizes are (a) $\text{Li}_{14}\text{F}_{12}$, (b) $\text{Li}_{38}\text{F}_{18}$, (c) $\text{Li}_{62}\text{F}_{62}$, and (d) $\text{Li}_{92}\text{F}_{86}$. The yellow plane in (c) indicates the $z = 0$ layer of the cluster containing the vacancy.

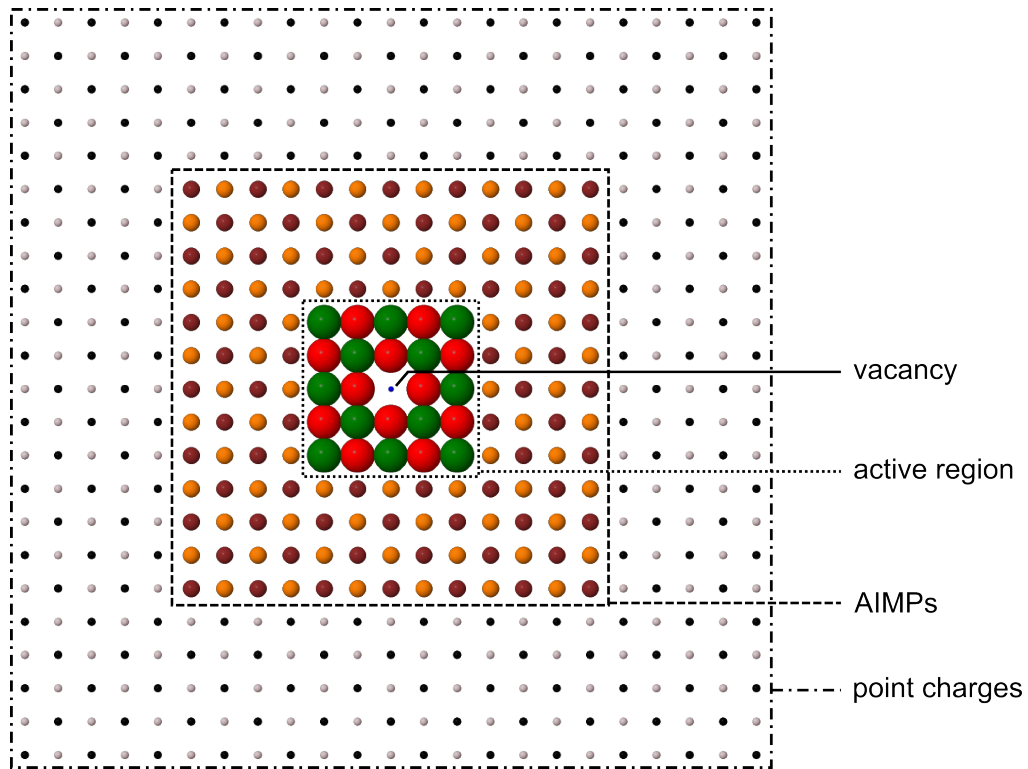


Figure 3.3.: $z = 0$ layer of the embedded $\text{Li}_{62}\text{F}_{62}$ cluster (fig. 3.2 (c)). Inner region contains the active F^- and Li^+ ions (red and green spheres) with the vacancy in the center (blue sphere). The second region contains the AIMP of F^- and Li^+ ions (brown and orange spheres). The outermost layer is composed of singly charged positive and negative point charges (pink and black spheres).

3.3. The Hartree–Fock absorption energy and the F-center orbitals

To get an overview of the electronic structure we study the RHF single-particle energy spectrum of an embedded $\text{Li}_{38}\text{F}_{18}$ cluster *without* the defect electron trapped in the F^- vacancy (fig. 3.4). We leave out the defect electron in order to treat all orbitals to be occupied by the defect electron on the same footing meaning they are subject to the same potential. All energies of unoccupied orbitals correspond, according to Koopmans’ theorem, to electron addition energies and differences between these energies can be interpreted as electron transition energies. Since the calculations are performed in the D_{2h} point-group symmetry (for an application-oriented introduction to group theory see, e.g., [65]) the orbital energies are sorted by the eight irreducible representations of D_{2h} . Orbital energies below 0 eV correspond to the doubly occupied F-2p orbitals, i.e., the valence orbitals. All orbitals with higher energies are unoccupied. The LUMO, the lowest unoccupied orbital, has A_g symmetry and is indicated by a black arrow. It is energetically well separated from the valence orbitals and also from higher lying orbitals. It will host the defect electron in its ground state. A dipole excitation of an electron occupying this A_g orbital is only possible to an orbital of B_u symmetry since excitations to orbitals of all other symmetries lead to vanishing dipole matrix elements. Indeed, the next highest orbital energies (LUMO+1) belong to three degenerate B_u orbitals, also marked by a black arrow. They are energetically well separated from higher lying orbital energies, too and will host the defect electron in its excited state. The single-particle energy difference of the LUMO and the LUMO+1 orbitals can be interpreted as the F-center absorption energy leading to a value of 6.03 eV not too far from the experimental value of ~ 5 eV. However, this interpretation completely neglects the response of the host-crystal electrons to the presence of the defect electron.

A more realistic description is obtained when the absorption energies of the embedded clusters are determined in so-called ΔSCF calculations, i.e., as the total energy difference of two restricted open-shell Hartree–Fock (ROHF) N -electron wave functions corresponding to the ground and the first optically allowed excited state, respectively. Similar to the findings of Adachi [63] for the F-center in NaCl we do not encounter any significant difference in the orbital shape and absorption energy between ROHF and unrestricted HF (UHF) calculations. The distinction between ground and excited state is again determined by symmetry. The ground and excited-state wave functions are “ground states” within the A_g and B_u symmetry sectors, respectively.

Size and shape of the occupied defect orbitals are well converged already for the $\text{Li}_{38}\text{F}_{18}$ cluster with the cc-pVTZ basis set. For this configuration the ROHF A_g and one of the B_u orbitals are plotted in fig. 3.5. A two-dimensional cut through

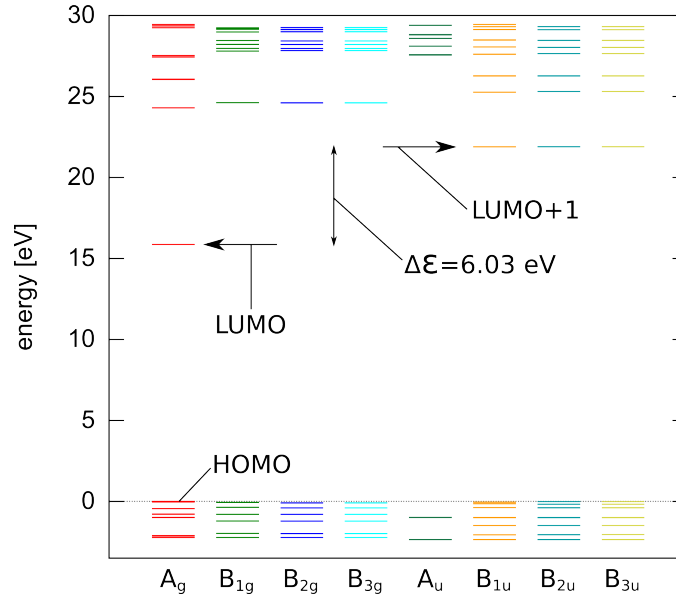


Figure 3.4.: Single-particle energy spectrum of a closed-shell HF calculation *without* the defect electron for a $\text{Li}_{38}\text{F}_{18}$ cluster with the cc-pVTZ basis set. Energies are sorted by the irreducible representations of the D_{2h} point group. Defect-orbital energies to be occupied by the defect electron in its ground (LUMO) and excited (LUMO+1) state are indicated by horizontal arrows. The orbital energy difference, $\Delta\epsilon$, between them approximates the F-center absorption energy. The origin of the energy scale is at the HOMO level.

the three-dimensional wave functions is shown in fig. 3.6. Both orbitals are well localized within the vacancy and they qualitatively resemble a hydrogen-like 1s and 2p wave function, respectively. The shape of the s-type orbital is in good qualitative agreement with the one from earlier calculations by Ewig and co-workers[54]. In this reference the p-type orbital, however, is highly delocalized and spread over adjacent lattice sites. Cuts through the electron density show hardly any accumulation of charge within the vacancy in strong contrast to our results. The delocalized nature of the excited state may be due to the pure point charge embedding and to the use of a moderate basis set size. As a function of the basis set size we find two extreme cases in our calculation for pure point charge embedding. A small basis set leads to s and p-type orbitals artificially localized within the vacancy. For large basis sets both the s- and p-type orbital show charge leakage, i.e., they are not localized on the active cluster. The calculations of Ewig and co-workers seem to be an intermediate case where the basis set is too large to artificially localize the excited state but is still too small to allow charge leakage. The use of AIMP embedding stabilizes the defect-electron charge on the active cluster and leads to more compact and localized ROHF orbitals within the vacancy region [66]. In this

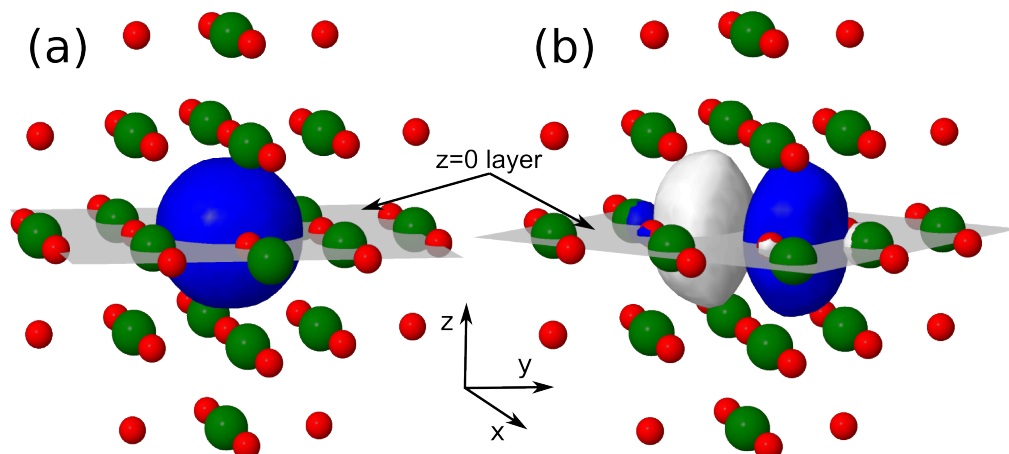


Figure 3.5.: Isosurfaces of the F-center electron wave function in the (a) ground state with A_g symmetry and (b) the excited state with B_u symmetry. The F-center vacancy is located in the $z = 0$ layer (grey planes). Blue and white color indicate the different sign of the wave functions.

sense only embedding schemes beyond pure point charges allow for a meaningful convergence study of the orbital properties as a function of cluster and basis-set size.

The influence of the AIMP on the absorption energy can be understood in terms of the particle-in-the-box model and can explain the fact that most of the early calculations with pure point charge embedding [50, 51, 54, 55] underestimate the absorption energy of the F-center. While pure point-charge embedding underestimates the absorption energy due to the diffuse p-type orbitals, the inclusion of additional repulsive forces (exchange) in the embedding narrows the width of the box and leads to a larger separation of energy levels, i.e., to an increase of the absorption energy. With AIMP embedding, we typically find ROHF absorption energies higher than the experimental value. With increasing cluster and basis-set size our results, however, systematically decrease approaching the measured absorption energy. The Hartree–Fock absorption energies we find are listed in table 3.1 as a function of basis set and cluster size and they are also plotted in fig. 3.8 in the following section. Table 3.1 also contains the converged-basis set (CBS) limit [67]. The Hartree–Fock absorption energies systematically decrease as a function of cluster and basis-set size but show only a rather small variation of approximately 0.1 eV. The lowest value we find is 6.19 eV for the CBS limit of the $\text{Li}_{62}\text{F}_{62}$.

A technical issue to be addressed is the symmetry of the problem and the, related, orientation of the p-type orbital. In figs. 3.5 and 3.6 the p-type orbital is oriented towards the second nearest neighbor F^- ions. This orientation, however, is not unique. When the HF equations are solved for the excited state of the F-center we

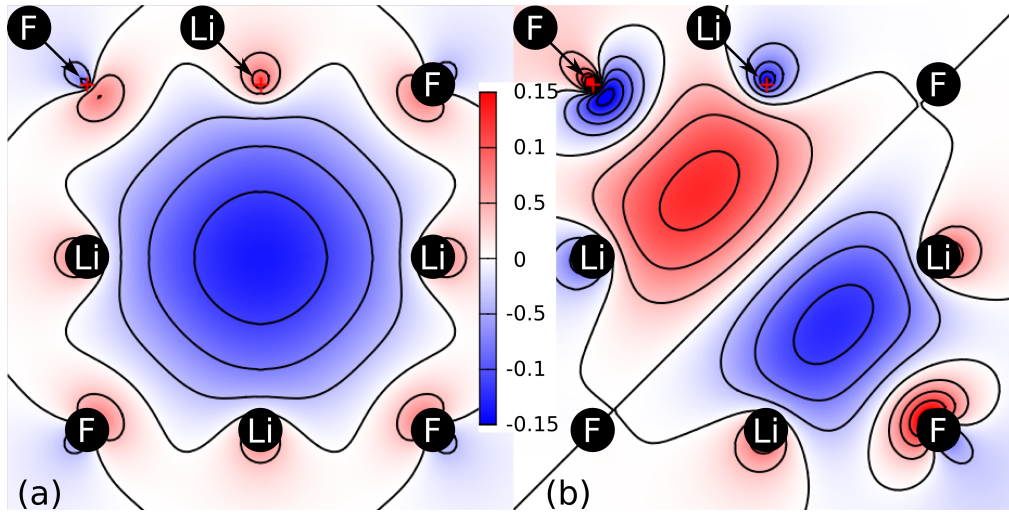


Figure 3.6.: Cuts through the ROHF orbital of the F-center electron in the (a) ground state with A_g symmetry and (b) the excited state with B_u symmetry. The cuts show the wave functions within the $z = 0$ layer in fig. 3.5.

Basis set	Li ₁₄ F ₁₂	Li ₃₈ F ₁₈	Li ₆₂ F ₆₂	Li ₉₂ F ₈₆
cc-pVDZ	6.31	6.27	6.24	6.21
cc-pVTZ	6.27	6.23	6.20	–
cc-pVQZ	6.26	6.23	–	–
CBS limit	6.26	6.22	6.19	–

Table 3.1.: Hartree–Fock F-center absorption energies in eV as a function of basis set and cluster size in clusters with the experimental anion-cation distance of 3.81 a.u..

can place the electron either in a B_{1u} , B_{2u} , or B_{3u} orbital leading to three perfectly degenerate solutions. Any linear combination of these three orbitals is, therefore, also a solution to the HF equations with the same total energy and allows for an arbitrary rotation of the excited-state defect orbital while leaving the absorption energy unchanged. An example of such a rotation is shown in fig. 3.7 where the defect orbital points towards the nearest neighbor Li ions.

The reason for finding three degenerate excited states corresponding to three different irreducible representations (B_{1u} , B_{2u} , B_{3u}) is due to the fact that our results are reduced symmetry solutions: while the embedded clusters in fig. 3.2 have O_h symmetry, the point group with the highest symmetry supported by MOLCAS and used in the calculations is D_{2h} . In the O_h point-group symmetry the excited state orbitals belong to the t_{1u} representation but the three degenerate t_{1u} components reduce to three different representations of the D_{2h} . This implies that a

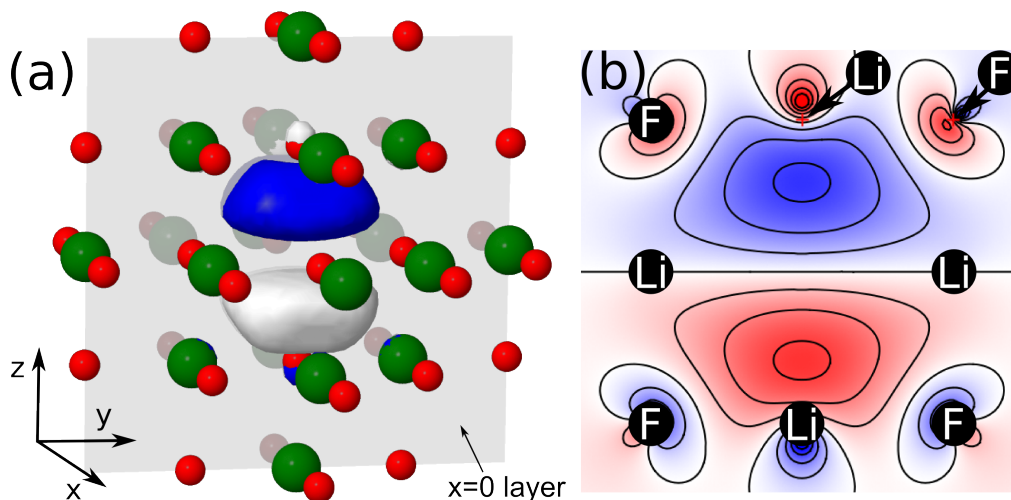


Figure 3.7.: The excited-state defect orbital pointing towards the nearest neighbor Li^+ ions. Panel (a) shows a wave function isosurface and (b) shows a cut through the wave function within the $x = 0$ layer. The blue and white color (a) and the blue and red color (b) indicate the sign of the orbital.

CASSCF calculation with these three orbitals in one CAS is not feasible and that static correlation between the corresponding configurations, i.e., the possible multi-determinant character of the total wave function is not captured.

Sousa and Illas [68] encountered the same problem in their study of the F center in MgO. They suggested to remove all symmetry constraints (C_1 point group) allowing for a CAS comprising the ground state s-type orbital and the three degenerate p-type orbitals. Unfortunately, a calculation without symmetry constraints becomes computationally quite expensive which is why we only do a partial reduction of symmetry. The C_{2h} point-group has only four irreducible representations and two of the three degenerate p-type defect orbitals correspond to B_u symmetry and can be part of the same CAS. For the $\text{Li}_{38}\text{F}_{18}$ cluster (cc-pVTZ basis set) the C_{2h} -CASSCF absorption energy of the F-center electron is 0.003 eV lower than the ROHF energy using the D_{2h} symmetry. Application of CASPT2 (see below) increases this value to 0.017 eV which is still negligible and confirms that the D_{2h} solution hardly introduces any error.

The independence of the absorption energy on the p-orbital orientation is only valid for the highly symmetric pristine (and relaxed ground state (sec. 3.5.2)) geometry. For photo-emission, starting from the geometry of the so-called relaxed-excited state, the orientation of the p-type orbital is crucial in order to find the minimum total energy of the excited state as a function of cluster geometry (sec. 3.5.6).

3.4. Beyond Hartree–Fock: absorption energies including correlation

Quantum chemistry offers a variety of methods to include the effect of correlations (see section 2.2) which we apply in the following to the F center in embedded clusters. We investigate the influence of static correlation, now within a single irreducible representation, by applying the CASSCF method and subsequently comparing CASPT2 absorption energies based on a ROHF wave function (CASPT2(ROHF)) and a multi-determinant CASSCF wave function (CASPT2(CAS)). The CAS for the ground state calculation (A_g symmetry) is formed by correlating all occupied valence orbitals (F-2p orbitals) of A_g symmetry plus a number of virtual orbitals also of A_g symmetry. For the excited state, the same procedure is applied within one of the B_u representations. The largest CASs are tested within the $\text{Li}_{38}\text{F}_{18}$ cluster with the cc-pVTZ basis set and read (19,13), corresponding to 19 electrons in 13 orbitals, and (17,11) for the ground and excited state, respectively. The absorption energies of the F-center are hardly affected by including the static correlation contribution. We find a difference between CASPT2(ROHF) and CASPT2(CAS) of less than 0.02 eV. This indicates the strong single-determinant nature of the problem at hand.

We test the influence of dynamic correlation with CASPT2(ROHF), CCSD, and CCSD(T). For this group of methods, the starting point is the ROHF wave function of either ground or excited state, discussed in sec. 3.3. Absorption energies of the F-center in the $\text{Li}_{14}\text{F}_{12}$ embedded cluster are summarized in table 3.2 for various basis sets. Since CCSD and CCSD(T) calculations are computationally quite demanding they can not be applied for all basis sets. The last line in table 3.2 shows values for the converged basis set (CBS) limit obtained by employing the extrapolation scheme proposed by Truhlar [67, 69]. This scheme is tailored to extrapolate perturbation theory, CCSD, and CCSD(T) energies from the cc-pVDZ and cc-pVTZ basis sets to the CBS limit allowing for application to cases in which cc-pVQZ calculations are not feasible. Where available, we compare the Truhlar CBS energies to values from extrapolation schemes involving the energy of the larger cc-pVQZ basis set [70], which show a deviation of less than 0.01 eV in the absorption energy. Results in table 3.2 prove the reliability of the CASPT2(ROHF) method since it very closely reproduces the absorption energies of the more accurate CCSD and CCSD(T) methods. For example, the CBS limits of the CASPT2(ROHF) and the CCSD differ by only 0.04 eV. A comparison between CASPT2(ROHF) and CCSD(T) absorption energies is only possible for the cc-pVDZ basis set for which the CCSD(T) energy is 0.05 eV lower than the CASPT2(ROHF) value.

These small deviations ($\lesssim 1\%$ of the experimental absorption energy) make the numerically relatively cheap CASPT2(ROHF) method the perfect candidate to study the convergence of the absorption energy as a function of cluster size. CASPT2

Basis set	ROHF	CASPT2(ROHF)	CCSD	CCSD(T)
cc-pVDZ	6.31	5.99	6.00	5.94
cc-pVTZ	6.27	5.84	5.86	–
cc-pVQZ	6.26	5.79	–	–
CBS limit	6.26	5.73	5.77	–

Table 3.2.: F-center absorption energies of the $\text{Li}_{14}\text{F}_{12}$ cluster calculated with different methods and basis sets using the unperturbed crystal geometry and the experimental lattice constant.

Basis set	$\text{Li}_{14}\text{F}_{12}$	$\text{Li}_{38}\text{F}_{18}$	$\text{Li}_{62}\text{F}_{62}$	$\text{Li}_{92}\text{F}_{86}$
cc-pVDZ	5.99	5.87	5.76	5.74
cc-pVTZ	5.84	5.73	5.62	–
cc-pVQZ	5.79	5.70	–	–
CBS limit	5.73	5.63	5.50	–

Table 3.3.: CASPT2(ROHF) absorption energies of the F-center in LiF calculated with different cluster sizes and basis sets using the unperturbed crystal geometry and the experimental lattice constant.

(ROHF) absorption energies for different cluster sizes, different basis sets, and their CBS limits are listed in table 3.3 and plotted together with the Hartree–Fock values in fig. 3.8. Since for the cc-pVDZ basis set the difference between the $\text{Li}_{62}\text{F}_{62}$ and the $\text{Li}_{92}\text{F}_{86}$ cluster is only 0.02 eV, we consider the absorption energy of the $\text{Li}_{62}\text{F}_{62}$ cluster converged within a satisfactory level of accuracy.

Beyond Hartree–Fock the single-particle picture is not applicable any more. Natural orbitals (sec. 2.3), however, offer the possibility to qualitatively study the influence of correlations on the defect-electron density. In the CASPT2 case the natural orbitals diagonalize the one-particle reduced density matrix obtained from the exact first-order wave function. Although the difference between CASPT2(ROHF)-natural orbitals and ROHF orbitals is four orders of magnitude smaller than their actual value, the difference between their absolute magnitudes (fig. 3.9) clearly shows the tendency of correlations to slightly delocalize the F-center electron shifting the density from the vacancy site to the surrounding F^- ions. In the simple picture of a particle in the box this suggests correlation to enlarge the box a little leading to larger defect orbitals and to a reduction of the absorption energy.

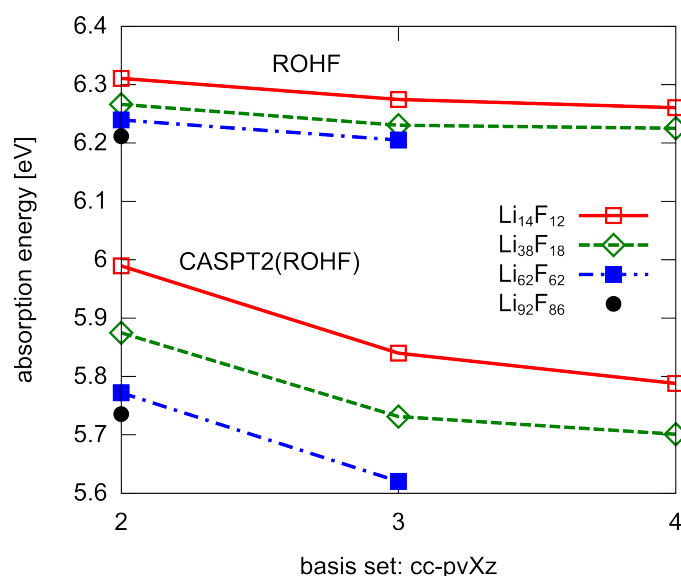


Figure 3.8.: ROHF and CASPT2(ROHF) F-center absorption energies as a function of cluster and basis set size using the unperturbed crystal geometry and the experimental lattice constant.

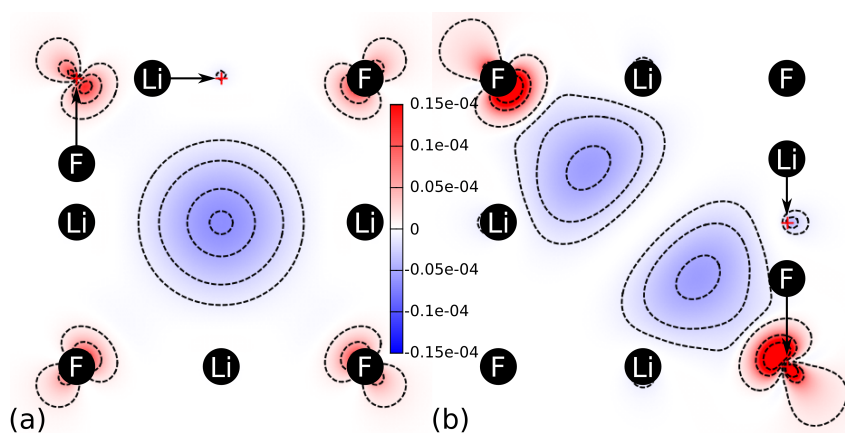


Figure 3.9.: Difference $\Delta = |\phi_{nat}|^2 - |\phi_{HF}|^2$ between the absolute magnitudes of the CASPT2(ROHF) first-order natural orbitals and the Hartree-Fock orbitals of the electron in the F-center vacancy for the (a) ground state (s-state) and (b) excited state (p-state) configuration. Orbitals from calculations using the Li₃₈F₁₈ cluster and the cc-pVTZ basis set are shown.

3.5. Comparison with experiment

In the first section we discuss the so-called Fermi contact term which allows for probing experimentally the total spin density at the ionic sites surrounding the F-center defect by electron-nuclear spin resonance. The absorption energy of the F-center in LiF is determined by optical absorption spectroscopy leading to an absorption peak with a maximum at 5.08 eV and a width (full width at half maximum) of 0.62 eV at a temperature of about 5 K [71]. In order to compare our result with the experimental absorption spectrum we need to take into account further effects neglected so far. These effects comprise the change of geometry around the defect (sec. 3.5.2) and the influence of lattice vibrations on the the line width (sec. 3.5.3) as well as the maximum of the absorption peak (sec. 3.5.4). In sec. 3.5.6 we briefly touch the problem of photoluminescence, the emission of light during the deexcitation of the F-center electron, which has been detected in many alkali-halide crystals except for LiF. Closely related is the problem of the so-called relaxed excited state.

3.5.1. Fermi Contact term

The Fermi contact term A_0 in the hyperfine interaction between the defect electron and nuclei surrounding it is experimentally accessible through electron-nuclear double resonance (ENDOR), developed by Feher [72]. It can be determined for each nucleus individually and it is proportional to the spin density, the total density difference of spin up and spin down electrons $|\psi_{\uparrow}(0)|^2 - |\psi_{\downarrow}(0)|^2$, at the selected nuclear site of the host crystal [73]:

$$A_0 = -\frac{2}{3}\mu_0 g_e \beta_e g_n \beta_n (|\psi_{\uparrow}(0)|^2 - |\psi_{\downarrow}(0)|^2), \quad (3.1)$$

with the Bohr magneton β_e , the nuclear magneton β_n , the electron g_e and nuclear g_n factors. The A_0 values at the first, second, and third nearest neighbor ions of the F-center electron in LiF were measured by, e.g., Holton and Blum [74]. Mallia et al. performed UHF calculations [75] with periodic boundary conditions. Experimental and theoretical spin densities are listed in table 3.4 together with results from our embedded cluster UHF and ROHF calculations. At the nearest-neighbor Li^+ ion embedded cluster and periodic boundary UHF spin densities are within $\sim 2\%$ of the experimental value. The errors, however, increase substantially for the second and third nearest neighbor ions. ROHF considerably underestimates the spin densities at all ionic sites due to the neglect of spin dependent polarization of core and valence electrons. In the ROHF approach doubly occupied orbitals do not contribute to the spin density and, therefore, the spin density is determined solely by the F-center electron. Leitão et al. found this effect [62] for F centers in other alkali-halides where core and valence electrons account for up to 30 % of the spin density. Despite this substantial difference between ROHF and UHF we find essentially

identical single-particle defect wave functions for the F-center electron (fig. 3.10) and identical Fermi contact terms if, in UHF, only the defect orbital is considered. Since experimentally the two contributions, defect and core electrons, can not be disentangled the Fermi contact term can not be used to unambiguously map out the defect-electron wave function. Nevertheless the good agreement of A_0 at the nearest-neighbor Li ions between theory and experiment shows that the central part of the ROHF/UHF defect wave functions are reliable. The Fermi contact term of ions beyond the nearest neighbor only probe subtle local effects on the tail of the defect wave function strongly influenced by the properties of the on-site ionic cores.

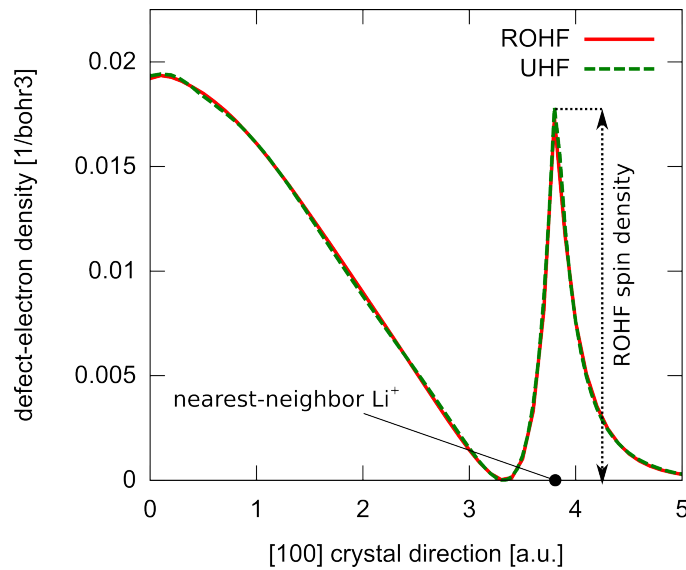


Figure 3.10.: Cut through the ROHF (solid-red line) and UHF (dashed green) defect-electron density function along the $[100]$ crystal direction. Vertical dashed arrow marks the ROHF spin density, i.e., UHF spin density neglecting the spin dependent polarization of the Li-1s orbitals.

3.5.2. Relaxation of the ground state - The Franck–Condon absorption energy

All convergence studies in secs. 3.3 and 3.4 are performed for an unperturbed crystal geometry. The formation of the F-center defect, however, leads to forces on the ions close to the vacancy displacing them from their position in pristine LiF. We calculate these forces for the electronic ground state, the s-type state, on the CASPT2(ROHF) level and optimize the structure of the $\text{Li}_{33}\text{F}_{18}$ cluster using the cc-pVTZ basis set. For the absorption energy we only need to optimize the electronic

$ \psi_{\uparrow}(0) ^2 - \psi_{\downarrow}(0) ^2$ [a.u.]			
	Li_{100}^+	F_{110}^-	Li_{111}^+
ROHF (ECA)	0.0177	0.0125	0.00014
UHF (ECA)	0.0229	0.0200	0.00009
UHF (PBC)	0.0225	0.0182	0.00006
experiment	0.0225	0.0252	0.00029

Table 3.4.: Spin densities in $1/\text{bohr}^3$ at the first (Li_{100}^+), second (F_{110}^-), and third (Li_{111}^+) nearest neighbor ions of the F center in LiF. Experimental data [74] are compared with ab initio calculations within the framework of the embedded cluster approach (ECA) and periodic boundary conditions (PBC) [75]. In the ECA calculations of the Fermi contact term the lattice constant and the geometry relaxation found in [75] is used.

ground state since the electronic excitation happens essentially instantaneously compared with the time scale of the motion of the nuclei (vertical transition in fig. 3.12). The relaxation is performed under the constraint that only nearest and second-nearest neighbors are allowed to move. This constraint is imposed due to two reasons. First, periodic-boundary DFT calculations [47] show essentially no movement of ions further away and, second, potentially unphysical relaxation of ions in the outermost layer of the active cluster neighboring AIMP should be avoided. We find an outward movement (away from the vacancy) of the nearest neighbor Li^+ ions of 0.08 bohr and also an outward movement of the second nearest neighbor F^- ions of 0.03 bohr. With this relaxed geometry the F-center absorption energy of the $\text{Li}_{62}\text{F}_{62}$ cluster in the CBS limit is 5.96 eV on the Hartree–Fock and 5.31 eV on the CASPT2(ROHF) level. This corresponds to a decrease of the absorption energy compared to the unrelaxed geometry calculation by 0.21 eV and 0.19 eV for the HF and CASPT2(ROHF) case, respectively.

3.5.3. Line width of the absorption spectrum

The line width of the F-center absorption in alkali halides is dominated by electron-phonon interactions, i.e. the change of electronic energy with ion position. Lifetime broadening can be neglected due to the long lifetime of the excited state [45] of up to $\sim 10^{-6}$ s. Typically one local vibrational mode of ions close to the vacancy dominates the line width and the absorption process [8, 76]. In the case of LiF, this mode is the symmetric breathing mode of the six Li^+ ions around the vacancy in which they oscillate in phase towards/away from the vacancy (inset in fig. 3.11). We calculate the configuration-coordinate diagram for this mode for the $\text{Li}_{38}\text{F}_{18}$ cluster and the cc-pVTZ basis set (fig. 3.11) and extract a vibrational frequency of 15.78 THz (65.2 meV) and a line width of 0.27 eV due to the zero-point fluc-

tuations. According to a “rule of thumb” by Stoneham [8], this result seems to be reasonable since this frequency is comparable to the transverse optical phonon frequency of bulk LiF of ~ 10 THz [77, 78]. Also the theoretical line width is in reasonable agreement with experimental values at low temperature ranging from 0.42 to 0.61 eV [71, 79] since this single-mode estimate should be considered as a lower bound to the experiment. Further effects not included such as additional modes including ions beyond the nearest neighbors, thermal broadening, broadening due to imperfections (inhomogeneous broadening) would increase the theoretical line width. The same is true for broadening due to folding of the line with the experimental resolution.

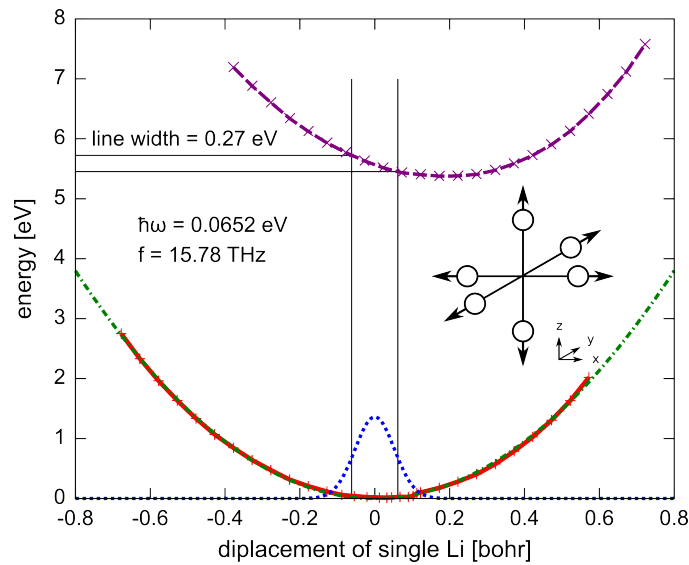


Figure 3.11.: Calculated configuration coordinate curves for ground (red full line) and excited (turquoise dashed) state of the F center in LiF as a function of the elongation along the symmetric breathing vibration of the six Li^+ ions surrounding the defect (inset). Calculations are performed for the $\text{Li}_{38}\text{F}_{18}$ cluster and the cc-pVTZ basis set. The blue (dotted) line is the absolute magnitude squared of the ground-state wave function of an harmonic potential with $\hbar\omega=0.0652$ eV (green dash-dotted line).

3.5.4. Electron-phonon coupling

The coupling of electronic and nuclear degrees of freedom may lead to a redshift of the absorption line of the F center with respect to its Franck–Condon value. We estimate contributions to this shift by analyzing the energy surfaces of ground and excited states and, alternatively, by estimating the self-energy of a “small” polaron. Fig. 3.12 shows two schematic potential energy surfaces of ground and excited state

of the F center as a function of an effective configuration coordinate. The Franck–Condon absorption is indicated by a vertical arrow, i.e., a vertical transition from the potential minimum of the ground state to the excited state. The lowest possible absorption energy, however, is given by the so-called zero-phonon line which is a non-vertical transition from the minimum of the ground state to the minimum of the excited state. The difference between the Franck–Condon and the zero-phonon line, E_{relax} , is an upper bound $E_{\text{relax}} = \Delta E_{\text{e-ph}}^{\text{max}}$ to the contribution of electron-phonon coupling to the redshift of the absorption line. E_{relax} corresponds to the relaxation energy of the excited state which we estimate in sec. 3.5.6 to be at least $E_{\text{relax}} \sim 0.5$ eV.

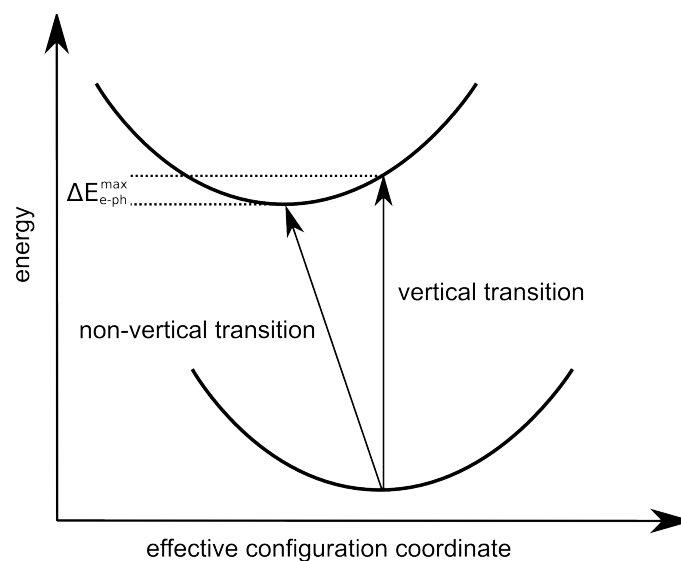


Figure 3.12.: Schematic picture of electronic potential energy surfaces of ground and excited state of the F-center as a function of an effective configuration coordinate. Arrows indicate the vertical (Franck–Condon like) transition and the non-vertical transition to the minimum of the excited state potential energy surface. The difference $\Delta E_{\text{e-ph}}^{\text{max}}$ in energy between these two excitations is an upper bound for the red shift of the absorption line due to electron-phonon interactions.

A proper way to determine the absorption spectrum and the influence of local vibration modes would be to calculate the Franck–Condon factors between the nuclear eigen states of the PESs of the F-center ground and excited states. For reliable results, however, the inclusion of more local modes as well as a proper description of the minimum of the excited state PES (the relaxed excited state) is necessary. An ab-initio realization of the latter, as will be shown in sec. 3.5.6, is, however, highly non trivial. Alkauskas and co-workers recently calculated the luminescence lineshape for a transition in the nitrogen-vacancy center in diamond and included

not only quasi-localized modes but also bulk phonons on equal footing [80]. Alternatively, within a polaron model the correction to an electronic energy level is given by the polaron self-energy induced by virtual excitations of electrons to the conduction band and their interaction with longitudinal optical phonons. Accordingly, differences between the polaron self-energies for the electronic ground and excited state of the color center contributes to the shift of the absorption line with respect to its Franck-Condon value. Since in alkali halides electron-phonon coupling is large we employ Feynman's strong-coupling limit for the polaron self-energy [81] $E_{\text{polaron}} = -(0.106\alpha^2 + 2.83)\hbar\omega$, where α is the Fröhlich coupling constant [82] and ω is the longitudinal optical phonon frequency. We estimate the shift of the absorption line as $\Delta E_{\text{e-ph}}^{(Q_j)} = -(0.106\alpha^2 + 2.83)\hbar\Delta\omega_{Q_j}$ through the largest difference in vibration frequency $\Delta\omega_{Q_j}$ of the local normal mode Q_j involving the six neighboring Li^+ ions between ground and excited state of the color center. The frequencies are obtained from parabolic fits to configuration coordinate curves calculated with the $\text{Li}_{38}\text{F}_{18}$ and the cc-pVTZ basis set. As dominant contribution we find $\Delta\omega_{Q_2} \approx 0.015$ eV, where Q_2 corresponds to the stretch vibration shown in fig. 3.13. Using the Fröhlich coupling constant of pristine LiF ($\alpha = 5.25$) yields $\Delta E_{\text{e-ph}} = 0.09$ eV.

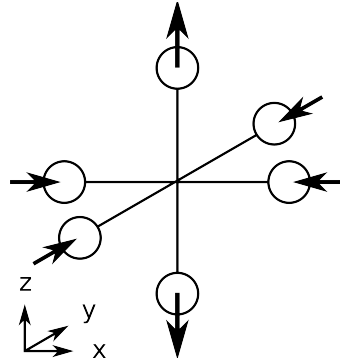


Figure 3.13.: Schematic picture of the stretch vibration of the six Li^+ ions neighboring the vacancy responsible for the dominant contribution $\Delta\omega_{Q_2} \approx 0.015$ eV.

In addition we explore dynamical corrections to the Born-Oppenheimer energy surfaces (see sec. 5.2) which scale with the inverse of the effective mass. The lowest-order non-Born-Oppenheimer (NBO) corrections $\Delta E^{(\text{NBO})}$ are given by the eigenvalues of the Hamiltonian matrix

$$\begin{aligned} \Delta H_{i,j} = & - \sum_a \frac{1}{M_a} \int dR \langle \phi_j | \nabla_a | \phi_i \rangle \chi_j \nabla_a \chi_i \\ & + \int dR \langle \phi_j | T_R | \phi_i \rangle \chi_j \chi_i, \end{aligned} \quad (3.2)$$

where ϕ_i is the electronic wave function of the i -th state, χ_i is the nuclear wave function in the i -th electronic state, and

$$T_R = \sum_a -\frac{1}{2M_a} \nabla_a^2$$

$$\nabla_a = \left(\frac{\partial}{\partial X_a}, \frac{\partial}{\partial Y_a}, \frac{\partial}{\partial Z_a} \right). \quad (3.3)$$

The index a runs over the atoms in the embedded cluster. The shift of the F-center absorption line due to electron-vibrational coupling is then given by the difference $\Delta E^{(\text{NBO})} = E_p^{(\text{NBO})} - E_s^{(\text{NBO})}$. We estimate $\Delta E^{(\text{NBO})}$ from a strongly truncated matrix including only the lowest-lying s and p-type states and with only the six-nearest neighbour Li^+ ions closest to the vacancy allowed to vibrate. The electronic matrix elements are evaluated on the multi-state CASPT2 level using finite differences (appendix A.4). For the nuclear wave functions χ_i the harmonic approximation is used. As expected, this estimate leads to a negligible energy shift below 0.0001 eV. We conclude that these dynamical corrections are completely negligible compared to the corrections due to quasi-static lattice distortion and relaxation.

3.5.5. Comparison of the theoretical and experimental spectrum

In this section we combine the effects discussed in the sections above and plot the theoretical spectrum together with the experimental one at $T \sim 5$ K in fig. 3.14. The theoretical spectrum is represented by a Lorentzian centered at 5.22 eV and a width (full width at half maximum) of 0.27 eV (sec. 3.5.3). The value for the peak position is composed of the CBS limit of the relaxed $\text{Li}_{62}\text{F}_{62}$ cluster (sec. 3.5.2) and the red shift due to electron phonon coupling $\Delta E_{\text{e-ph}}$ of 0.09 eV (sec. 3.5.4). Parameters for the experimental spectrum are taken from ref. [71] in which the spectrum is described by a Gaussian centered at 5.08 eV with a FWHM of 0.61 eV. Both spectra are in unprecedented agreement with each other

3.5.6. Photoluminescence and the relaxed excited state

So far we have only considered the absorption of light by the F-center electron but not the remaining processes in the optical cycle (fig. 3.15(a)). After the Franck-Condon absorption (1) the ions surrounding the vacancy respond to the new electronic configuration by changing their position (2) and the system ends up in the so-called relaxed excited state. The energy released in the relaxation is termed the relaxation energy E_{relax} . The relaxation proceeds quite quickly, taking only of the

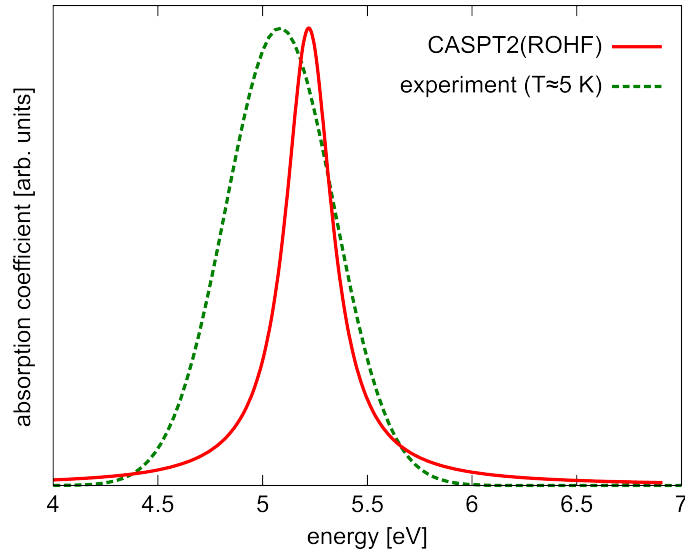


Figure 3.14.: Experimental [71] (green-dashed line) and calculated (red-solid lines) absorption spectra of the F center in LiF. The experimental spectrum is measured at $T \approx 5$ K and is depicted as a Gaussian function with a peak position of 5.08 eV and a full width at half maximum of $\text{FWHM} = 0.61$ eV. The quantum chemistry result is obtained from a CASPT2(ROHF) calculation in the converged basis set limit of the relaxed $\text{Li}_{62}\text{F}_{62}$ embedded cluster (sec. 3.5.2). It is plotted as a Lorentzian with a calculated line width at zero temperature (sec. 3.5.3) of 0.27 eV and contains a red shifted due to electron phonon-coupling of $\Delta E_{\text{e-ph}} = 0.09$ eV (sec. 3.5.4).

order of 10^{-12} seconds [45, 83], while the relaxed excited state is comparably long lived, $\sim 10^{-6}$ seconds [45, 83], before it decays via emission of light, the photoluminescence (3), to the unrelaxed ground state. A further relaxation back to the initial geometry (4) closes the optical cycle. The difference between the absorption energy and the emission energy, $E_{\text{abs}} - E_{\text{em}}$, is called the Stokes shift and is mainly determined by the geometry of the relaxed excited state.

As we have shown in detail in this chapter, the absorption process of the F-center in LiF (and also in other alkali-halide crystals (see next chapter)) is well understood and ab initio results are in good agreement with experiment. This is, however, not the case for the other steps of the optical cycle, especially for the relaxed excited state and the emission process. To our knowledge there are two (related) unsolved problems. First, although F-center luminescence and the relaxed excited state have been measured in detail in many alkali-halide crystals [45, 84] (also the dynamics of the nuclear wave packet after excitation has been measured [83]) there is no ab initio theory that could explain the large Stokes shifts ranging up to $E_{\text{abs}} - E_{\text{em}} = 3.70 - 1.66 = 2.04$ eV for the F-center in NaF. Second, there is

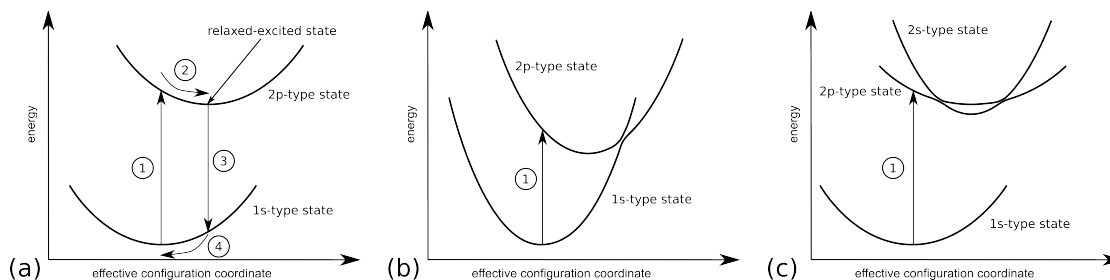


Figure 3.15.: Schematic picture of: (a) the optical cycle of (1) the absorption, (2) relaxation into the relaxed excited state, (3) photoluminescence, and (4) relaxation back to the initial ground state geometry; (b) radiationless emission via an avoided crossing between the s-type and p-type potential energy surface; (c) mixing of the PES of 2s and 2p-type excited state.

no observed luminescence of the F-center in LiF [85]. There are estimates [86, 87] that E_{em} should be in the range of ~ 1.4 eV (a Stokes shift of ~ 3.6 eV) but it has not been found experimentally and it is also not clear why this is the case. Possible explanations are that the signal is overshadowed by the emission from other defects [87], or that the light emitted by the F-center matches the absorption energy of another defect and, therefore, a large part is absorbed and reemitted at another energy. Also radiationless deexcitation is possible [84, 88] either due to an avoided crossing between the potential energy surfaces of the 1s and 2p level (fig. 3.15 (b)) or between the PESs of the 2s and the 2p levels (fig. 3.15 (c)) leading to a vanishing dipole matrix element between the relaxed excited state and the ground state. A partial reduction of the dipole element, the so-called 2s-2p mixing, is experimentally found [83] to be the reason for the long lifetimes of the relaxed excited F-center states in, e.g., KCl.

We try to shed some light on these questions by examining the relaxed excited state in LiF by means of state specific geometry relaxation. For the highly symmetric ground state geometry the three B_u levels are degenerate and the orientation of the excited p-type orbital is irrelevant (sec. 3.3). This is no longer true for the relaxed excited state. When the geometry of the excited state is optimized symmetry is reduced and the degeneracy is lifted in a Jahn–Teller like distortion. The orientation of the p-type orbital then crucially influences the emission energy. Within the D_{2h} point-group symmetry there are two (classes of) orientations of the p-type orbital, realized by different orientations of the D_{2h} symmetry planes with respect to the active cluster. The p-type orbital can point either towards the nearest neighbor Li^+ ions (fig. 3.7) or towards the second nearest neighbor F^- ions (figs. 3.5 (b) and 3.6 (b)). Using a CASPT2(ROHF) relaxation (cc-pVTZ basis set) of the nearest and second nearest neighbors in an $\text{Li}_{38}\text{F}_{18}$ cluster [47], we find the orientation towards F^- the more favorable one, i.e., the energetically lower one with $E_{\text{relax}} \approx 0.5$ eV,

$E_{\text{em}} = 4.49$ eV, and a corresponding Stokes shift of ~ 1 eV. This E_{em} value, however, is clearly too large compared to the estimate of 1.4 eV and the luminescence energy of the F-center in NaF, $E_{\text{em}}(\text{NaF}) = 1.66$ eV, the alkali halide with the lattice constant closest to LiF.

The overestimation of E_{em} in LiF is, at least partially, due to the limited cluster size and, thus, the limited number of ions involved in the relaxation as well as the symmetry constraints imposed by the D_{2h} point-group symmetry. We remove these restrictions by allowing also for third-nearest neighbor relaxation and by using the C_{2h} point-group symmetry. The calculations become computationally more demanding and, therefore, only a CASSCF relaxation with the cc-pVDZ basis set is used. In the C_{2h} point-group symmetry two of the p-type levels are in the CAS which allows for a rotation of the occupied p-type orbital within a plane. We orient this plane such that it contains the defect vacancy and is perpendicular to the [100] crystal direction (fig. 3.16 (a)). This choice comprises the p-type orbital orientation towards the third nearest neighbor Li^+ ion (fig. 3.16 (b)), i.e., orientation along the space diagonal of the LiF unit cell. This is, indeed, the orientation with the lowest energy found in the CASSCF relaxation. At this relaxed geometry, the CASPT2(ROHF,cc-pVTZ) emission energy is 3.99 eV (Stokes shift of 1.5 eV) which is 0.5 eV lower than the emission energy for the orientation towards F^- . Although this emission energy is still too high, it clearly shows that a more general relaxation protocol, in terms of number of ions involved and symmetry constraints, considerably reduces the emission energy and increases the Stokes shift.

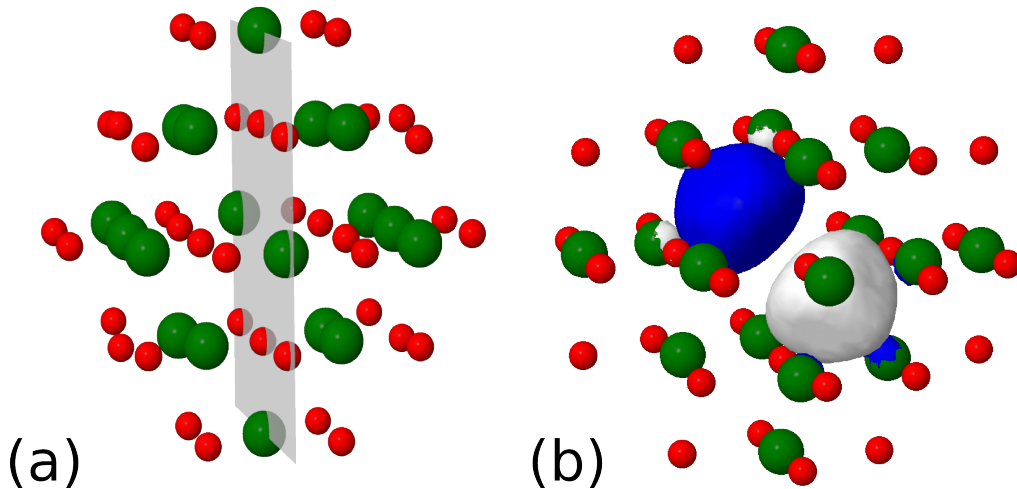


Figure 3.16.: (a) Plane in which the p-type orbital is allowed to rotate during the geometry optimization of the relaxed excited state using the C_{2h} point-group symmetry. (b) Isosurface of the F-center electron in the relaxed excited state. The orbital points towards the third nearest neighbor Li^+ ion along the space diagonal of the LiF unit cell.

Within the relaxed geometry with the p-type orbital oriented along the space diagonal we search for signs of a radiationless decay of the relaxed excited state but we neither find avoided crossings nor a reduction of the dipole matrix element. A definite answer to the problem of the luminescence of the F center in LiF (and other alkali-halide crystals) awaits further calculations with larger cluster sizes and more advanced relaxation strategies possibly also including long-range polarization.

3.6. Solid-state physicist's and quantum chemist's approach to the F-center in LiF: a comparison

In this section we compare the quantum chemistry results discussed above with results on the F center in LiF from periodic boundary (post-) DFT calculations conducted by Karsai [47, 48]. First, however, we illustrate the conceptual differences between the two approaches (fig. 3.17) using an oversimplified model: we approximate the defect electron by a particle in a square-well potential of finite height. The upper edge of the square well marks the onset of the conduction band, E_c . The ground-state energy of the electron, E_s , lies deep in the band gap of LiF, i.e., the square well. Since the square well has a finite depth, the p-state energy, E_p , does not necessarily lie below the continuum onset, i.e., the conduction-band edge, but may appear as a resonance within the conduction band.

The quantum chemistry approach to optical excitation energies typically sets out from Hartree–Fock calculations of the ground and excited state configurations, which are depicted in panel I(a) and I(b), respectively. The absorption, i.e. excitation energy is then the total energy difference of the N-electron wave functions. Excitonic effects are naturally included since the potential “seen” by the excited F-center electron in panel I(b) contains the hole the electron left behind after excitation. The Hartree–Fock approximation typically overestimates band gaps and, therefore, the depth of the potential well in fig. 3.17. As a consequence both, the s- and the p-orbital energies, lie below the onset of the continuum independent of the configuration.

DFT is known for underestimating the band gap leading to a more shallow potential well and to a p-state appearing as a broad resonance within the conduction band in panel I(a). In periodic boundary calculations the band gap is usually corrected by employing many-body perturbation theory on the level of the *GW* approximation [89]. The resulting quasi-particle energies correspond then to electron *addition* and *removal* energies. Therefore, the quasi-particle energy E_p in panel II(b) is the energy of an electron added to the system in the presence of an electron occupying the s-state. While *GW* considerably increases the depth of the potential well, the p state is still in the conduction band due to the mutual repulsion with the electron

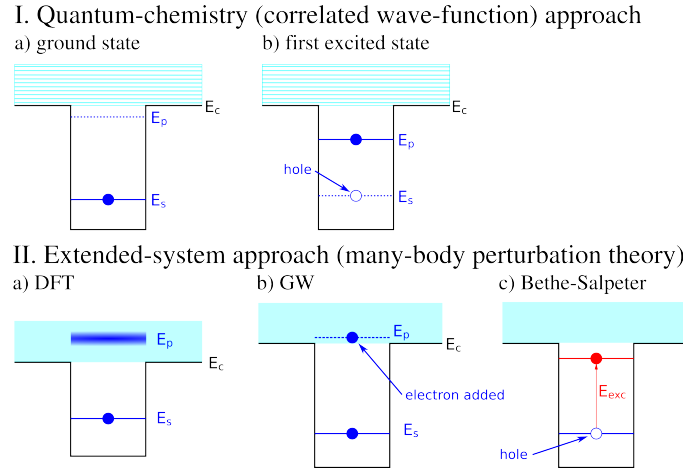


Figure 3.17.: Alternative strategies for calculating F-center excitation energies. The F-center electron is represented by a particle in the box. E_s denotes the single-particle level of the electron in the ground-state (“s-type wave function”) of the F center, E_p denotes the energy of the first excited state (“p-type wave function”). The shaded area marks the conduction band with the band edge at E_c . In the extended system approach (I) of solid-state physics, the addition energy is determined by the GW approximation (Ib) and the correction due to the excitonic interaction with the hole (Ic) is described by the Bethe–Salpeter equation. In embedded-cluster approaches employing quantum chemistry, the total N-electron energy of the two lowest states of opposite parity (II a and b) are calculated and subtracted from each other.

in the s-state. However, it has been localized more strongly, as indicated by the narrowing of the energy level. A further correction is necessary to account for the screened Coulomb attraction within the solid-state approach between the hole in the s level and the electron in the p level. This gives rise to an excitonic state which, in the present case, lies below the edge of the conduction band in panel II(c). Excitonic corrections are typically calculated by solving the Bethe–Salpeter equation [90].

On the single-particle level we can compare the defect orbitals from quantum chemistry and DFT calculations. s- and p-type Kohn–Sham orbitals extracted at the Γ point from DFT-SCF runs using the Tran–Blaha modified Becke–Johnson (TB-mBJ) exchange–correlation potential [91] are plotted in fig. 3.18 (a) and (b), respectively. The occupied s-type orbitals (ROHF: fig. 3.18 (c) and DFT: fig. 3.18 (a)) qualitatively agree in size and shape. Note that in both figures the same values for the contour lines are used. For a comparison of the p-type orbitals (ROHF: fig. 3.18 (d) and DFT: fig. 3.18 (b)) a few explanations are necessary. One obje-

tive from DFT point of view in our study in ref. [47] is the performance of the TB-mBJ exchange-correlation potential compared to the application of the numerically more expensive GW perturbation theory to correct the band gap. The TB-mBJ exchange-correlation potential is designed for materials with large band gaps, such as LiF, and corrects for the band-gap underestimation known for “standard” exchange-correlation potentials. It predicts the LiF band gap to be 14.51 eV in good agreement with experiment (14.2 eV). As a consequence we find a situation different to the one depicted in panel II(a) in fig. 3.17. The TB-mBJ potential leads to a p-state orbital energy below the onset of the conduction band and to the formation of localized, *unoccupied* p orbitals, one of which is shown in fig. 3.18 (b). This orbital should not be compared to the *occupied* Hartree–Fock p orbital in fig. 3.6 (b). Rather it should be compared to the unoccupied HF-p orbital with the defect electron in the ground state. As discussed above, HF leads to a large overestimation of the band gap and, therefore, the excited (unoccupied) p levels also lie below the conduction band. The unoccupied HF-p orbital (fig. 3.18 (d)) is somewhat more diffuse than the DFT-p orbital (and also the occupied HF-p orbital) but both are still in qualitative agreement.

Qualitative agreement is also found for the relaxation parameters for the ground state of the F center. DFT(PBE) and CASPT2(ROHF) lead to an identical outward relaxation of 0.08 bohr of the nearest-neighbor Li^+ ions and to a similarly small outward relaxation of the next-nearest neighbor F^- ions (0.03 bohr in CASPT2(ROHF) and 0.02 bohr in DFT). Such a degree of agreement between periodic DFT and quantum-chemistry cluster calculations is not typical. In magnesium oxide, for example, the relaxation of Mg^+ ions surrounding the (two electron) F-center vacancy obtained from periodic DFT [92] and embedded cluster HF calculations [93] differ by a factor of ~ 5 . PBE is used for the geometry relaxation since TB-mBJ does not provide total energies [91] and, thus, forces on the ionic cores are not available.

Also a comparison of the absorption spectra obtained from solving the Bethe–Salpeter equation, the one from CASPT2(ROHF), and the experimental one (fig. 3.19) shows excellent agreement between the two theoretical methods and the experiment. Please note that all theoretical spectra are plotted with the width determined in sec. 3.5.3 and contain the shift due to electron-phonon coupling (sec. 3.5.4).

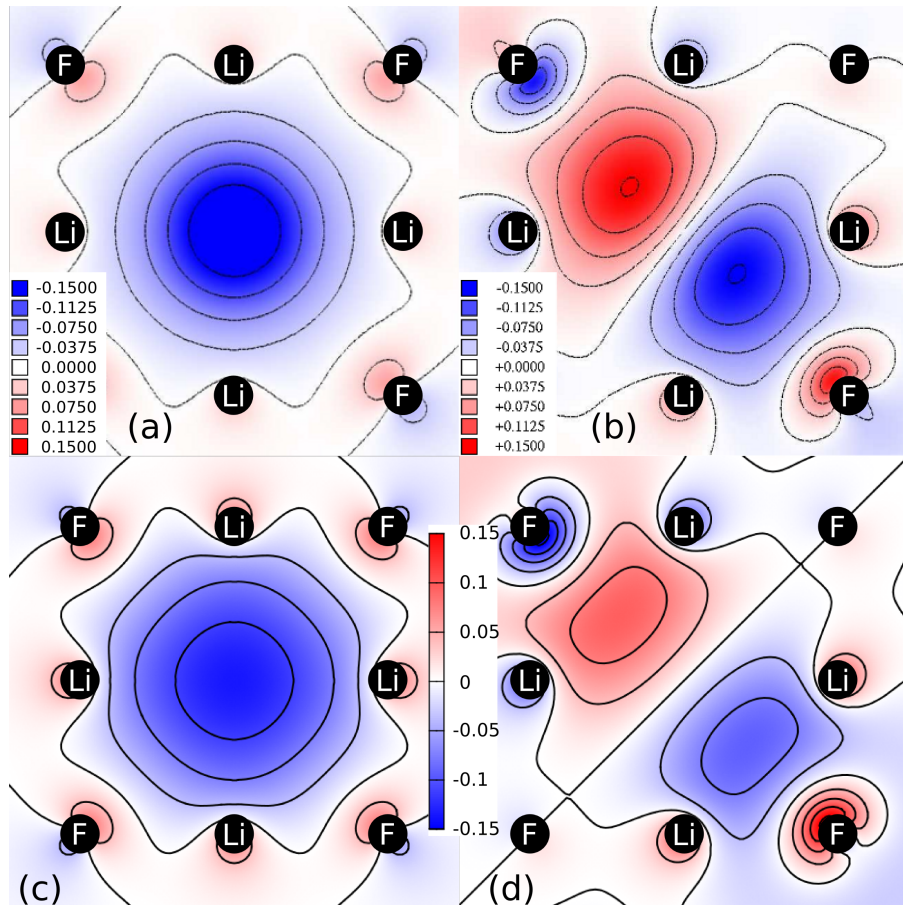


Figure 3.18.: Upper panels: Kohn-Sham wave function (exchange-correlation potential: TB-mBJ) contour plot within the (100) plane at the Γ point for the (α -spin) F-center bands in the $\text{Li}_{32}\text{F}_{31}$ supercell: (a) occupied s-orbital, (b) one of the three degenerate unoccupied p-orbitals. Lower panels: ROHF wave function of (c) the occupied s-orbital and (d) the unoccupied p-type orbital in an embedded $\text{Li}_{38}\text{F}_{18}$ embedded cluster.

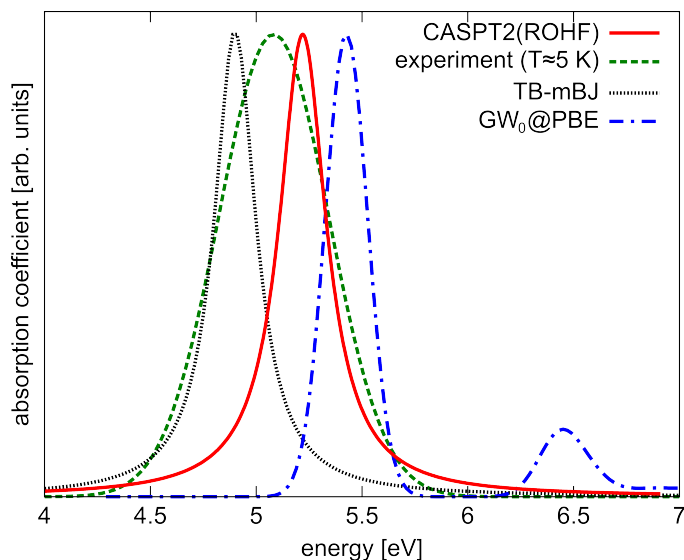


Figure 3.19.: Experimental [71] (green, dashed line) and calculated absorption spectra of the F center in LiF. The experimental spectrum is measured at $T \approx 5$ K and is depicted as a Gaussian function with a peak position of 5.08 eV and a full width at half maximum of $\text{FWHM} = 0.61$ eV. Spectra calculated from post DFT methods [TB-mBJ + BSE (black, fine-dashed line) and $\text{GW}_0\text{PBE} + \text{BSE}$ (blue, dash-dotted line)] are determined within a $\text{Li}_{16}\text{F}_{15}$ unit cell. The quantum chemistry result (solid-red line) is obtained from a CASPT2(ROHF) calculation in the converged basis set limit of the relaxed $\text{Li}_{62}\text{F}_{62}$ embedded cluster (sec. 3.5.2). All theory data are plotted with a calculated line width at zero temperature (sec. 3.5.3) of 0.27 eV and contain a red shifted due to electron phonon-coupling of $\Delta E_{\text{e-ph}} = 0.09$ eV (sec. 3.5.4).

4. The Mollwo–Ivey relation for F-centers in alkali halide crystals

In this chapter we extend the investigation of F-center absorption energies to other alkali halides. In particular, we focus on the scaling of the absorption energy with the lattice constant known as the Mollwo–Ivey (MI) relation. Mollwo [9] first observed in 1931 that the F-center absorption energy E_{abs} in various alkali-halide crystals scales like $\sim 1/a^2$, where a is the anion-cation distance. Later Ivey [10] found, based on a larger data set of alkali halides, the scaling

$$E_{\text{abs}} = C \cdot a^{-n} \quad (4.1)$$

for various defects, where C is a constant and n is the so-called Mollwo–Ivey exponent. A fit of this expression to experimental absorption energies of F centers in rock-salt structure alkali halides [12, 71] leads to $n = 1.81 \pm 0.1$ and $C = 17.3 \pm 2.8$ eV with a given in Ångström. In the years to follow many theoretical studies were conducted [7, 94–97] aiming at an explanation of this seemingly simple scaling relation and resulting in a variety of qualitative and semi-quantitative models. These models differ in detail but have a common underlying picture which is a simple particle-in-the-box model: the F-center electron is the particle and the Madelung potential of the ionic crystal provides the confining box. Also common to these models is the neglect of the electronic structure of the actual chemical elements building up the crystal. Their influence on the MI relation is summarized under the term ion-size effects. Since they are not expected to follow any simple a -scaling, they were made responsible only for small element-specific deviations from the scaling in eq. 4.1. Refinements accounting for ion-size effects [56, 57, 98] were proposed when, e.g., experimental data on the pressure shift of E_{abs} [99] showed stronger deviations from the MI relation.

To our knowledge, however, a systematic ab-initio study of the Mollwo–Ivey relation still seems to be missing. We, therefore, apply the quantum chemistry approach, described in the previous chapter, to the F-center absorption in various rock salt alkali-halide crystals and conduct a detailed study of the MI relation and the role of ion-size effects. We find that earlier particle-in-the-box models need to be substantially refined. Instead of the Madelung potential element-specific effects, i.e.,

ion-size effects are key for understanding the Mollwo–Ivey relation and its exponent. Similar to the previous chapter this work has been done in collaboration with the group of P. Blaha, in particular with Ferenc Karsai, who applied post-DFT methods to the problem at hand. To develop a more complete picture of the MI relation we also show parts of his results in this work. Further post-DFT results as well as details on the DFT calculations can be found in [100] and in Karsai’s doctoral thesis [48].

This chapter is structured as follows. First, we briefly review in sec. 4.1 previously proposed models for explaining the Mollwo–Ivey exponent. Second, in sec. 4.2 we investigate the potential landscape in the defect region. In sec. 4.3 we introduce the concept of a scaled alkali-halide crystal which helps to disentangle ion-size effects from effects due to varying lattice constants. Ion-size effects and their influence on the F-center absorption energies in various alkali halides are presented in sec. 4.4. We do not repeat the computational details given in chapter 3. Only deviations from this protocol will be mentioned.

4.1. Previous work

The experimental discovery of the Mollwo–Ivey relation triggered a considerable amount of theoretical work intended to explore the physical background of the Mollwo–Ivey relation and the origin of the experimental Mollwo–Ivey exponent of $n_{exp} = 1.81$. The first explanation was given by Fröhlich [94] who deduced $n = 2$ from the energy spacing between bands of a delocalized nearly free electron in a potential of period $2a$, $\Delta E \sim \frac{1}{2m^*}(2\pi/2a)^2$, with m^* the effective mass. Stöckmann, on the other hand, started out from a completely localized electron confined in a hard-wall box potential [95–97] leading to the same a^{-2} scaling. This box potential served as an approximation of the Madelung potential (see below) and was further refined in subsequent works [7]. The two seemingly contradicting models both yield $n = 2$ since both probe the kinetic energy of an electron either confined to a periodic structure or to a hard wall box potential. The two most recent and widely accepted explanations are given by Wood [11] and by Smith and co-workers [12, 98, 101–103] and are briefly reviewed in the two following sections.

4.1.1. The point-ion model

In the point-ion model of Wood [11] the defect electron is described by a test wave function the parameters of which are optimized to find the lowest energy of ground and excited state. All other ions are represented by pure point charges. Wood showed that, within this model, the energy of the F-center electron solely depends on terms scaling with either a^{-1} (the Madelung potential energy) or with a^{-2} (the

quantum-confined kinetic energy) leading to the absorption energy

$$E_{\text{abs}} = c_{-1}a^{-1} + c_{-2}a^{-2}. \quad (4.2)$$

Using two experimental data points he determined the constants c_{-1} and c_{-2} and fitted the power series expansion (eq. 4.2) to a single exponent Mollwo–Ivey type relation resulting in $n \approx 1.8$ in good agreement with experiment. Wood also explored, what he called, the extended-ion model in which he included exchange terms and effects arising from orthogonalization of the test wave function to the core electrons of neighboring cations. These contributions were estimated to scale with powers in $(1/a)$ larger than 2 and they hardly change Wood’s MI relation but are responsible for slight, element-specific deviations only. Also in other studies using similar models [56, 57, 99] ion-size effects are used to describe small deviations from the MI exponent 1.8.

4.1.2. Relation between the extent of the F-center wave function and its absorption energy

The Vinti sum rule [104] allows to connect the extent of the defect wave function in its ground state, $|s\rangle$, with the defect absorption energy, E_{abs} . For single-electron systems one can show [105] that the expectation value $\langle s|r^2|s\rangle$ is connected to moments of the energy dependent absorption coefficient $K(\omega)$ by (in SI units)

$$\langle s|r^2|s\rangle = \frac{3\hbar}{2m_e} \frac{\mu_{-1}}{\mu_0}, \quad (4.3)$$

where m_e denotes the free-electron mass and the n -th moment of $K(\omega)$ is given by

$$\mu_n = \int \omega^n K(\omega) d\omega. \quad (4.4)$$

Application of this single-electron result to the absorption of defects in solids is possible when the absorption of the defect and the one of the solid are separated and when an effective electron mass m^* is introduced. This leads to an approximate defect sum rule. Due to the large band gap in alkali halides the absorption contributions from the F-center and the solid are typically easy to separate. Furthermore, since the F-center hosts a strongly bound and highly localized electron, the free electron mass is supposed to be a good approximation for the effective mass. Nevertheless, to indicate the approximate nature of the defect sum rule we keep the notation m^* in the following.

F-center absorption spectra typically feature one dominant band, the F-band, corresponding to the excitation of the defect electron from the ground state to the first optically allowed excited state. Excitations to higher lying states are possible [106],

the so-called K and L absorption bands, but are much weaker [12]. Approximating all individual bands of the F-center absorption spectrum $K(\omega)$ by δ functions with oscillator strength f_i and energy E_i leads to the alternative expression

$$\langle s|r^2|s \rangle \approx \frac{3\hbar^2}{2m^*} \frac{\sum_i f_i E_i}{\sum_i f_i} \quad (4.5)$$

for the Vinti sum rule. Neglecting all but the F absorption band with $f_i \approx 1$ leads to

$$E_{\text{abs}} \approx \frac{3\hbar^2}{2m^*} \frac{1}{\langle s|r^2|s \rangle}, \quad (4.6)$$

connecting the defect-absorption energy E_{abs} with the mean-square radius of its ground state wave function.

Malghani and Smith [12] analyzed the moments of experimental absorption spectra [71, 106] and extracted the root-mean square (rms) radius $\langle s|r^2|s \rangle^{1/2}$ of the F-center defect wave function via eq. 4.3 for different alkali-halide crystals (fig. 4.1). They found an almost perfectly linear increase of the rms radii with the anion-cation distance and concluded: (i) the spatial extent of the wave function needs to be a continuous function of a and (ii) additional effects like, for example, ion sizes and ion-dependent polarization are small and are only responsible for the scatter of the data points around the fitted straight line. In other words, since the effects of the ionic species involved are negligible, the crystal field, i.e., the Madelung potential is responsible for the formation of the Mollwo–Ivey relation with an exponent of $n_{\text{exp}} = 1.81$.

Further, Malghani and Smith used their root-mean square radii extracted from the F-center absorption spectra (eq. 4.3) to calculate absorption energies via the Vinti sum rule (eq. 4.6). This protocol leads to excellent agreement with experimental absorption energies. Malghani and Smith argue that this agreement supports the validity of the Vinti sum rule for the F-center defect and the reliability of the root-mean square radii extracted (4.1). This conclusion, however, is based on a circular reasoning. The root-mean square radii in eq. 4.3 hardly depend on the shape of the absorption spectra $K(\omega)$ but are almost exclusively dominated by the center of the dominant F absorption line, i.e., by E_{abs} , the experimental absorption energy. Therefore, Malghani and Smith effectively used eq. 4.6 in both directions. First, they extract the rms-radii from the experimental absorption energies and, second, they used these radii to determine their own absorption energies, which are, of course, in close agreement with the experimental ones.

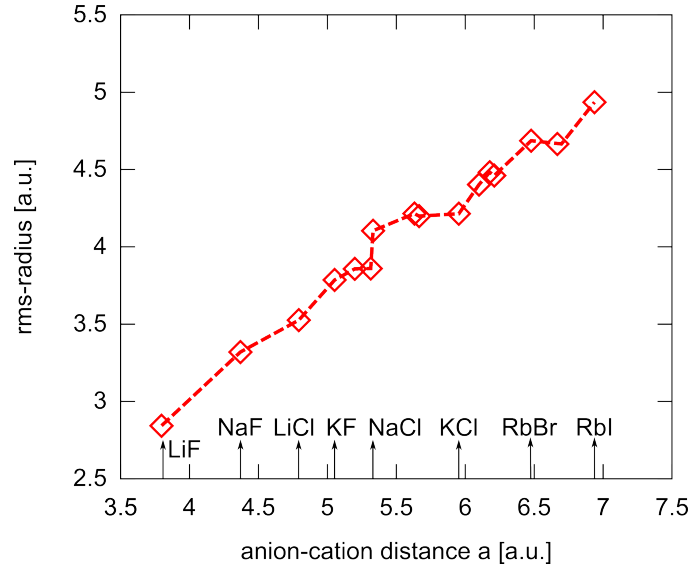


Figure 4.1.: Root-mean square radii $\langle s|r^2|s\rangle^{1/2}$ of ground state F-center defect wave functions in various alkali-halide crystals as extracted by Malghani and Smith [12] from experimental absorption spectra [71] via eq. 4.3.

4.2. The “box” potential

In all the models above the Madelung potential is attributed a crucial role in forming the box potential and in the explanation of the Mollwo–Ivey exponent. In this section we compare the Madelung potential of LiF, the alkali halide with the smallest ions, and, therefore, with smallest ion-size effects, to the potentials confining the defect electron in ab initio calculations. The Madelung potential (fig. 4.2 (a)) is flat in the vacancy region and the second-nearest neighbor anions, or better, negative charges form a confining potential well of ~ 7.5 eV depth. This potential well initially motivated the particle-in-the-box model by Stöckmann. We have shown in the previous chapter that the F-center electron is well localized within the vacancy region and has only little weight on the neighboring ions. From the shape of the Madelung potential, however, one would expect a significant “spill-out” to the nearest-neighbor cations. This suggests that the confinement of the F-center electron is due to the exchange interaction and the orthogonality of the defect-wave function to core levels of the surrounding ions. Both effects strongly depend on the specific elements of the alkali-halide crystal showing that ion-size effects, rather than the Madelung potential, are responsible for the confinement and, therefore, determine the Mollwo–Ivey relation.

DFT is a suitable tool to study the potential well in the defect region due to the local representation of the single-electron potential, i.e., the Kohn–Sham (KS) po-

tential. In contrast to the Madelung potential the Kohn–Sham potential within the local-density approximation (LDA) $V_{\text{KS}}^{(\text{LDA})}$ (fig. 4.2 (b)) to the exchange–correlation potential appears to lack any confining potential. This is due to the fact that the KS potential is a potential common to all electrons and does not display the effects of orthogonalization between single-particle levels. After the self-consistent determination of the orbitals of all electrons, the defect electron is localized within the vacancy due to orthogonalization constraints imposed by the core and valence electrons of neighboring ions. The presence of a potential barrier is indicated by the point of inflection in the LDA defect-wave function (fig. 4.3) where the wave function enters the classically forbidden region.

A pronounced potential barrier is present (fig. 4.2 (c)) in the Kohn–Sham potential $V_{\text{KS}}^{(\text{TB-mBJ})}$, calculated with the TB-mBJ approximation to the exchange–correlation potential. Its depth varies between 17 and 25 eV depending on the crystallographic direction. A cut through the potential surface along the [111] direction (fig. 4.4) clearly shows that the electrostatic potential, consisting of the electrostatic contributions of the point nuclei and the self-consistent electron density, gives rise to a local maximum in the potential near the location of the color center. Within the TB-mBJ approximation, it is the exchange–correlation potential that is responsible for the formation of an attractive potential well in the total effective Kohn–Sham potential and the confinement of the s-like defect-electron orbital with Kohn–Sham energy $\epsilon_{\text{KS}}^{(\text{TB-mBJ})}(s)$ (Fig. 4.4 (b)). The large differences between $V_{\text{KS}}^{(\text{LDA})}$ and $V_{\text{KS}}^{(\text{TB-mBJ})}$ are not surprising. The LDA severely underestimates the band gap of alkali halides. The TB-mBJ exchange–correlation potential is designed to reproduce the experimental alkali-halide band gaps by raising the effective potential in the interstitial regions. It is, therefore, expected to yield a ground state electron density considerably different from LDA or Hartree–Fock. In view of these differences, an interpretation in terms of a realistic landscape should be taken with caution as the confinement of the wave function stems largely from the orthogonality requirement built into the non-local potential. We will use $V_{\text{KS}}^{(\text{TB-mBJ})}$ in the following rather as a useful approximation to the effective potential that an isolated defect electron would feel in an otherwise fixed charge distribution.

Despite the pronounced differences between the potentials $V_{\text{KS}}^{(\text{LDA})}$ and $V_{\text{KS}}^{(\text{TB-mBJ})}$ (Fig. 4.4 (a) and (b), respectively), as well as the non-local Hartree–Fock potential in ROHF calculations the resulting wave functions of the defect electron are very similar (Fig. 4.3). All of them feature a point of inflection indicative for an effective confining potential well. Our current observations shed new light on previous work: what was earlier considered to be a small “ion-size” correction to the leading exponent $n = 1.8$, is in fact the dominant contribution to the formation of the (effective) well and, thus, to the Mollwo–Ivey exponent itself. It should be noted, however, that the effective size of the potential well in terms of the classically allowed region of the wave function, as marked by the point of inflection, cannot be determined

for all spatial directions. Along, e.g., [100] no point of inflection can be found in LDA and ROHF wave functions (Fig. 4.3 (b)). Also $\epsilon_{\text{KS}}^{(\text{TB-mBJ})}$ lies above the barrier top in this direction, but still the TB-mBJ wave function displays a point of inflection due to orthogonalization. We introduce in the following as effective measure for the size of the F-center function the position of the (first) zero of the s state along the [100] direction which accounts for the required orthogonality to the nearest-neighbor ionic states. Another measure of the size of the F-center is the mean-square radius of the wave-function $\langle s|r^2|s\rangle$.

The analysis of the Fermi contact term A_0 (sec. 3.5.1) at nuclear sites surrounding the vacancy shows that an experimental mapping of the defect wave function and, i.e., the confining potential is not unambiguously possible using experimental ENDOR data. The good agreement between experiment and UHF results for A_0 , however, shows that the UHF and the identical ROHF defect wave functions are reliable at least for distances from the vacancy up to the nearest-neighbor ions which covers more than 80 % of the defect density. Therefore, we focus in the following on the ROHF defect wave functions as they are the starting point for the CASPT2(ROHF) calculations of the F-center absorption energies. $V_{\text{KS}}^{(\text{LDA})}$ confines the defect electron too weakly, leading to an overestimation of the Fermi contact term at the nearest-neighbor Li^+ ion of ~ 10 %. LDA calculations using periodic boundary conditions [75] overestimate A_0 by even 20 %. Due to its deep potential well $V_{\text{KS}}^{(\text{TB-mBJ})}$ localizes the defect electron too strongly leading to an underestimation of A_0 by ~ 75 %.

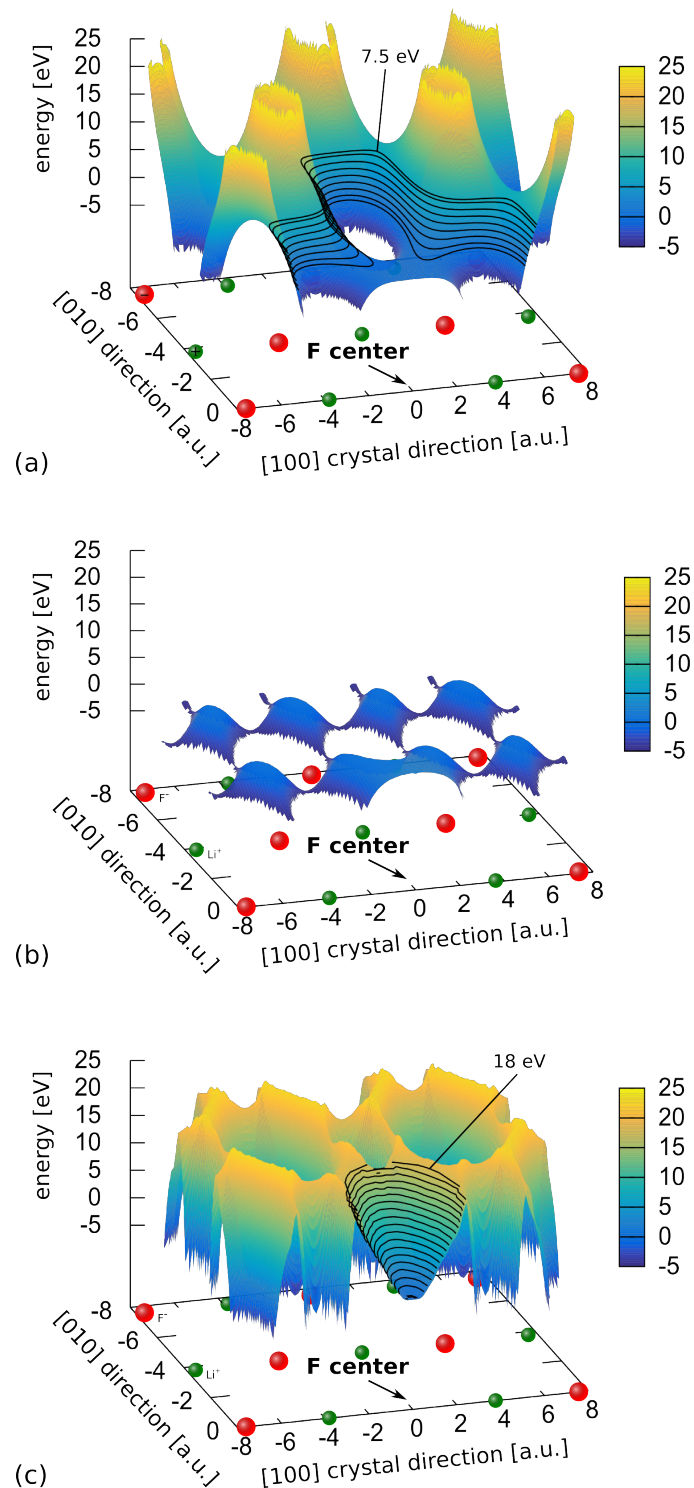


Figure 4.2.: Two-dimensional cut through (a) the Madelung potential, (b) the effective Kohn–Sham potential $V_{\text{KS}}^{(\text{LDA})}$ (within the LDA), and (c) the effective KS potential $V_{\text{KS}}^{(\text{TB-mBJ})}$ (with the TB-mBJ exchange–correlation potential) in the F-center vacancy region of an LiF crystal. The vacancy is located at the origin of the (100) plane shown.

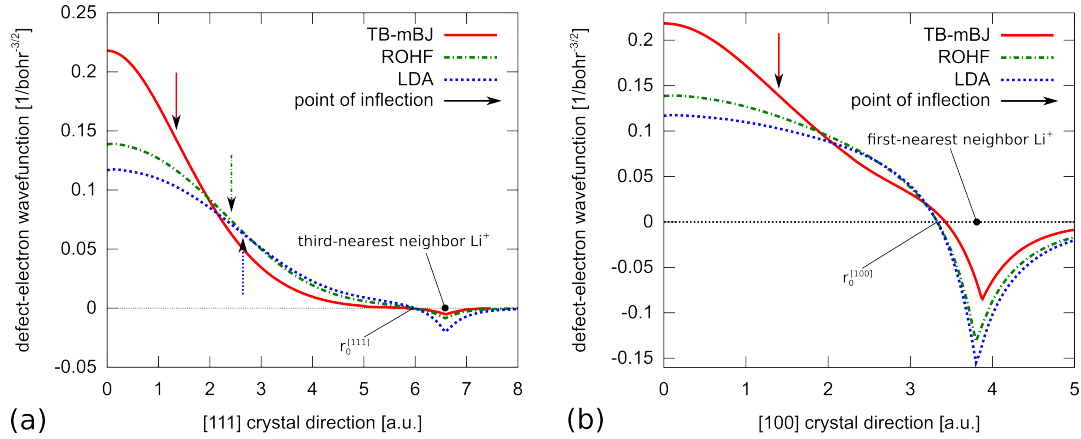


Figure 4.3.: Cut through the ground state TB-mBJ (solid red line), ROHF (dash-dotted green), and LDA (blue dotted) orbital of the F-center electron in LiF along the (a) [111] and (b) [100] crystal directions. Vertical arrows indicate points of inflection where the wave function enters a classically forbidden region and penetrates the effective potential barrier. $r_0^{[111]}$ and $r_0^{[100]}$ denote the position of the first radial node of the ROHF wave function in the [111] and [100] direction, respectively.

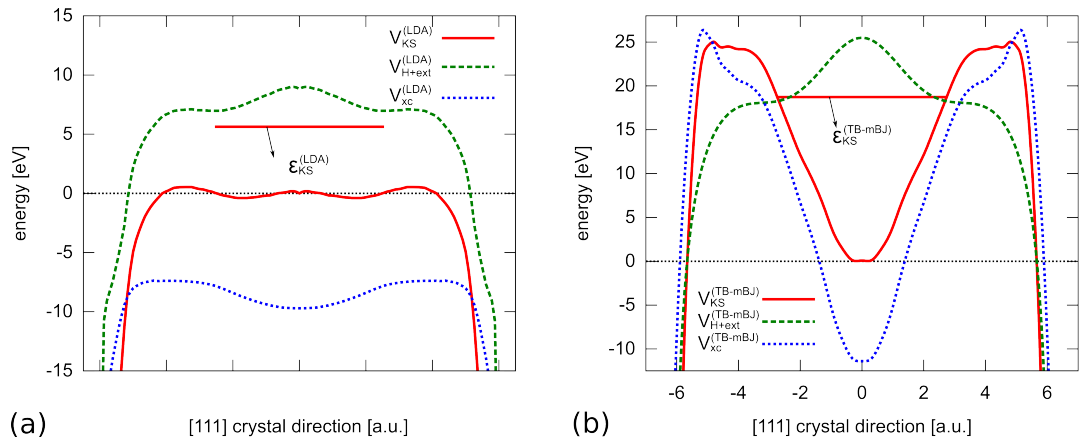


Figure 4.4.: Cut through the effective Kohn–Sham potential V_{KS} (red solid line) (a) in the local-density approximation and (b) using the TB-mBJ exchange–correlation potential in the F-center defect region of an LiF crystal along the [111] direction. Green (dashed) and blue (dotted) lines are the electrostatic potential V_{H+ext} (Hartree plus “external” ion-core potential) and the exchange–correlation potential V_{xc} , respectively. The horizontal lines labeled with $\epsilon_{KS}^{(LDA)}$ and $\epsilon_{KS}^{(TB-mBJ)}$ denote the Kohn–Sham single-particle energy level of the localized F-center electron in using the LDA and the TB-mBJ exchange–correlation potential, respectively.

4.3. Scaling with the lattice constant

In this section we introduce the model system of the F center in a “scaled alkali-halide crystal”. We calculate the absorption energy and the defect wave function for arbitrary anion-cation distance, a , while keeping the anionic and cationic species constant. This allows for a disentanglement of ion-size effects and effects induced by a “pure” increase of the lattice constant. If earlier explanations were true and ion sizes indeed play a minor role in the formation of the Mollwo–Ivey relation we would expect to find good agreement between the experimental MI relation and the one of a scaled alkali halide. More precisely, we would expect to find a Mollwo–Ivey exponent close to 1.8. We neglect for the study of the scaling with a any lattice relaxation or corrections due to electron-phonon coupling.

4.3.1. F-center absorption energies in scaled LiF

Lithium fluoride is the alkali halide with the smallest ions and, therefore, also with the smallest ion-size effects. In this sense scaled lithium fluoride is the closest ab initio analogue to the point-ion model. Independent of the anion-cation distance the defect electron in its ground state is well localized within the vacancy region similar to the F-center in LiF with its real lattice constant shown, e.g., in fig. 3.5 (a). ROHF, CASPT2(ROHF), and DFT+BSE absorption energies in scaled LiF smoothly decay with increasing a (fig. 4.5) and fits of Mollwo–Ivey type relations yield MI exponents of $n_{\text{ROHF}} = 2.14$, $n_{\text{CASPT2}} = 2.04$, and $n_{\text{BSE}} = 2.01$. Exponents n_{CASPT2} and $n_{\text{DFT+BSE}}$ are clearly larger than $n_{\text{exp}} = 1.81$ and almost perfectly match the prediction of $n = 2$ from the particle in the hard-wall potential box.

The exponent $n_{\text{ROHF}} = 2.14$ is even larger due to the neglect of correlations. Both, the absolute as well as the relative difference between ROHF and CASPT2(ROHF) absorption energies decrease with increasing lattice constant. It seems as if this was due to the short-range nature of correlation energy. The further the ions are apart, the more the defect electron behaves like an isolated single-particle system. From a computational viewpoint it should be noted that also in terms of convergence there appears a dependence on the lattice parameter. To converge the absorption energy of the F-center in real LiF we need to use the $\text{Li}_{62}\text{F}_{62}$ cluster and extrapolate to the converged-basis set limit (see chap. 3). Already for $\text{LiF}(a_{\text{NaF}})$, lithium fluoride with the anion-cation distance of sodium fluoride (NaF), however, the absorption energy is essentially converged for the $\text{Li}_{38}\text{F}_{18}$ cluster and the cc-pVTZ basis set. Except for the absorption energy in $\text{LiF}(a_{\text{LiF}})$ all energies in fig. 4.5 are obtained with this cluster and basis-set size.

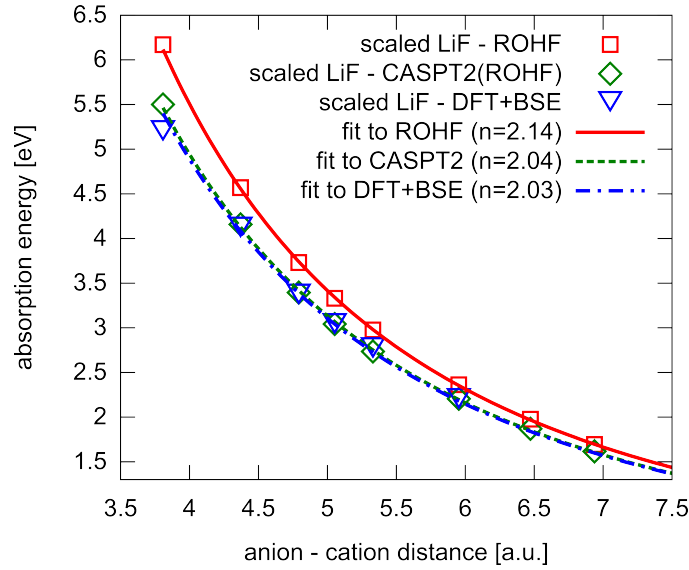


Figure 4.5.: Converged F-center absorption energies in scaled LiF as a function of the anion-cation distance. Red squares, green diamonds, and blue triangles are ROHF, CASPT2(ROHF), and DFT+BSE results, respectively. Lines through the data points are fits of Mollwo–Ivey type relations with exponents $n_{\text{ROHF}} = 2.14$, $n_{\text{CASPT2}} = 2.04$, and $n_{\text{BSE}} = 2.03$.

4.3.2. Spatial extent of the F center in scaled LiF

We study now the shape of the F-center defect wave function in scaled LiF in its ground state and its dependence on the anion-cation distance a . According to the F-center defect version of the Vinti sum rule (eq. 4.6), the rms radius $\langle s|r^2|s\rangle^{1/2}$, a measure for the spatial extent of the wave function, is directly related to the absorption energy. We calculate the rms radii by approximating $|s\rangle$ by the singly occupied s-type ROHF orbital localized within the vacancy region (see, e.g., fig. 3.5 (a)). The ROHF defect orbitals are well converged for the $\text{Li}_{38}\text{F}_{18}$ cluster and the cc-pVTZ basis set used for this calculation. The continuous stretching of the LiF crystal leads to a continuous, or, to be more precise, an almost perfectly linear growth of the rms-radius of the F-center with increasing anion-cation distance (fig. 4.6 (a)).

The evaluation of the rms radii comprises integration over all directions in space which obscures the dependence of the defect’s extent on the crystallographic directions. To resolve this dependence we investigate the first radial nodes of the defect s-type wave function $r_0^{[100]}$, $r_0^{[110]}$, and $r_0^{[111]}$ along the [100], [110], and [111] crystal directions, respectively. Starting from the vacancy site they correspond to the directions towards the nearest neighbor cation [100], the second-nearest neighbor anion [110], and the third-nearest neighbor cation [111]. Similar to the rms radius

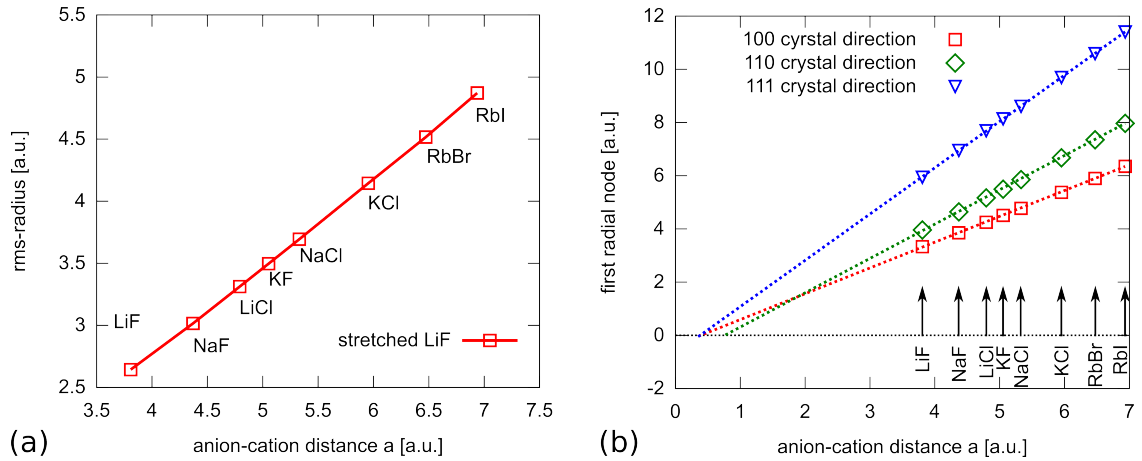


Figure 4.6.: (a) Root-mean square radii of scaled LiF and (b) positions of the first radial nodes of the s-type F-center defect wave function in scaled LiF along the [100] (red squares), [110] (green diamonds), and [111] (blue triangles) crystal directions. Dotted lines are linear fits $\alpha(a - d_0)$ (see table 4.1) with slopes close to 1, $\sqrt{2}$, and $\sqrt{3}$, respectively. The d_0 values, the position where the fits cross the $y = 0$ axis, are measures for the effective size of Li⁺ ([100] and [111] direction) and F⁻ ions ([110] direction).

they show, independent of the crystal direction, an almost perfectly linear increase with a (fig. 4.6 (b)). Linear fits of the form $r_0 = \alpha(a - d_0)$ (table 4.1) yield slopes close to 1 ([100]), $\sqrt{2}$ ([110]), and $\sqrt{3}$ ([111]), respectively, which can be understood in terms of the particle in the box model. Consider a hard-walled cube with the vacancy in its center and a side length of $2a$. The effective distance between the vacancy and the cube walls along the [100], [110], and [111] directions scales then like the side length ($1 \cdot a$), the face diagonal ($\sqrt{2} \cdot a$), and the space diagonal ($\sqrt{3} \cdot a$), respectively. The largest deviation from this simple picture is found for $\alpha^{[110]}$, the slope of $r_0^{[110]}$. It is a little lower than $\sqrt{2}$ due to the fact that the effective size of the F⁻ ion is smaller in the LiF crystal [107] than for an isolated F⁻. When stretching the scaled LiF the effective size of F⁻ grows leading to a reduced increase of the defect orbital along the [110] direction $r_0^{[110]}$. The influence of ion sizes also becomes manifest in the displacement of the intercept with the x-axis d_0 , which correspond to an effective range of the exchange potential. For the [100] and [111] directions, pointing towards an Li⁺ ion, we find $d_0^{[100]} = d_0^{[111]} = 0.38$ a.u. while $d_0^{[110]} = 0.76$ a.u. reflecting the larger size of the F⁻ ion.

direction	[100]	[110]	[111]
α :	0.97	1.29	1.74
d_0 :	0.38	0.76	0.38

Table 4.1.: Fit parameters α and d_0 for the position of the radial nodes $r_0 = \alpha(a - d_0)$ of the ground state defect wave function along different crystallographic directions in scaled LiF. The r_0 values scale approximately like a , $\sqrt{2}a$, and $\sqrt{3}a$ just like the side length, the face diagonal, and the space diagonal of a cube with side length a . The d_0 values, the position where the fits cross the $y = 0$ axis in fig. 4.6, are measures for the effective size of Li^+ ([100] and [111] direction) and F^- ions ([110] direction).

4.3.3. Scaled LiF and the Vinti sum rule

The Vinti sum rule (eq. 4.6) establishes a direct connection between the root-mean square radius of the ground-state defect wave function $\langle s|r^2|s\rangle^{1/2}$ and the F-center absorption energy. In this section we conduct an ab-initio test of the Vinti-sum rule in scaled LiF. We compare in fig. 4.7 the ROHF absorption energies with energies derived via the Vinti sum rule (in atomic units)

$$E_{\text{abs}} = \frac{3}{2} \frac{1}{\langle s|r^2|s\rangle}, \quad (4.7)$$

where $|s\rangle$ is the ROHF ground state defect orbital. For anion-cation distances a beyond the one of NaF we find perfect agreement between the Vinti sum rule and the ab-initio ROHF absorption energies. For small a , however, there is some discrepancy which calls for further explanation.

Use of the Vinti-sum rule in the form of eq. 4.6 implies three major approximations. First, for the mass of the defect electron the mass of the free electron is used, second, only a single absorption peak, the F-band, is taken into account, and third, the system is considered a single-electron system. The free electron mass seems to be a reasonable choice since the defect electron is strongly bound and very localized. Excitations of the F-center to higher excited states, the K- and L bands, have been shown experimentally to be negligible [12, 106]. We also test this approximation by evaluation of the oscillator strength for the $s \rightarrow p$ transition of the F-center which yields a value close to one in scaled LiF as well as in the real materials. The third approximation concerns the single-particle nature of the F-center. In principle, the HF approximation is a single-particle approach. However, it does not agree with the Vinti-sum rule for small a since we determine the ROHF absorption energy in a Δ SCF approach: E_{abs} is the total energy difference between two independent ROHF calculations for the ground and excited state. In a single-electron problem, the potential the electron is bound to, is independent of the electronic state. Due

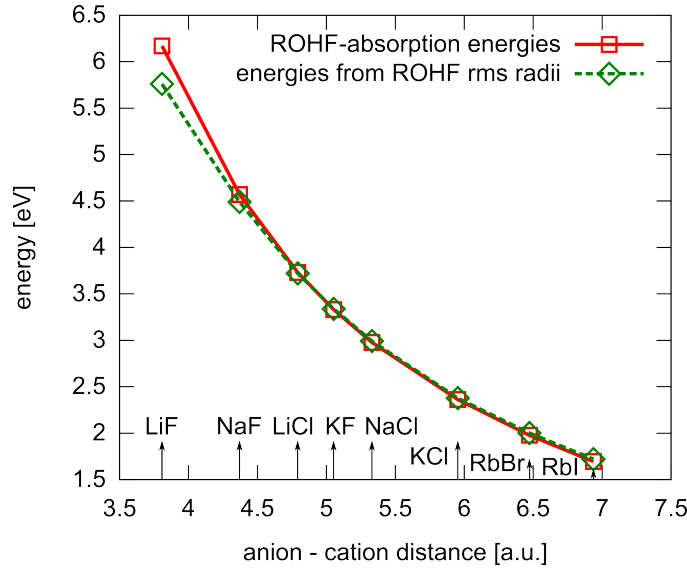


Figure 4.7.: ROHF F-center absorption energies in scaled LiF obtained from ab-initio Δ SCF calculations (squares and solid red line) and from the Vinti sum rule (diamonds and dashed green line), eq. 4.7, using the ROHF-rms radii of the ground state defect wave function (fig. 4.6 (a)).

to the Δ SCF approach, however, the effective F-center potentials of the ground and excited state differ which explains the discrepancy. For small anion-cation distances, for which the defect is most compressed and has the largest overlap with the host-crystal electrons, the discrepancy is largest. For larger a the overlap diminishes leading to a decreasing difference between ground and excited state F-center potentials and, therefore, good agreement between the Vinti-sum rule and the ROHF absorption energies in scaled LiF.

4.4. Ion-size effects on F centers in real materials

In the previous sections the model system of a scaled alkali halide yielded an F-center absorption energy obeying $E_{\text{abs}} \propto 1/a^2$. In this section we study the influence of ion-size effects on the spatial extent of the defect wave function and on the F-center absorption energies in real alkali-halide crystals. In general we find reduced growth of the extent of $|s\rangle$ with increasing anion-cation distance compared to a scaled alkali halide since, in real materials, with a also the size of the anions and cations grow. This reduced growth translates, via the Vinti sum rule, to a Mollwo-Ivey relation with an exponent below 2 in real alkali-halide crystals.

Before we turn to real alkali-halide crystals we introduce another ab-initio model system that helps to establish a qualitative but very intuitive picture of element-

specific ion-size effects on the defect state. Consider an alkali-halide crystal with *fixed* anion-cation distance $a = a_{\text{KCl}} = 5.95$ Bohr while varying the ionic species. We study the density variation within the vacancy region under the exchange of ionic species. In the following $M \in \{\text{Li}, \text{Na}, \text{K}\}$ denotes the alkali metal, $X \in \{\text{F}, \text{Cl}\}$ the halide, and ρ_{MX} denotes the F-center electron density in the crystal MX. Exchange of the metal, $\rho_{\text{NaF}} - \rho_{\text{LiF}}$, (fig. 4.8 (a)) and exchange of the halide, $\rho_{\text{LiCl}} - \rho_{\text{LiF}}$ (fig. 4.8 (b)), both lead to an accumulation (or compression) of defect electron density in the central vacancy region within the nearest-neighbor ions and displays a strong directionality. Replacing the Li cation by an Na cation strongly compresses the defect electron along the [100] and the [010] crystal direction. When the F anion is replaced by a Cl anion the defect electron is compressed along the [110] and [1-10] crystal axis, the two diagonals in fig. 4.8 (b), and the compression is weaker than for the exchange of cations. These findings are in contradiction to the results of Smith and Inokuti [98] who concluded that the rms of the F-center wave function increases with the ionic size of the cation. For this model alkali-halide system we find a decrease of the rms value from 4.14 to 4.04 Bohr when replacing LiF by NaF and from 4.18 to 4.04 Bohr when replacing LiCl by NaCl. We note that the rms radii are almost independent of the anionic constituent.

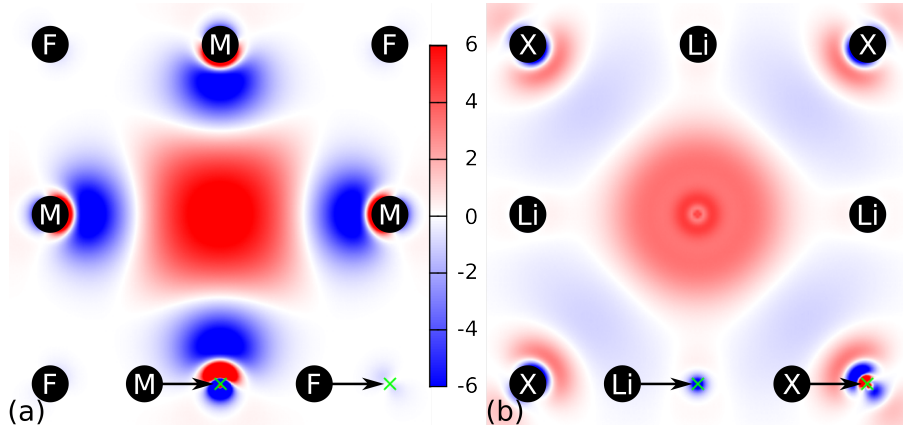


Figure 4.8.: Defect-electron density differences in $10^{-4}/\text{Bohr}^3$ for the F center in (a) NaF and LiF ($\rho_{\text{NaF}} - \rho_{\text{LiF}}$) and (b) in LiCl and LiF ($\rho_{\text{LiCl}} - \rho_{\text{LiF}}$) for a constant anion-cation distance of 5.95 a.u. Replacing Li and F ions with the larger Na and Cl ions, respectively, compresses the defect-electron density in the anion vacancy.

Apart from the accumulation of defect-electron density at the vacancy site we also observe an increase of density at the ionic neighbor to be exchanged. The ROHF Fermi contact term at the corresponding metal or halide site increases by a factor ~ 3 upon replacing Li^+ by Na^+ or F^- by Cl^- . This increase of density is due to the increasingly stringent orthogonality requirement on the defect wave function

imposed by larger ionic cores. Thus, the density increases both at the vacancy site and at the neighboring ionic site. While the former is the consequence of the compression of the defect wave function, the latter is a subtle local effect on the tails of the wave function due to orthogonalization and should not be taken as a measure for the effective size of the confining “box” potential.

4.4.1. Spatial extent of the F center in real alkali-halide crystals

A quantitative analysis of the extent of the defect wave function in real materials is performed via the root-mean square radius of $|s\rangle$ and its first radial nodes along different crystallographic directions. Instead of a continuous linear increase with a , like in the scaled alkali halides, we find a highly non-linear dependence of the rms-radii of LiF, NaF, KF, LiCl, NaCl, and KCl on their actual anion-cation distance (fig. 4.9). For a given anion X the rms radius does increase with a , however, slower than the one in, e.g., scaled LiF. Further, there is a pronounced offset between the rms radii of fluorides and chlorides.

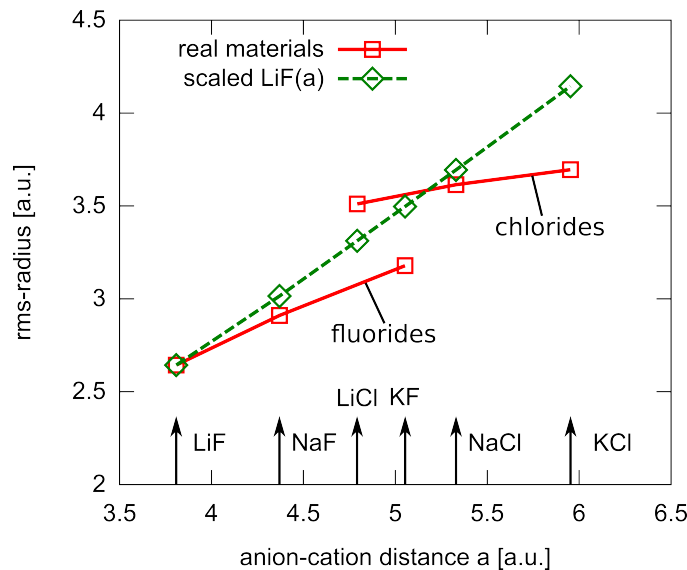


Figure 4.9.: Root-mean square radii of the ground state F -center electron wave function in real alkali-halide crystals (red squares and solid lines) and in scaled LiF (green diamonds and dashed line).

The reduced growth with a for each anion species can be understood qualitatively by the cation size, increasing with a , and the resulting compression of the F -center electron. The offset between fluorides and chlorides can be understood in terms of the positions of the first radial nodes (fig. 4.10) of the defect ground state wave

function. Let us first focus on the [100] direction. As shown above, the scaled alkali halide shows almost perfect linear growth of $r_0^{[100]}(a)$ with slope ~ 1 . In the real materials, however, we find effectively a -independent $r_0^{[100]}$ values (fig. 4.10 (a)) of 3.4 a.u. and 4.3 a.u. for fluorides and chlorides, respectively. The difference of 0.9 a.u. can be interpreted as the difference in radius between a Cl^- and an F^- ion. This value indeed matches the prediction by the effective-ion-radii-in-pristine-crystals model [108]. The model assumes crystal-independent effective radii r_M and r_X for cations M and anions X , respectively, which are extracted from measurements of the lattice constants in different alkali-halide crystals. Adding up the radii r_M and r_X yields, to a good degree of approximation, the anion-cation distance a_{MX} of the crystal MX . Within this model the $r_0^{[100]}$ offset between chlorides and fluorides comes about as follows. When going from, e.g., LiF to LiCl the effective size of the vacancy in the [100] direction grows by $r_{\text{Cl}^-} - r_{\text{F}^-} = 0.9$ a.u. The constant $r_0^{[100]}$ values for fluorides and chlorides are due to the increasing size of the nearest neighboring cations surrounding the vacancy. When going from, e.g., LiF to NaF the gain in vacancy space along the [100] direction $a_{\text{NaF}} - a_{\text{LiF}}$ is completely compensated for by the increasing cation size $r_{\text{Na}^+} - r_{\text{Li}^+}$. As a consequence the nearest constriction of the defect potential, formed by the nearest neighbor cations, is constant for fluorides and chlorides, respectively.

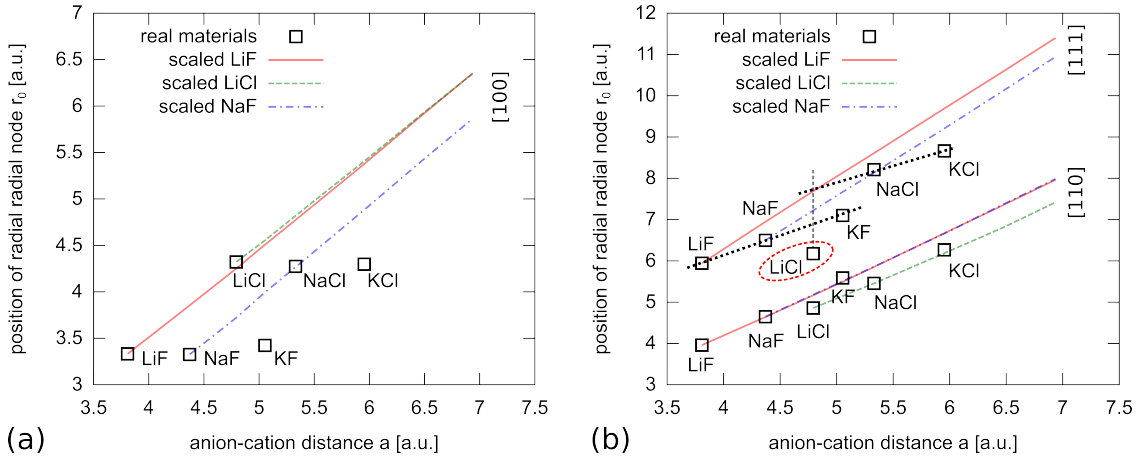


Figure 4.10.: Positions of the first radial node r_0 along the (a) [100] direction and (b) the [110] and [111] direction of the ground state F-center wave function in real alkali-halide crystals (black squares), scaled LiF (solid red line), scaled LiCl (dashed green line), and scaled NaF (dash-dotted blue line).

Such a complete compensation of vacancy volume by increasing ion sizes is not possible along the [110] and [111] directions because the distance from the origin, the center of the vacancy, to the second- and third-nearest neighbors scales with $\sqrt{2}a$ and $\sqrt{3}a$, respectively. Therefore, the radial nodes $r_0^{[110]}(a)$ and $r_0^{[111]}(a)$ in

real materials (fig. 4.10 (b)) increase with a . Along the [110] direction towards the second-nearest neighbor anion, the radial nodes behave as expected. $r_0^{[110]}(a)$ of real fluorides lies on a straight line which coincides with $r_0^{[110]}(a)$ of scaled LiF and scaled NaF. $r_0^{[110]}(a)$ of real chlorides forms a straight line, too, which coincides with the one of scaled LiCl. The chloride line, however, is located a little below the fluoride line due to the larger size of the chloride ion.

The $r_0^{[111]}$ data seem to be more complicated but the scaled materials help to interpret them. Let us first focus on the fluorides. $r_0^{[111]}$ of real LiF, NaF and KF lie again on a straight line which has a smaller slope than the one of scaled LiF and scaled NaF. The difference of 0.44 a.u. between $r_0^{[111]}$ of real NaF and scaled LiF(a_{NaF}) at the NaF lattice constant as well as the difference 1.03 a.u. between real KF and LiF(a_{KF}) are also in reasonable agreement with the effective-radii-in-crystals model predicting 0.49 a.u. and 1.17 a.u. Clearly, the downward shift of $r_0^{[111]}$ in real NaF and KF with respect to scaled LiF is induced by the larger third-nearest neighbor anions Na^+ and K^+ . The same argument holds for $r_0^{[111]}$ in real NaCl and KCl. $r_0^{[111]}$ of real NaCl lies on the $r_0^{[111]}(a)$ line of scaled NaF again 0.44 a.u. below the scaled LiF and $r_0^{[111]}$ of KCl lies 1.04 a.u. below scaled LiF. Therefore, also for these two chlorides the size of the third-nearest neighbor anion determines $r_0^{[111]}$.

LiCl is the exception. A line through the points for real NaCl and KCl intersects the $r_0^{[111]}(a)$ line of scaled LiF essentially at an anion-cation distance of LiCl, i.e., exactly where one would expect $r_0^{[111]}(a)$ of real LiCl. However, the $r_0^{[111]}(a)$ of real LiCl lies clearly below this point due to “blocking” of the [111] direction by the large second-nearest neighbor Cl^- ions. This means, instead of being determined by the third-nearest neighbor Li^+ cation the [111] direction is pointing towards, $r_0^{[111]}$ in real LiCl is governed by the orthogonalization requirement of the F-center wave function to the second-nearest neighbor Cl^- ion core states. We investigate this “blocking” in more detail in appendix A.1 where we discuss the properties of scaled NaF and LiCl. In appendix A.2 we use the r_0 parameters (fig. 4.10) to incorporate ion-size effects into a new, refined qualitative particle in the box model. The exceptional behavior of LiCl suggests a dependence of the physics of the F center on the ratio of anion to cation radii. Such a strategy was followed by Buchenauer and Fitchen [99] as well as Bartram and co-workers [57] investigating the deviations from the Mollwo–Ivey relation due to ion-size effects as a function of r_X/r_M . Unfortunately, their results are not comparable to ours because they found the largest deviations from the Mollwo–Ivey relation for small r_X/r_M , alkali-halides with large cations and small anions in disagreement with what our results of LiCl would suggest. The largest deviations were observed for the extreme cases of RbF and CsF, materials we cannot treat on the same level of theory as the ones presented in this work.

4.5. F-center absorption energies and the Mollwo–Ivey relation in real alkali-halide crystals

Compared to the F center in scaled alkali-halide crystals, root-mean square radii and the radial nodes of the F center in real alkali-halide crystals indicate a reduced growth of the spatial extent of the defect wave function with anion-cation distance. The reduced growth is due to ion-size effects and translates, via the Vinti-sum rule (eq. 4.6), into a weaker decay of the absorption energies, E_{abs} , with a , i.e., a reduced Mollwo–Ivey exponent. This is exactly what we find in ROHF (fig. 4.11 (a)) as well as CASPT2(ROHF) and TB-mBJ+BSE absorption energies in real alkali-halide crystals (fig. 4.11 (b)). CASPT2(ROHF) and TB-mBJ+BSE yield MI exponents of $n_{\text{CASPT2}} = 1.63$ and $n_{\text{TB-mBJ+BSE}} = 1.83$, respectively, both clearly below $n = 2$ as found in the scaled alkali halides. We conclude that in experiment ion-size effects are responsible for the reduction from $n = 2$ to $n = 1.81$ and not only for subtle deviations from this exponent as previously thought. Further, the Madelung potential, in previous works involved in the explanation of the deviation of the exponent from 2, is only of minor relevance in the present context.

The TB-mBJ data are in excellent agreement with experiment and seem to be more accurate than the CASPT2(ROHF) data. This agreement, however, needs to be taken with caution since the error bar in DFT calculations due to the choice of the exchange correlation potential can be substantial. The F-center absorption energy in LiF calculated with the Perdew–Burk–Ernzerhof (PBE) exchange-correlation potential followed by perturbation theory (GW_0) and the solution of the BSE (fig. 3.19) is ~ 0.5 eV larger than the TB-mBJ+BSE solution.

Not only the reduced growth of the rms radii and the position of the radial nodes translate to the F-center absorption energies but also their ion-specific offsets and slopes. They are, however, more pronounced in the simulations than in experiment. We highlight these effects in fig. 4.12, where we present the same CASPT2 (ROHF) data as in fig. 4.11 (b), however, now with lines connecting data points corresponding to crystals with the same anionic (fig. 4.12 (a)) and cationic (fig. 4.12 (b)) constituent. Fitting the data separately for every anion with a Mollwo–Ivey type relation leads to exponents smaller than the one obtained by a fit of all absorption energies. When the cation species is kept constant a steeper decrease is found because the size of the narrowest constriction formed by the nearest-neighbor cations continuously increases. This analysis shows that the effective Mollwo–Ivey line is a “smoothed” average over discrete ion-size effects. In an earlier work by Smakula [11, 109] cation specific Mollwo–Ivey fits were presented. However, because of the weak dependence of the experimental data final conclusions were difficult to draw.

In the ab-initio calculations we find an anion-specific relaxation of the nearest-

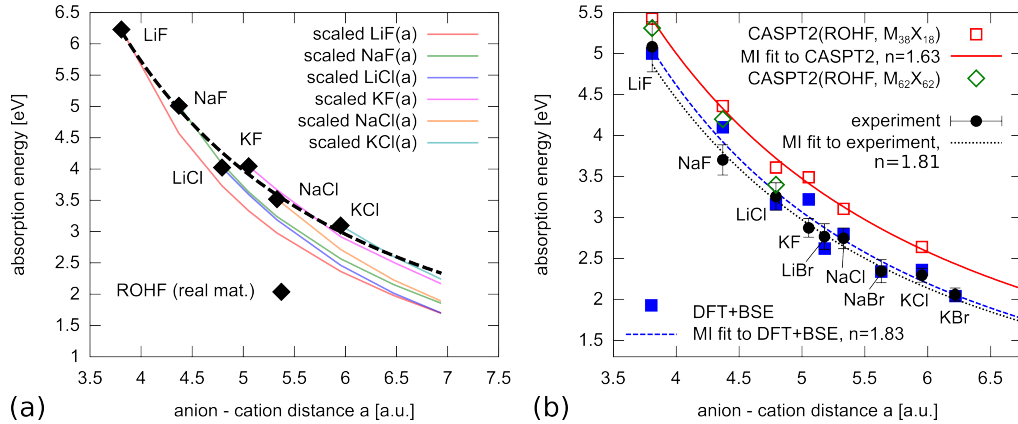


Figure 4.11.: (a) ROHF F-center absorption energies in various real alkali-halide crystals (black solid diamonds). Dashed black line is a Mollwo–Ivey fit through these points which decreases weaker with a than the absorption energies of the scaled materials (solid lines) due to ion-size effects. (b) CASPT2(ROHF) (red empty squares and green diamonds), TB-mBJ+BSE (blue full squares), and experimental [71] (black dots) F-center absorption energies in various alkali-halide crystals. Lines through the data points are Mollwo–Ivey type fits with exponents $n_{\text{CASPT2}} = 1.63$, $n_{\text{TB-mBJ+BSE}} = 1.83$, and $n_{\text{exp}} = 1.81$. Error bars of the experimental data indicate the full width at half maximum of the F-center absorption peak. CASPT2(ROHF) absorption energies (red squares) are converged basis set limit values within embedded $M_{38}X_{18}$ clusters. Use of larger $M_{62}X_{62}$ embedded clusters, computationally feasible only for LiF, NaF, and LiCl, leads to a reduction of the absorption energy between 0.12 eV (LiF) and 0.21 eV (LiCl). In all calculations we use the experimental lattice constant with relaxed geometries from periodic boundary DFT(PBE) calculations.

neighbor cations: in fluorides the cations move away from the vacancy while in chlorides they move towards the vacancy site. This effect counteracts the ion size specific offsets in the rms radii since it leads to a weaker/stronger compression of the defect wave function in fluorides/chlorides. Via the Vinti sum rule this translates into a downward/upward shift of the F-center absorption energy for fluorides/chlorides (fig. 4.13 (a)) with respect to an unrelaxed geometry around the defect. The variation of the absorption energies due to relaxation lies between -0.2 eV (LiF) and $+0.1$ eV (LiCl) and its absolute magnitude, in general, diminishes with increasing lattice constants. These variations are too weak to significantly change the Mollwo–Ivey exponent but large enough to weaken ion-size specific offsets.

Despite this anion-specific relaxation, ion-size specific offsets in theory are more

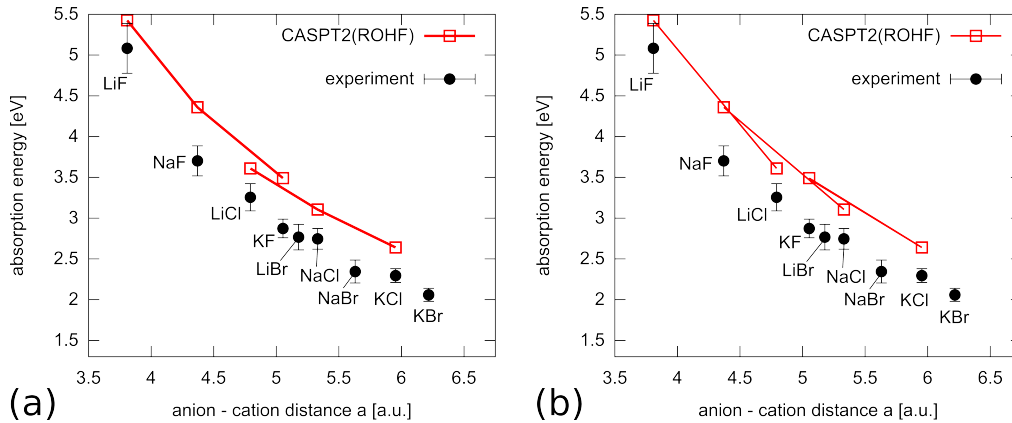


Figure 4.12.: Same as fig. 4.11 (b). CASPT2(ROHF) absorption energies of crystals with the same anion species (a) and the same cation species (b), respectively, are connected.

pronounced than in experiment. A possible explanation could be the yet not completely reliable description of the lattice relaxation around the defect due to the discrepancy between theoretical and experimental lattice constants. In the calculations of the F-center absorption energies (fig. 4.11) we use the experimental lattice constants while employing the PBE exchange-correlation potential for the geometry relaxation. PBE is used since TB-mBJ does not provide total energies [91] and, thus, forces on the ionic cores are not available. PBE, however, is known to overestimate the lattice constants of alkali halides by up to $\sim 2\%$ [110]. Also Hartree-Fock [111] tends to overestimate the lattice constants of these materials by a similar amount which is in the range of the nearest-neighbor ion displacements. Therefore, final conclusions about the influence of lattice relaxation on the ion-size specific offsets are difficult to draw.

In experiment, a clearer signature of ion-size effects is visible in the widths of the F-center absorption lines (fig. 4.13 (b)) corresponding to the error bars in fig. 4.11 (b). We estimate the line widths via the symmetric breathing vibration of the nearest-neighbor cations around the defect (sec. 3.5.3). This single mode approximation underestimates the line widths but it yields qualitative agreement with the experimental anion-specific offset.

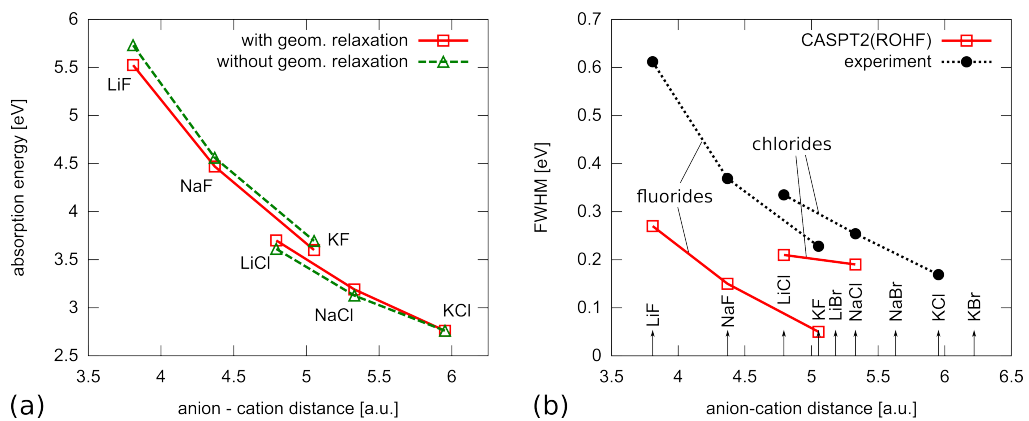


Figure 4.13.: (a) Effect of lattice relaxation around the defect on the absorption energy. Data shown are CASPT2(ROHF) absorption energies (basis set: cc-pvtz) within embedded $M_{38}X_{18}$ clusters. (b) Full width at half maximum (FWHM) of the F-center absorption line in various alkali-halide crystals. Black dots are experimental data [71] and red-empty squares are results from CASPT2(ROHF) calculations. The theoretical line width is estimated via a single mode approximation describing the symmetric breathing mode of the nearest-neighbor cations (sec. 3.5.3).

5. Non-adiabatic molecular dynamics in a nutshell

The term non-adiabatic dynamics refers to the coupled motion of nuclei and electrons in, e.g., ion-atom collisions. It is determined by the molecular Hamiltonian (eq. 2.1) and in this chapter we introduce the necessary tools to solve the time-dependent Schrödinger equation: first, we introduce the concept of the Born–Oppenheimer adiabatic approximation (sec. 5.1) as well as its break-down in the context of non-adiabatic dynamics (sec. 5.2). Further, we briefly discuss the concept of diabatic states (sec. 5.3) and the methods used to (approximately) solve the time-dependent Schrödinger equation of the combined nuclear and electronic motion (sec. 5.4). Throughout this chapter the charge exchange in the scattering of an Si^{3+} ion off a helium atom ($\text{Si}^{3+} + \text{He} \rightarrow \text{Si}^{2+} + \text{He}^+$) serves as a test case since charge transfer is the prototypical example for a non-adiabatic process. In the final section (sec. 5.5) we calculate the charge-transfer cross section of this reaction and compare it to experiment. This chapter is again only a brief and incomplete introduction into the topic of non-adiabatic molecular dynamics. Interested readers are referred to the literature along which this chapter is created [112–114].

5.1. The Born–Oppenheimer adiabatic approximation

In chapter 2 we discussed methods to solve the electronic Hamilton operator \hat{H}_e (see eq. 2.6) neglecting the motion of the nuclei. They are fixed at a given position \vec{R} which is the only parameter entering \hat{H}_e . This approximation was first formulated in the PhD thesis of Wolfgang Pauli [115] and was later called the Born–Oppenheimer or adiabatic approximation. It is based on the notion that in, e.g., atoms, molecules, or solids the characteristic velocity of electrons is much larger than the one of the nuclei $v_e \gg v_n$ due to the large difference in mass $M_n \gg m_e$. This approximation implies that, at any instance in time, the electrons can instantaneously adapt to the positions of the nuclei and that the motion of these two entities is decoupled. From the view of the electrons the nuclei move infinitely slow, or, adiabatically slow, a term borrowed from statistical physics. As a consequence, a system in, e.g., its electronic ground state will always remain in the ground state irrespective of

the position and the motion of the nuclei as long as $v_e \gg v_n$ holds.

Mathematically, the decoupled motion is expressed in a product ansatz for the total wave function of the combined system

$$\Phi_{\text{total}}(\vec{r}, \vec{R}) = \Psi_{\text{electron}}(\vec{r}; \vec{R}) \times \chi_{\text{nuclear}}(\vec{R}). \quad (5.1)$$

\vec{R} and \vec{r} comprise all the nuclear and electronic degrees of freedom, respectively. The nuclear wave function χ_{nuclear} depends solely on \vec{R} . The electronic wave function Ψ_{electron} is a solution of the electronic Hamiltonian \hat{H}_e (eq. 2.3) and, therefore, depends *parametrically* on the position of the nuclei, \vec{R} , via \hat{V}_{ne} and \hat{V}_{nn} . This parametric dependence is denoted by the semicolon between the \vec{r} and \vec{R} . Plugging this ansatz into the Schrödinger equation for the combined system, $\hat{H}_{\text{tot}} \Phi_{\text{tot}} = (T_n + \hat{H}_e) \Phi_{\text{tot}} = E_{\text{tot}} \Phi_{\text{tot}}$ (eqs. 2.2 and 2.3), multiplication from the left with Ψ_{electron}^* and integration over the electronic degrees of freedom leads to

$$\left(\hat{T}_n + E(\vec{R}) \right) \chi_n(\vec{R}) = E_{\text{tot}} \chi_n(\vec{R}), \quad (5.2)$$

with $E(\vec{R})$ being the \vec{R} -dependent solution of $\hat{H}_e \Psi_{\text{electron}} = E(\vec{R}) \Psi_{\text{electron}}$. This nuclear Schrödinger equation shows that the motion of the nuclei is governed by the effective potential $E(\vec{R})$ generated by the nuclear Coulomb repulsion and the (instantaneous) interaction between electrons and nuclei. Therefore, the function $E(\vec{R})$ is called a potential energy surface (PES).

From the PES of the electronic ground state of the, e.g., diatomic H_2 molecule (fig. 5.1) one can derive the quantized energy levels of the vibration of the molecule by solving the Schrödinger equation 5.2. One can also derive the bonding distance, the dissociation energy, and the force acting on the nuclei, $\vec{F} = -\nabla_R E(\vec{R})$.

The Born–Oppenheimer approximation is also applied in much more complex situations such as the scattering of slow ($v_n \ll v_e$) projectiles off metallic and insulating crystal surfaces [116, 117].

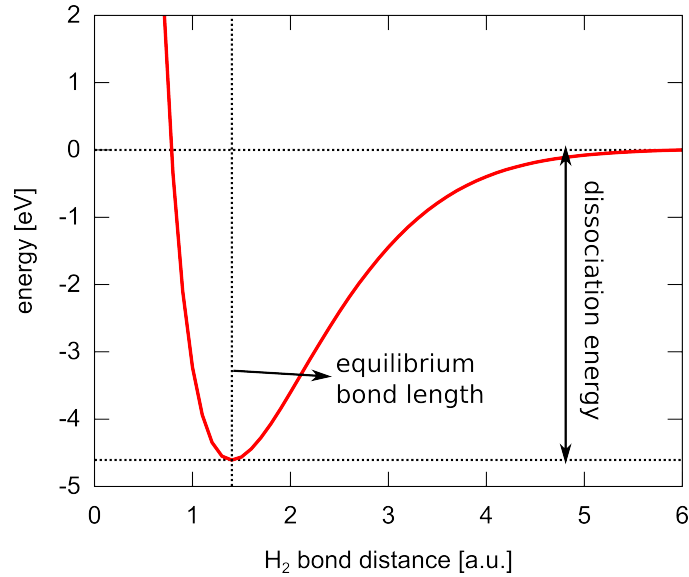


Figure 5.1.: CASPT2 electronic ground state energy of the H_2 molecule as a function of nuclear distance. Basis set used: cc-pvtz.

5.2. Beyond the Born–Oppenheimer adiabatic approximation: the non-adiabatic couplings

When v_n becomes large enough such that the electrons can not instantaneously follow the nuclear motion anymore (breakdown of adiabaticity) the electronic system will be excited and the motion of nuclei and electrons is no longer decoupled. A quantitative measure for the strength of this coupling is the so-called non-adiabatic coupling vector which we derive in the following. Due to the excitation of the electronic system we need to include more than one electronic state in the description of Φ_{total} . The total wave function is expanded in terms of the adiabatic electronic wave functions $\Psi_i(\vec{r}; \vec{R})$, eigenfunctions to the electronic Hamiltonian \hat{H}_e (see eq. 2.6)

$$\Phi_{\text{total}}(\vec{r}, \vec{R}) = \sum_i^{\infty} \chi_i(\vec{R}) \cdot \Psi_i(\vec{r}; \vec{R}), \quad (5.3)$$

with expansion coefficients $\chi_i(\vec{R})$ being functions of the nuclear coordinates. This so-called Born–Oppenheimer expansion is exact if the set Ψ_i is complete. Errors are, however, introduced by truncation which is necessary in practice. Inserting the Born–Oppenheimer expansion into the Schrödinger equation $\hat{H}_{\text{tot}} \cdot \Phi_{\text{total}} = E_{\text{tot}} \cdot \Phi_{\text{total}}$ multiplication from the left with Ψ_j^* , and integration over the electronic

degrees of freedom leads to the nuclear equations of motions

$$\left(-\frac{1}{2M}\vec{\nabla}^2 + E_j(\vec{R})\right) \chi_j(\vec{R}) - \sum_i \gamma_{ji}(\vec{R}) \chi_i(\vec{R}) = E_{\text{tot}} \chi_j(\vec{R}), \quad (5.4)$$

where we used the kinetic operator

$$\hat{T}_n = -\frac{1}{2M}\vec{\nabla} \cdot \vec{\nabla} = -\frac{1}{2M}\vec{\nabla}^2, \quad (5.5)$$

and $\vec{\nabla}$ is the gradient vector in the nuclear space.

$$\gamma_{ji} = \frac{1}{2M} \left(2\vec{F}_{ji} \cdot \vec{\nabla} + G_{ji} \right) \quad (5.6)$$

are the non-adiabatic couplings describing the dynamical interaction between the motion of nuclei and electrons. They split in two contributions: the so-called *non-adiabatic derivative coupling* or the *non-adiabatic vector coupling*

$$\vec{F}_{ji}(\vec{R}) = \langle \Psi_j(\vec{r}; \vec{R}) | \vec{\nabla} \Psi_i(\vec{r}; \vec{R}) \rangle \quad (5.7)$$

and the *non-adiabatic scalar coupling*

$$G_{ji} = \langle \Psi_j(\vec{r}; \vec{R}) | \vec{\nabla}^2 \Psi_i(\vec{r}; \vec{R}) \rangle. \quad (5.8)$$

Both quantities are connected to each other (see appendix A.3) by,

$$G_{ji} = \left(\vec{\nabla} \cdot \vec{F}_{ji} \right) + \sum_k \vec{F}_{jk} \cdot \vec{F}_{ki}, \quad (5.9)$$

where the brackets in the first term indicate that the $\vec{\nabla}$ operator acts only on \vec{F}_{ji} . With this relation and by dropping the indices (vectors and matrices in the “state space” are bold) we can rewrite the coupled Schrödinger equation for the nuclear wave functions 5.4 in the more compact form

$$\left(-\frac{1}{2M} \left(\vec{\nabla} + \vec{\mathbf{F}} \right)^2 + \mathbf{E} \right) \boldsymbol{\chi} = E_{\text{tot}} \boldsymbol{\chi}, \quad (5.10)$$

with

$$\left(\vec{\nabla} + \vec{\mathbf{F}} \right)^2 = \left(\vec{\nabla}^2 + 2\vec{\mathbf{F}}\vec{\nabla} + \mathbf{G} \right). \quad (5.11)$$

For real electronic wave functions $\Psi_i(\vec{r}; \vec{R})$ the vector matrix \vec{F}_{ji} vanishes on the diagonal and is anti-Hermitian. The scalar coupling matrix G_{ji} , however, has both

non-vanishing diagonal and off-diagonal entries which are usually termed the diagonal correction and the second-order non-adiabatic coupling elements, respectively. The coupling elements γ_{ji} in eq. 5.6 scale with $1/M$ and are, therefore, smaller than the PESs, E_j , by a factor equal to the ratio of electronic and nuclear masses. In the Born–Oppenheimer approximation they are neglected completely. The BO approximation fails for increasing nuclear velocity which is reflected in the first term of γ_{ji} in eq. 5.6 reading $\vec{F}_{ji} \cdot \frac{\vec{v}}{M}$. Since \vec{v}/M is proportional to the nuclear velocity the efficiency of the coupling increases for larger nuclear velocities. A measure for the efficiency is the so-called Massey parameter. In the following we study the PES, non-adiabatic coupling and the Massey parameter for the electron transfer in the scattering of Si^{3+} from a helium atom.

The charge transfer reaction $\text{Si}^{3+} + \text{He} \rightarrow \text{Si}^{2+} + \text{He}^+$ is an important recombination process, i.e., loss mechanism of Si^{3+} in gaseous nebulae in outer space [118, 119] (see also references in [120]). It has been investigated extensively in theory [121–124] while experimental data on the low energy charge transfer are scarce [120, 125]. Consider a head-on collision between Si^{3+} and He with a single nuclear degree of freedom: the inter-nuclear distance R (inset in fig. 5.2 (a)). At large R the two energetically lowest potential energy surfaces Σ_1 and Σ_2 of the combined system (fig. 5.2 (a)) are energetically well separated and correspond to the configurations

$$\begin{aligned}\Sigma_1 &: \text{Si}^{2+}(3s^2) + \text{He}^+(1s) \\ \Sigma_2 &: \text{Si}^{3+}(3s) + \text{He}(1s^2).\end{aligned}$$

At $R \approx 6.5$ the two PES approach each other and form a so-called avoided crossing which comes about as follows (for a review see [126]). When calculating PESs of ground and excited states of a system they can, in principle, touch each other, i.e., $E_i = E_j$. This touching is called a conical intersection and gives rise to many interesting effects well studied in the literature [112]. Conical intersections, however, appear only when the potential energy surfaces depend at least on two independent parameters. In diatomic molecules with a single-internal nuclear degree of freedom (the inter-nuclear distance R), the Wigner–von Neumann non-crossing rule holds. It states: potential energy curves corresponding to electronic states of the same symmetry cannot cross.

To understand the non-crossing rule we perform a qualitative derivation. Consider we want to determine the ground and the first excited charge-transfer electronic wave function of the $\text{Si}^{3+} + \text{He}$ system by using the variational principle. The test wave function

$$\Psi_{\text{test}}(\vec{r}; R) = c_1 \psi_1(\vec{r}; R) + c_2 \psi_2(\vec{r}; R), \quad (5.12)$$

is expanded into the basis ψ_1 and ψ_2 which are not eigenfunctions of the electronic Hamiltonian H_e . In the basis of ψ_1 and ψ_2 , H_e reads

$$\begin{pmatrix} H_{11}(R) & H_{12}(R) \\ H_{21}(R) & H_{22}(R) \end{pmatrix}, \quad (5.13)$$

where all matrix elements are functions of the parameter R . In order to find a conical intersection, i.e., a degenerate solution, it is necessary that

$$H_{11} - H_{22} = F_1(R) = 0 \text{ and } H_{12} = H_{21} = F_2(R) = 0. \quad (5.14)$$

In general it is not possible to find one value of the parameter R to satisfy both conditions simultaneously leading to the avoided crossing [126]. Another formulation says that the interaction, the off-diagonal terms, between ψ_1 and ψ_2 induces the avoided crossing by lifting the degeneracy at the point where the $H_{11}(R)$ and $H_{22}(R)$ intersect. In an N -atomic molecule, however, the number of independent inter-atomic distances is $S = 3N - 6$ for $N > 2$. For a three-atomic molecule there are three parameters available to simultaneously fulfill conditions 5.14. Therefore, conical intersections can be found in such molecules.

Let us return now to the PES Σ_1 and Σ_2 in fig. 5.2. The charge state of the He atom/ion in Σ_1 and Σ_2 (fig. 5.2 (b)) is determined by the Mulliken population analysis. For $R \lesssim 3$ a.u. charge states need to be taken with a grain of salt since a clear separation between Si and He is not possible. At the avoided crossing, the He-charge state almost perfectly switches from 1 to 0 (0 to 1) for Σ_1 (Σ_2). In other words, if we follow the adiabatic PES of Σ_1 from $R \approx 8$ to $R \approx 6$ the system changes its configuration and an electron is transferred from Si to He (and vice versa for Σ_2). The non-adiabatic coupling vector $\langle \Psi_1 | \partial / \partial R | \Psi_2 \rangle$ (fig. 5.2 (c), appendix A.4), which is a scalar in this single-nuclear dimension example, is essentially zero except at the avoided crossing. There it features a sharp and narrow peak indicating the strong non-adiabaticity of this region. Avoided crossings with a such a structure (narrow avoided crossing with narrow change of configuration, and narrow and peaked non-adiabatic coupling vector) are referred to as Landau–Zener-type crossings.

As discussed above the efficiency of the coupling between the two electronic states Σ_1 and Σ_2 depends mainly on the velocity of the two nuclei, i.e., on how strongly the Born–Oppenheimer approximation is violated. The Massey parameter $\xi = \omega_{el} \tau_n$ is a measure for the efficiency of the coupling. It is the product of ω_{el} , the electronic transition frequency, and τ_n , the characteristic time for the change of electronic wave functions upon nuclear motion. In our example $\omega_{el} = \Sigma_2 - \Sigma_1 = \Delta E \approx 0.18$ eV at the point of the avoided crossing $R \approx 6.65$. $\tau_n = \Delta L / v_n$, where $\Delta L \approx 0.3$ a.u. is the characteristic length scale of the non-adiabatic coupling (the full width at half maximum of the peak in fig. 5.2 (c)) and v_n is the nuclear velocity. This leads to

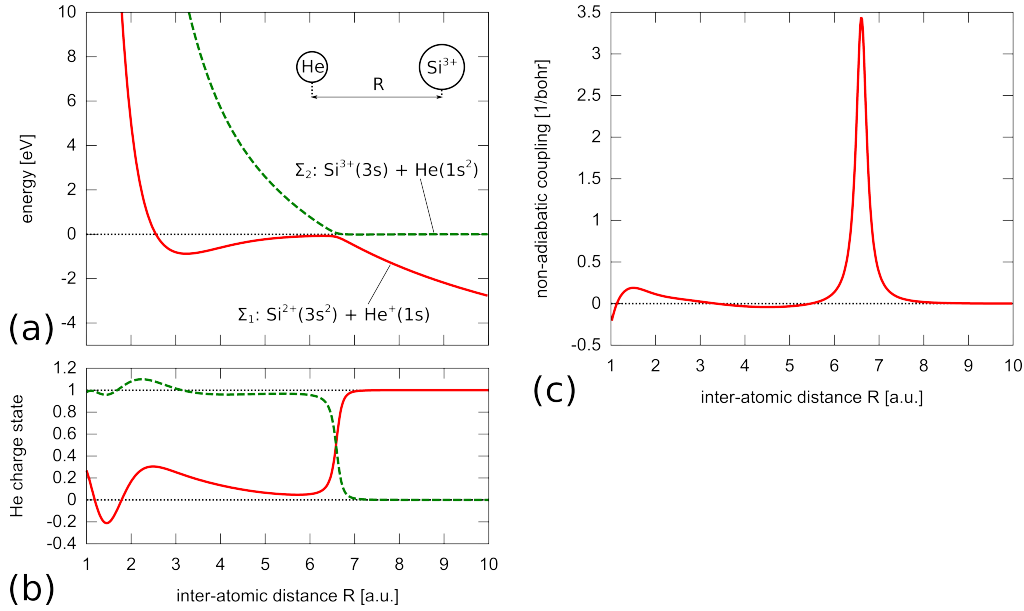


Figure 5.2.: (a) The two energetically lowest adiabatic MCSCF potential energy surfaces (basis set: cc-pvtz) Σ_1 and Σ_2 responsible for the charge transfer reaction $\text{Si}^{3+} + \text{He} \rightarrow \text{Si}^{2+} + \text{He}^+$. (b) Charge state, i.e., Mulliken charges of the He constituent. (c) Non-adiabatic coupling vector $\langle \Sigma_1 | \partial_R | \Sigma_2 \rangle$.

(for v_n in a.u.)

$$\xi(R) = \frac{\Delta E \Delta L}{v_n} \approx \frac{0.002}{v_n}. \quad (5.15)$$

For the passage of the system through the interaction region the non-adiabatic coupling is efficient when ξ is in the order of unity or below and inefficient when $\xi \gg 1$. Therefore, we expect the onset of charge transfer at a relative nuclear velocity of $v_n \approx 0.002$ a.u. which corresponds to a momentum of 12 a.u. and a kinetic energy of 0.3 eV in the center of mass frame.

In terms of the Massey parameter the validity of the BO approximation reads as follows. For a system in a given electronic state Γ the nuclear motion is governed by a single adiabatic potential energy surface $E_\Gamma(R)$ when $\xi \gg 1$ (low velocities v_n). For the other limiting case $\xi \ll 1$ (high velocities v_n) the concept of diabatic states, introduced in the following section, is more suitable.

5.3. The diabatic representation

In situations where $\xi \ll 1$ nuclear velocities are so large that electrons cannot adapt to the nuclear motion any more. This means the electrons do not change

their configuration when the system runs through an interaction region and the dynamics is governed by a single, so-called, diabatic potential energy surface. In this section we derive the matrix A for the $\text{Si}^{3+} + \text{He}$ which allows for transformation from the adiabatic to the diabatic picture and vice versa. Further, we discuss how the diabatic picture simplifies the solution of the time-dependent Schrödinger equation.

In the following we drop the electronic-state indices of $\chi_i(\vec{R})$ and $\Psi_i(\vec{r}; \vec{R})$ and consider χ and Ψ to be column vectors of the nuclear and electronic wave functions, respectively. With this notation the Born–Oppenheimer expansion (5.3) reads

$$\Phi_{\text{total}}(\vec{r}, \vec{R}) = \chi(\vec{R}) \cdot \Psi(\vec{r}; \vec{R}), \quad (5.16)$$

which can further be modified by inserting the unitary adiabatic-to-diabatic transformation matrix A

$$\Phi_{\text{total}} = \Psi(\vec{r}; \vec{R}) \cdot \chi(\vec{R}) = \Psi(\vec{r}; \vec{R}) A(\vec{R}) A^\dagger(\vec{R}) \chi(\vec{R}). \quad (5.17)$$

We further drop the dependence of the wave functions on the coordinates and define a new set of electronic basis functions $\tilde{\Psi}$ and nuclear wave functions $\tilde{\chi}$

$$\begin{aligned} \tilde{\Psi} &= \Psi A \\ \tilde{\chi} &= A^\dagger \chi. \end{aligned} \quad (5.18)$$

With this definition (and dropping the factor $-1/2M$) we can rewrite the first term of equation 5.10 as

$$\begin{aligned} (\vec{\nabla} + \vec{F})^2 \chi &= (\vec{\nabla} + \vec{F})^2 A \tilde{\chi} \\ &= A \vec{\nabla}^2 \tilde{\chi} + 2(\vec{\nabla} A + \vec{F} A) \cdot \vec{\nabla} \tilde{\chi} + \{(\vec{F} + \vec{\nabla}) \cdot (\vec{\nabla} A + \vec{F} A)\} \tilde{\chi}, \end{aligned} \quad (5.19)$$

where the $\vec{\nabla}$ -operators in the last term act only within curly brackets. If A is chosen to be a solution of the equation

$$\vec{\nabla} A + \vec{F} A = 0 \quad (5.20)$$

only the first term in the above equation is non-zero. After multiplication with A^\dagger from the left the nuclear Schrödinger equation 5.10 becomes

$$-\frac{1}{2M} \vec{\nabla}^2 \tilde{\chi} + \tilde{E} \tilde{\chi} = E_{\text{tot}} \tilde{\chi}. \quad (5.21)$$

\tilde{E} is the diabatic potential matrix given by

$$\tilde{E} = A^\dagger E A, \quad (5.22)$$

which is, in general, a full matrix. The diagonal contains the so-called diabatic potential energy surfaces and the off-diagonal part contains the diabatic couplings. The adiabatic-to-diabatic transition simplifies the form of the time-dependent Schrödinger equation by eliminating the non-adiabatic coupling vector \vec{F} in eq. 5.10. The prize to be paid are the off-diagonal terms in \tilde{E} , the diabatic potential matrix. In this context this transition is said to transform the kinetic coupling $\vec{F} \cdot \vec{\nabla}$ (adiabatic picture) into a potential coupling in \tilde{E} (diabatic picture). The elimination of \vec{F} eases the solution of the nuclear motion in two ways. First, the non-adiabatic couplings \vec{F} are quite often very narrow (see fig. 5.2 (c)) which requires a high spatial resolution in the ab-initio calculation of the PES and \vec{F} and it requires a high temporal resolution to correctly describe the motion of the system through the narrow avoided crossing. The diabatic couplings, on the other hand, vary typically much smoother with R . Second, the “book keeping” is somewhat simplified since \vec{F} is a vector of matrices while the entries in \tilde{E} are scalars.

The matrix A can be found by solving equation 5.20, which is called strict diabatization [127–130]. Unfortunately, an unambiguous solution only exists for a single adiabatic parameter, i.e., for a single nuclear degree of freedom R . In higher-dimensional nuclear spaces $A(\vec{R})$ depends on the path $\vec{R}(t)$, where t is the integration parameter, along which eq. 5.20 is integrated. For the one-dimensional case equation 5.20 reduces to

$$\frac{\partial}{\partial R} A(R) = -F(R) A(R), \quad (5.23)$$

which comprises the important case of diatomic molecules. For more complex systems strategies different from strict diabatization have to be applied. Such strategies include property based diabatization, energy based diabatization, the concept of regularized diabatic states, and local diabatization (see, e.g, [112, 131]). The numerical solution of eq. 5.23 is given by a Crank-Nicholson-like equation [132] for the transformation matrix propagation

$$\left(\mathbb{1} + F \frac{\Delta R}{2} \right) A(R + \Delta R) = \left(\mathbb{1} - F \frac{\Delta R}{2} \right) A(R), \quad (5.24)$$

where ΔR is the integration step. For the $\text{Si}^{3+} + \text{He}$ system the integration is done as follows. We start in the region $R > 10$ where $F = 0$ (fig. 5.2 (c)) and the adiabatic and diabatic representations are equivalent. We set $A = \mathbb{1}$, propagate eq. 5.24 from $R = 12$ towards smaller distances, and calculate for every distance R the diabatic potential matrix.

Fig. 5.3 (a) shows the diagonal elements of $\tilde{E}_{ji}(R)$, the diabatic potential energy surfaces, panel (b) shows the He charge state attributed to the diabatic PES, and panel (c) shows the diabatic coupling elements, the off-diagonal entry of \tilde{E} . The charge state of He are the diagonal elements of a matrix $\tilde{M} = A^\dagger M A$, where M is a matrix with the adiabatic Mulliken charges on the diagonal and zeros in the off-diagonal parts. For this specific case (narrow avoided crossing) the diabatic

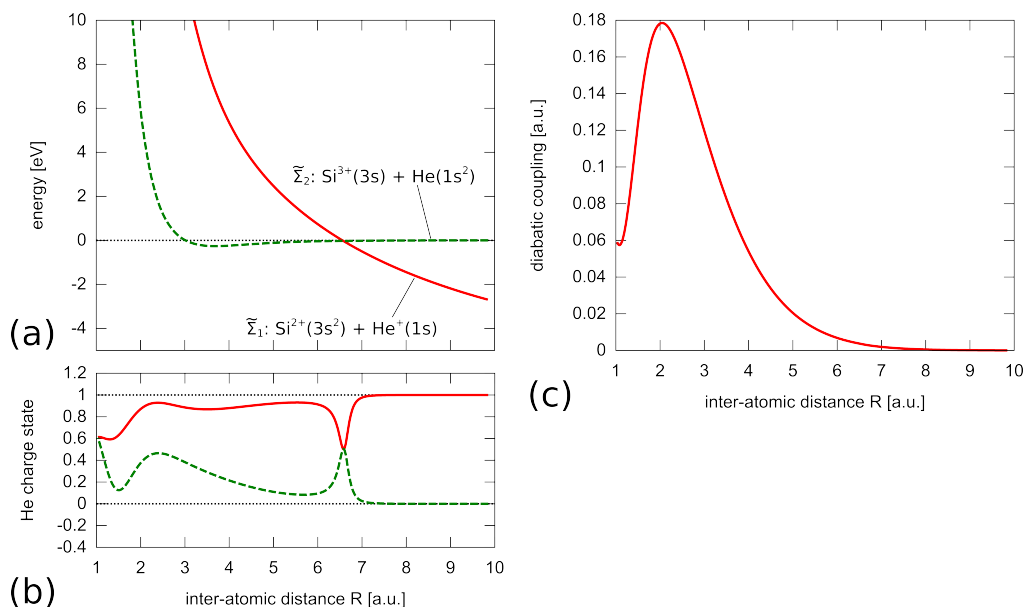


Figure 5.3.: (a) The two energetically lowest diabatic MCSCF potential energy surfaces (basis set: cc-pvtz) $\tilde{\Sigma}_1$ and $\tilde{\Sigma}_2$ contributing to the charge transfer reaction $\text{Si}^{3+} + \text{He} \rightarrow \text{Si}^{2+} + \text{He}^+$. (b) Diabatic charge state, i.e., diabaticized Mulliken charges of the He constituent and (c) diabatic coupling element $\tilde{E}_{12}(R)$.

and adiabatic PES look qualitatively similar. The difference between them is, that, instead of the avoided crossing in the adiabatic case, the diabatic PES do cross. They are allowed to do so since the diabatic electronic wave functions $\tilde{\Psi}_i$ are not eigenfunctions of the electronic Hamiltonian. The charge state for the diabatic states $\tilde{\Sigma}_1$ and $\tilde{\Sigma}_2$ do behave exactly in the opposite way. While they cross in the adiabatic picture they form an anti-crossing in the diabatic representation. When the system moves along the adiabatic PES Σ_1 (or Σ_2) and passes the avoided crossing, electron transfer between Si and He occurs which is reflected by the change in the He charge state before and after the avoided crossing. Moving along a diabatic PES ($\tilde{\Sigma}_1$ or $\tilde{\Sigma}_2$) the He charge state is the same before and after the crossing, which means charge transfer does not occur upon passage of the crossing, i.e., the electronic configuration does not change. The diabatic couplings in panel (c) vary smoother with R than the non-adiabatic couplings in fig. 5.2 (c).

5.4. Solution of the time-dependent Schrödinger equation for the nuclear motion

In this section we review methods used to (approximately) solve the time-dependent Schrödinger equation

$$i\frac{\partial}{\partial t}\chi = -\frac{1}{2M}\left(\vec{\nabla} + \vec{F}\right)^2\chi + \mathbf{E}\chi \quad (5.25)$$

(or its diabatic analog) for the nuclear motion on several potential energy surfaces. The methods considered can be divided into three groups. First, we discuss analytical approximations for the transition probability between two electronic states upon passage of an interaction region. Second, the semi-classical Tully surface-hopping algorithm is discussed which combines both a quantum propagation of the electronic degrees of freedom (from which transition probabilities are derived) and a classical propagation for the motion of the nuclei. Third, we investigate a full quantum-mechanical solution of the scattering event by wave packet propagation. We introduce these methods with the help of the model system $\text{Si}^{3+} + \text{He}$ with two electronic states and calculate the charge transfer probability in a head-on collision with R , the inter-nuclear distance, being the only nuclear degree of freedom.

5.4.1. Approximate analytic solutions

There are two typical shapes of potential energy surfaces describing charge transfer in diatomic scattering events. Their characteristics is determined by the charge states of the two scatterers at asymptotic distances $R \rightarrow \infty$. First, consider the reaction $A^{3+} + B \leftrightarrow A^{2+} + B^+$ to which our model system $\text{Si}^{3+} + \text{He}$ belongs. In a two-state model each side of this reaction corresponds to one PES, at large distances R . The PES of $A^{3+} + B$ typically varies only slowly with R since the species B is neutral and the interaction between the scatterers is governed by the weakly attractive ion-induced dipole force, i.e., the interaction between the ion A^{3+} and the polarized atom B . The PES of $A^{2+} + B^+$, however, scales like $1/R$ due to the Coulomb repulsion of the scatterers. This large difference in R -dependence forms a very narrow avoided crossing (fig. 5.2) which is called a Landau–Zener–Stückelberg (LZS) type of avoided crossing. Second, consider the reaction $A^+ + B \leftrightarrow A + B^+$. In this case, there is a neutral scatterer on both sides of the reaction and the PESs of both sides are governed by the induced-dipole attraction. Therefore, the PESs are rather flat at large R and almost run in parallel (fig. 5.6). Although they do not feature a conspicuous narrow avoided crossing the charge transfer occurs quite locally and one speaks of a hidden crossing. PES of this type are described by the Rosen–Zener–Demkov (RZD) model.

In this section we will briefly introduce both models (for a review see, e.g., [133] and

references in there) and apply them to calculate the charge-transfer probability in two model systems. There are also “intermediate models”, e.g., the Nikitin model dealing with PES that are neither parallel lines nor have a narrow avoided crossing. We do not describe such models here but refer the interested reader to the literature (see, e.g., [133])

The Landau–Zener–Stückelberg approximation

Landau [134, 135], Zener [136] and Stückelberg [137] considered a two-state model with crossing linear-diabatic PES and a constant diabatic coupling between them. Upon diagonalization one finds adiabatic PES with a narrow avoided crossing just like the one of $\text{Si}^{3+} + \text{He}$ (fig. 5.2). Landau derived an expression for p_{12}^{LZ} the transition probability between two adiabatic states by the complex contour integral method after analytic continuation of the adiabatic PES into the complex plane. Zener solved the time-dependent Schrödinger equation in the diabatic representation.

In the following we apply the Landau–Zener–Stückelberg model to the $\text{Si}^{3+} + \text{He}$ two-level system. The non-adiabatic couplings are approximated to be non-zero only in a very narrow region of space ΔL . Outside of this region adiabatic and (quasi)-diabatic PES lie exactly on top of each other. Inside of ΔL the adiabatic PES feature the avoided crossing while the (quasi)-diabatic states cross at R_c and are approximated by straight lines. We use the term quasi-diabatic in this context since the diabatic PES are not determined by solving eq. 5.23 but are, within ΔL , drawn “by hand” and coincide with the adiabatic PES elsewhere. R_c is the real part of R^* , the complex crossing point of the adiabatic potentials. Approximating the diabatic couplings to be constant within ΔL leads to the Landau-Zener diabatic potential matrix

$$\begin{aligned}\tilde{E}_{11}^{\text{LZ}}(R) &= \tilde{E}_0 - k_1 (R - R_c) \\ \tilde{E}_{22}^{\text{LZ}}(R) &= \tilde{E}_0 - k_2 (R - R_c) \\ \tilde{E}_{12}^{\text{LZ}}(R) &= V = \text{const.},\end{aligned}\tag{5.26}$$

with

$$k_i = \left. \frac{d\tilde{E}_{ii}^{\text{LZ}}(R)}{dR} \right|_{R_c},\tag{5.27}$$

the slopes k_i of the Landau–Zener diabatic states $\tilde{E}_{ii}^{\text{LZ}}(R)$ at $R = R_c$. Via a diagonalization one can derive a connection between the diabatic coupling V and

the spacing between the adiabatic PES at R_c reading

$$(\Delta E)^2 = 4V^2. \quad (5.28)$$

With $\Delta k = |k_1 - k_2|$ the transition probability between the adiabatic PES upon a single passage of R_c reads

$$p_{12}^{\text{LZ}} = e^{-2\pi \frac{V^2}{\Delta k v_n}} = e^{-2\pi \xi_{\text{LZ}}}, \quad (5.29)$$

which varies between 0 ($v_n \ll 1$) and 1 ($v_n \gg 1$). v_n is the nuclear velocity and ξ_{LZ} is the Massey parameter within the Landau-Zener approximation

$$\xi_{\text{LZ}} = \frac{V^2}{\Delta k v_n}. \quad (5.30)$$

For the determination of the charge-transfer probability in the $\text{Si}^{3+} + \text{He}$ scattering we extract $\Delta E = 0.18$ eV and $\Delta k = 0.045$ a.u. from the adiabatic and diabatic PES in figs. 5.2 and 5.3, respectively. The Landau-Zener Massey parameter then reads (for v_n in a.u.)

$$\xi_{\text{LZ}} \approx \frac{0.00024}{v_n}, \quad (5.31)$$

suggesting the onset of charge transfer to be at $v_n \approx 0.00024$ a.u. which corresponds, with the reduced mass $\mu = 6386$ a.u., to a momentum of ~ 1.5 a.u. in the center of mass frame.

During the head-on rescattering collision the system passes the avoided crossing twice which leads to a total charge-transfer probability of

$$\langle \mathcal{P}_{12}^{\text{LZ}} \rangle = 2p_{12}^{\text{LZ}}(1 - p_{12}^{\text{LZ}}). \quad (5.32)$$

It is written in brackets because it denotes an average value neglecting the quantum nature of the scattering process. $\langle \mathcal{P}_{12}^{\text{LZ}} \rangle$ is shown in fig. 5.4 as a function of the initial relative nuclear momentum $P_{\text{init}} = \mu v_n$ and the initial kinetic energy $P_{\text{init}}^2/2\mu$ in the center of mass frame. Since the PES of the initial state Σ_2 is quite flat we approximate the nuclear velocity at the avoided crossing R_c by the initial velocity. Charge transfer sets in at a momentum of ~ 1 a.u. and features a maximum at $P_{\text{init}} \approx 14.5$, exactly where $p_{12}^{\text{LZ}} = 0.5$ corresponding to the Massey maximum. If v_n is very small ($p_{12}^{\text{LZ}} \approx 0$) the system stays on the initial adiabatic potential surface upon both passages through the avoided crossing and no charge transfer occurs. For very large velocities ($p_{12}^{\text{LZ}} \approx 1$) the system switches the adiabatic PES upon both passages and there is no net charge transfer. The maximum probability for charge transfer is, therefore, reached in an intermediate velocity regime where the single-

passage probability p_{12}^{LZ} equals 50%. This analysis implies that for low velocities, near the adiabatic limit, the nuclear motion is governed by a single adiabatic PES while in the diabatic limit of very fast nuclei, to motion takes place on a single diabatic PES.

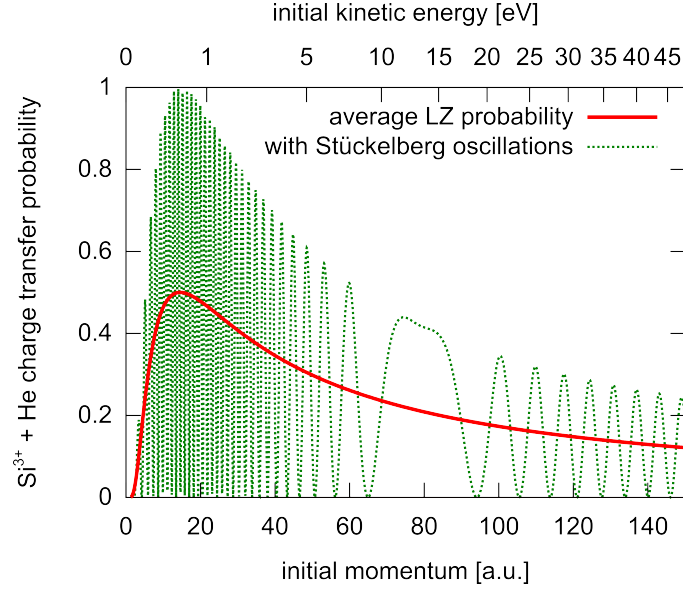


Figure 5.4.: Landau-Zener charge transfer probability for a head-on collision of Si^{3+} and He as a function of initial relative momentum and kinetic energy in the center of mass frame. The initial momentum reads $P_{\text{init}} = \mu v_n$ with the reduced mass $\mu = 6386$ a.u. The solid red line is the average probability while the dotted green line shows Stückelberg oscillations due to quantum interference.

Consider the system initially in state Σ_2 . During the scattering event the system has two options to end up in state Σ_1 . It can change from Σ_2 to Σ_1 either upon the first passage of R_c (the inward motion) or upon the second passage of R_c (the outward motion). Semiclassically, these two options correspond to two alternative pathways giving rise to quantum interference and, therefore, a modulation of the charge-transfer probability, the so-called Stückelberg oscillations [137]. The phase difference between the two paths is given by

$$\Delta\phi_{12} = 2 \left(\int_{R_c}^{R_{t1}} p_1(R) dR - \int_{R_c}^{R_{t2}} p_2(R) dR \right). \quad (5.33)$$

R_{t1} and R_{t2} are the classical turning points of a particle with mass μ propagating on the PES of Σ_1 and Σ_2 , respectively, and depend on the initial momentum P_{init} . Accordingly, $p_1(R)$ and $p_2(R)$ are the momenta of the particle at a given R on the

PES of the two electronic states. With this phase difference the charge transfer probability reads

$$\mathcal{P}_{12}^{\text{LZ}} = 2p_{12}^{\text{LZ}}(1 - p_{12}^{\text{LZ}})(1 - \cos \Delta\phi_{12}). \quad (5.34)$$

It shows oscillations (fig. 5.4) around $\langle \mathcal{P}_{12}^{\text{LZ}} \rangle$ the frequency of which varies with the initial velocity and depend via eq. 5.33 on the shape of the PES. The phase difference $\Delta\phi_{12}$ depends on the initial momentum P_{init} via the turning points in eq. 5.33. Interferences in the charge-transfer probability, therefore, cause oscillations with frequency

$$\Omega = \frac{d\Delta\phi_{12}}{dP_{\text{init}}}. \quad (5.35)$$

At $P_{\text{init}} \approx 80$ a.u., $\Delta\phi_{12}(P_{\text{init}})$ has an extremum, i.e. $\Omega = 0$, leading to a broad oscillation in $\mathcal{P}_{12}^{\text{LZ}}$. This extremum is due to the different shapes of the potential energy surfaces Σ_1 and Σ_2 . Approximating Σ_1 by an L-shaped potential (fig. 5.5) and Σ_2 by a straight line allows for analytic solution of the two phase-space integrals in eq. 5.33. Within this approximation, the first term, corresponding to Σ_1 , is proportional to P_{init} while the second term, corresponding to Σ_2 , scales with P_{init}^3 . For initial momenta below 80 a.u., the first term grows faster with P_{init} than the second one. For momenta above 80 a.u. this tendency is reversed leading to the extremum in $\Delta\phi_{12}(P_{\text{init}})$.

The Rosen–Zener–Demkov approximation

The Rosen–Zener–Demkov (RZD) model represents the opposite limit of diabatic PESs. They are approximated by two parallel lines around R_c unlike the Landau–Zener model for two crossing straight lines around R_c . For the diabatic coupling an exponential dependence on R is assumed. R_c again denotes the real part of R^* , the crossing point in the complex plane. Rosen and Zener [138], and Demkov [139, 140] solved the time-dependent Schrödinger equation for such a system exactly and derived an expression for p_{12}^{RZD} the transition probability between the two states. PESs, charge states, and non-adiabatic coupling vector of RZD type (fig. 5.6) are found for the charge transfer between a proton H^+ and a cluster Li_5F_1 representing a LiF crystal surface. The cluster is embedded in a matrix of point charges which is constructed such that cluster plus embedding is neutral. The charge-transfer reaction can, therefore, be written as $\text{H}^+ + \text{Li}_5\text{F}_1 \leftrightarrow \text{H} + (\text{Li}_5\text{F}_1)^+$. This system is studied in more detail in chapter 6. The nuclear coordinate R denotes the distance between H^+ and the surface. Since PES of RZD type have no narrow avoided crossing the position of R_c is not as obvious as in the LZ case. For large R , the two potential energy surfaces are essentially parallel. At R_c the non-adiabatic coupling has a maximum and the adiabatic PES start to diverge. Also the diabatic PES of

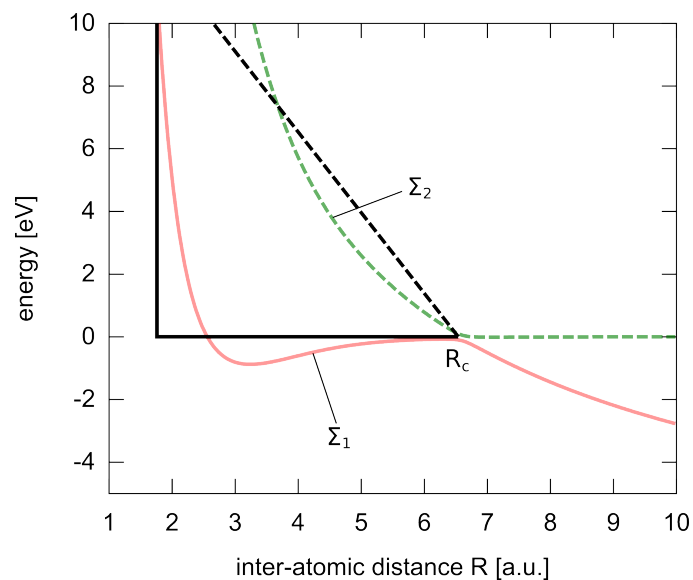


Figure 5.5.: The two energetically lowest adiabatic MCSCF potential energy surfaces (basis set: cc-pvtz) Σ_1 (solid-red line) and Σ_2 (dashed-green line) responsible for the charge transfer reaction $\text{Si}^{3+} + \text{He} \rightarrow \text{Si}^{2+} + \text{He}^+$. Solid-black and dashed-black lines are approximations to the PES used in the analytic solution of the phase integral in eq. 5.33.

this model system cross but the crossing point is at $R < R_c$ while at R_c the diabatic PESs are parallel.

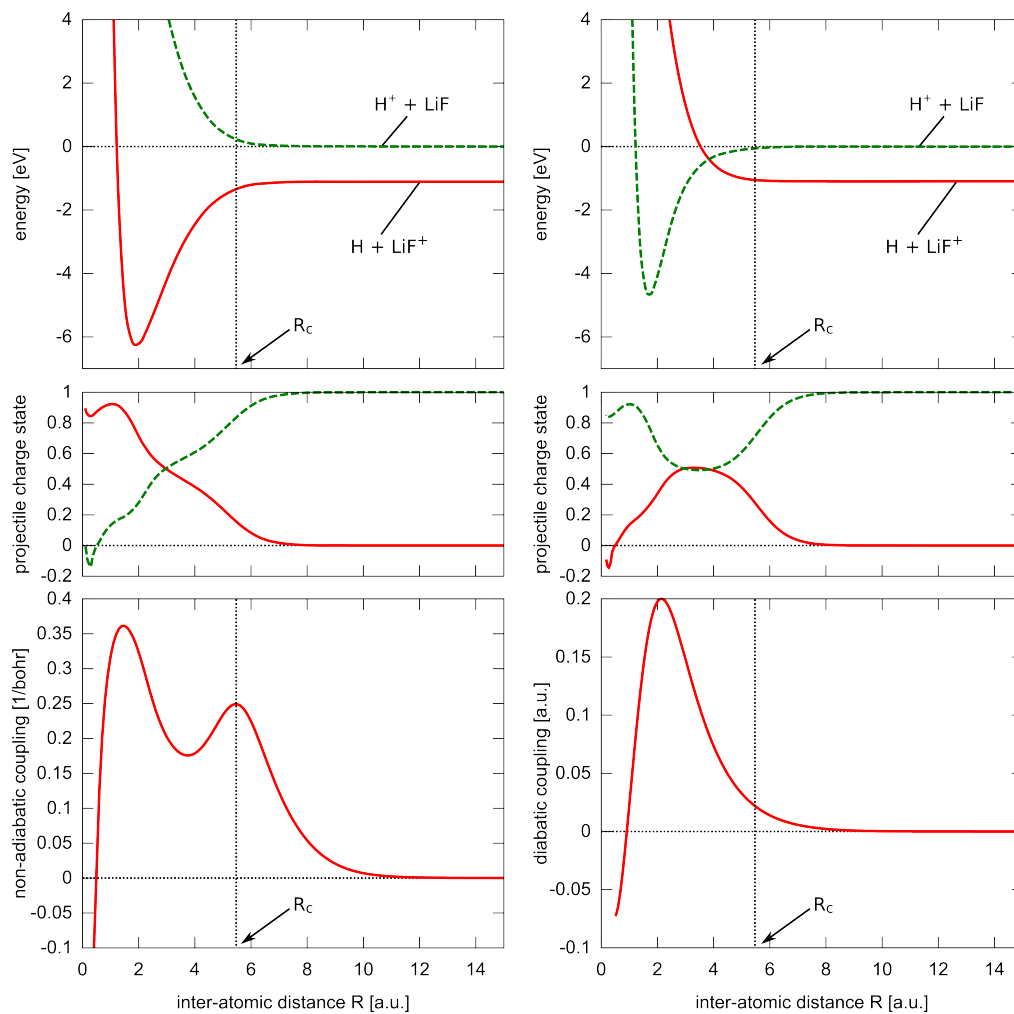


Figure 5.6.: Schematic adiabatic (left panels) and diabatic (right panels) potential energy curves, couplings, and charge states of the $\text{H}^+ + \text{LiF}$ -surface \leftrightarrow $\text{H} + (\text{LiF})^+$ -surface charge transfer as a function of the inter-nuclear distance R . PES are of Rosen–Zener–Demkov type.

The RZD diabatic Hamiltonian approximates the two PES and the diabatic coupling around R_c by

$$\begin{aligned}\tilde{E}_{11}^{\text{RZD}} &= \tilde{E}_{\text{avg}} - \Delta\tilde{E}/2 \\ \tilde{E}_{22}^{\text{RZD}} &= \tilde{E}_{\text{avg}} + \Delta\tilde{E}/2 \\ \tilde{E}_{12}^{\text{RZD}} &= A_0/2 e^{-\alpha R}.\end{aligned}\quad (5.36)$$

The choice of $\tilde{E}_{12}^{\text{RZD}} = A_0/2 e^{-\alpha R}$ in terms of a single exponential is due to Demkov, Rosen and Zener originally treated a symmetric ($t \rightarrow -t$) coupling $\tilde{E}_{12}^{\text{RZD}}(t) \propto \cosh^{-1}(t/\tau_0)$. For the present scattering system eq. 5.36 is more appropriate. The RZD-transition probability for a single passage of R_c is given by

$$p_{12}^{\text{RZD}} = \frac{e^{-\pi\xi_{\text{RZD}}}}{1 + e^{-\pi\xi_{\text{RZD}}}}, \quad (5.37)$$

with $\xi_{\text{RZD}} = \Delta\tilde{E}/v_n\alpha$ the Massey parameter for the RZD model. $\Delta\tilde{E}$ is the energy spacing between the two parallel diabatic PES at R_c , v_n is the nuclear velocity and α is the exponent describing the decay of the diabatic coupling. We determine the parameters $\Delta\tilde{E}$ and α by fitting to the diabatic PES in fig. 5.6 yielding $\Delta\tilde{E} = 0.0409$ a.u. (1.11 eV) and $\alpha = 0.77$ a.u. \tilde{E}_{avg} and A_0 in eq. 5.36 are R -independent constants. The average neutralization probability after rescattering, i.e., after the double passage of R_c reads

$$\langle \mathcal{P}_{12}^{\text{RZD}} \rangle = 2p_{12}^{\text{RZD}}(1 - p_{12}^{\text{RZD}}) = \frac{1}{2} \frac{1}{\cosh^2(\frac{\pi}{2}\xi_{\text{RZD}})} \quad (5.38)$$

and is plotted as solid-red line in fig. 5.7 with $\mu = 1837$ a.u., the mass of the hydrogen projectile. Conceptual differences to a LZ crossing model become obvious. In the present case the RZD crossing is much more inefficient than a LZ crossing which is reflected in the RZD-Massey parameter (for v_n in a.u.)

$$\xi_{\text{RZD}} \approx \frac{0.053}{v_n}, \quad (5.39)$$

which approaches $\xi_{\text{RZD}} \approx 1$ only for much larger velocities than ξ_{LZ} (eq. 5.31). Therefore, $\langle \mathcal{P}_{12}^{\text{RZD}} \rangle$ stays close to zero up to much larger nuclear velocities. Another difference is the absence of a Massey maximum in the RZD model (as long as the average neutralization probability after double passage can be approximated by two independent single passages like in eq. 5.38). For LZ crossings the single-passage probability p_{12}^{LZ} takes values between 0 and 1 leading to a Massey maximum in the double passage probability $\langle \mathcal{P}_{12}^{\text{LZ}} \rangle$ at $p_{12}^{\text{LZ}} = 0.5$. The RZD single-passage probability varies only between 0 and 0.5. $\langle \mathcal{P}_{12}^{\text{RZD}} \rangle$, therefore, has no maximum but rises from 0 to 0.5 with increasing nuclear velocity. This implies for the dynamics in the RZD

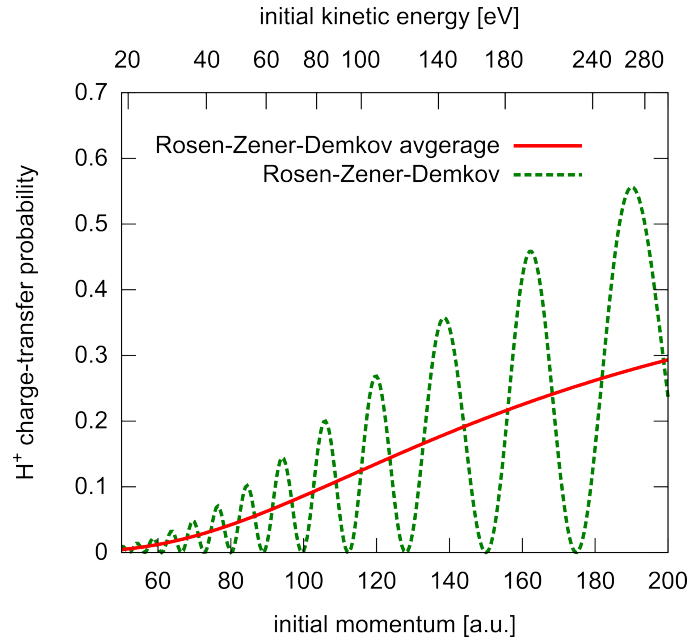


Figure 5.7.: Rosen–Zener–Demkov neutralization probability of H^+ for the $\text{H}^+ + \text{LiF}$ -surface $\leftrightarrow \text{H} + (\text{LiF})^+$ -surface charge-transfer reaction as a function of the initial momentum and kinetic energy in the center of mass frame. The mass used is $\mu = 1837$ a.u. (the mass of a hydrogen atom). Solid-red line is the average probability while the dotted-green line shows Stückelberg oscillations due to quantum interference.

model the following picture. In the adiabatic limit the nuclear motion is governed by a single adiabatic PES while in the diabatic limit the motion is determined by both diabatic PES.

The Stückelberg oscillations are determined analogously to the LZ case by numerically calculating the phase difference $\Delta\phi_{12}$ in equation 5.33. The total neutralization probability P_{12}^{RZD} (fig. 5.7) then reads

$$P_{12}^{\text{RZD}} = \frac{1}{\cosh^2\left(\frac{\pi}{2}\xi_{\text{RZD}}\right)} \sin^2(\Delta\phi_{12}/2). \quad (5.40)$$

5.4.2. The Tully surface-hopping algorithm

For systems with more than two states as well as arbitrarily shaped avoided crossings and couplings the application of such analytical approximations becomes problematic. The full quantum-mechanical solution of the TDSE handles any type of avoided crossing but it becomes numerically very demanding and in many cases impossible to solve for many nuclear degrees of freedom. An alternative to the

full quantum-mechanical solution is the use of semi-classical approaches such as the Tully surface-hopping (TSH) algorithm [141–143]. It is based on a separate treatment of the nuclear and electronic degrees of freedom. While for the electronic degrees of freedom the time integration is performed quantum-mechanically within a set of coupled channel equations, the nuclear motion is treated purely classical. Therefore, the system is described by a classical particle moving on, at each instance of time, a single PES according to Newton's equations of motion. It is the locality introduced by the classical treatment of the nuclear motion that eases the time integration compared to full quantum solution. Within the TSH approach, the coupling between electronic and nuclear motion is introduced via a stochastic algorithm based on a non-vanishing probability for the classical particle to jump, or, to hop between the PES in every time step of the integration. This hopping probability depends on the non-adiabatic coupling vector, the amplitudes of the electronic channels, and the nuclear velocity as will be shown in the following. The probabilistic character of a full quantum solution by a nuclear-wave packet propagation is regained by using an ensemble of classical nuclear trajectories for each initial condition in a classical Monte Carlo type of approach. For the two-state example of the charge transfer in a $\text{Si}^{3+} + \text{He}$ collision this is done in practice as follows. A large number of trajectories is started on the PES of Σ_2 at $R = 12$ with a given momentum pointing towards the origin (schematically depicted in fig. 5.8 (a)). On their inward motion the trajectories pass the avoided crossing the first time leading to hopping from Σ_2 to Σ_1 . Trajectories are reflected at their classical turning points R_{t1} and R_{t2} (fig. 5.8 (b)). After passing the avoided crossing a second time rescattered trajectories can either return on the PES of Σ_1 or Σ_2 (fig. 5.8 (c)) and the charge-transfer probability is given by the fraction of trajectories returning in Σ_1 divided by the number of started trajectories.

Under the assumption of nuclei moving on classical trajectories $\vec{R}(t)$ the time dependent many-electron wave function can be written as

$$\Psi_{\text{electron}}(\vec{r}, \vec{R}, t) = \sum_{j=1}^N c_j(t) \cdot \Psi_j(\vec{r}; \vec{R}(t)), \quad (5.41)$$

where \vec{r} encompasses all electronic degrees of freedom. In the adiabatic representation $\Psi_j(\vec{r}; \vec{R}(t))$ is the j^{th} eigenfunction of the electronic Hamiltonian $H_e \Psi_j(\vec{r}; \vec{R}) = E_j(\vec{R}) \Psi_j(\vec{r}; \vec{R})$. Inserting this ansatz into the time-dependent electronic Schrödinger equation $i\hbar \partial_t \Psi_{\text{electron}} = H_e \Psi_{\text{electron}}$ leads to a set of coupled differential equations for the expansion coefficients, the so-called coupled channel equations,

$$i \frac{\partial}{\partial t} c_j(t) = E_j(\vec{R}(t)) c_j(t) - i \sum_i \langle \Psi_j | \frac{\partial}{\partial t} | \Psi_i \rangle c_i(t). \quad (5.42)$$

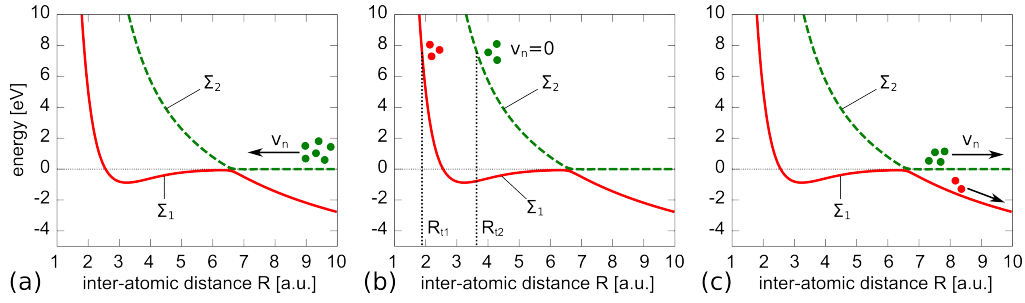


Figure 5.8.: Schematic illustration of the Tully surface hopping approach applied to the $\text{Si}^{3+} + \text{He}$ charge transfer. Initially, an ensemble of trajectories is prepared in the electronic state of Σ_2 with a velocity pointing towards the origin (a). During their inward motion they pass the avoided crossing giving rise to a non-zero probability for hopping between the potential energy surfaces. The trajectories are rescattered at their classical turning points R_{t1} and R_{t2} (b). On their outward motion they pass the avoided crossing a second time. (c) After rescattering a fraction of the trajectories, equal to the charge-transfer probability, has changed the electronic state and returns on the PES of Σ_1 .

They represent the semi-classical version of non-Born-Oppenheimer dynamics. With the relation

$$\langle \Psi_j | \frac{\partial}{\partial t} | \Psi_i \rangle = \langle \Psi_j | \frac{\partial}{\partial \vec{R}} | \Psi_i \rangle \frac{\partial \vec{R}}{\partial t} = \vec{F}_{ji} \cdot \dot{\vec{R}}, \quad (5.43)$$

this can be written as

$$i \frac{\partial}{\partial t} c_j(t) = E_j(\vec{R}(t)) c_j(t) - i \dot{\vec{R}} \sum_i \vec{F}_{ji} c_i(t). \quad (5.44)$$

$\vec{F}_{ji}(\vec{R}(t))$ is the non-adiabatic coupling vector between the states j and i and $\dot{\vec{R}}(t)$ is the nuclear-velocity vector. The nuclear motion at a given instance of time is governed by Newton's equation of motion on a single potential energy surface

$$M \frac{\partial^2}{\partial t^2} \vec{R}(t) = -\nabla E_j(\vec{R}), \quad (5.45)$$

where M is the nuclear mass. In the simulation Newton's equation of motion and the equations for the amplitudes $c_j(t)$ are integrated simultaneously.

In the following we give a “qualitative” derivation of the probability $g_{i \rightarrow f}$, proposed by Tully [141], that the system hops from the initial state i to a final state f within the time step Δt . One key aspect of Tully's surface hopping approach is the fewest

switches criterion. $g_{i \rightarrow f}$ is defined such that as few jumps between PESs as possible occur to retain as much “quantum information” as possible. In an algorithm with a very high jump probability per time step a trajectory effectively evolves on an average PES which affects the regions the trajectories explore and, consequently, also the phase of c_j accumulated during propagation. Consider a two-state system and a large number N of trajectories. At time t_0 there is a number of $N'_i = a'_{ii} N$ (with $a_{kl} = c_k c_l^*$ and $a_{kk} = |c_k|^2$ being the state populations) trajectories associated with state i and $N'_f = a'_{ff} N$ with state f . Let us assume at a later time $t_0 + \Delta t$ the state populations have changed to $a_{ii} < a'_{ii}$ and $a_{ff} > a'_{ff}$ and so have the number of trajectories associated with these states $N_i = N a_{ii} < N'_i = N a'_{ii}$. In principle, trajectories can switch in both directions: from i to f and from f to i . In total, however, the number of trajectories switching from i to f must be larger. The smallest number of switches is achieved when no switches from f to i are allowed and $(a'_{ii} - a_{ii})N$ switches from i to f occur. The switching probability is given by $(a'_{ii} - a_{ii})/a'_{ii}$ which can be rewritten for small time intervals Δt :

$$\frac{(a'_{ii} - a_{ii})}{a'_{ii}} \approx \frac{(a_{ff} - a'_{ff})}{a_{ii}} \Delta t \approx \frac{\dot{a}_{ff} \Delta t}{a_{ii}}. \quad (5.46)$$

Generalization to a multiple-state model [141] leads, with eq. 5.44, to

$$g_{i \rightarrow f} = -\Delta t \cdot \frac{1}{a_{ii}} \cdot 2\Re\{c_i^* c_f \dot{\vec{R}} \cdot \vec{F}_{if}\}. \quad (5.47)$$

The quantity $g_{i \rightarrow f}$ is not positive definite. We follow in this work the ad-hoc proposal of Tully [141] and set $g_{i \rightarrow f} = 0$ if $g_{i \rightarrow f} < 0$. During every time step, $g_{i \rightarrow f}$ is compared to a random number between 0 and 1 to decide if a jump occurs. Upon a jump the nuclear velocity vector is rescaled to preserve the total energy.

The coupled channel equations (eq. 5.44) and $g_{i \rightarrow f}$ are derived in the adiabatic picture. The TSH algorithm can, however, be easily transformed into the diabatic representation. The coupled channel equations become

$$i \frac{\partial}{\partial t} \tilde{c}_j(t) = \sum_i \tilde{E}_{ij}(\vec{R}(t)) c_j(t), \quad (5.48)$$

and the transition probability from the initial state i to the final state f reads

$$\tilde{g}_{i \rightarrow f} = \Delta t \cdot \frac{1}{a_i} \cdot 2\Im\{c_i^* c_f \tilde{E}_{if}\}. \quad (5.49)$$

Also the classical propagation of the nuclei (eq. 5.45) must then be performed on the diabatic PES $\tilde{E}_{jj}(\vec{R})$.

The classical treatment of the nuclei typically lowers the computational effort to

solve the TDSE. Despite this classical approach the TSH algorithm is capable of approximately accounting for Stückelberg oscillations, i.e., the interference between different paths. This is achieved by the integration of amplitudes $c_i(t)$ of the electronic channels in eq. 5.44. The main approximation entering the coupled channel equations is the use of the classical, local velocity $\vec{R}(t)$ determined by a single PES at a given instance in time. Due to this fact the coherence between different states is only approximate. This effect is discussed in, e.g., [144] and so-called decoherence corrections are available. Quantum effects which are not accounted for by the TSH algorithm are the treatment of the zero-point energy and tunneling.

For the $\text{Si}^{3+} + \text{He}$ charge transfer probability the TSH approach yields quite similar results as the Landau–Zener approximation (fig. 5.9) and the full quantum solution (fig. 5.11). The onset of the charge transfer, the Massey maximum as well as the decrease at higher momenta are essentially equal. Only the phase and the frequency of the Stückelberg oscillations deviates from the Landau–Zener and the full-quantum result. Also the low-frequency oscillation at $P_{\text{init}} \approx 80$ a.u. is absent in the TSH. At higher momenta the frequency of the TSH–Stückelberg oscillations seem to approach the ones of the other results when the initial kinetic energy ($P_{\text{init}}^2/2\mu$) of the trajectories exceeds the potential-energy difference of the PES in the phase difference integral

$$\Delta\phi_{12} = 2 \left(\int_{R_c}^{R_{t1}} p_1(R) dR - \int_{R_c}^{R_{t2}} p_2(R) dR \right), \quad (5.50)$$

with

$$p_i(R) = \sqrt{P_{\text{init}}^2 - 2\mu\Sigma_i(R)}. \quad (5.51)$$

5.4.3. Wave-packet propagation

For a full quantum-mechanical solution of the TDSE the time-dependent expansion coefficients $\chi_i(R, t)$ in eq. 5.25 are interpreted as the nuclear wave functions and are propagated on several, coupled potential-energy surfaces. The charge-transfer probability in the $\text{Si}^{3+} + \text{He}$ scattering is then determined as schematically depicted in fig. 5.10. Initially, at $t = t_0$ a normalized Gaussian wave packet $\chi_2(R, t_0)$ is placed at $R = 12$ on the PES of Σ_2 with an initial central momentum P_{init} pointing towards the origin. The form of the initial wave packet does not influence the average neutralization probability. Its width in momentum space, however, determines the resolution of the Stückelberg oscillations. During the scattering process the wave packet splits and probability density is transferred to $\chi_1(R)$, the wave packet on the PES of Σ_1 . When both wave packets are rescattered and leave the interaction region

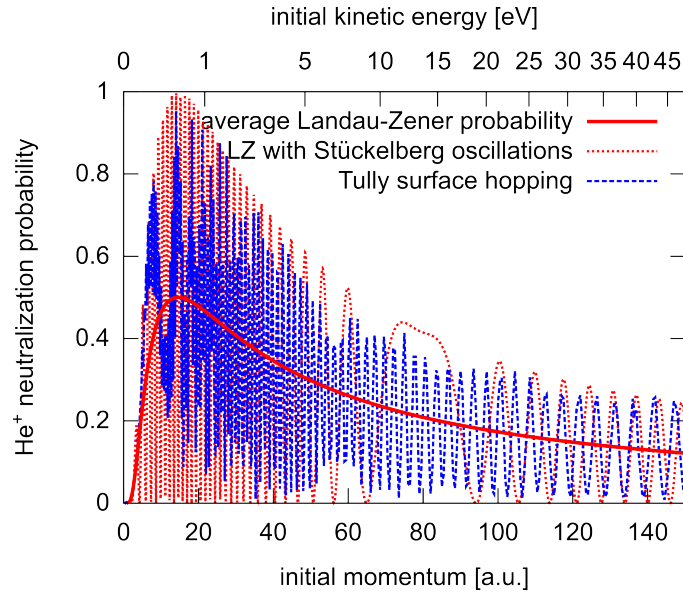


Figure 5.9.: Landau–Zener–Stückelberg approximation (solid and dotted-red line) and Tully surface-hopping charge transfer probability (dashed-blue) for a head-on collision of Si^{3+} and He as a function of initial relative momentum and kinetic energy in the center of mass frame.

at $t = t_\infty$ the charge-transfer probability is determined by $\int_0^\infty |\chi_1(R, t_\infty)|^2 dR$. The integration of the TDSE is done within the diabatic representation using the so-called split-operator method. The propagator is approximated by

$$e^{-iH\Delta t} \approx e^{-i\hat{T}/2\Delta t} \cdot e^{-i\hat{E}\Delta t} \cdot e^{-i\hat{T}/2\Delta t}, \quad (5.52)$$

with an error of the order of $\mathcal{O}(\Delta t^3)$. The three evolution steps in eq. 5.52 are successively applied to the nuclear wave packets with Fourier transforms in between to switch from real space to momentum space and vice versa.

The full quantum solution for charge transfer probability of the $\text{Si}^{3+} + \text{He}$ scattering almost perfectly matches the Landau–Zener results (fig. 5.11 (a)). Not only the overall behavior is equal but also the phase and frequency of the Stückelberg oscillations at higher momenta agree. This is quite remarkable and shows the accuracy of the Landau–Zener approximation. For small momenta, however, the Stückelberg oscillations vanish due to averaging. The initial width of the wave packet in momentum space ΔP_{init} is chosen to be constant independent of the initial momentum P_{init} . This leads to a large relative width $\Delta P_{\text{init}}/P_{\text{init}}$ for small momenta and, therefore, to a “smearing” of the Stückelberg oscillations. Better resolution at low momenta can be reached by refining ΔP_{init} with decreasing P_{init} . This leads, however, to large widths of the wave packet in real space and, therefore,

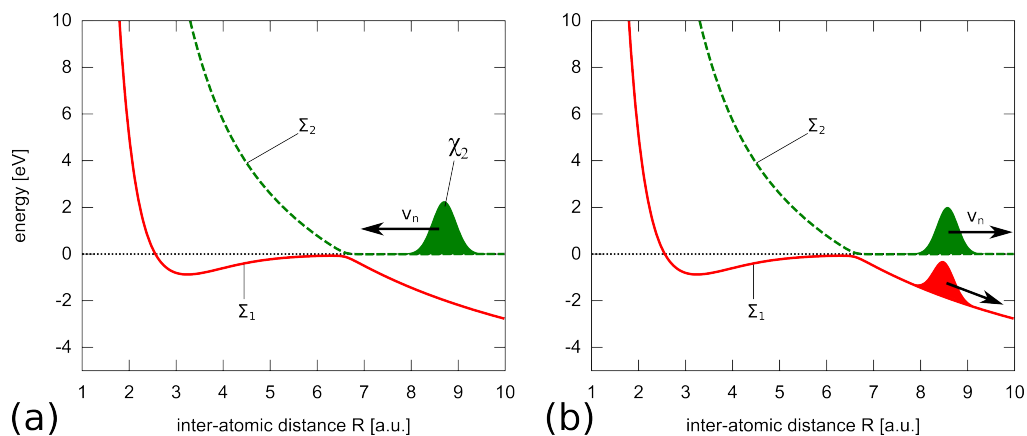


Figure 5.10.: Schematic illustration of the wave packet propagation on two coupled potential energy surfaces. (a) A normalized wave packet χ_2 is initialized at $t = t_0$ on the PES of Σ_2 with a momentum pointing towards the origin. (b) After rescattering and the double passage of the avoided crossing at $t = t_\infty$ the wave packet has split and probability density has been transferred to χ_1 on the PES of Σ_1 . The charge transfer probability is then given by $\int_0^\infty |\chi_1(R, t_\infty)|^2 dR$.

to large calculation boxes and considerably longer computing times.

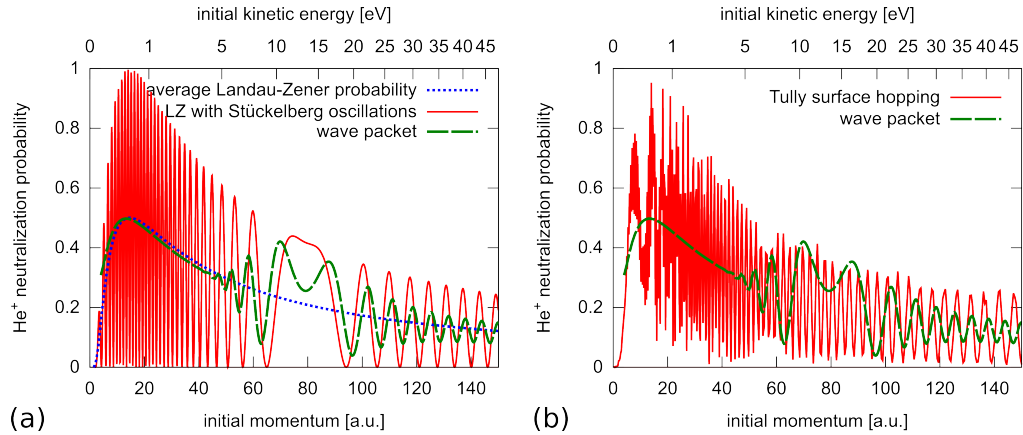


Figure 5.11.: Full-quantum solution of the charge transfer probability in a head-on collision of Si^{3+} and He as a function of initial relative momentum and kinetic energy in the center of mass frame compared to (a) results of the Landau–Zener–Stückelberg approximation and (b) to results of the Tully surface-hopping algorithm.

5.5. $\text{Si}^{3+} + \text{He}$ charge-transfer cross section

In this section we compare the total charge-transfer cross section σ_{tot} for the $\text{Si}^{3+} + \text{He}$ scattering from our time-domain calculations with experimental data as well as other theoretical works using different approaches to solve the scattering problem. Rabli et al. [124] used a one-electron model Hamiltonian to determine the PES of Σ_1 and Σ_2 as well as the non-adiabatic coupling between them. Stancil et al. [123] calculated ab-initio CASSCF wave functions and included in total five electronic states in their dynamics calculation. The three additional states correspond, for large inter nuclear distances, to excitations of the $\text{Si}^{3+}/\text{Si}^{2+}$ ion. In both works σ_{tot} is determined by using a partial wave expansion of the nuclear wave function and subsequent solution of the stationary coupled radial equations [145] from which the scattering matrix and the cross section can be derived. For a spherical symmetric scattering potential this is, indeed, a very effective way of solving the inelastic scattering problem. As soon as this symmetry is broken, as, for example, in the scattering of a projectile from a crystal surface, many partial waves couple with each other making this approach inefficient.

The total cross section of Rabli et al. and Stancil et al. (fig. 5.12 (a)) show equivalent shapes as a function of the collision energy E_{col} . In the low-energy limit σ_{tot} features the orbiting singularity since even for zero velocity the two particles approach each other due to the polarization of the He atom by the Si^{3+} ion leading to the orbiting singularity. The He atom cannot escape the Si^{3+} ion and the system runs through the avoided crossing infinitely many times. This leads to a probability of 1 for charge

transfer independent of the initial position, i.e., impact parameter and, therefore, to a diverging cross section. In the high energy limit the system is in the diabatic regime. The non-adiabatic coupling is so effective, that the dynamics is governed by a single, diabatic PES suppressing charge transfer and leading to a vanishing cross section. The maximum at intermediate energies lies near the Massey maximum (see, e.g., fig. 5.4). Although there are some deviations between the data of Rabli and Stancil they do, in general, agree well. The discrepancies between the two theoretical cross sections are not due to the influence of higher excited states in the calculation of Stancil but must be due to differences in the PES and the couplings used. An analysis of partial, state-specific cross sections by Stancil [123] shows that states with an excited Si ion contribute less than 0.6% to the total cross section in the energy range shown. We also perform calculations with two and five states leading to almost the same result. Interestingly, the experimental data seem to split into two groups. The two data points for the lowest collision energy lie almost exactly on the cross section of Rabli while the other points almost perfectly agree with the cross section of Stancil. This match, however, is fortuitous since both curves lie well within the experimental error bars and, as discussed above, can not be explained by the opening of additional channels.

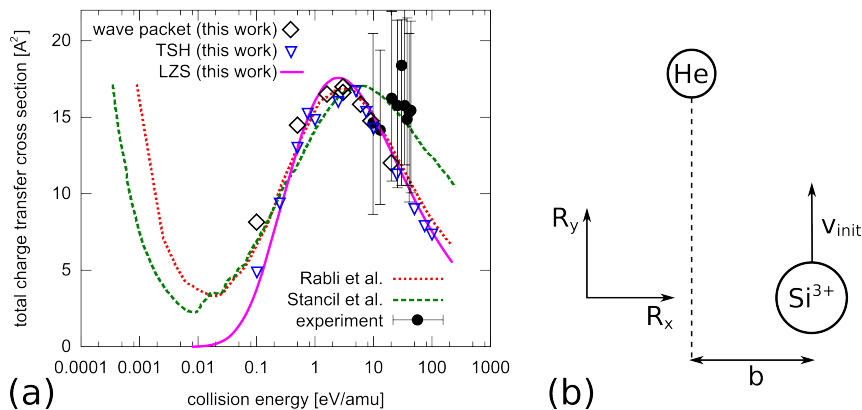


Figure 5.12.: (a) Total charge transfer cross section for the reaction $\text{Si}^{3+} + \text{He} \rightarrow \text{Si}^{2+} + \text{He}^+$ calculated with nuclear-wave packet propagation, Tully surface hopping (TSH), and the Landau–Zener–Stückelberg (LZS) approximation. The collision energy is given in the center-of-mass frame. Black dots are experimental data [125] and lines are partial-wave calculations by Stancil et al. [123] and Rabli et al. [124]. (b) Sketch of the initial scattering geometry in the lab frame with the impact parameter b .

We calculate σ_{tot} using the Landau–Zener approximation, Tully’s surface hopping

approach, and wave packet propagation. The total cross section is given by [146]

$$\sigma_{\text{tot}}(E_{\text{col}}) = 2\pi \int_0^{\infty} b f(b, E_{\text{col}}) db, \quad (5.53)$$

where $f(b, E_{\text{col}})$ is the charge transfer probability for a given impact parameter b (fig. 5.12 (b)) and a given collision energy. The Landau–Zener solution is determined “semi-analytically”: for simplicity, we approximate the trajectories of Si^{3+} (fig. 5.12 (b)) by straight lines with constant velocities which leads to an analytic expression of the integral in eq. 5.53 (see appendix A.5). We calculate σ_{tot} by solving this integral numerically for several collision energies. The “straight-line approximation” is not suitable for describing the low energy part of the cross section since orbiting is neglected. For collision energies above 0.1 eV/amu there is, however, good agreement of the LZS approximation with other methods (fig. 5.12 (a)). This shows what a powerful tool the LZS approximation is since the application of Tully-surface hopping and wave packet propagation is much more involved: in order to calculate $f(b, E_{\text{col}})$ we apply a two-dimensional (R_x, R_y) version of Tully’s surface hopping approach and the wave packet propagation with radial symmetric PES and non-adiabatic coupling vector (figs. 5.2). For every value of E_{col} we calculate $f(b, E_{\text{col}})$ on a grid of b values with a spacing of $\Delta b = 0.0625$ a.u. For each set of initial conditions we start 2000 trajectories in the Tully surface hopping approach and one wave packet for a full quantum solution.

Results of all methods agree rather well with the data of Rabli (fig. 5.12 (a)), are essentially independent of the number of electronic states included, and lie within the error bars of experiment. This confirms the accuracy of all time domain solutions presented in this chapter and justifies their application to charge-transfer. We do not calculate data for low initial momenta since the impact-parameter method (fig. 5.12 (b)) as well as the time-domain approach are not suitable in this energy range. One would have to include infinitely large impact parameters and propagate an infinitely long time to describe the diverging part of the total-cross section for $E_{\text{col}} \rightarrow 0$.

6. Charge transfer between a proton and a lithium-fluoride surface

Non-adiabatic effects play an important role in particle-surface interaction, for example, in chemical reactions at surfaces (see, e.g., [147]). The theoretical description of non-adiabatic effects in this context is, however, difficult due to the large number of coupled nuclear and electronic degrees of freedom involved. There are several advanced studies based on ab-initio potential energy surface that account for excited states in an approximate fashion (see, e.g., [147] and references in there). For metal surfaces the effect of excited electronic states is often included as a friction term for the nuclear motion [148–151]. In photodesorption of molecules from insulating surfaces [28, 30, 152] the nuclear wave packet is propagated on excited states for an average lifetime τ that is used as a fit parameter to match experimental data. In this chapter we present a study on particle-surface interaction that incorporates the non-adiabatic coupling on an ab-initio level. To this end we focus on the prototypical non-adiabatic effect of charge transfer in ion-surface collisions.

Resonant charge transfer and Auger-type processes (fig. 6.1) are the two basic mechanisms for charge transfer. The former refers to the transition of a single electron between the continuous band of a solid and a discrete level of the projectile which are close in energy (fig. 6.1 (a)). In Auger processes the charge-transfer levels are out of resonance and energy conservation is enforced by the accompanied by the energy transfer to an additional surface electron. In the Auger neutralization of a singly charged projectile in front of a metal surface (fig. 6.1 (b)) an electron is transferred to a deep projectile level accompanied by the ejection of a conduction band electron.

Charge transfer processes were understood first for metal surfaces [153–155] and there is a large amount of literature on experimental and theoretical studies on various combinations of projectiles and surfaces. Extensive lists of literature can be found in [156, 157]. Initially, charge transfer was described using jellium-type models of the surface which facilitated calculations by conserving, together with the projectile, cylindrical symmetry (see, e.g., [155, 158–162]). Neglect of the atomistic surface structure, however, lead to failures of the jellium models [163, 164] and called for more accurate DFT and TD-DFT approaches (see, e.g., [165–168]).

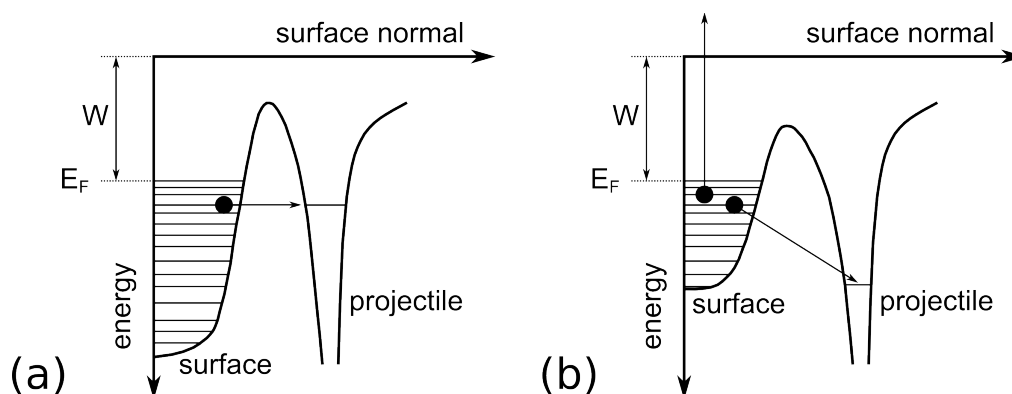


Figure 6.1.: Schematic of two basic charge transfer mechanisms: (a) resonant and (b) Auger-type charge transfer between a surface and a projectile. E_F denotes the Fermi energy and W is the work function.

While these methods are mainly applied to resonant charge transfer, also for Auger processes models beyond the jellium approximation are available [157].

Studies of charge transfer near insulating surfaces are much more scarce (see, e.g., [156, 169, 170]) probably due to the fact that, initially, the charge transfer from insulators was thought to be rather inefficient due to the tightly bound valence electrons, narrow band widths, and large work functions. This was proven wrong, however, when in grazing scattering experiments by Winter and co-workers [13, 14] charge transfer probabilities of close to unity were observed for O and F atoms scattered off alkali-halide surfaces. This finding triggered many theoretical studies most of which involve the embedded cluster approach based on the notion of the valence electron being tightly bound to the anions in alkali-halide crystals and, therefore, the charge transfer being a very local process involving the projectile and a single surface anion only.

Souda et al. [171, 172] studied neutralization and negative ion conversion of H^+ , H, and He projectiles scattered from LiF and LiCl. They investigated HF single-particle energy level diagrams of molecular orbitals in embedded clusters containing up to 9 anions. Goldberg et al. [173, 174] investigated the negative-ion conversion of H^+ during large-angle scattering at a LiF surface in the framework of the time-dependent Anderson Hamiltonian. Parameters for this model Hamiltonian were deduced from HF calculations of small embedded clusters. Zeijlmans van Emmichoven et al. [175] studied the negative-ion conversion and subsequent electron emission during grazing-incidence scattering of protons at an LiF surface. They investigated energy-level diagrams of molecular orbitals of the $H + F^-$ system in a crystalline environment from which they constructed diabatic and adiabatic potential-energy surfaces. Borisov et al. performed HF calculations for the negative-ion conversion of F^0 during grazing incidence on LiF and MgO surfaces. They used small embed-

ded surface clusters with one [14, 176] and two [177, 178] negative ions as electron donor and constructed diabatic PESs and coupling-matrix elements from calculations of atomic-like states. Also Darling et al. [179, 180] studied the negative ion conversion of F^0 scattered off LiF and KI under a grazing angle of incidence. They constructed PESs using a semi-empirical valence bond method developed for gas-phase studies of alkali-metals scattered off halides. The charge transfer dynamics was determined in a two-dimensional nuclear wave packet propagation. Wirtz et al. [16, 181, 182] were the first ones to conduct a detailed study of ab-initio PESs of various projectiles in front of embedded LiF surface clusters of various sizes. They applied high-level quantum chemistry methods to investigate the level ordering, i.e., the relative position of valence band and projectile level involved in the charge transfer.

We first present in this chapter an extension of the work of Wirtz et al. in terms of the accuracy of quantum-chemistry methods and active cluster sizes. Most importantly, we perform full quantum as well as semi-classical charge transfer dynamics simulations of projectiles rescattered from the embedded surface clusters. This provides a fully ab-initio treatment of the charge transfer process which is, to our knowledge, missing so far. We focus on the (100) surface of LiF since it is the experimentally most studied insulating material, and, LiF is the alkali-halide with the smallest possible ionic constituents. It allows for larger cluster sizes than other insulating crystals. Further, we focus on resonant charge transfer rendering the proton H^+ the optimal projectile since its $H(1s)$ capture level lies approximately in the center of the LiF valence band.

The chapter is organized as follows. In sec. 6.1 we discuss the electronic structure of the combined system $LiF + H^+$, the effect of applying the embedded cluster approach to particle surface scattering, and give details on quantum-chemistry calculations. The work function of the LiF clusters is a crucial figure of merit for the reliability of the embedded cluster calculations since it determines the position of the LiF valence band and, therefore, shows if the resonance condition between valence band and capture level is met. We investigate the work function of various embedded clusters in sec. 6.2 and test its dependence on parameters such as cluster and basis set size. In sec. 6.3 we perform one- and three-dimensional charge-transfer dynamics simulations of a proton rescattered from an embedded Li_5F_1 surface cluster and study the characteristics of the PESs involved in the charge transfer. This study is extended to larger clusters containing up to 14 F^- ions in up to three surface layers in sections 6.4 and 6.5 where we also compare our results on the charge transfer with preliminary experimental data.

6.1. Setting up the calculation: electronic structure of $\text{LiF} + \text{H}^+$ and the embedded cluster approach

The valence band, formed by the F(2p) orbitals, and the conduction band, formed by the Li(2s) orbitals, of pristine LiF are schematically depicted in fig. 6.2 (a). The top of the valence band lies approximately 12 eV below the vacuum level [183] corresponding to a work function, W_{LiF} , of 12 eV. The width of the valence band is approximately 3.5 eV [184]. LiF has a band gap of 14.2 eV [43] rendering the bottom of the conduction band to lie at about 2.2 eV above vacuum. The electronic ground state H(1s) level of the projectile (fig. 6.2 (b)) is located at an energy of -13.6 eV approximately in the center of the LiF valence band. Upon motion of the H^+ ion towards the surface quasi-resonant electron transfer from the valence band to the H(1s) capture level is likely to occur. We term the process quasi-resonant because the H(1s) level is subject to an upward level shift upon approaching the surface due to the image charge interaction [171]. This shift dynamically changes the relative position of the H(1s) and the valence band levels as a function of the distance between projectile and surface.

In this work we exclusively treat the electron transfer from the valence band to the H(1s) level. Only these states are included in the CAS of our calculations. We neglect the influence of the conduction band and the H(2s) level which are energetically well separated from the valence band by more than 10 eV. This is only approximately valid because the kinetic energies of the H^+ projectile used in our simulations are larger than 10 eV and make the conduction band and the H(2s) level in principle accessible. In view of the weaker coupling due to this energy gap, they are neglected. Furthermore, due to the quickly increasing sizes of the complete-active spaces we are limited to very small cluster sizes when including these higher lying energy levels and neglect them also for computational reasons. In the outlook (chap. 7) we briefly discuss effects such as the electronic stopping power of ions and atoms in LiF as well as Auger neutralization processes where excitations to these levels are explicitly needed.

Employing the embedded-cluster approach (ECA) implies the approximation of the continuous valence band in LiF by a discrete set of F(2p) levels (to be more precise, molecular orbitals formed by linear combinations of F(2p) orbitals). Their number equals three times the number of F^- ions in the embedded cluster. This discretization is schematically depicted in fig. 6.3 (a) for large distances between surface and projectile. The H(1s) level is separated from the top of the valence band by approximately $W_{\text{H}} - W_{\text{LiF}} = 1.6$ eV, the difference in energy between the H(1s) binding energy and the LiF work function. Converting this single-particle picture into a total-energy picture yields fig. 6.3 (b). In the initial state of our system, the H^+ ion approaching the LiF surface, the valence band levels are fully occupied

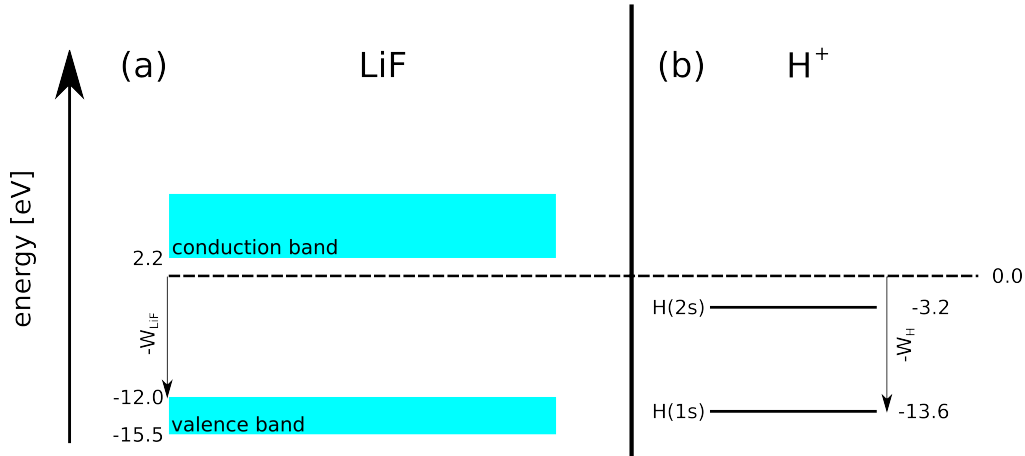


Figure 6.2.: Schematic picture of the electronic structure of (a) bulk lithium fluoride and (b) an isolated H^+ ion. $W_{\text{LiF}} \approx 12$ eV is the work function of bulk LiF, the minimum energy needed to remove an electron from an LiF crystal. $W_H = 13.6$ eV is the (negative) energy of the H(1s) level which lies approximately in the center of the LiF valence band.

while the H(1s) level is empty. This configuration, however, is not the electronic ground state E_1 of the combined system, i.e., it does not correspond to the lowest eigenvalue of the electronic Hamiltonian of the embedded cluster. The ground state is realized by the configuration in which the the H(1s) level is occupied by one electron, taken out of the topmost level of the valence band. Likewise one can think of a hole transferred from H(1s) to the topmost valence-band level. Pushing the hole downwards in energy in panel (a) successively leads to the higher excited states and allows for building up the energy spectrum of total energies E_j in panel (b).

In doing so we can deduce the following rules for the number and the configurations of the electronic states entering in our calculations. When the valence band is discretized by N F(2p) levels then the number of electronic states to be taken into account is $N+1$. For large distances between projectile and surface, N of these states correspond to the configuration $(\text{LiF})^+ + \text{H}$, denoted as (asymptotic) covalent states in the following, and one corresponds to the configuration $\text{LiF} + \text{H}^+$ (E_4 in fig. 6.3 (b)), denoted in the following as the (asymptotic) ionic state. The latter serves as initial state in our dynamics calculations. Furthermore, if the embedded cluster is large enough to reasonably sample the valence band of LiF then the energy difference $\Delta E_{\text{g-ion}}$ between the ionic state and the electronic ground state E_1 (fig. 6.3 (b)) is approximately 1.6 eV, again for a large distance between projectile and surface. This statement can be reformulated in terms of the work function. Since $W_H - W_{\text{LiF}} = 1.6$ eV and W_H is independent of the cluster size W_{LiF} is the only

quantity determining the energy difference between the $\text{LiF}+\text{H}^+$ state and E_1 . In the following section we study the convergence of W_{LiF} with cluster size.

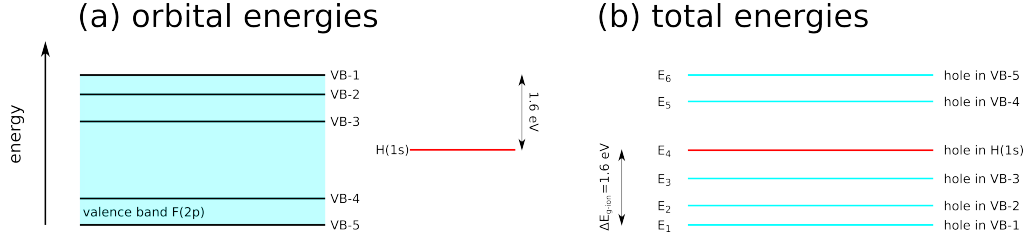


Figure 6.3.: Schematic picture of (a) the discretization of the LiF valence band (blue shaded area) by single particle F(2p) levels when applying the embedded cluster approach and (b) total energy spectrum of the embedded $\text{LiF} + \text{H}^+$ cluster. The electronic ground state of the cluster at large distances between LiF surface and projectile corresponds to the configuration $(\text{LiF})^+ + \text{H}$ in which the H(1s) level is occupied by an electron taken out from the single particle level denoted by VB-1 localized at the LiF surface. Pushing the hole further down in the single particle picture (a) gives rise to the total energy spectrum in (b). If the embedded cluster is large enough to reliably sample the (top of the) LiF valence band the total energy difference ΔE_{g-ion} between electronic ground and the ionic ($\text{LiF} + \text{H}^+$) state equals $W_{\text{H}} - W_{\text{LiF}} = 1.6$ eV.

6.2. Convergence of the electronic structure of embedded LiF clusters

Crucial for an accurate description of the charge transfer is the relative position in energy of valence band and the H(1s) level. Since the H(1s) level is independent of the LiF-cluster size and correctly reproduced on the independent-particle level we focus in this section on the valence band and investigate in detail the dependence of its properties on cluster size, quantum-chemical method, basis-set size, embedding, and symmetry. The valence band is determined by two parameters: its width and the work function W_{LiF} (fig. 6.2). In photo-emission experiments [183] the work function of evaporated LiF films is found to be $W_{\text{LiF}} = 11.8 \pm 0.3$ eV and the experimental band width [184] is ≈ 3.5 eV.

Wirtz and co-workers used embedded clusters completely surrounded by point charges to model the bulk electronic structure. The band width was estimated [16, 182] as the difference between the HF-orbital energies of the highest occupied (HO) and the lowest occupied (LO) F(2p) orbital of the active embedded cluster, $\epsilon_{\text{HO[F(2p)]}} - \epsilon_{\text{LO[F(2p)]}}$, (fig. 6.4 (a)). The band width increases with cluster size and

extrapolation to an infinite number of active F^- ions leads to $\epsilon_{\text{HO}[F(2p)]} - \epsilon_{\text{LO}[F(2p)]} \approx 3.46$ eV in good agreement with experiment (fig. 6.4 (b)). For a number of ~ 15 active F^- ions, approximately the cluster size we use in the following section for the calculation of the charge transfer, the band width is of the order of 2 eV which is considerably smaller than in experiment but large enough such that the H(1s) level lies within the valence band (fig. 6.3).

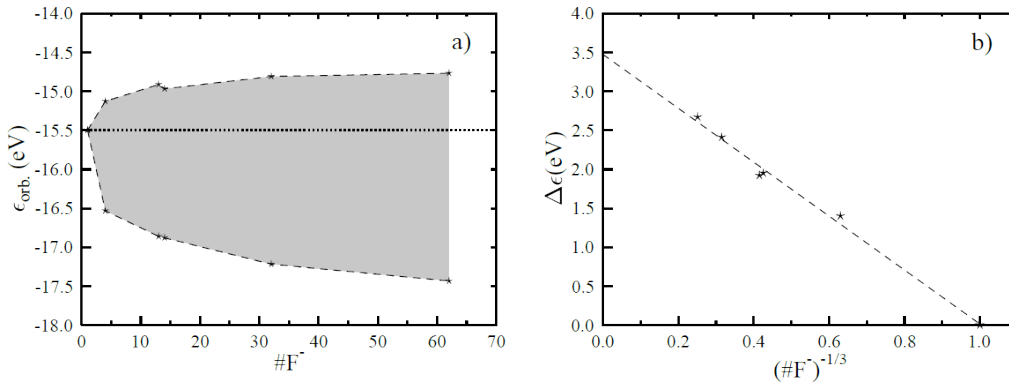


Figure 6.4.: Picture taken from [181]. (a) Hartree–Fock single particle energies of the highest and lowest (occupied) F(2p) like orbitals in embedded clusters of various sizes. The x-axis denotes the number of active F^- ions. Active clusters are completely surrounded by point charges to approximate the Madelung potential in bulk LiF. (b) “Valence band width” of embedded clusters extrapolated to infinite cluster size. The width is approximated by the energy difference between highest and lowest (occupied) F(2p) like orbitals.

Wirtz and co-workers also studied W_{LiF} and its dependence on several parameters entering the quantum-chemical calculation. Due to the lack of computing power they were, however, restricted in the choice of the quantum-chemistry methods and limited to small basis sets and cluster sizes. We extend this previous study to larger basis sets and clusters and, most importantly, to more accurate quantum-chemistry methods. We determine W_{LiF} for the (100) surface of LiF that we also use in the calculation of the charge transfer. We split the study into two parts, the first part (sec. 6.2.1) discusses the change of W_{LiF} with cluster size and the quantum-chemistry method used. In the second part (sec. 6.2.2), we investigate the dependence of W_{LiF} on basis set size, embedding, cluster shape and symmetry.

6.2.1. Dependence of W_{LiF} on quantum-chemistry method and cluster size

Throughout this section we use the basis set consisting of the DZ basis [185] for the Li^+ ions and the cc-pVTZ basis [61] for the F^- ions. The latter is a quite large basis set leading typically to reliable results (see chaps. 3 and 4) while the DZ basis set for the lithiums is rather small. It is chosen as a compromise as larger basis sets limit the feasible cluster size. Further the influence of the basis set on the lithiums on W_{LiF} is smaller than the one of the F^- basis since only the core orbitals of Li^+ are occupied which only weakly contribute to the screening of the hole. We use clusters with various sizes and shapes (fig. 6.5) comprising clusters with active F^- ions only in the first layer of the surface (fig. 6.5 (a)) up to clusters with active F^- ions in the first three layers (fig. 6.5 (c)). The notation in following is $\text{Li}_A\text{F}_B\text{-F}_C\text{-F}_D$, where A denotes the number of active Li^+ ions and B, C, and D denote the number of active F^- ions in the first (B), second (C), and third (D) surface layer, respectively. All clusters are constructed such that all active F^- ions are surrounded by active Li^+ ions and not by an embedding point charge to avoid artificial polarization due to the lack of the Pauli repulsion. All clusters are embedded in a matrix of point charges large enough to converge W_{LiF} to an accuracy of better than 0.01 eV. Further, all clusters have a four-fold rotation symmetry (C_{4v}) around the symmetry axis (the surface normal) going through the central F^- ion of the topmost surface layer. Since MOLCAS, however, does not support the C_{4v} point-group symmetry all calculations are done within C_{2v} .

The simplest estimate for W_{LiF} are the HF single-particle energies of the HOMO, ϵ_{HOMO} , of the embedded clusters since they can be associated with the ionization potential via Koopmans' theorem. We find quite similar results as Wirtz (fig. 6.4 (a)). ϵ_{HOMO} varies only slightly with cluster size from, e.g., $\epsilon_{\text{HOMO}}(\text{Li}_{17}\text{F}_5) = -14.53$ eV to $\epsilon_{\text{HOMO}}(\text{Li}_{65}\text{F}_{21}\text{-F}_{12}) = -14.35$ eV. Koopmans' theorem neglects the relaxation of orbitals due to the missing electron, i.e., polarization effects. Performing two separate calculations for the neutral (LiF) and the singly charged surface $(\text{LiF})^+$ allows for inclusion of polarization. The difference of the total energies of the two surface configurations is then the work function $W_{\text{LiF}}^{\text{HF}} = E^{\text{HF}}(\text{LiF}) - E^{\text{HF}}(\text{LiF}^+)$. Unfortunately, there is some arbitrariness in the calculation of $E^{\text{HF}}(\text{LiF})^+$ due to a numerical difficulty: the shape of the hole orbital strongly and somewhat randomly depends on the shape of the active cluster. For strongly localized hole orbitals the polarization reduces the work function by ~ 3 eV while for more weakly localized hole orbitals the polarization contributions are below 0.5 eV (fig. 6.6). Parenthetically we note that this is independent from whether an ROHF or an UHF calculation is performed.

Equivalent to the ROHF calculation is the MCSCF method in its "standard setup". The latter refers to a total-energy difference between the (LiF) and the $(\text{LiF})^+$ configuration for both of which the CAS comprises all F(2p) orbitals of the A_1 ir-

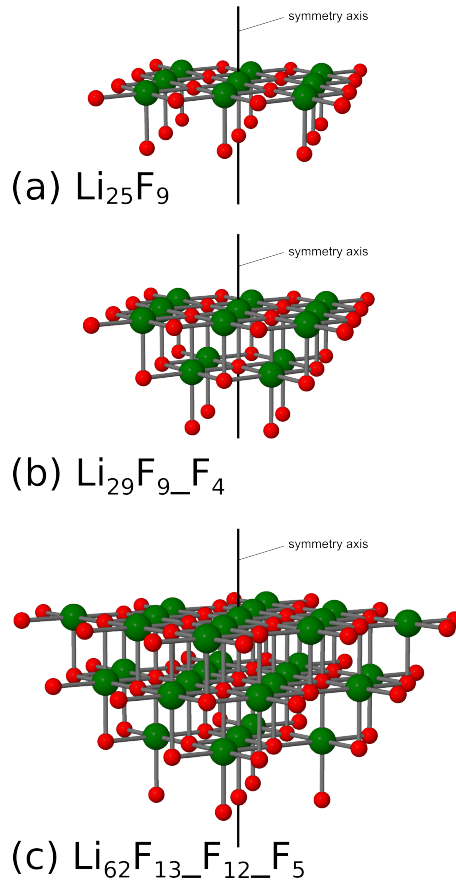


Figure 6.5.: Active clusters with (a) 9 active F^- ions (large-green spheres) in the top-most surface layer (b) 9 active F^- ions in the first and four in the second layer, and (c) 13 active F^- ions in the first, 12 in the second and 5 in the third surface layers. Lithium ions are depicted by small-red spheres. The black vertical line denotes the four-fold rotation symmetry axis.

reducible representation. In the neutral configuration all $\text{F}(2p)$ orbitals are doubly occupied rendering the MCSCF an effective closed-shell HF calculation. For the $(\text{LiF})^+$ configuration there is a single hole in the CAS allowing only for singly excited determinants in the expansion of the many-electron wave function. According to Brillouin's theorem [32], singly excited determinants do not improve the total energy of the initial ROHF wave function. Optimizing the ground state energy (no state average is performed) renders this approach an effective ROHF calculation. Resulting work functions (fig. 6.6 (a)), show strong dependence on the shape of the hole orbital governed by the cluster size and shape. As function of the number of active F^- orbitals the MCSCF work function $W_{\text{LiF}}^{\text{MCSCF}}$ strongly oscillates between values of 11.5 eV and 14.25 eV.

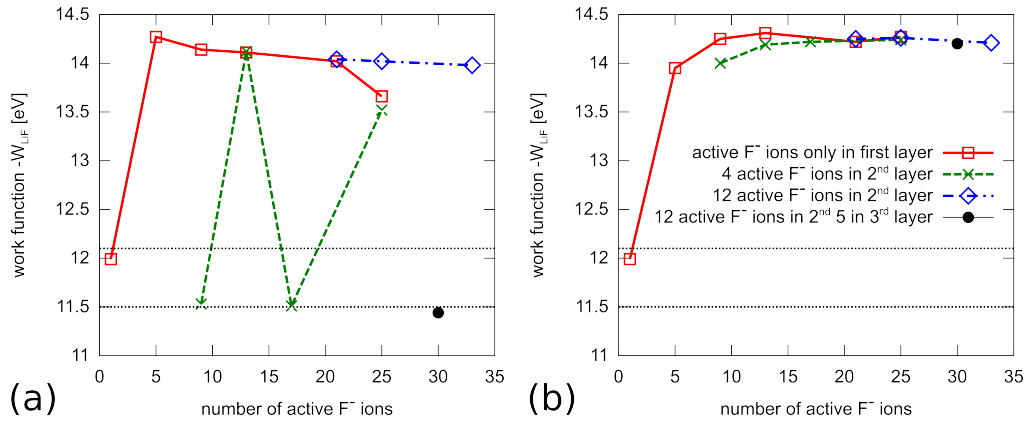


Figure 6.6.: MCSCF work functions of embedded clusters as function of cluster size and arrangement of the active F^- ions (a) without performing a state average (equivalent to ROHF work functions) and (b) with a state average comprising all possible states in the CAS. Dashed horizontal lines denote the range for the experimental LiF work function [183].

These oscillations vanish (fig. 6.6 (b)) when in the calculation of the total energy of the singly charged active cluster, $E^{\text{MCSCF-avg}}(\text{LiF}^+)$, a state average is performed that includes all possible excited states in the CAS. For N orbitals in the CAS, there are N possible electronic states the energetically lowest of which is $E^{\text{MCSCF-avg}}(\text{LiF}^+)$. Performing a state average might seem counterintuitive since calculation of the work function typically requires the optimal, i.e., energetically lowest many-electron wave function. However, for the $\text{LiF} + \text{H}^+$ charge transfer problem we need to determine excited states including a state average. Therefore, we also perform the state average in the calculation of W_{LiF} since we want both calculations (with and without H^+) to be compatible. In calculations with H^+ the work function is given by $13.6 \text{ eV} - \Delta E_{\text{g-ion}}$ (fig. 6.3 (b)). 13.6 eV is the energy of the $\text{H}(1\text{s})$ level. The MCSCF work function including the state average $W_{\text{LiF}}^{\text{MCSCF-avg}} = E^{\text{MCSCF-avg}}(\text{LiF}) - E^{\text{MCSCF-avg}}(\text{LiF}^+) = E^{\text{HF}}(\text{LiF}) - E^{\text{MCSCF-avg}}(\text{LiF}^+)$ (fig. 6.6 (b)) does not oscillate and it follows a quite clear trend as a function of the number of active F^- ions. After reaching a maximum of 14.31 eV , $W_{\text{LiF}}^{\text{MCSCF-avg}}$ very slowly decreases with increasing number of active F^- ions. This decrease is physically reasonable since larger clusters lead to a better screening of the hole and, therefore, to a reduction of $W_{\text{LiF}}^{\text{MCSCF-avg}}$. For the cluster sizes used, $W_{\text{LiF}}^{\text{MCSCF-avg}}$ is more than 2 eV higher than the experimental value and its slow decay with cluster size suggests that also for very large clusters $W_{\text{LiF}}^{\text{MCSCF-avg}}$ cannot be reached. This makes the MCSCF-avg unreliable for the $\text{LiF} + \text{H}^+$ charge transfer since it de-tunes the LiF-VB and the $\text{H}(1\text{s})$ level such that they are out of resonance by $\sim 0.7 \text{ eV}$.

Including dynamic correlation corrects for this shortcoming. CASPT2 reduces $W_{\text{LiF}}^{\text{MCSCF}}$ substantially (fig. 6.7) bringing it close to the experimental value. Since

CASPT2 is based on the MCSCF wave functions the oscillations in $W_{\text{LiF}}^{\text{MCSCF}}$ are also present in the CASPT2 work function $W_{\text{LiF}}^{\text{CASPT2}}$ (fig. 6.7 (a)). Their value ($12 \leq W_{\text{LiF}}^{\text{CASPT2}} \leq 13.5$), however, is smaller than in the MCSCF case. With the state averaged MCSCF wave functions we apply MS-CASPT2 and determine the work function $W_{\text{LiF}}^{\text{MS-CASPT2}}$ which again shows no oscillations (fig. 6.7 (b)). It decays monotonically with the number of active F^- ions and, for a large number of clusters, lies within the experimental error bars. Further, it hardly depends on the cluster shape since clusters with the same number of active F^- ions arranged in different ways give almost exactly the same MS-CASPT2 work function. The monotonic decay of $W_{\text{LiF}}^{\text{MS-CASPT2}}$ suggests that it is not yet converged. With increase of the number of active F^- ions, $W_{\text{LiF}}^{\text{MS-CASPT2}}$ drops further and seems to converge at a value below the experimental data range. We estimate $W_{\text{LiF}}^{\text{MS-CASPT2}}$ for an infinite number of active F^- ions to lie between 10.2 eV and 10.8 eV (appendix A.7). There are, however, mechanisms possibly explaining this behavior. First, it is well known that perturbation theory of second order, such as MP2, overestimates the effect of dynamic correlations [33] and that higher orders typically correct for this error. In terms of our problem the effect of dynamic correlation is a reduction of the work function by $W_{\text{LiF}}^{\text{MCSCF-avg}} - W_{\text{LiF}}^{\text{MS-CASPT2}} \approx 3$ eV. Therefore, higher order perturbation theory lead to higher values of $W_{\text{LiF}}^{\text{MS-CASPT2}}$ as Wirtz found [181] using MP3. Second, as we show in the following, basis sets, the embedding, cluster shape, and symmetry constraints also influence $W_{\text{LiF}}^{\text{MS-CASPT2}}$.

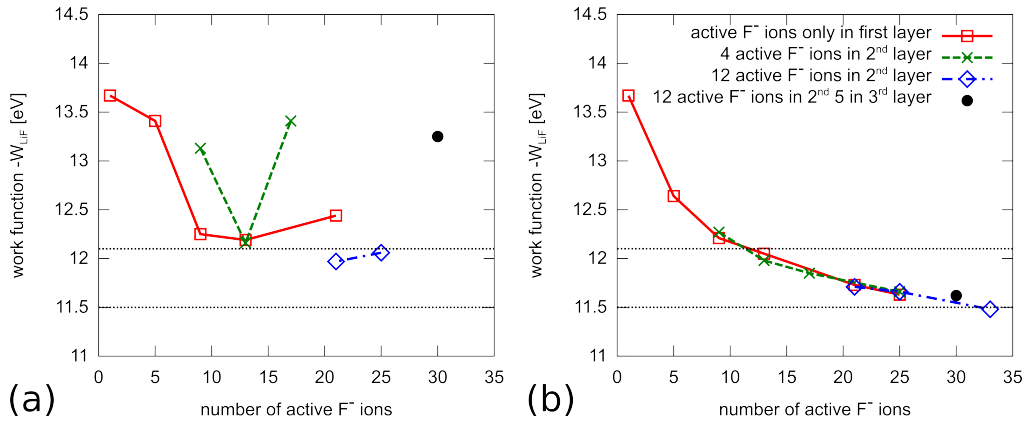


Figure 6.7.: MS-CASPT2 work functions of embedded clusters as function of cluster size and arrangement of the active F^- ions (a) without performing a state average in the preceding MCSCF and (b) with a state average in the MCSCF comprising all possible states in the CAS. Dashed-horizontal lines denote the range for the experimental LiF work function [183].

Completely converged calculations with respect to cluster size and correlation energy are computationally not feasible. The MS-CASPT2 protocol described above,

however, leads to cluster realizations of the system with $W_{\text{LiF}}^{\text{MS-CASPT2}}$ within the error bars of the experiment and with a realistic level ordering of the LiF valence band and the H(1s) level. Therefore we expect these clusters to give a realistic description of the $\text{LiF} + \text{H}^+$ charge transfer and we apply this protocol in section 6.4 to determine the PES of the combined system entering the dynamics calculations.

6.2.2. Dependence of $W_{\text{LiF}}^{\text{MS-CASPT2}}$ on basis-set size, embedding, cluster shape, and symmetry

For the sake of completeness we very briefly study the dependence of $W_{\text{LiF}}^{\text{MS-CASPT2}}$ on the parameters kept constant in the previous section: basis set size, embedding, cluster shape, and symmetry constraints. To this end we focus on the $\text{Li}_{29}\text{F}_9\text{-F}_4$ cluster (fig. 6.5 (b)) with $W_{\text{LiF}}^{\text{MS-CASPT2}} = 11.98$ eV obtained with pure point charge embedding and the basis sets DZ for the lithium ions and cc-pVTZ for the fluoride ions. Changing the Li basis set from DZ to cc-pVDZ shifts $W_{\text{LiF}}^{\text{MS-CASPT2}}$ upwards by 0.12 eV. Similarly, the larger cc-pVQZ (and, equally, the aug-cc-pVTZ) basis set for the F^- ions increase $W_{\text{LiF}}^{\text{MS-CASPT2}}$ by 0.15 eV. Surrounding the active cluster with two layers of AIMP (plus the point charge matrix) has the opposite effect lowering $W_{\text{LiF}}^{\text{MS-CASPT2}}$ by 0.25 eV.

As discussed above, $W_{\text{LiF}}^{\text{MS-CASPT2}}$ only depends on the number of active F^- ions not on their arrangement (fig. 6.7 (b)). All clusters used in the above study have an active F^- ion in the very center of the topmost surface layer. We check if the structure independence also holds for clusters hosting an Li^+ ion in the surface center by inverting the $\text{Li}_{29}\text{F}_9\text{-F}_4$ cluster, i.e., by exchanging Li^+ by F^- and vice versa. This swap, however, calls for slight rearrangement of the Li^+ ions since we still want to make sure that no F^- ion is located at the border of the active cluster leading to a $\text{Li}_{34}\text{F}_4\text{-F}_9$ cluster with $W_{\text{LiF}}^{\text{MS-CASPT2}} = 12.16$ eV (basis sets: Li: DZ; F: cc-pVTZ; embedding: point charges only) only 0.18 eV larger than the work function of the $\text{Li}_{29}\text{F}_9\text{-F}_4$ cluster.

All calculations described above used the C_{2v} symmetry and a CAS comprising only F(2p) orbitals of the A_1 irreducible representation. By lifting all symmetry constraints we can create a CAS using all F(2p) orbitals. Unfortunately, this leads to a strong increase of the number of active electrons which restricts this approach to quite small cluster sizes. Without any symmetry constraints we find for the Li_{17}F_5 cluster (basis sets: Li: DZ; F: cc-pVTZ; embedding: point charges only) $W_{\text{LiF}}^{\text{MS-CASPT2}} = 12.41$ eV which is 0.23 eV lower than the high-symmetry C_{2v} result.

6.3. The embedded Li_5F_1 cluster

Before studying the potential energy surfaces of large $\text{LiF} + \text{H}^+$ embedded clusters with a complex electronic structure we focus on the small $\text{Li}_5\text{F}_1 + \text{H}^+$ cluster

depicted in fig. 6.8 (a). It consists of five Li^+ ions surrounding a single F^- ion and the H^+ projectile at a distance of R_z above the LiF surface (the $R_x - R_y$ plane). The F^- ion features three $\text{F}(2p)$ orbitals giving rise, together with the $\text{H}(1s)$ orbital, to four electronic states (three covalent states and one ionic state) to enter the charge-exchange calculation. Despite this small number of states involved, their PES already show characteristic features also found for larger clusters. This fact supports the assumption that the charge transfer is a very local process. Studying these features in this simple system allows for better understanding of the main mechanisms involved in the charge transfer. In sec. 6.3.1 we specify details of the calculation of the electronic structure and analyze the PES of the $\text{Li}_5\text{F}_1 + \text{H}^+$ cluster. Details of the motion of the projectile and the calculation of the charge-transfer probability are discussed in sections 6.3.2 and 6.3.3.

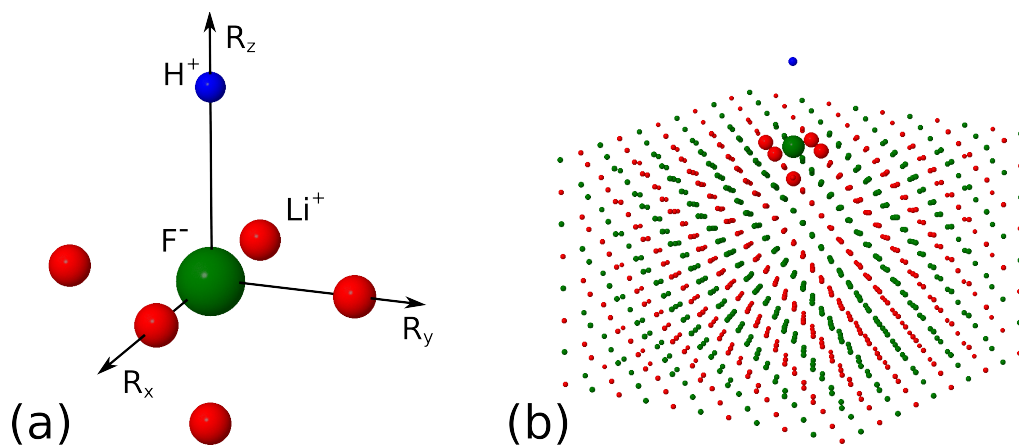


Figure 6.8.: $\text{Li}_5\text{F}_1 + \text{H}^+$ surface cluster (a) without and (b) with point-charge matrix.

6.3.1. Potential energy surfaces of Li_5F_1

Fig. 6.8 (b) shows the active Li_5F_1 cluster embedded into a matrix of 962 singly-charged positive and negative point charges. The projectile is placed at $R_z = 10.0$ a.u. above the surface. For both, active cluster and embedding matrix, the experimental anion-cation distance (3.81 a.u.) of pristine LiF is used. The point-charge matrix accounts for the Madelung potential within the active-cluster region with an accuracy better than 10^{-2} eV and enforces charge neutrality of the unperturbed surface.

The PESs of the active $\text{Li}_5\text{F}_1 + \text{H}^+$ cluster are determined by consecutive Hartree-Fock, CASSCF and MRCI-SD calculations using the DZ basis set. HF delivers the starting molecular orbitals for the CASSCF. The complete-active space comprises six valence electrons in four HF energy levels corresponding, for large R_z , to the three $\text{F}(2p)$ and the $\text{H}(1s)$ leading to 10 configurations in the CAS. With the

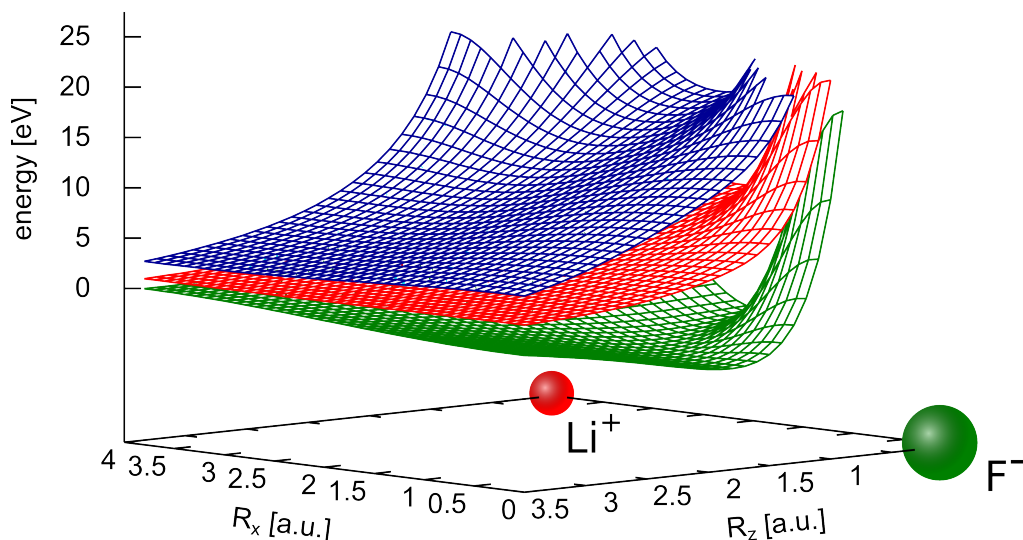


Figure 6.9.: MRCI-SD potential energy surfaces of the embedded $\text{Li}_5\text{F}_1 + \text{H}^+$ cluster as function of R_x and R_z (see fig. 6.8), Cartesian coordinates of the projectile nucleus parallel and perpendicular to the LiF surface, respectively.

CASSCF we produce a new set of orbitals emerging from a state-average calculation comprising the four energetically lowest total energies. Since HF as well as CASSCF lead to a wrong level ordering, both find the electronic ground state configuration $\text{LiF} + \text{H}^+$, we need to apply the MRCI-SD method. Parenthetically we note that MS-CASPT2 leads to almost equivalent results as MRCI-SD for this combination of basis set and cluster size. Using the CAS as reference space leads to a total of 8200 Slater determinants as basis for the total electronic wave functions. The MRCI-SD leads, for large R_z , to a $(\text{LiF})^+ + \text{H}$ ground state in agreement with the experimental electronic structure (sec. 6.1). Also the energy spacing between the ground state and the ionic state of 1.1 eV (fig. 6.10 (a)) is in fair agreement with the experimental value of 1.6 eV. We stress, however, that this agreement is fortuitous due to the choice of the relatively small basis set. The active cluster used cannot account for (long range) polarization effects giving rise to an incomplete screening of an electron hole in the surface. This, in return, leads to an overestimation of the work function and, therefore, a de-tuning of the valence band and the H(1s) level (see fig. 6.2). By using a small basis set we artificially decrease the work function to almost the experimental value leading to a correct level ordering and a reasonable energy spacing between ground and ionic state. This ad-hoc procedure is justified a posteriori by the fact that, with the basis set used, the small Li_5F_1 cluster already shows the key features of the charge transfer also seen in calculations using larger basis sets and clusters.

A further approximation used throughout this work is the frozen-surface approx-

imation. We do not include the motion of the surface atoms but only consider the movement of the projectile along its three Cartesian coordinates \vec{R} . Fig. 6.9 shows a two-dimensional cut through the three-dimensional adiabatic PESs of three electronic states along R_z . In fact we calculate four electronic states, for better visibility, however, only three of them are plotted. A one-dimensional cut along R_z is plotted in fig. 6.10, with $R_x = R_y = 0$, the projectile located at a high-symmetry point exactly above the active F^- ion. Panel (a) shows the PESs of the four electronic states and panel (b) shows the corresponding projectile charge. Due to the high symmetry two of the four PESs are degenerate leading to only three visible lines in panel (a) and (b). The origin of the degeneracy becomes clear when studying the configurations underlying the four PESs at large R_z . In all four electronic states there is a single hole which is either located at the projectile ($LiF + H^+$, ionic state) or in the 2p orbitals of the F^- ion ($(LiF)^+ + H$, covalent states). In the ground state the hole is in the $F(2p_z)$ orbital pointing out of the surface towards the projectile. In the ionic state the hole sits at the projectile in the $H(1s)$ level. The two degenerate covalent states are characterized by the hole being located in two linear combinations of the $F(2p_x)$ and $F(2p_y)$ orbitals both of which lie in the surface plane. Panel (c) shows $F_{ij}^{(z)} = \langle \Psi_i | \partial / \partial R_z | \Psi_j \rangle$, the z-component of the non-adiabatic coupling vector \vec{F}_{ij} . There is only one non-vanishing coupling element for the state indices $i=1$ and $j=4$ due to symmetry. States 1 and 4 correspond to the ground and ionic state, respectively. Both states belong to the same irreducible representation as does the $\partial / \partial R_z$ operator. This is not true for the covalent states 2 and 3 leading to the vanishing of matrix elements $\langle \Psi_i | \partial / \partial R_z | \Psi_j \rangle$ involving one of these indices.

The PESs of all states in fig. 6.10 are essentially parallel to each other for $R_z > 7$ a.u. At $R_z \approx 6$ a.u. the PESs of the coupled ground and ionic state separate from each other. $R_z \approx 6$ a.u. is also the position where the projectile charge states indicate the onset of a change of configuration (panel (b)) and where the non-adiabatic coupling element (panel (c)) has a maximum. This is the typical shape of Rosen–Zener–Demkov interacting potential-energy surfaces (see chapter 5) for which the change of configuration as well as the non-adiabatic coupling span over a quite large region of space. In the present case both range from essentially $R_z = 0$ to $R_z \approx 8$ a.u. The diabatic version of these PESs is shown in fig. 6.11. Dynamics and the charge transfer probability on these PESs will be discussed in detail in sec. 6.3.2 and sec. 6.3.3 for one-dimensional and three-dimensional motion of the projectile, respectively.

6.3.2. 1-D dynamics in $Li_5F_1 + H^+$

In this section we study the charge-transfer dynamics between a proton and the Li_5F_1 embedded cluster under the constraint $R_x = R_y = 0$. The projectile is mov-

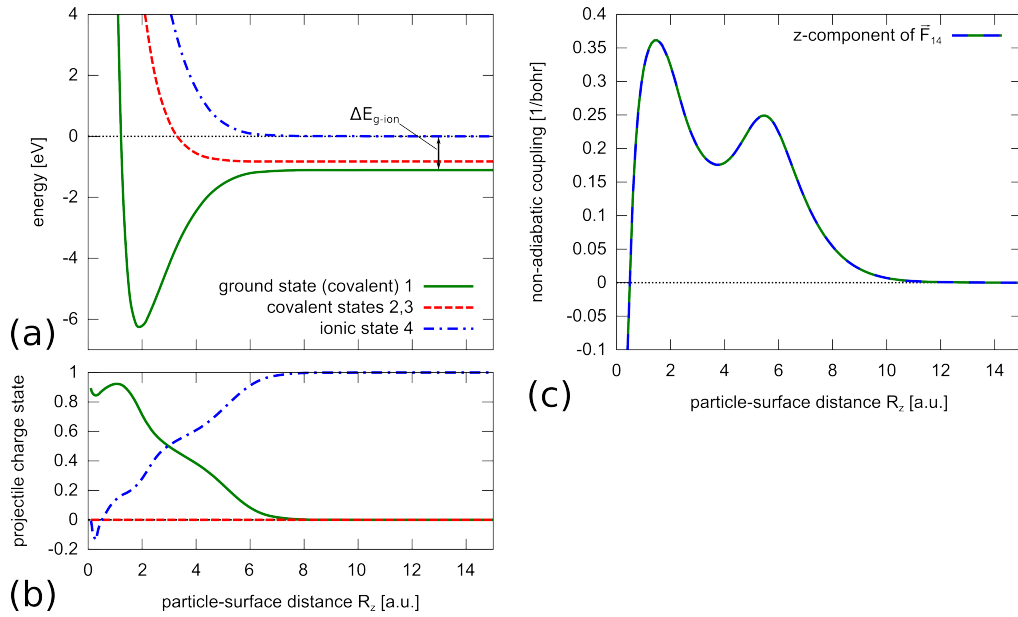


Figure 6.10.: One-dimensional cut along R_z ($R_x = R_y = 0$) through (a) the MRCI-SD adiabatic potential energy surfaces and (b) projectile charge states for the $\text{Li}_5\text{F}_1 + \text{H}^+$ embedded cluster. (c) Non-adiabatic coupling matrix element $\langle \Psi_1 | \partial / \partial R_z | \Psi_4 \rangle$ between the ground state and the ionic state.

ing along the surface normal and remains centered above the active, surface F^- ion. R_z denotes the distance between the surface and the projectile. For this high-symmetry geometry the charge transfer is an effective two-state problem defined by the PESs of the (covalent) ground state, the ionic state in fig. 6.10, and the coupling between them. Initially the system is prepared in the ionic state ($\text{LiF} + \text{H}^+$) and we determine the probability for electron transfer from the surface to the projectile, i.e., the neutralization probability of the proton as a function of the proton's initial momentum.

In fig. 6.12 (a) we plot results of the Rosen–Zener–Demkov model (for details see sec. 5.4.1) which agree well with Tully's surface-hopping approach and the full quantum solution of the projectile dynamics (fig. 6.12 (b)). Initial conditions in the Tully surface-hopping calculation and the wave-packet simulation are selected as follows. In the surface-hopping approach the trajectories of a particle with the hydrogen mass (the mass of the surface is infinite) are started at $R_z = 14$ a.u. on the PES of the ionic state with the initial momentum pointing towards the surface. For a given initial momentum $N = 2500$ trajectories are started. The initial kinetic energy of each individual trajectory is randomly selected from a Gaussian distribution which is centered at the nominal value and has a width of 2.35 eV [186]. The initial amplitudes of the coupled-channel equations are $|c_1(t = 0)|^2 = 0$ and

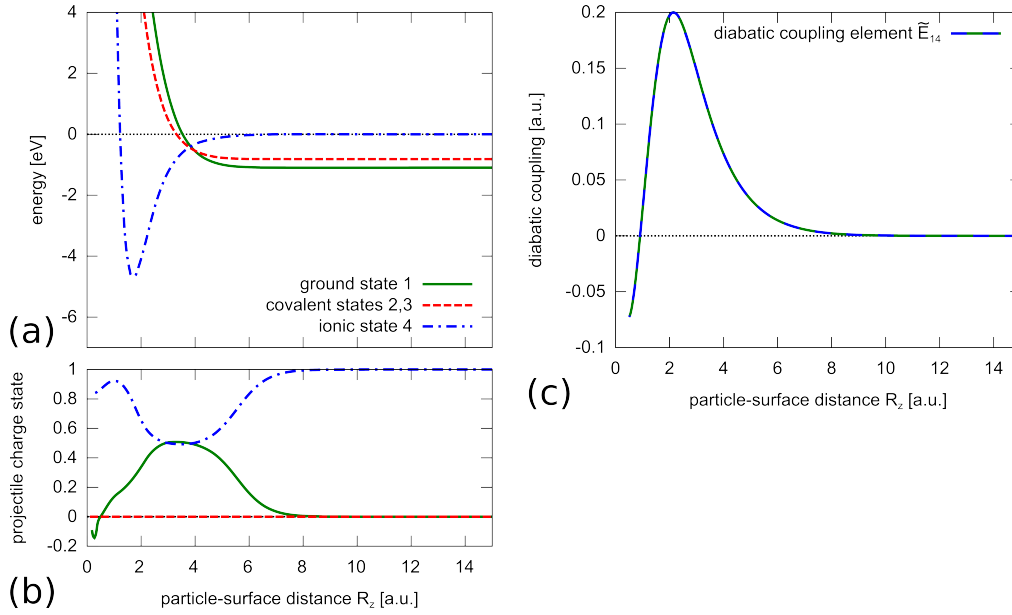


Figure 6.11.: One-dimensional cut along R_z ($R_x = R_y = 0$) through (a) the diabatic MRCI-SD potential energy surfaces and (b) projectile charge states for the $\text{Li}_5\text{F}_1 + \text{H}^+$ embedded cluster obtained by strict diabaticization. (c) Diabatic coupling element \tilde{E}_{14} between the ground state and the ionic state.

$|c_4(t=0)|^2 = 1$. Upon return of the trajectories to $R_z = 14$ a.u. after rescattering the neutralization probability is given by the ratio N_1/N where N_1 is the number of trajectories returning in the covalent ground state. Analogously, the initial wave packets are set to $\chi_1(R_z, t=0) = 0$ and $\chi_4(R_z, t=0) \propto e^{-\kappa(R_z - R_{\text{init}})^2} e^{ip_{\text{init}}(R_z - R_{\text{init}})}$, where p_{init} is the initial, central momentum towards the surface. κ is chosen such that the full-width at half maximum of the wave packet in energy space is 2.35 eV. After rescattering, i.e., after the wave packets χ_1 and χ_4 passed R_{init} on their way out, the neutralization probability is given by $\int_{-\infty}^{\infty} |\chi_1(R_z)|^2 dR_z$ when the initial wave packet is normalized.

The agreement between all three methods is quite good. The RZD model slightly underestimates the neutralization probability but it clearly shows the Rosen-Zener-Demkov nature of the PESs in fig. 6.10. Also the Stückelberg oscillations are, in terms of their frequency, in good agreement with the quantum solutions. This, a-posteriori, justifies the local treatment of the avoided crossing around $R_c = 5.46$ a.u. and shows that the charge transfer indeed occurs in close vicinity around R_c . Surface-hopping results almost perfectly match the full quantum solution except for slight deviations in positions and the amplitude the Stückelberg oscillations. Both effects are due to the approximate coherence in the semi-classical treatment.

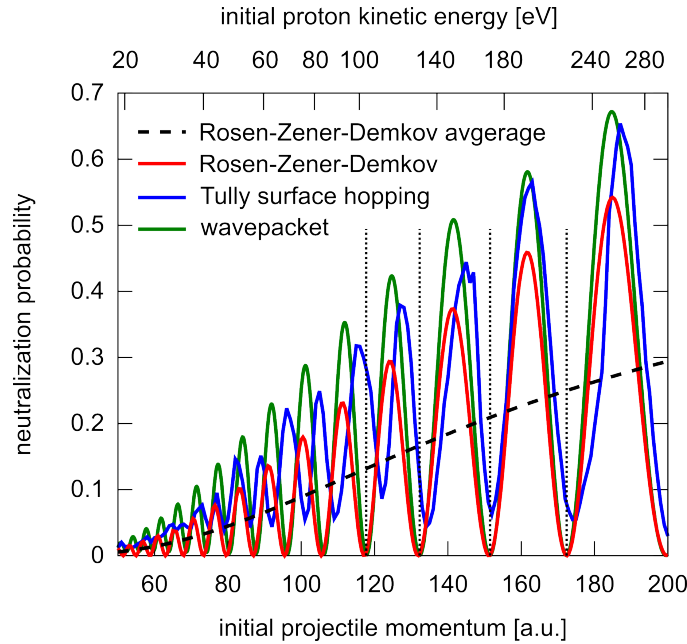


Figure 6.12.: Neutralization probability of H^+ rescattered from an Li_5F_1 embedded cluster, under perpendicular incidence along R_z ($R_x = R_y = 0$). Results are obtained by the Rosen–Zener–Demkov model (solid-red and dashed-black line), within Tully’s surface-hopping approach (solid-blue line), as well as in a full quantum wave-packet simulation (solid-pink line).

This result suggests the application of the numerically cheaper surface-hopping approach to the full three-dimensional treatment of the projectile motion without a considerable loss of accuracy.

6.3.3. 3-D dynamics in $\text{Li}_5\text{F}_1 + \text{H}^+$

In this section we determine the neutralization probability of the H^+ projectile using Tully’s surface hopping approach under more realistic conditions. First, the motion of the projectile is no longer limited to R_z but all its Cartesian coordinates \vec{R} are taken into account. Second, in experiment the proton beam hitting the surface covers the entire surface unit cell and, therefore, the neutralization probability is calculated as an average over the unit cell. To this end we use 2485 initial positions (R_x, R_y) uniformly distributed over the irreducible surface unit cell. For a given initial energy/momentum and each initial position 2500 trajectories are started at $R_z = 14$ a.u. above the surface. Initial energies are Gaussian distributed around the nominal value with a full-width at half maximum of 2.35 eV. Propagation of trajectories is stopped when they reach $R_z = 14$ a.u. again after being rescattered from the surface, or, when they penetrate the surface, i.e., when $R_z \leq 0.0$ a.u. The

last condition reflects the fact that in the interstitial regions the PESs are only weakly repulsive. In the present work we neglect the dynamics of projectiles below the surface and also neglect their possible rescattering from lower-lying surface layers. This approximation is justified since in experiment particles reflected from sub-surface layers can be distinguished from the ones reflected from the topmost surface layer by their energy loss and their scattering angle (see sec. 6.5.3). Fig. 6.13 shows the fraction of projectiles reflected from the surface and the fraction of trajectories being reflected as protons, i.e., on the PES of the ionic state. In our model only 5% of the projectiles are reflected at an initial kinetic energy of 55 eV which is in reasonable agreement with molecular-dynamics simulation (see appendix A.6) based on binary O’Conner-Biersack potentials [187].

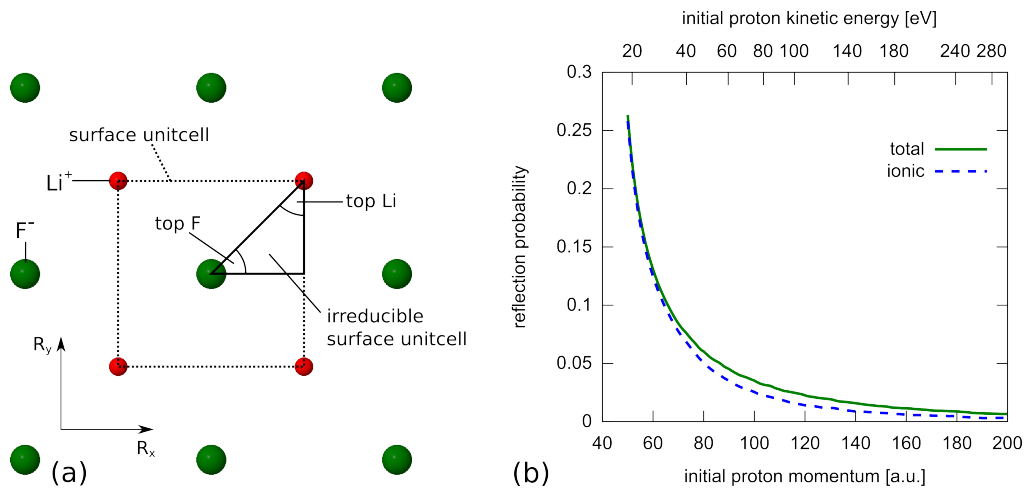


Figure 6.13.: (a) Top view of an LiF surface. The dashed square is the surface unitcell and the solid triangle the irreducible surface unitcell. Fractions “top F” and “top Li” within the irreducible surface unitcell indicate areas in the $R_x - R_y$ -plane in which trajectories denoted by top F and top Li are started at $R_z = 14$ a.u. (b) Fraction of projectiles reflected from an embedded Li_5F_1 surface cluster (perpendicular incidence) irrespective of the charge state of the reflected projectile (solid-green line). Fraction of projectiles reflected in the ionic (H^+) state (dashed-blue line). Results are obtained in a three-dimensional Tully-surface hopping propagation of the projectile and are averaged over initial projectile positions uniformly distributed over the surface unit cell.

The total neutralization probability (normalized to the number of initial trajectories) in fig. 6.14 (a) is given by the difference between the total reflection probability and the ionic reflection probability (fig. 6.13). It shows a maximum at an initial momentum of ≈ 90 a.u. (60 eV) formed by two competing processes. With increasing nuclear velocity the neutralization probability rises due to increasing efficiency

of the avoided crossing. On the other hand, a higher nuclear velocity leads to an increasing number of trajectories entering the surface and, therefore, to a lowering of the reflection and the neutralization probability. The ratio of reflected neutral trajectories to reflected trajectories is the so-called partial neutralization probability (fig. 6.14 (b)). It is a steadily increasing function of the initial momentum. Both neutralization probabilities show modulations at higher momenta which can be identified as traces of Stückelberg oscillations. Vertical lines in fig. 6.14 indicate the minima of the Tully surface-hopping neutralization probability of the 1-D dynamics with $R_x = R_y = 0$ (fig. 6.12). They coincide with the minima of the modulations in the 3-D neutralization probability. This means the 3-D neutralization probability is governed by trajectories reflected from the surface within a narrow region around the F^- ion. We confirm this by the so-called top F contributions to the partial neutralization probability (fig. 6.14 (b)). The top-F contributions are influenced by the number of reflected particles from both F^- and Li^+ (see appendix A.8) and must not be interpreted as the neutralization probability of a proton scattered at an “isolated” F^- surface ion (neglecting the Li^+). Top-F trajectories are started at $R_z = 14$ a.u. within a lateral circle with radius 1 a.u. ($R_x^2 + R_y^2 \leq 1$ a.u.) around the F^- ion (see fig. 6.13 (a)). For momenta larger than 130 a.u. these trajectories account for more than 50% of the partial neutralization probability. For lower momenta, however, there is a significant top Li contribution from trajectories started within a radius of 1 a.u. above an Li^+ ion. The top Li and top F contribution together fully account for the partial neutralization probability for momenta larger than 90 a.u. On first sight the large contribution of the top Li trajectories seems counterintuitive since the charge transfer obviously occurs between the active F^- ion and the projectile. A comparison of the nearest-neighbor distance (3.81 a.u.) and the first maximum of the non-adiabatic coupling ($R_c = 5.46$ a.u.) shows that even a trajectory started exactly on top of an Li^+ ion comes close enough to the F^- ion to pass the avoided crossing at R_c . This, in turn, implies the need of larger cluster sizes for a more realistic description of the charge transfer. Active clusters need to be large enough such that a projectile approaching an Li^+ ion can interact with four active surface F^- ions.

Another issue to be addressed is the periodicity of the LiF surface. In the model discussed above we apply periodic boundary conditions which lead, however, to unphysical situations. Consider the projectile propagating on the ionic PES and jumping to a covalent PES, i.e., becoming a hydrogen atom. When the hydrogen atom leaves the surface unit cell it “sees” a neutral F-surface atom in the neighboring cell to which it can lose its electron again. This leads to an underestimation of the neutralization probability since, in reality, the hydrogen “transfers” the electron to the neighboring unit cell leading to the new configuration $\text{LiF}+\text{H}$ for which a charge transfer (H^- formation) is much less probable. To approximate this effect we use the following protocol: whenever a projectile leaves the initial surface unit cell the PES it is moving on is recorded. For the PES of the ionic state (state number

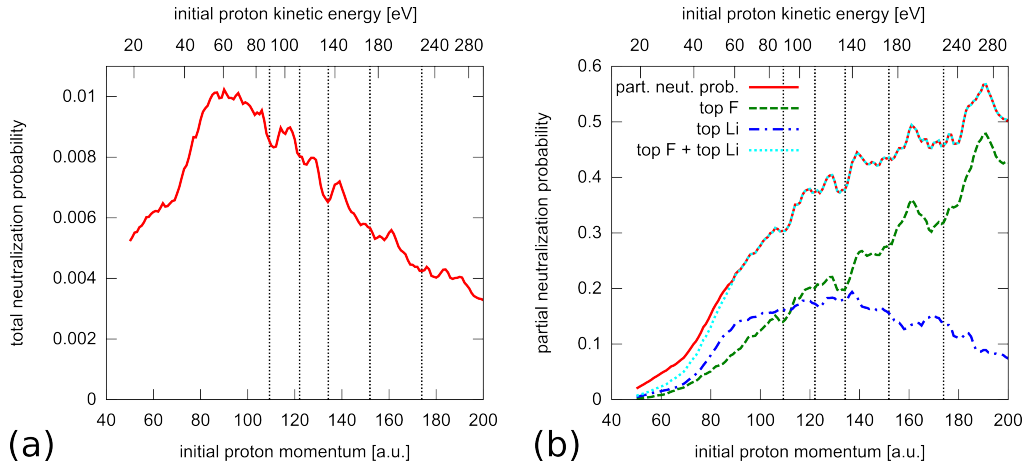


Figure 6.14.: (a) Total and (b) partial neutralization probability of H^+ scattered off a Li_5F_1 embedded surface cluster (perpendicular incidence). Results are obtained in a three-dimensional Tully-surface hopping propagation of the projectile and are averaged over initial projectile positions uniformly distributed over the surface unit cell leading to a reflection from an F^- ion. The total neutralization probability is normalized to the number of initial trajectories, the partial neutralization probability is normalized to the number of reflected trajectories (solid-green line in fig. 6.13 (b)). Top F and top Li contributions (see fig. 6.13 (a)) denote trajectories started in the $R_z = 14$ a.u. plane within a circle of radius 1 a.u. around an F^- and an Li^+ ion, respectively. Dashed-vertical lines indicate the minima of the Stückelberg oscillations in the one-dimensional neutralization probability from fig. 6.12.

4) the periodic boundary conditions hold and the propagation is continued. For PESs of covalent states (hydrogenic projectile, states 1 to 3) the jump probability is set to zero for the remaining path of the projectile. This should mimic the reduced charge transfer probability for the $\text{LiF}+\text{H}$ configuration. Clearly, this method is an approximation and is likely to overestimate the neutralization probability since, first, for small R_z covalent and ionic states are not distinguishable, and, second, charge transfer from the projectile to the neutral F atom, after leaving and returning to the initial surface unit cell, is neglected. Therefore, this protocol yields an upper bound for the neutralization probability: we find an increase of $\sim 30\%$ relative to the application of “standard” periodic boundary conditions but, apart from that, qualitatively identical results as shown in fig. 6.14. Clearly the optimal solution for the periodicity problem is the use of clusters large enough such that projectiles under perpendicular incidence do not leave the surface area covered by the active cluster. Unfortunately, such cluster sizes are currently computationally

out of reach.

6.4. 1-D charge-transfer dynamics in larger clusters

Now that we have analyzed in detail the charge transfer dynamics of the $\text{Li}_5\text{F}_1 + \text{H}^+$ embedded cluster surface we extend this study to clusters containing more than a single active F^- ion. We restrict the study in this section again to clusters with four-fold rotation symmetry and an active F^- ion in the center of the topmost surface layer, i.e., the point where the rotation-symmetry axis penetrates the embedded cluster surface. Also the projectile is laterally always positioned exactly on the rotation axis R_z ($R_x = R_y = 0$; see e.g. fig. 6.8 (a)) rendering the dynamics a 1-dimensional problem where the degree of freedom considered is R_z , the distance between projectile and surface.

We use MCSCF and, subsequently, MS-CASPT2 with pure point-charge embedding and basis sets: cc-pVTZ for F and H and DZ for Li. All calculations are performed within the C_{2v} pointgroup symmetry and the complete active space in the MCSCF contains all F(2p) orbitals of A_1 symmetry plus the H(1s) orbital which is also of A_1 symmetry. For N F(2p) orbitals of A_1 symmetry the CAS consequently hosts $2N$ electrons in $N + 1$ orbitals. The state average includes all PESs considered in the dynamics comprising 1 ionic state ($\text{LiF} + \text{H}^+$) and N covalent states ($(\text{LiF})^+ + \text{H}$). These $N + 1$ MCSCF many-electron wave functions are used as starting point for the MS-CASPT2. One remark on the symmetry is due. The clusters used belong to the C_{4v} point-group symmetry. Since MOLCAS does not support C_{4v} the calculations are performed in C_{2v} and there are electronic states within the A_1 irreducible representation of different symmetry. These two classes of states do not interact and the non-adiabatic coupling element between them vanishes. In the following we only plot PESs of states with a non-zero coupling to the asymptotic ionic state, the initial state in the charge-transfer simulation.

6.4.1. Clusters with active F^- ions in the topmost layer only

First, we focus on clusters containing active F^- ions only in the topmost surface layer. MS-CASPT2 adiabatic PESs of the Li_{25}F_9 cluster and their corresponding projectile charges (fig. 6.15 (a)) show a feature independent of the quantum chemistry method used: the PES split into three “groups” for $R_z < 5$ a.u. Group (1) and (3) each consists of a single state below and above group (2). The splitting can be understood on the molecular orbital level in terms of the hole orbital. There is a single hole in the combined system which can be either located at the projectile

(LiF + H⁺) or in the surface ((LiF)⁺ + H). States of group ② are covalent states with the hole located on the surface F⁻ ions *except* for the F⁻ ion in the very center of the cluster. At $R_z = 1.5$ a.u. the hole in state ① (fig. 6.15 (b)) is mainly located at the p_z orbital of the central F⁻ ion and in state ③ (fig. 6.15 (b)) the biggest contribution to the hole is located at the projectile. In this sense the splitting is interpreted as the hybridization of the p_z orbital of the central F⁻ and the H(1s) level leading to a bonding ③ (ionic bond between F⁻ and H⁺) and anti-bonding ① solution suggesting a strong coupling between these two PESs.

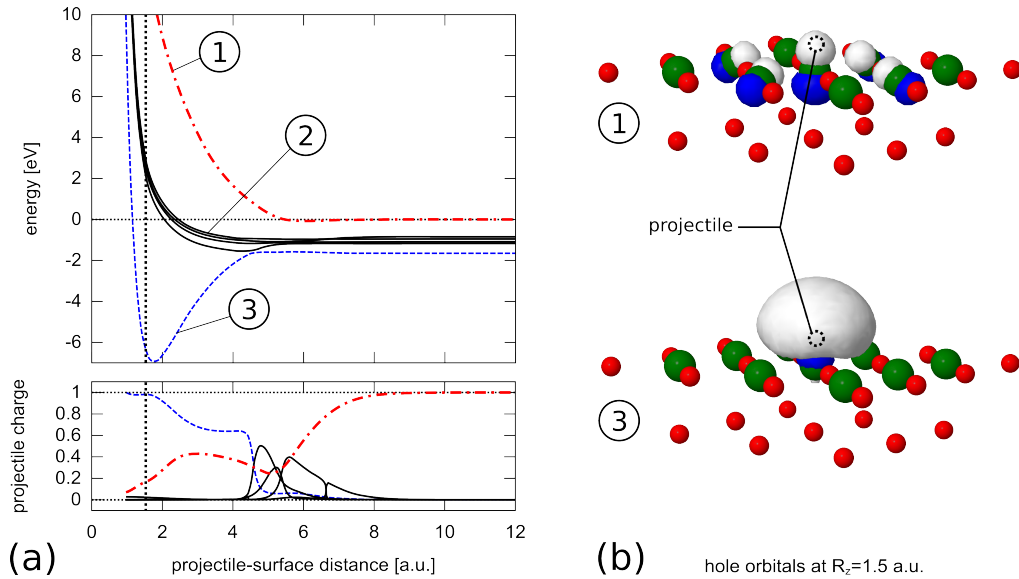


Figure 6.15.: (a) MS-CASPT2 adiabatic potential energy surfaces and corresponding projectile charges along R_z ($R_x = R_y = 0$) of the Li₂₅F₉ embedded surface cluster. Dash-dotted red line and dashed blue line mark the asymptotic ionic and the ground state, respectively. Black lines are asymptotic covalent states. (b) Hole orbital of states ① and ③ for $R_z = 1.5$ a.u. (dashed-vertical line in panel (a)).

For $R_z = 12$ a.u. the MS-CASPT2 electronic ground state is of covalent character and the energy difference between ground and ionic state $\Delta E_{\text{g-ion}} = 1.65$ eV corresponding to $W_{\text{LiF}}^{\text{MS-CASPT2}} = 13.6 - \Delta E_{\text{g-ion}} = 11.95$ eV (fig. 6.16). This is in good agreement with experiment and also with the “direct” calculation of $W_{\text{LiF}}^{\text{MS-CASPT2}}(\text{Li}_{25}\text{F}_9)$ without the projectile (sec. 6.2). Since at $R_z \approx 2$ a.u. the electronic ground state, however, is of ionic character due to the F⁻ - H⁺ bonding there must be a change of configuration of the asymptotic-ionic PES with R_z . This change is indeed visible in the projectile charges (fig. 6.16 (a)). At intermediate projectile-surface distances ($4 < R_z < 6$ a.u.) the PESs of the asymptotic-covalent states lie within a narrow energy window and there are several narrow, Landau–

Zener-like, avoided crossings between them. The asymptotic-ionic state lies a little above the covalent ones and there seems to be a Rosen–Zener–Demkov type of hidden crossing between the ionic and one of the covalent states indicated by the splitting of the PESs at $R_z \approx 5$ a.u. It becomes clearer when the narrow crossings between the covalent states are replaced by hand by linear crossings and when the two following states are highlighted (fig. 6.16 (b)): the asymptotic-ionic state and the new “diabatized” asymptotic-covalent state which is the electronic ground state at $R_z = 2$ a.u. The evolving picture features two PESs running in parallel for $R_z > 5$ a.u. which diverge at $R_z \approx 5$ a.u. “Diabatized” projectile charges show an almost complete change of configuration. Both, the PES and the projectile charges of these two states strongly resemble the ones found for $\text{Li}_5\text{F}_1 + \text{H}^+$ (fig. 6.10) suggesting also the $\text{Li}_{25}\text{F}_9 + \text{H}^+$ charge transfer to be an effective 2-state Rosen–Zener–Demkov problem. However, only as long as the projectile velocity is large enough such that the Landau–Zener single-passage probability is $p_{ij}^{\text{LZ}} \approx 1$ at the narrow avoided crossings in fig. 6.16 (a).

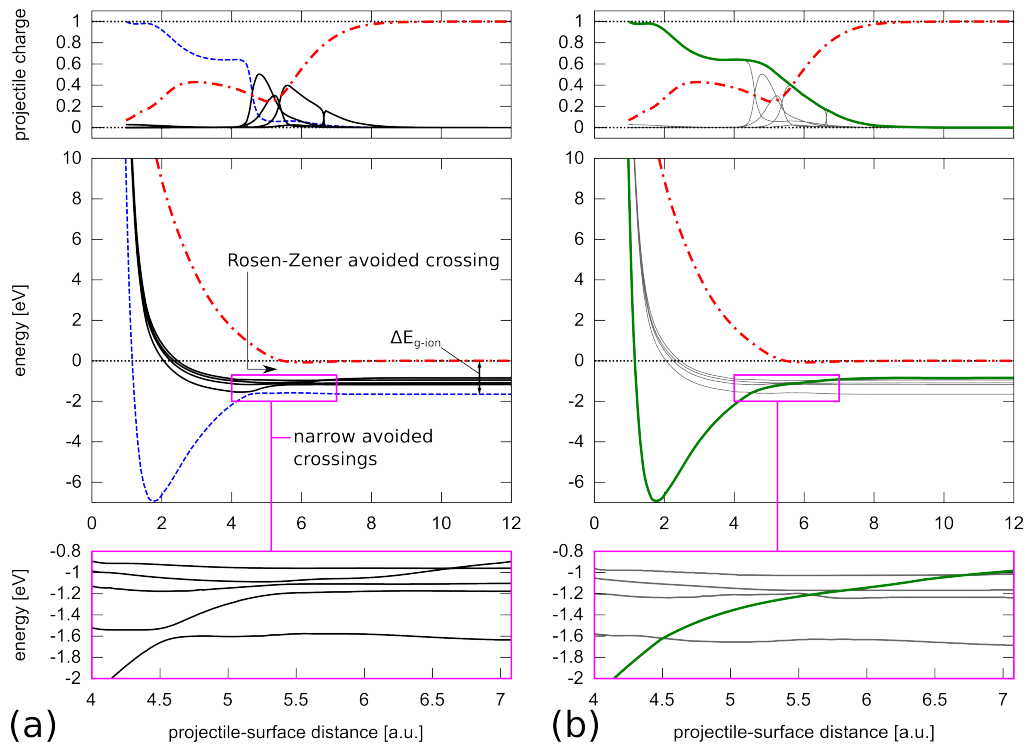


Figure 6.16.: (a) MS-CASPT2 adiabatic potential energy surfaces and corresponding projectile charges along R_z ($R_x = R_y = 0$) of the Li_{25}F_9 embedded-surface cluster. $\Delta E_{\text{g-ion}}$ is the energy difference between the electronic ground state and the ionic state. (b) Same as (a) with narrow avoided crossings replaced by linear crossings.

Quantitatively, the effective two-state character of the $\text{Li}_{25}\text{F}_9 + \text{H}^+$ PES can be shown in their diabaticized version (fig. 6.17) obtained by strict diabaticization (see sec. 5.3). There is one single diabatic coupling element (fig. 6.17 (c)) connecting the ionic state (③) and one of the covalent states (①). For $R_z \gtrsim 8$ a.u., these two states are equivalent with the two states found by “diabatization by hand” in fig. 6.16 (b). In the covalent state (①) the hole orbital for $R_z = 12$ a.u. is located almost exclusively on the p_z orbital of the central F site (inset in fig. 6.17 (a)) which is strong evidence that the charge transfer in $\text{Li}_{25}\text{F}_9 + \text{H}^+$ scattering takes place between the central F^- and the projectile only.

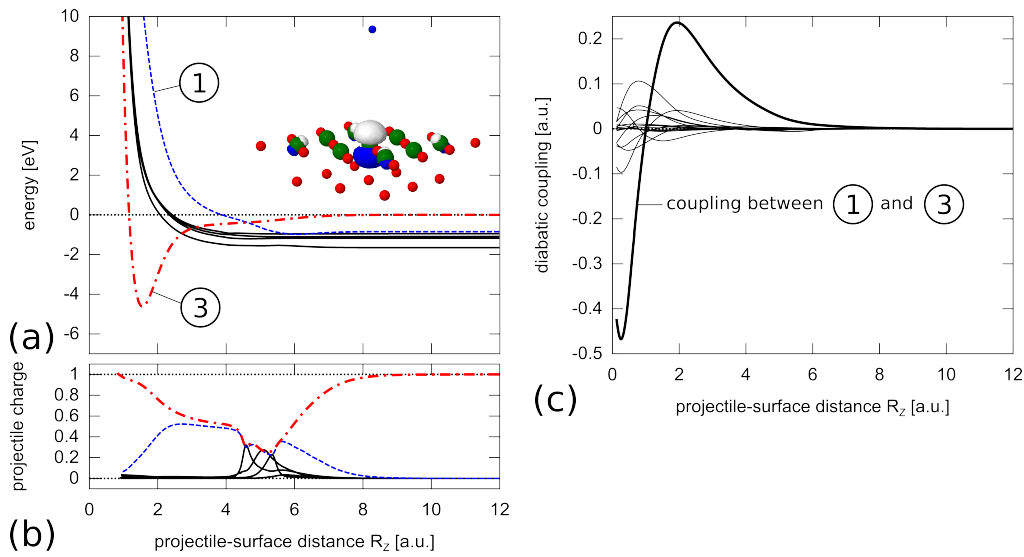


Figure 6.17.: (a) MS-CASPT2 diabatic potential energy surfaces, (b) corresponding projectile charges, and (c) diabatic coupling elements \tilde{E}_{ij} along R_z ($R_x = R_y = 0$) of the Li_{25}F_9 embedded surface cluster obtained by strict diabaticization. Inset in panel (a) shows the hole orbital located at the central F in state (1) for $R_z = 12$ a.u.

The same analysis holds true also for the MS-CASPT2 potential energy surfaces of the $\text{Li}_5\text{F}_1 + \text{H}^+$ and the $\text{Li}_{17}\text{F}_5 + \text{H}^+$ embedded clusters. In all three cases the charge transfer occurs almost exclusively between two PES and the electron transferred from the surface to the projectile comes from the central F^- ion. Therefore, also the H^+ neutralization probability for all these systems look quite similar (fig. 6.18). Since only two states are involved clean Stückelberg oscillations are found, the phase of which seems to be converged already for $\text{Li}_{17}\text{F}_5 + \text{H}^+$. The increase of the average neutralization probability with projectile momentum to ~ 0.5 confirms the Rosen–Zener nature of the hidden crossing responsible for the charge transfer. There are, however, distinct differences between the neutralization probabilities of the different cluster sizes for low initial proton momenta. They arise due to a vari-

ation of the energy splitting of the two diabatic charge-transfer states. For $\text{Li}_5\text{F}_1 + \text{H}^+$ the PES of these states are essentially degenerate leading to a neutralization probability of 0.5 at low proton momenta in agreement with the Rosen–Zener model. These results differ from the ones found in sec. 6.3 for the same cluster due to the different basis-set size. The largest splitting is found for $\text{Li}_{25}\text{F}_9 + \text{H}^+$ translating into the smallest value of the neutralization probability. With increasing proton momenta the differences get smaller since the probabilities of all clusters oscillate about their maximum average value of 0.5.

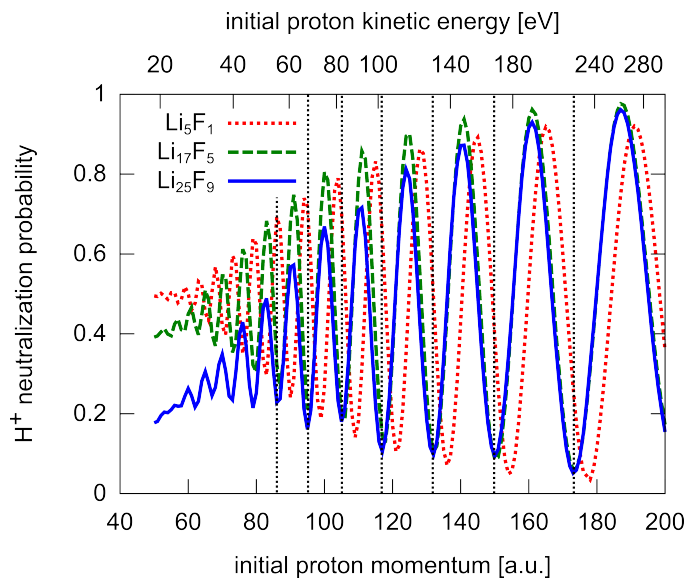


Figure 6.18.: Neutralization probability of H^+ reflected from embedded Li_5F_1 , Li_{17}F_5 , and Li_{25}F_9 surface clusters determined in a one-dimensional ($R_x = R_y = 0$) wave packet simulation. Dashed-vertical lines indicate the minima of the Stückelberg oscillations in the Li_{17}F_5 and Li_{25}F_9 data.

The decrease of the neutralization probability with cluster size at low proton momenta reflects the decrease of $W_{\text{LiF}}^{\text{MS-CASPT2}}$ (fig. 6.7 (b)) resulting in a downward shift of the asymptotic covalent states with respect to the ionic state. In the $\text{Li}_{25}\text{F}_9 + \text{H}^+$ cluster the asymptotic ionic state lies ~ 1 eV above the highest asymptotic covalent state (fig. 6.16). In the following we show that by changing the positions of the active F^- ions in the cluster this splitting changes while the work function of the cluster remains unchanged.

6.4.2. Clusters with active F^- ions in deeper surface layers

While $W_{\text{LiF}}^{\text{MS-CASPT2}}$ only depends on the number of active F^- ions, the width of the valence band is also sensitive to their positions within the active cluster. By re-ordering the $\text{Li}_{25}\text{F}_9 + \text{H}^+$ cluster to form a $\text{Li}_{25}\text{F}_5\text{-F}_4 + \text{H}^+$ cluster with four active

F^- ions in the second surface layer the width of the “valence band” (measured by the energy difference between the highest and lowest asymptotic covalent PES) increases from 1 eV (fig. 6.16) to 1.8 eV (fig. 6.19). As a consequence the asymptotic ionic state is no longer separated from the covalent ones and the asymptotic PES with the highest energy is of covalent character.

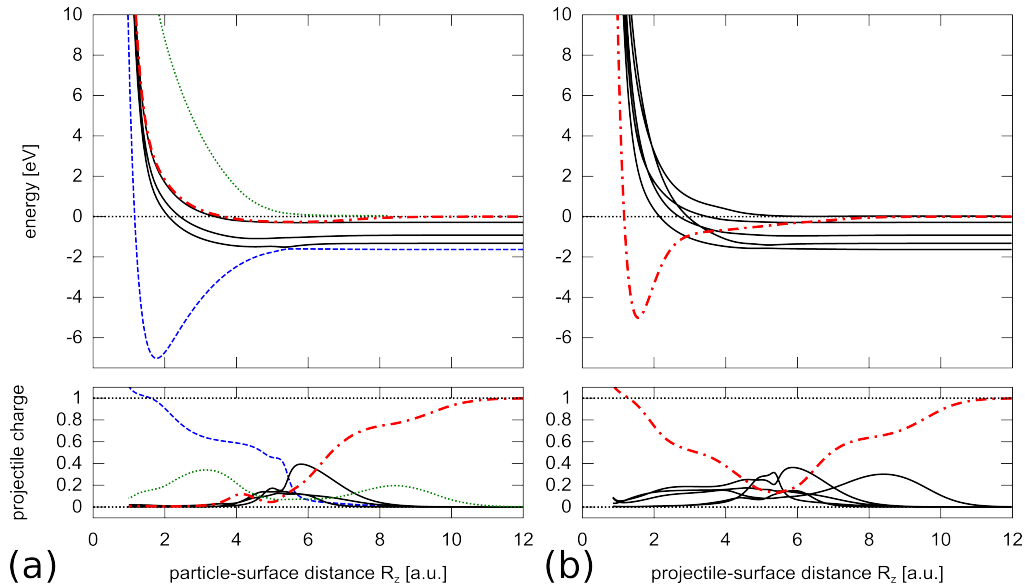


Figure 6.19.: (a) Adiabatic and (b) diabatic potential energy surfaces and projectile charges along R_z ($R_x = R_y = 0$) of the $Li_{25}F_5F_4 + H^+$ embedded surface cluster. Diabatic PESs are obtained by strict diabaticization. The dashed-green line in (a) is the energetically highest adiabatic state. The dashed-blue line is the adiabatic ground state. In both panels the dash-dotted red line is the asymptotic-ionic state.

Broadening of the valence band also affects the charge transfer dynamics (fig. 6.20). The picture of only two PES responsible for the $LiF + H^+$ charge transfer does not hold as soon as active F^- ions are placed into deeper surface layers. Although the number of contributing states is still small (3-4) for the clusters used ($Li_{25}F_5-F_4$, $Li_{26}F_5-F_4-F_1$, $Li_{38}F_5-F_4-F_5$) the neutralization probability changes considerably. Yet there are similarities to the single-layered cluster results. The Stückelberg oscillations for multi-layered clusters (fig. 6.20) are somewhat “smeared out” but all minima of the neutralization probability can be identified with the ones of single-layered clusters (fig. 6.18). Further, only in covalent states contributing to the charge transfer there is a portion of the hole located at the p_z orbital of the central F^- ion emphasizing the locality of the charge transfer.

Apparently two layers of active F^- ions are enough to obtain approximately converged results for the neutralization probability (fig. 6.20) as there are only small

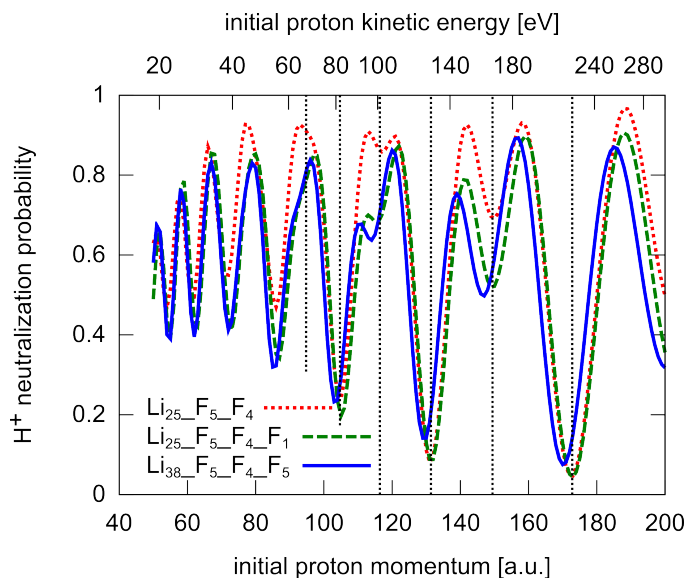


Figure 6.20.: Neutralization probability of H^+ reflected from an embedded $Li_{25}F_5-F_4$, $Li_{25}F_5-F_4-F_1$, and $Li_{38}F_5-F_4-F_5$ surface cluster determined in a one-dimensional ($R_x = R_y = 0$) wave-packet simulation. Dashed-vertical lines indicate the minima of Stückelberg oscillations in the neutralization probabilities using clusters with active F^- ions in the topmost surface layer only (fig. 6.18).

changes when a third layer is added. Also the number of active F^- ions in the topmost layer (fig. 6.18) seems to be converged for five active F^- ions, at least in terms of the Stückelberg oscillations. Definite answers in terms of convergence, however, can only be found with even larger active clusters which are, unfortunately, computationally not yet feasible. The limiting factor are “instabilities” in the MS-CASPT2 calculations due to intruder states (see, e.g., [188]). They lead to unphysical kinks and jumps in the PES and, also, in the non-adiabatic couplings which make a charge transfer analysis impossible. Usually, problems with intruder states are solved via real [188, 189] or imaginary [190] shifts in the energy denominator which dampen the influence of these states in the perturbation expansion. Unfortunately, the shifts needed to get continuous PES and couplings are so large that the perturbation correction to the MCSCF calculation becomes negligible. Alternatively, the CAS can be enlarged such that it includes the intruder states. Adding virtual orbitals to the CAS, however, considerably increases the computational effort and is, therefore, an impractical solution.

The optimal cluster size for the charge transfer problem is such that $W_{LiF}^{MS-CASPT2} \approx W_{LiF}^{experiment}$. Further, the width and density of the valence band, i.e., the number of asymptotic covalent states, should be large enough such that the ionic state is

closely surrounded by them. Our 1-D calculation with the largest number of PES is done for the $\text{Li}_{25}\text{F}_5\text{-F}_4 + \text{H}^+$ cluster with reduced symmetry. We use the C_s point-group symmetry (one mirror plane) and move the projectile slightly away from the R_z axis ($R_x = 0.15$ a.u., $R_y = 0.0$). This reduces the number of irreducible representations and increases the number of interacting states in the CAS to 16. For this setup we vary the projectile-surface distance and calculate the neutralization probability. As it turns out a total number of 5 PESs contribute to the charge transfer and we find essentially the same result as for the high-symmetry case in fig. 6.20.

6.5. 3-D charge-transfer dynamics in $\text{Li}_{20}\text{F}_6\text{-F}_1 + \text{H}^+$

The convergence of the neutralization probability with cluster size in the previous section shows that the 3-D projectile dynamics calculation based on the small Li_5F_1 cluster is not reliable. In this sections we perform 3-D projectile dynamics using a cluster that is (a) large enough to yield reasonable agreement with the largest clusters tested and (b) small enough such that a calculation of 3-D PESs is computationally feasible. In the following sections we introduce such a cluster (fig. 6.21) and discuss details of the quantum-chemistry and dynamics calculations (6.5.1). Further, we calculate the charge-transfer probability and analyze it in view of results of previous sections (6.5.2). We also compare our results with preliminary experimental data (6.5.3).

6.5.1. The $\text{Li}_{20}\text{F}_6\text{-F}_1 + \text{H}^+$ embedded cluster

The $\text{Li}_{20}\text{F}_6\text{-F}_1$ surface cluster (fig. 6.21 (a)) is the smallest cluster that obeys the convergence criteria found in the previous sections: it has more than five active F^- ions in the topmost and one active F^- in the second surface layer. Further, the atoms are arranged such that the two active ions in the irreducible unit cell used for the PES calculation (fig. 6.21 (b)) are surrounded by five active nearest-neighbor ions (four in the first and one in the second surface layer). Additionally, all other active F^- ions are also surrounded by five active nearest-neighbor Li^+ ions. The active cluster is surrounded by one layer of fluoride AIMP since, otherwise, charge leak occurs when no symmetry constraints are employed. AIMP and cluster are embedded into a large matrix of point charges.

We determine three-dimensional PESs and non-adiabatic couplings (see appendix A.4) on a grid by varying the projectile position \vec{R} with R_x and R_y within the irreducible surface unit cell and R_z between 0.1 and 15.0 a.u. Distances between adjacent grid points are 0.1 a.u. for the lateral grid along R_x and R_y and 0.05 a.u. for the R_z grid. The latter is chosen finer since we simulate (near) perpendicular

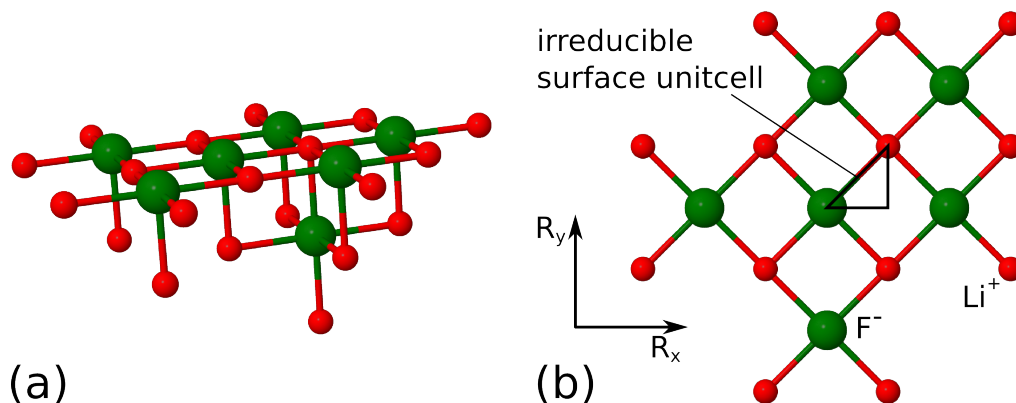


Figure 6.21.: (a) $\text{Li}_{20}\text{F}_6\text{-F}_1$ active cluster. (b) Top view of the $\text{Li}_{20}\text{F}_6\text{-F}_1$ cluster and the irreducible surface unitcell. The cluster is constructed such that the F^- and the Li^+ ion in the irreducible surface unitcell are surrounded by 4 active neighbors in the first and one active neighbor in the second surface layer. The origin of the projectile-coordinate system ($R_x = R_y = R_z = 0$) is defined at the F^- ion in the irred. surface unitcell.

incidence of the projectile for which an accurate sampling of the narrow avoided crossings along R_z is crucial. The PES and non-adiabatic coupling grids within the irreducible unit cell are continued periodically to simulate the extended crystal surface. We calculate 22 PESs and the couplings between them on the MCSCF level with a (43,22) CAS since the MS-CASPT2 calculation, without any symmetry constraints, features unphysical kinks and discontinuities due to intruder states. MCSCF combined with the cc-pVDZ basis set yields a cluster-work function of $W_{\text{LiF}}^{\text{MCSCF-avg}} = 13.1$ eV clearly larger than the experimental one. Nevertheless, we expect reliable results for the charge transfer since the relative level ordering of the PESs at large R_z is reasonable with the ionic state centered in the ~ 2 eV broad band of covalent states (fig. 6.22).

6.5.2. 1-D and 3-D projectile dynamics

Despite the differences in the quantum-chemistry treatment (cluster size, basis set, quantum-chemistry method, embedding) of the $\text{Li}_{20}\text{F}_6\text{-F}_1$ cluster and the clusters in the previous section we find good agreement for the charge transfer probability in a one-dimensional ($R_x = R_y = 0$) projectile dynamics calculation (fig. 6.23). Stückelberg oscillations obtained with the different clusters do not match perfectly but their frequencies are in reasonable agreement. Fig. 6.23 also indicates the excellent agreement of the Tully-surface hopping and the wave packet approach for $\text{Li}_{20}\text{F}_6\text{-F}_1$. For initial momenta $P_{\text{init}} > 120$ a.u. also the phase and frequency of the Stückelberg oscillations agree and, therefore, we expect the Tully surface-hopping

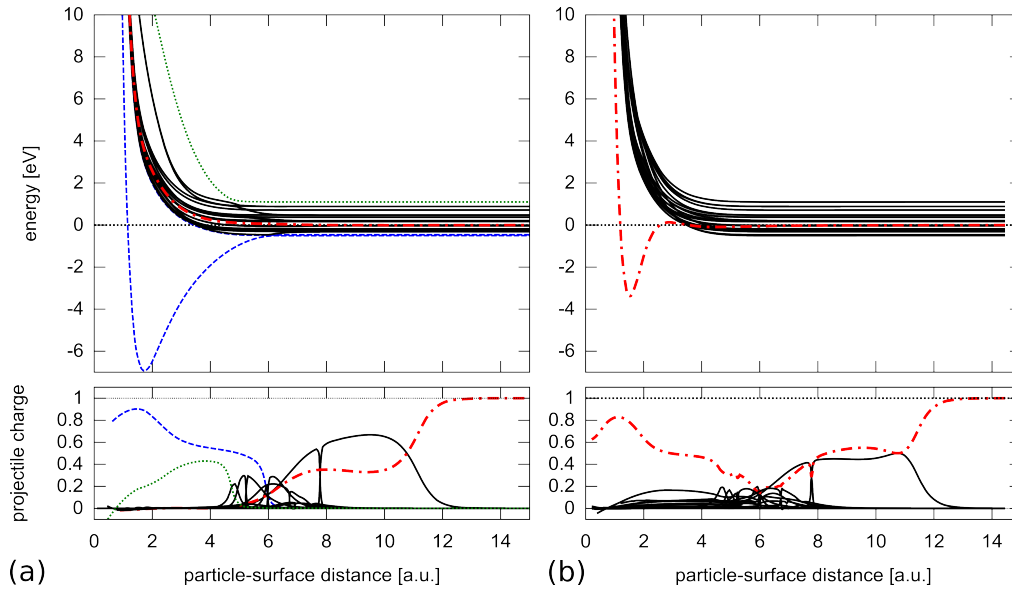


Figure 6.22.: (a) MCSCF adiabatic and (b) diabatic potential energy surfaces and projectile charges along R_z ($R_x = 0.1$ a.u., $R_y = 0$) of the embedded $\text{Li}_{20}\text{F}_6\text{-F}_1$ cluster. The projectile is positioned at $R_x \neq 0$ to break the cluster symmetry. Diabatic PESs are obtained by strict diabaticization. The dash-dotted red line marks the asymptotic-ionic adiabatic and diabatic state. Dotted-green and dashed-blue lines in (a) indicate the electronic ground state and the highest excited state in the adiabatic representation, respectively.

algorithm to generate reliable quantum results also in three-dimensional dynamics calculations discussed in the following.

The proton beam perpendicularly incident on the surface is simulated analogously to sec. 6.3.3: we take into account all three Cartesian components of the projectile motion and average observables using 3916 initial projectile positions (R_x, R_y) uniformly distributed over the irreducible unit cell. For a given initial proton energy/momentum ($P_x = P_y = 0, P_z = -P_{\text{init}}$) and each initial position 1000 trajectories are started at $R_z = 14.5$ a.u. above the surface. The propagation is stopped when the particles pass again the $R_z = 14.5$ plane after being rescattered from the surface. We neglect projectiles rescattered from lower surface layers and the projectile motion within the LiF crystal by stopping the propagation when the particles penetrate the surface, i.e., when $R_z \leq 0.0$ a.u. The fraction of projectiles reflected from the topmost surface layer (fig. 6.24) agrees reasonably well with results obtained with the embedded Li_5F_1 cluster (fig. 6.13) and with simulations based on the binary potentials of O’Conner and Biersack (see appendix A.6). For an initial projectile kinetic energy of 55 eV, 4% of the projectiles are reflected.

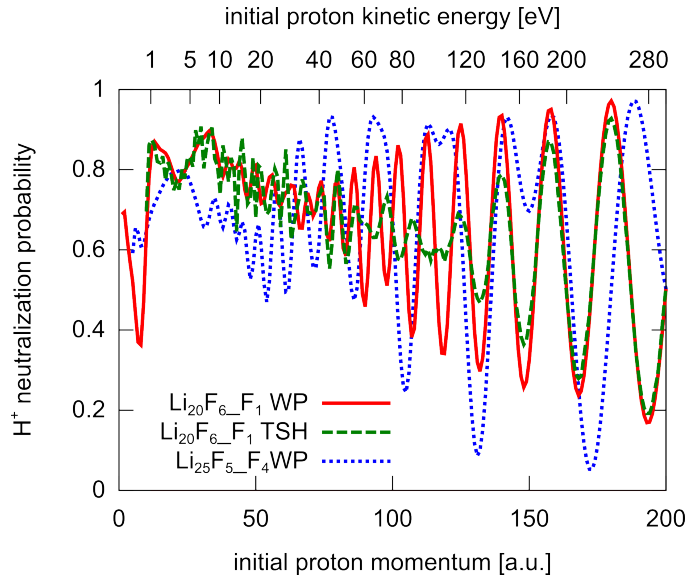


Figure 6.23.: Neutralization probability of H^+ reflected from embedded $\text{Li}_{20}\text{F}_6\text{-F}_1$ (solid-red and dashed-green lines) and $\text{Li}_{25}\text{F}_5\text{-F}_4$ (dotted-blue line) surface clusters determined in a one-dimensional ($R_x = R_y = 0$) wave-packet and Tully-surface hopping simulation along R_z .

The fraction of protons (trajectories on the ionic PES) reflected from the embedded $\text{Li}_{20}\text{F}_6\text{-F}_1$ surface cluster (fig. 6.24) is, however, considerably lower than the one found for the Li_5F_1 cluster (fig. 6.13). This is due to the fact that in the $\text{Li}_{20}\text{F}_6\text{-F}_1$ cluster there are 21 channels available for neutralization compared to only three in the Li_5F_1 cluster. Furthermore, the level spacing between the ionic and the covalent states is smaller in $\text{Li}_{20}\text{F}_6\text{-F}_1$. Consequently, the total neutralization probability normalized to the number of initial projectiles (fig. 6.25 (a)), is larger by about one order of magnitude than its Li_5F_1 equivalent (fig. 6.14). Since the total reflection probability dominates the ionic one, also the dependence of the total neutralization probability on the initial proton momentum is governed by the monotonic decay of the total reflection probability. Normalizing the neutralization probability to the number of rescattered trajectories leads to the partial neutralization probability (fig. 6.25 (b)) which shows a weak decrease with initial proton momentum. Also the average 1-D neutralization probability decays with increasing momentum (fig. 6.23), however, the decay is faster and the neutralization probability is clearly lower. 3-D trajectories started in the vicinity of the central F^- ion are responsible for the enhanced 3-D neutralization probability. Trajectories with initial positions $R_x^2 + R_y^2 < r_c^2$ around the F^- ion, with r_c being a critical radius, yield very similar results to a 1-D calculation. Trajectories starting beyond r_c , however, have a slowly varying neutralization probability close to unity. Since their weight is

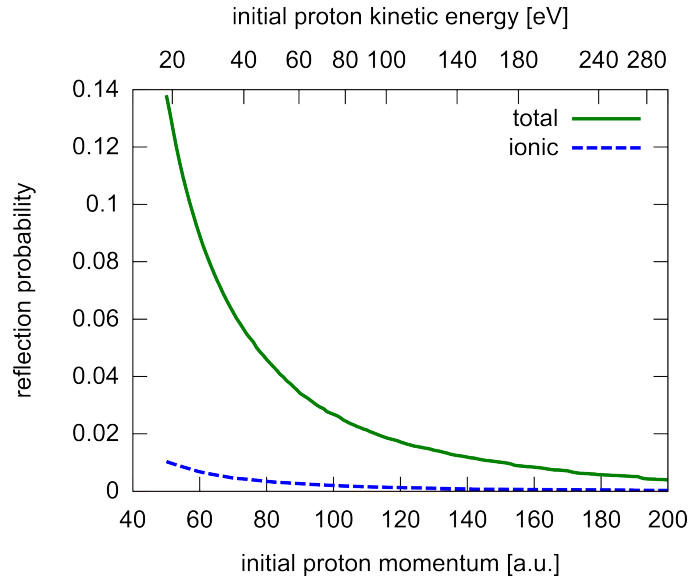


Figure 6.24.: Fraction of projectiles reflected from an embedded $\text{Li}_{20}\text{F}_6\text{-F}_1$ surface cluster (perpendicular incidence) irrespective of the charge state of the reflected projectile (solid-green line). Fraction of projectiles reflected in the ionic (H^+) state (dashed-blue line). Results are obtained in a three-dimensional Tully-surface hopping propagation of the projectile averaged over initial projectile positions uniformly distributed over the surface unit cell.

larger for geometric reasons they dominate the full 3-D neutralization probability. The top F and top Li weights show that for small momenta trajectories rescattered from F^- and Li^+ equally contribute to the partial neutralization probability while for larger momenta the top F^- contribution dominates.

6.5.3. Comparison with experiment

In both total and partial neutralization probabilities (6.25 (b)) there are only weak traces of Stückelberg oscillations. The multitude of projectile paths on different PESs and varying scattering angles average them out and slightly shift the maxima relative to the 1-D result. In large-angle scattering experiments, however, trajectories with certain scattering angles can be selected by the scattering geometry which should make more pronounced Stückelberg oscillations accessible. A typical experiment suitable for measuring the neutralization probability is the large angle Time-of-Flight Low-Energy Ion Spectroscopy (TOF-LEIS) of Bauer and co-workers [191]. Ions are accelerated towards a sample surface under an angle of incidence of 25.5° relative to the surface normal. The position of the detector is such that it records specularly reflected projectiles within a scattering angle of $\theta_{\text{scat}} = 129^\circ \pm \sim 1.5^\circ$.

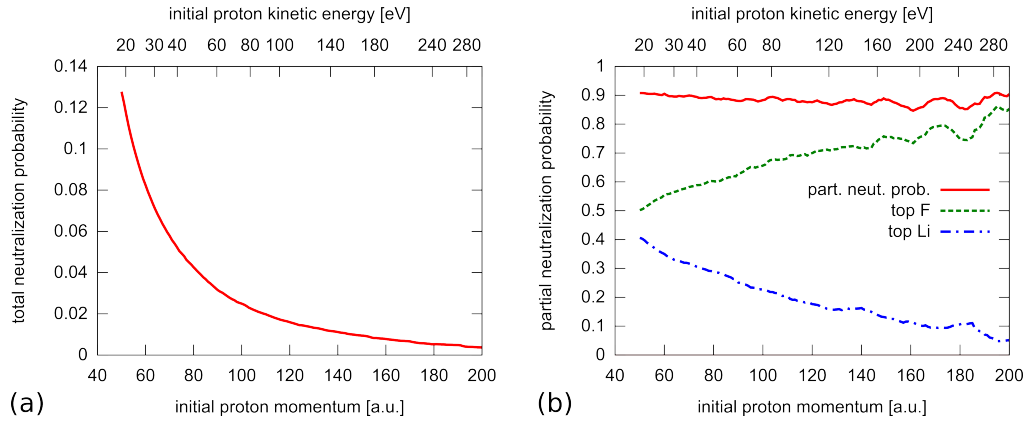


Figure 6.25.: (a) Total and (b) partial neutralization probability of H^+ scattered off a $\text{Li}_{20}\text{F}_6\text{-F}_1$ embedded surface cluster (perpendicular incidence). Results are obtained in a three-dimensional Tully-surface hopping propagation of the projectile and are averaged over initial projectile positions uniformly distributed over the surface unit cell. The total neutralization probability is normalized to the number of initial trajectories, the partial neutralization probability is normalized to the number of reflected trajectories (solid-green line in fig. 6.24). Top F and top Li contributions (see fig. 6.13 (a)) denote trajectories started in the $R_z = 14.5$ a.u. plane within a circle of radius 1 a.u. around an F^- and an Li^+ ion, respectively.

With a TOF setup the energy spectrum of the rescattered particles is determined which allows for separation of projectiles reflected from the topmost and sub-surface layers. Particles reflected from sub-surface layers suffer energy loss due to nuclear and electronic stopping on their path through the crystal and, therefore, appear in the low-energy part of the spectrum. Further, an acceleration lens between sample and detector allows for the separation of ionic and neutral particles arriving at the detector.

Bauer and co-workers investigate with this system the charge transfer between the surface of an evaporated LiF film and a proton beam. Their preliminary data on the ratio of backscattered hydrogen atoms to backscattered protons are compared in fig. 6.26 with our calculations. We use the $\text{Li}_{20}\text{F}_6\text{-F}_1$ cluster and protons with an angle of incidence of 25.5° relative to the surface normal. In the calculation we only consider projectiles reflected from an F^- surface ion. Particles reflected from an Li^+ ion do not contribute to the hydrogen-proton ratio in experiment since they also appear in the low energy part of the spectrum due to the larger energy transfer in the collision with the lighter Li^+ ion. For theoretical data shown in fig. 6.26 only a single azimuthal angle of incidence is chosen: the momentum component of the projectiles parallel to the surface points into the $[110]$ crystal direction. Considering only backscattered trajectories with a scattering angle of $129.5^\circ \pm 20^\circ$

leads to pronounced Stückelberg oscillations which are partially averaged over but still visible, when all backscattered trajectories are taken into account.

We find agreement in terms of the order of magnitude of the hydrogen to proton ratio between theory and experiment. The Stückelberg oscillations, however, are not visible in the experimental data for two reasons. First, the use of an undefined LiF surface structure and, second, the fact that the scatter of the measured data points is quite large. According to our experimental collaborators, the F^- ion is not a very effective back scatterer due to its small atomic number. This makes long opening times of the choppers in the TOF setup necessary and ultimately leads to a limited resolution in the energy spectrum of reflected particles. The limited resolution influences the evaluation of the hydrogen to proton ratio by making a clear separation between projectiles rescattered from the topmost and sub-surface layers more difficult. Further, the accelerator used for the primary protons and the projectile detectors are not optimized for initial kinetic energies below 1 keV which also worsens the spectral resolution. Low-energy projectiles are, however, crucial to minimize the influence of degradation of the LiF surface due to sputtering during the measurement. Sputtering is already present at initial proton kinetic energies of 20 eV [192] but stays relatively constant at 0.5 sputtered LiF molecules per initial projectile up to at least 100 eV. Apart from modifying the surface we do not expect sputtering to influence the experimental results. Even Stückelberg oscillations should remain mostly unaffected since the characteristic time for sputtering off a surface ion is large compared to the time in which the projectile is reflected from the surface. At very low initial kinetic energies, however, this can change. When the time, the projectile spends in a region with non-zero coupling, becomes comparable to the period of lattice vibrations then sputtering, excitation of phonons, and sticking of the projectile at the surface alter the PESs. The coherence of the proton wave packet is thereby destroyed making Stückelberg oscillations hard to observe. However, for the lowest proton momentum used in our simulations ($P_{\text{init}} \approx 50$ a.u.), a phonon period is about a factor of ten larger than the time the projectile spends in the interaction region.

For better future comparison between theory and experiment one either needs to average the theory results over several azimuthal angles of incidence or use crystalline and oriented LiF samples in experiment instead of the evaporated films with an undefined surface structure. Further, more experimental data points are needed and the use of accelerators and detectors optimized for the energy range of interest could help to reduce the error bar in the experiment.

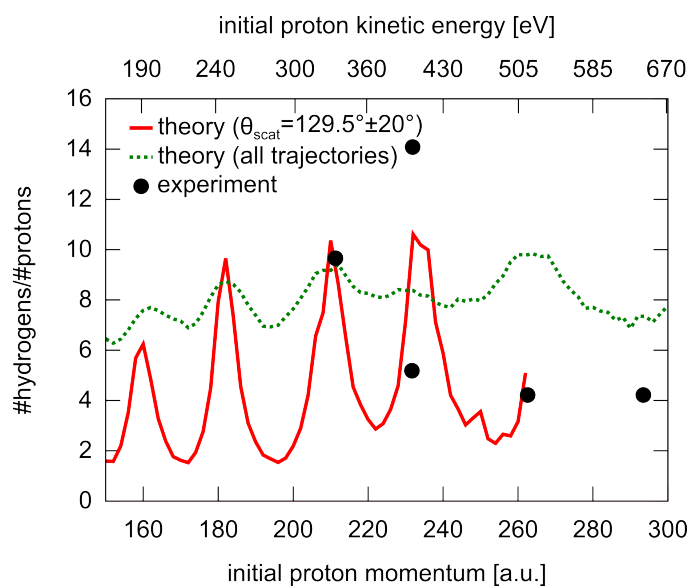


Figure 6.26.: Number of backscattered hydrogen atoms divided by the number of backscattered protons as a function of initial proton momentum. Theory data (solid red and dashed green line) are obtained in a three-dimensional TSH propagation. The projectiles are directed towards the surface under an angle of incidence of 25.5° relative to the surface normal. Initial positions are uniformly distributed over the surface unit cell. The dashed green line shows the hydrogen to proton ratio taking into account all backscattered projectiles while for the solid red line only backscattered trajectories with a scattering angle of $\theta_{scat} = 129.5^\circ \pm 20^\circ$ are used. These parameters simulate the TOF-LEIS setup of Bauer and co-workers [191] used to measure the data points shown.

7. Summary and Outlook

In this work we have investigated localized electronic excitations of (i) defects in bulk insulators and (ii) surfaces during reactive scattering of impinging projectiles on a state-of-the-art ab-initio level. In particular, we have studied the absorption of light by F-type color center defects in alkali halides and the non-adiabatic charge-transfer dynamics during the scattering of a proton off a lithium-fluoride surface. We have employed quantum-chemistry methods in the framework of the embedded cluster approach which allow for (a) including correlation effects of localized electrons in extended systems beyond standard DFT approaches, (b) the accurate calculation of excited electronic states, and (c) investigating non-adiabatic effects, i.e., the coupling of nuclear and electronic degrees of freedom.

Our investigation of the light absorption of the F center in LiF is, up to now, the most advanced available leading to unprecedented agreement between the experimental and theoretical absorption energy. We have also determined the Fermi contact term at ions surrounding the defect, the approximate width of the F-center absorption line, and we have estimated the influence of electron-phonon coupling. Although the F center, being a single-electron defect, seems to have a simple electronic structure state-of-the-art methods are required in order to find satisfying agreement with experiment. A proper embedding of the active cluster by AIMPs turns out to be crucial for a reliable description of the excited state of the color center. In contrast to earlier studies we have found a much more localized p-type orbital. Our results are not only in unprecedented agreement with experiment but also agree with calculations based on post-DFT methods. F-center orbital shapes as well as the ground state geometry and the F-center absorption energy agree.

Further effort, however, needs to be invested in the photoluminescence of F-centers in alkali halides where theory lags behind experiment. First, ab initio methods need to be found which can reliably describe the relaxation of the excited state, the energy of the emitted photon and the large Stokes shifts observed in experiment. If this prerequisite is met a fully ab-initio description of the nuclear wave packet dynamics during the optical cycle as measured in [83], the influence of electron-phonon coupling becomes feasible, and the open question of the, up to now unobserved, F-center luminescence in LiF can be addressed.

We have also, for the first time, performed an investigation of the experimentally observed Mollwo–Ivey (MI) relation on an ab-initio level. It connects the absorption energies, E_{abs} , of F-type color centers in alkali-halides with the anion-cation distance, a , of the corresponding crystals by $E_{\text{abs}} \propto 1/a^{1.8}$. Previous explanations

of the MI relation and its exponent, $n_{\text{exp}} = 1.81$, rely mainly on the Madelung potential and attributed to ion-size effects only a minor influence. Only small deviations from the MI relation were interpreted as signatures of ion-size effects. By introducing the model system of a scaled alkali halide, in particular scaled LiF the alkali halide with the smallest ions, we have been able to disentangle ion-size effects and effects due to the increase of the lattice constant. We have found ion-size effects to be the predominant mechanism for the formation of the potential well the defect electron is bound to. Therefore, the size of the ions surrounding the vacancy shape the defect electron wave function and are responsible for the fractional MI exponent. Without ion-size effects we find an exponent of $n = 2$ just like a simple three-dimensional square well potential model by Stöckmann suggests. We have verified that larger ions cause a compression of electron density in the F-center vacancy. This compression leads, compared to scaled LiF, to a reduced growth of the defect wave function's extent with the lattice constant and ultimately translates, via the Vinti sum rule, to a reduced Mollwo–Ivey exponent in real alkali-halide crystals.

An interesting question for future work is what such an analysis would yield for more complex defects, hosting more than one electron, and for color centers in materials different from alkali halides. For such defects Mollwo–Ivey relations exist [10, 193] with an exponent far from 2. Further open questions concern the emission process for which the Mollwo–Ivey relation fails completely. If the F center in the relaxed excited state, however, is interpreted as an electron-hole pair (an exciton), the Coulomb interaction of which is screened by a dielectric constant ϵ , the energy difference between ground and first excited state derived from the Rydberg law is given by

$$\Delta E_{\text{emission}} = E_{2p} - E_{1s} = \frac{3e^4 m^*}{128\pi^2 \hbar^2 \epsilon^2} \sim \epsilon^{-2}. \quad (7.1)$$

Eq. 7.1 is independent of the anion-cation distance a . A fit of experimental emission energies with C/ϵ^2 shows reasonable agreement [45]. Da Silva [194] suggested that large relaxations of ions surrounding the vacancy reshape the defect-potential well such that the pristine anion-cation distance, a , becomes unsuitable for fitting the emission energies. Rather the new, relaxed potential well sizes need to be used for ordering and fitting the emission energies in a Mollwo–Ivey type relation. An ab-initio analysis as presented in this chapter could shed light on this question. However, also for such an investigation, a proper description of the relaxed excited state is necessary.

Non-adiabatic effects such as charge transfer play an important role in the field of particle-surface interaction. However, the ab-initio treatment of charge transfer in terms of ion-surface scattering is numerically difficult due to the large number of coupled nuclear and electronic degrees of freedom. We have presented here the, to

our knowledge, first fully ab-initio analysis of the resonant electron transfer process during rescattering of a proton from an LiF surface. We have employed MCSCF, MRCI, and MS-CASPT2 to calculate the PESs of embedded LiF surface clusters and we have solved the time-dependent Schrödinger equation for coupled projectile and electronic degrees of freedom to determine the neutralization probability of the reflected proton. The influence of parameters such as cluster size and shape as well as basis-set sizes on the charge transfer and the electronic structure of the embedded clusters has been investigated. The work function of the embedded clusters used is, though not fully converged, in fair agreement with experiment. Analysis of the PESs of the embedded Li_5F_1 surface cluster reveals the charge transfer to be driven by a Rosen–Zener–Demkov like hidden crossing. In all clusters tested we have found pronounced Stückelberg oscillations in the neutralization probability of protons under perpendicular incidence on the central surface F^- . The oscillations are only weakly dependent on the cluster size and shape, confirming the picture of the charge transfer being a local process involving only a few surface atoms and electronic states. We have estimated the size of the charge transfer region to encompass five F^- ions in the first and four F^- ions in the second surface layer. Additional F^- ions hardly change the shape of the Stückelberg oscillations in the neutralization probability. These oscillations also appear in the ratio of backscattered hydrogen atoms to backscattered protons determined in a full three-dimensional proton scattering dynamics calculation simulating an experiment performed by Bauer and co-workers. We have found agreement in the order of magnitude between theory and preliminary experimental data. However, more accurate measurements in a lower energy range (to limit the surface degradation during measurement) would be highly desirable to confirm the presence of Stückelberg oscillations and the agreement between experiment and theory.

The ab-initio approach presented can be improved by enlarging the clusters to ensure an even better description of the surface electronic structure, in particular of the LiF valence band. So far we are able to account for realistic work functions but not for a dense sampling of the valence band over its full width. Enlarging the embedded clusters requires a reliable protocol to calculate accurate PESs as well as the non-adiabatic couplings between them. MS-CASPT2 seems to be the perfect tool, however, for very large cluster sizes the problem of intruder states leading to discontinuities in the PESs and, even more so, in the non-adiabatic couplings needs to be solved. In future work, the ab-initio approach presented can also be extended to grazing incidence scattering for which (a) plenty of experimental data are available and (b) the projectile-velocity component perpendicular to the surface can be as low as a few eV. This can be done according to the work of Borisov et al. [176] who approximated the grazing angle projectile trajectory by a piecewise motion of the projectile at constant distance to the surface, with one “piece” corresponding to the surface unit cell.

Apart from extensions of the $\text{LiF} + \text{H}^+$ neutralization problem the embedded clus-

ter approach can be applied to other scattering problems such as negative ion conversion, charge transfer from strongly localized 3d orbitals, Auger neutralization, and electronic stopping of projectiles in LiF. Each of these four topics is briefly introduced in the following sections.

Negative-ion conversion of H scattered off LiF

Negative-ion conversion denotes the single (double) electron capture of a neutral (singly positive charged) projectile and was extensively measured for particles scattered under grazing incidence from, e.g., alkali-halide surfaces [13, 195]. Negative ion fractions of close to 80% are reached for certain projectile-surface combinations due to the so-called diabatic energy level confluence [14] denoting the level shift that brings the projectile-affinity level into near resonance with the surface-valence band. There are “parameter free” models available, however, a fully ab-initio treatment of the conversion is still absent.

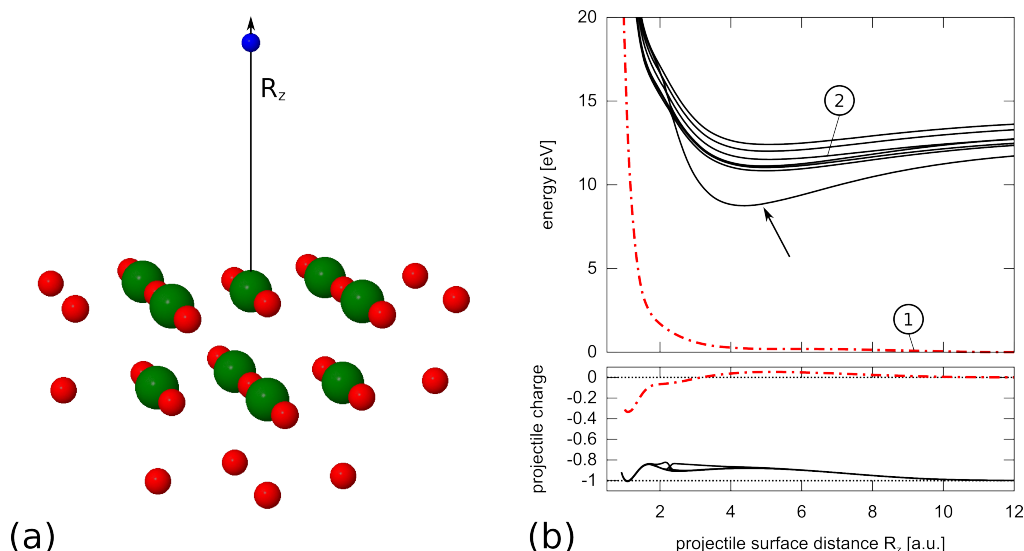


Figure 7.1.: (a) Embedded $\text{Li}_{25}\text{F}_5\text{-F}_4 + \text{H}$ surface cluster used to calculate (b) adiabatic MCSCF potential energy surfaces and corresponding projectile charges. Dash-dotted red line is the initial, covalent $\text{LiF} + \text{H}$ state and solid black lines are ionic $\text{LiF}^+ + \text{H}^-$ states. The arrow indicates the ionic state with the strongest coupling to the initial state.

To investigate hydrogen negative ion conversion $\text{H} + \text{LiF} \rightarrow \text{H}^- + (\text{LiF})^+$ we need to replace the H^+ projectile in the previous discussion by H. Adiabatic MCSCF PESs (fig. 7.1 (b)) of the $\text{Li}_{25}\text{F}_5\text{-F}_4 + \text{H}$ embedded cluster (fig. 7.1 (a)) separate into two groups: the initial, covalent $\text{LiF} + \text{H}$ state (1) and a set of ionic $\text{LiF}^+ +$

H^- states (2). One of the latter, indicated by the arrow in fig. 7.1 (b), however, is special. It is clearly lower in energy relative to the other covalent states since the surface hole in this very state is located exclusively at the central F and, therefore, has the shortest distance to the negatively charged projectile. In this sense the Coulomb attraction between H^- and the surface hole helps to localize the latter making the $LiF + H \rightarrow LiF^+ + H^-$ conversion an even more localized and effective two level process than the neutralization of H^+ . We, therefore, predict smaller cluster sizes being sufficient for convergence of the two relevant PESs which should ease the the ab-initio description of negative ion conversion compared to neutralization.

Neutralization of He^+ scattered off a Germanium surface

Neutralization-cross sections of He^+ ions reflected from a Germanium surface under large angle scattering were first measured by Erickson et al. [196] in 1974. More recently, Göbel et al. [197] provided a more detailed study with absolute values for the He^+ neutralization probability $P(He)$. Both experiments find oscillations in $P(He)$. Tolk and co-workers [198] interpreted this result as a quasi-resonant charge transfer between the strongly localized Ge(3d) orbitals and the He(1s) level. Due to this localization, similar to $LiF + H^+$, only a few states are involved in the charge transfer leading to pronounced Stückelberg oscillations in $P(He)$. Göbel applied a qualitative model [197] that, with a suitable choice of parameters, leads to good agreement with experimental data. However, information on underlying neutralization processes is impossible to extract from such a model, as the authors state.

Microscopic understanding of the charge transfer can be provided by quantum chemistry within the embedded cluster approach. The simplest embedded cluster modeling a germanium-surface or bulk atom is a single germane molecule (fig. 7.2 (a)). It consists of a single germanium atom the open bonds of which are saturated by four hydrogen atoms. A one-dimensional surface hopping dynamics simulation along R_z on seven MCSCF potential energy surfaces shows an enhanced coupling of the initial, ionic state ($H_4Ge_1 + He^+$) to covalent PESs ($(H_4Ge_1)^+ + He$) corresponding to a hole in the Ge(3d) orbitals (rather than in Ge(4s) and Ge(4p)). The resulting $P(He)$ fraction matches the frequency and the position of the Stückelberg oscillations in experiment (fig. 7.2 (b)) while their amplitude is larger than in experiment. The absolute value of the calculated $P(He)$ is smaller than the experimental one by a factor of ~ 3.5 , indicating that the He^+ neutralization is more effective than suggested by this simple model. An explanation for this mismatch is the inaccurate description of the surface leading to inaccurate positions of the $He^+(1s)$ and Ge(3d) levels. While in experiment the Ge(3d) levels (binding energy

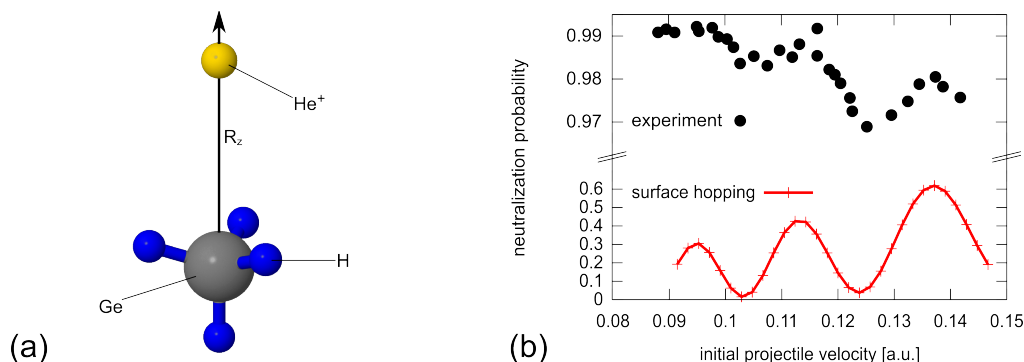


Figure 7.2.: (a) $\text{H}_4\text{Ge}_1 + \text{He}^+$ cluster simulating a surface Ge atom. This cluster is used for calculating seven potential energy surfaces as well as the non-adiabatic coupling between them. A one-dimensional Tully-surface hopping dynamics of the He^+ projectile along R_z yields (b) the fraction of neutral-reflected projectiles (solid red line). Black dots are experimental data [197]. Please note the different scale for theory and experimental data.

~ 30 eV, [199]) are separated from the $\text{He}^+(1s)$ level (24.59 eV) by ~ 5 eV the MCSCF total energies of the corresponding charge transfer states are separated by more than 10 eV. Also a possible level shift of the $\text{He}^+(1s)$ level upon approaching the surface is treated only approximately due to the small cluster size. Also the sign of the slope of the averaged $P(\text{He})$ seems to be different. This might be caused by the limited cluster size as we observed for the neutralization probability of $\text{H}^+ + \text{LiF}$. This system can serve as a playground for improving and testing embedding schemes as well as quantum-chemistry methods.

Auger neutralization of He^+ in front of a LiF surface

While electron transfer from an LiF surface to a H^+ projectile is governed by (quasi) resonant neutralization, for a He^+ projectile the capture level lies at -24.59 eV clearly out of resonance with the valence band (fig. 7.3 (a)). Nevertheless, neutralization of He^+ is possible via Auger neutralization (fig. 7.3 (a)). An electron is transferred from the valence band to the projectile while the surface is left in an excited state: an additional electron-hole pair is created leading to the formation of a trion (two holes and one electron) [200]. Since electron-electron interaction mediates the excitation of the surface, Auger neutralization is referred to as a two-electron process in contrast to resonant neutralization, a single electron process. This “orbital energy picture” in fig. 7.3 (a) translates to total energies, i.e., to MC-SCF potential energy surfaces (fig. 7.3 (c)) of a $\text{Li}_4\text{F}_2\text{-F}_2 + \text{He}^+$ embedded surface

cluster (fig. 7.3 (b)) as follows: there is a single asymptotic ionic state (2) corresponding to $\text{LiF} + \text{He}^+$. For the $(\text{LiF})^+ + \text{He}$ configuration there are, however, two types of states. First, a single hole can be located in the LiF valence band, the F(2p) orbitals, leading to the energetically lowest PESs (1). Additionally, there can be a second hole in the valence band due to the excitation of an F(2p) electron to the Li(2s) orbitals forming, in total, a trion. This configuration creates the energetically highest PESs (3). Due to the vicinity and the avoided crossings of the initial-ionic state and the covalent states with the trion at $R_z \approx 2$ a.u. we expect a strong coupling between them responsible for Auger neutralization of the He^+ projectile. Quantum-chemistry and a molecular dynamics simulations could provide an ab-initio determination of Auger neutralization probabilities and, therefore, a microscopic understanding of individual Auger neutralization processes.

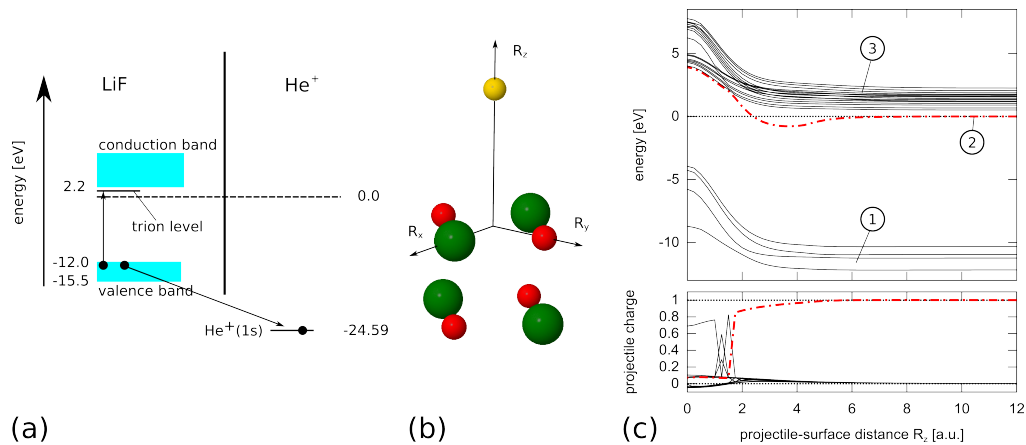


Figure 7.3.: (a) Auger neutralization of He^+ in front of an LiF surface, schematically. An electron is transferred to the He^+ capture level and the surface is excited by the creation of an additional electron-hole pair, leading to a trion. (b) Embedded $\text{Li}_4\text{F}_2\text{-F}_2$ surface cluster used to calculate (c) the adiabatic MCSCF potential energy surfaces of (1) and (3), asymptotic covalent states, and (2), the asymptotic ionic state, as well as corresponding projectile charges involved in the Auger neutralization. The dash-dotted red line denotes the only asymptotic ionic state while all solid black lines are covalent states.

Electronic stopping of He in an LiF crystal

Bauer and co-workers [201] measured the electronic stopping power of He and H projectiles traveling through an LiF crystal. Surprisingly, the threshold velocity of the projectiles for the onset of electronic stopping is much lower than predicted by a simple binary-encounter model. The latter is based on the momentum and energy

transfer in a head-on collision between the projectile and a target electron in the LiF valance band. The stopping power was studied within a time-dependent density-functional theory approach [202] by Pruneda et al. for channeling trajectories only. They found good agreement for the threshold velocity which they attributed to local excitations (charge transfer from F^- to Li^+) but could not explain the slope of the linear increase of the stopping power with projectile velocity.

In a quantum-chemistry study one can extend the understanding of the microscopic excitation process. Consider a single layer of LiF (approximated by an active Li_6F_6 cluster (fig. 7.4 (a) embedded in a two-dimensional point charge matrix). The He projectile moves perpendicular to the LiF layer (along the R_z axis) and penetrates the layer in the “channel” exactly between a Li^+ and an F^- ion. At large R_z the MCSCF potential energy surfaces (fig. 7.4 (b)) split into the electronic ground, or initial state (1) (surface and projectile are in their respective electronic ground state) and a large band of excited states (2) at ≈ 12 eV. Projectile charges of all PESs are almost independent of R_z confirming that no charge transfer takes place on this PES and, since excited states of He lie well above 12 eV, the excited states (2) correspond to excitations of the Li_6F_6 layer. Similar to the $LiF + H^+$ case, the coupling to only a few of the excited states dominates. These states “drop out” of the band of excited states (2) at $R_z \approx 2$ a.u. (see arrow in fig. 7.4 (b)) leading to a reduction of the energy gap to the initial state which could explain the low onset of electronic stopping found by Bauer.

A future study could investigate the nature of these excited states and their role in the electronic stopping power of LiF. Further, in a dynamics calculation, an impact-parameter (R_x, R_y) and projectile-velocity dependent excitation probability can be determined which can be used in a Classical-Trajectory Monte Carlo calculation simulating the slowing down of a He projectile in a LiF crystal by the passage and excitation of independent layers of LiF.

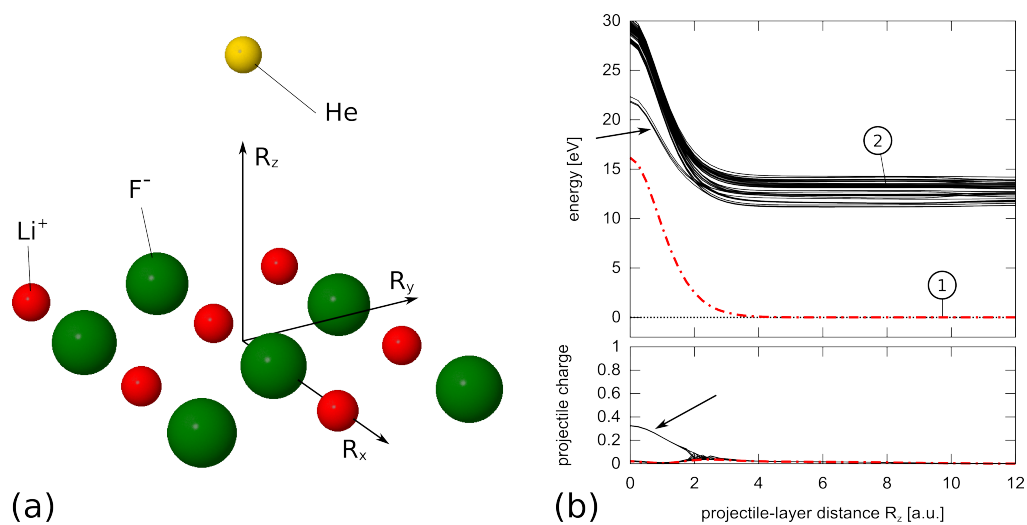


Figure 7.4.: (a) Embedded Li_6F_6 cluster simulating a single layer of LiF. (b) Adiabatic MCSCF potential energy surfaces and corresponding projectile charges as function of R_z the distance between the He projectile and the LiF layer. The dash-dotted red line (1) is the initial covalent state corresponding to the electronic ground state of the LiF layer and the He projectile. Solid black lines (2) are covalent states corresponding to electron-hole excitations in the LiF layer.

A. Appendices

A.1. Scaled NaF and LiCl

According to the picture developed in section 4.3 the F-center absorption energy in any alkali-halide crystal should scale with $1/a^2$ when the crystal is stretched. In this section we test this prediction and show that the $1/a^2$ scaling needs to be taken with care since also in scaled alkali halides ion-size effects are present.

Mollwo–Ivey fits of CASPT2(ROHF) F-center absorption energies in scaled LiF, NaF, and LiCl (fig. A.1 (a)) yield exponents of $n_{\text{LiF}} = 2.04$, $n_{\text{NaF}} = 2.02$, and $n_{\text{LiCl}} = 2.32$. While NaF nicely agrees with our prediction of $n = 2$ the F-center absorption energy in LiCl decreases, unexpectedly, faster. This can be qualitatively understood, however, by means of the radial nodes r_0 and the rms radii of the defect ground state wave function.

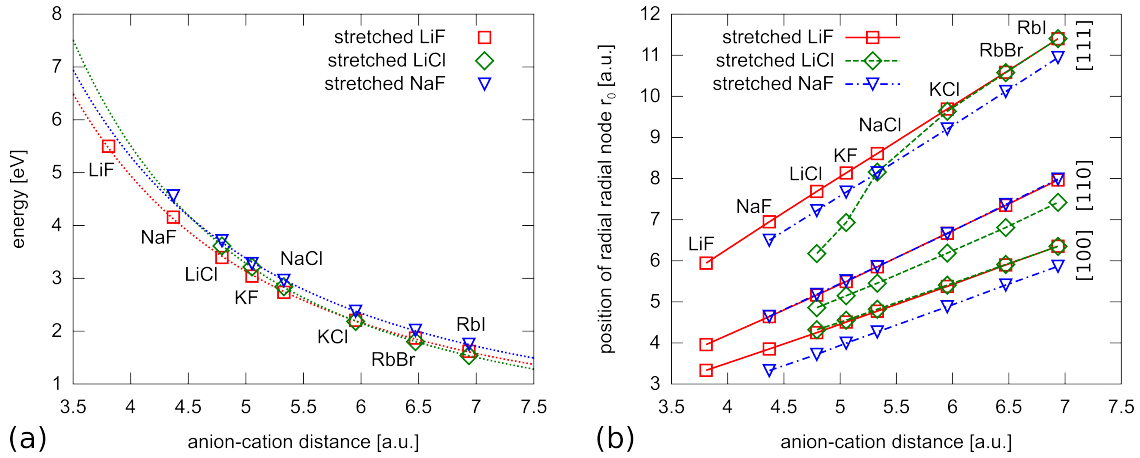


Figure A.1.: (a) CASPT2(ROHF) F-center absorption energies of stretched LiF, LiCl, and NaF. (b) First radial nodes r_0 of the s-type defect wave function along the [100], [110], and [111] direction in stretched LiF, LiCl and NaF.

Fig. A.1 (b) shows $r_0^{[100]}(a)$, $r_0^{[110]}(a)$, and $r_0^{[111]}(a)$ of the F-center defect wave function in scaled LiF, NaF and LiCl. Let us first focus on the r_0 values in NaF: they behave quite similarly to the ones of LiF showing almost perfectly linear increase with a slope of 1, $\sqrt{2}$, and $\sqrt{3}$ for the [100], [110], and [111] direction, respectively. Along the [110] direction, pointing in both cases towards F^- , $r_0^{[110]}(a)$ of LiF and

NaF coincide. $r_0^{[100]}(a)$ and $r_0^{[111]}(a)$ of NaF are shifted towards lower values with respect to the ones of LiF due to ion sizes. The [100] and [111] directions in NaF point towards an Na^+ ion while in LiF they point towards the smaller Li^+ ion. The downward shift is almost independent of a and it is almost equal for both directions (~ 0.5 a.u.). The latter value can be interpreted as the difference in radius of the Na^+ and the Li^+ ion. A value of 0.49 a.u. for this difference is predicted by the model of effective ionic radii in pristine crystals [108].

In scaled LiCl, $r_0^{[100]}(a)$ and $r_0^{[110]}(a)$ behave similarly as in scaled LiF. $r_0^{[100]}(a)$ of LiCl almost perfectly coincides with $r_0^{[100]}(a)$ of LiF since in both cases the nearest neighbor is an Li^+ ion. $r_0^{[110]}(a)$ of LiCl is lower relative to scaled LiF due to the larger second-nearest neighbor Cl^- ion. The downward shift varies between 0.35 a.u. and 0.55 a.u. which underestimates the difference in ion radii between Cl^- and F^- of 0.9 a.u. predicted by the effective ion model. $r_0^{[111]}(a)$ shows a highly non-linear behavior. Instead of coinciding with the $r_0^{[111]}(a)$ values of LiF, it is strongly pushed to lower values at small anion-cation distances. With increasing a , however, $r_0^{[111]}(a)$ of LiCl approaches the value of LiF and from $a \approx 6.5$ a.u. on, the lattice constant of RbBr, both curves coincide. We interpret this result as a blocking of the [111] direction due to the orthogonalization requirement of the F-center wave function with respect to the Cl^- ion core states. With increasing a the blocking is gradually released to the point where $r_0^{[111]}$ is determined by the orthogonalization of the defect electron to the third-nearest neighbor Li^+ ion core states.

The unblocking is also visible in the root-mean square radius of stretched LiCl. While the rms radii of LiF and NaF increase almost perfectly linear with a , the rms radius of LiCl grows, for small a , with a higher power of a . With the Vinti sum rule (eq. 4.7) this translates into a decay of E_{abs} in LiCl faster than $1/a^2$ and a Mollwo-Ivey exponent $n_{\text{LiCl}} = 2.32$ larger than 2.

We also extract F-center absorption energies from the rms radii in scaled LiCl and NaF via the Vinti sum rule and compare them with the ab-initio ΔSCF calculations. The result is quite similar to the one of scaled LiF in fig. 4.7. For small a the Vinti-sum rule energies overestimate the ΔSCF energies and both approach each other for larger a . The difference to LiF is that in LiCl and NaF one needs to go to larger anion-cation distances to find good agreement between the Vinti-sum rule and the ROHF absorption energies.

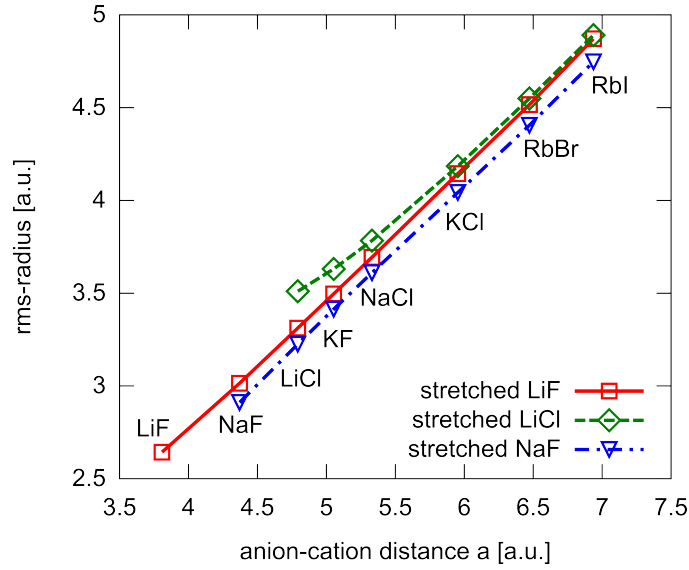


Figure A.2.: Root-mean square radii of the ground-state F-center wave function in scaled LiF, scaled LiCl, and scaled NaF as a function of the anion-cation distance.

A.2. A refined particle in the box model

For scaled LiF we illustrated the particle-in-the-box model to be a good approximation for the potential of the F-center electron. Scaled LiF shows a perfect $1/a^2$ dependence of E_{abs} and perfectly linear growth of the extent of the defect wave function. For the F centers in real materials, however, this model needs to be refined. Consider, for simplicity, a two-dimensional hard-walled box the size and shape of which is determined by two independent parameters. These parameters are $r_0^{[100]}$ the distance from the center of the box to the center of its edges and $r_0^{[110]}$ the distance from the center of the box to its corners. As the notation already suggests we use the radial nodes of the ROHF ground state F-center wave functions (figs. 4.6 and 4.10) as parameters in this model which leads to a star-like shaped potential as shown in fig. A.3 (a). The energy difference between the ground and the first excited state of this model potential (fig. A.3 (b)) do, of course, not reproduce the ab-initio F-center absorption energy, but they show qualitatively the same behavior. Especially the difference between the continuous decrease of the absorption energies in scaled LiF (fig. 4.5) and the anion-specific offset as well as the reduced decay of E_{abs} in real materials (figs. 4.11 and 4.12) is nicely reproduced.

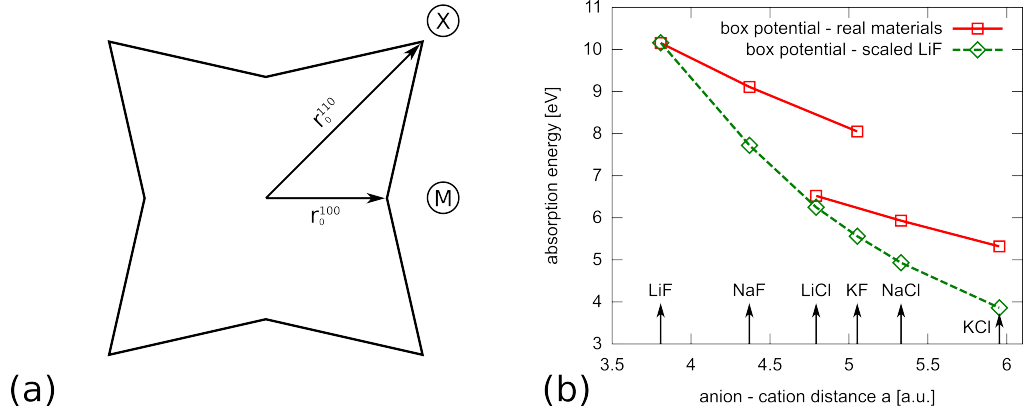


Figure A.3.: (a) Two-dimensional hard-wall model potential of the F-center electron potential well. Its shape is determined by the parameters $r_0^{[100]}$ and $r_0^{[110]}$ denoting the distances from the center of the box to the center of its edges and the distance from the center of the box to its corners, respectively. (b) Energy difference between the ground and the first excited state in the box potential in panel (a) when the position of the first radial nodes of the defect wave functions in real alkali-halide crystals and scaled LiF from figs. 4.6 and 4.10, respectively, are used as parameters $r_0^{[100]}$ and $r_0^{[110]}$.

A.3. Relation between the non-adiabatic vector \vec{F}_{ji} and scalar coupling G_{ji}

Applying $\vec{\nabla}$ onto \vec{F}_{ji} leads to

$$\begin{aligned} (\vec{\nabla} \cdot \vec{F}_{ji}) &= \vec{\nabla} \langle \Psi_j(\vec{r}; \vec{R}) | \vec{\nabla} \Psi_i(\vec{r}; \vec{R}) \rangle \\ &= \langle \vec{\nabla} \Psi_j | \vec{\nabla} \Psi_i \rangle + \langle \Psi_j | \vec{\nabla}^2 \Psi_i \rangle, \end{aligned} \quad (\text{A.1})$$

where brackets on the left hand side of the equation indicate that the $\vec{\nabla}$ operator acts only on \vec{F}_{ji} . The very last term in the upper equation equals G_{ji} which leads

to

$$\begin{aligned}
G_{ji} &= \left(\vec{\nabla} \cdot \vec{F}_{ji} \right) - \langle \vec{\nabla} \Psi_j | \vec{\nabla} \Psi_i \rangle \\
&= \left(\vec{\nabla} \cdot \vec{F}_{ji} \right) - \sum_k \langle \vec{\nabla} \Psi_j | \Psi_k \rangle \langle \Psi_k | \vec{\nabla} \Psi_i \rangle \\
&= \left(\vec{\nabla} \cdot \vec{F}_{ji} \right) + \sum_k \langle \Psi_j | \vec{\nabla} \Psi_k \rangle \langle \Psi_k | \vec{\nabla} \Psi_i \rangle \\
&= \left(\vec{\nabla} \cdot \vec{F}_{ji} \right) + \sum_k \vec{F}_{jk} \vec{F}_{ki},
\end{aligned} \tag{A.2}$$

where we used

$$\langle \vec{\nabla} \Psi_j | \Psi_i \rangle = -\langle \Psi_j | \vec{\nabla} \Psi_i \rangle, \tag{A.3}$$

since

$$\left(\vec{\nabla} \langle \Psi_j | \Psi_i \rangle \right) = \langle \vec{\nabla} \Psi_j | \Psi_i \rangle + \langle \Psi_j | \vec{\nabla} \Psi_i \rangle = 0. \tag{A.4}$$

A.4. Calculation of the non-adiabatic derivative coupling

Non-adiabatic derivative couplings

$$F_{ji}(R) = \langle \Psi_j(\vec{r}; R) | \vec{\nabla} \Psi_i(\vec{r}; R) \rangle \tag{A.5}$$

on the CASSCF and MS-CASPT2 level are approximated by finite differences. R denotes a nuclear coordinate and \vec{r} comprises all electronic degrees of freedom. Consider a real-space grid in the nuclear coordinate $\{R_m\}$ with a grid spacing of Δ . The non-adiabatic coupling vector at grid point R_m is then approximated by the symmetric difference quotient

$$\begin{aligned}
F_{ji}(R_m) &= \langle \Psi_j(\vec{r}; R_m) | \frac{\partial}{\partial R} \Psi_i(\vec{r}; R_m) \rangle \\
&= \langle \Psi_j(\vec{r}; R_m) | \frac{\Psi_i(\vec{r}; R_m + \Delta) - \Psi_i(\vec{r}; R_m - \Delta)}{2\Delta} \rangle + \mathcal{O}(\Delta^2) \\
&\approx \frac{1}{2\Delta} (\langle \Psi_j(\vec{r}; R_m) | \Psi_i(\vec{r}; R_m + \Delta) \rangle - \langle \Psi_j(\vec{r}; R_m) | \Psi_i(\vec{r}; R_m - \Delta) \rangle).
\end{aligned} \tag{A.6}$$

The overlaps $\langle \Psi_j(\vec{r}; R_m) | \Psi_i(\vec{r}; R_m + \Delta) \rangle$ and $\langle \Psi_j(\vec{r}; R_m) | \Psi_i(\vec{r}; R_m - \Delta) \rangle$ are calculated within the RASSI program of the MOLCAS program package. One- and two-electron integrals are evaluated for both types of overlaps at the geometry R_m .

The sign of CASSCF and MS-CASPT2 wave functions is random leading also to a random sign in the non-adiabatic derivative coupling. To solve this problem every wave function in eq. A.6 needs to be multiplied with a phase factor, $\phi_j(R_m) = \pm 1$. These phase factors are defined such that the overlaps between two wave functions (of the same electronic state j) at two adjacent nuclear-coordinate grid points are close to +1. How close the overlaps are to unity is determined by the grid spacing Δ . With the nuclear-coordinate grid index $m \in [1, \dots, N]$, the phase factors for each electronic state j read

$$\begin{aligned} \phi_j(R_m) &\stackrel{!}{=} 1, \quad m = N \\ \phi_j(R_m) &= \phi_j(R_{m+1}) \langle \Psi_j(\vec{r}; R_{m+1}) | \Psi_j(\vec{r}; R_m) \rangle \stackrel{!}{\approx} 1, \quad \forall m \in [1, \dots, N-1]. \end{aligned} \quad (\text{A.7})$$

A.5. Total Si³⁺ + He charge-transfer cross section within the Landau–Zener approximation

We approximate the trajectories of the Si³⁺ projectile by straight lines with constant velocity v_n (fig. A.4 (a)). When the system passes the narrow Landau–Zener like avoided crossing at R_c (fig. A.4 (b)) the radial velocity component v_{rad} is given by

$$v_{\text{rad}} = v_n \cos(\alpha). \quad (\text{A.8})$$

With $\sin(\alpha) = \frac{b}{R_c}$ this leads to

$$v_{\text{rad}} = v_n \sqrt{1 - \frac{b^2}{R_c^2}}. \quad (\text{A.9})$$

With this relation we can define an impact-parameter dependent Massey parameter which reads

$$\xi_{\text{LZ}}(b, v_n) = \frac{\gamma}{v_{\text{rad}}(b)} = \frac{\gamma}{v_n \sqrt{1 - \frac{b^2}{R_c^2}}}. \quad (\text{A.10})$$

For the Si³⁺ + He charge transfer $\gamma = 0.00024$, when v_n is given in a.u. (eq. 5.31). With the charge-transfer probability after double passage of the avoided crossing

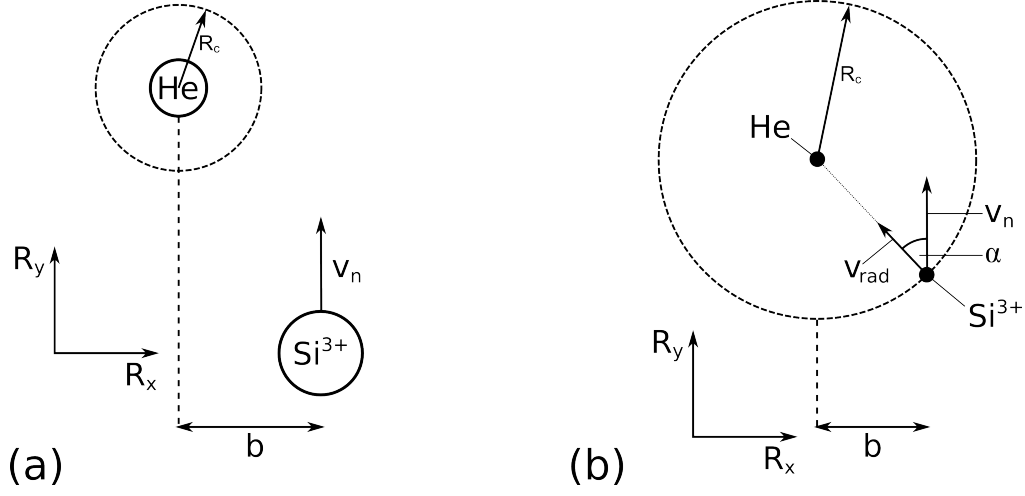


Figure A.4.: (a) Straight line approximation for the $\text{Si}^{3+} + \text{He}$ scattering. (b) Definition of the radial momentum component v_{rad} .

$\langle \mathcal{P}_{12}^{\text{LZ}} \rangle$ (eq. 5.32) the total charge-transfer cross section reads

$$\begin{aligned}
 \sigma_{\text{tot}}(v_n) &= 2\pi \int_0^\infty b \langle \mathcal{P}_{12}^{\text{LZ}} \rangle(b, v_n) db \\
 &= 4\pi \int_0^\infty b e^{-2\pi\xi_{\text{LZ}}(b, v_n)} (1 - e^{-2\pi\xi_{\text{LZ}}(b, v_n)}) db \\
 &= 4\pi \int_0^\infty b \left[e^{-\frac{2\pi\gamma}{v_n \sqrt{1 - \frac{b^2}{R_c^2}}}} - e^{-\frac{4\pi\gamma}{v_n \sqrt{1 - \frac{b^2}{R_c^2}}}} \right] db \quad (\text{A.11})
 \end{aligned}$$

A.6. Reflection probability of H^+ from an LiF surface

The potentials by O'Connor and Biersack (OCB) [187] are binary potentials for atoms that solely depend on the atomic number of the two scattering partners and the distance R between them. The potential is given by

$$V_{\text{OCB}} = \frac{Z_1 Z_2}{R} f(R/a_{\text{OCB}}), \quad (\text{A.12})$$

where Z_1 and Z_2 are the atomic numbers of the two atoms and $f(R/a_{\text{OCB}})$ is an interatomic “screening function” with a length scale referred to as the “screening

length” a_{OCB} . The screening function reads

$$f(R/a_{\text{OCB}}) = \sum_i b_i e^{-c_i R/a_{\text{OCB}}}, \quad (\text{A.13})$$

with the parameter sets $b_i = \{0.35, 0.55, 0.1\}$ and $c_i = \{0.3, 1.2, 6\}$. The screening length is given by

$$a_{\text{OCB}} = [0.045(\sqrt{Z_1} + \sqrt{Z_2}) + 0.54] \cdot 0.8854(\sqrt{Z_1} + \sqrt{Z_2})^{-2/3}. \quad (\text{A.14})$$

OCB-type potentials are successfully used to simulate projectile trajectories in atom-surface scattering experiments [170] by approximating the projectile-surface potential by a sum over binary potentials between projectile and target atoms. We use them to verify our results on the reflection probability of (initially) H^+ projectiles (perpendicular incidence) rescattered from embedded LiF clusters (see figs. 6.13 and 6.24). For every initial projectile momentum in the OCB approach, 3916 trajectories, uniformly distributed over the surface unit cell, are directed towards the surface. A projectile is considered to be absorbed when it penetrates the topmost surface layer. Embedded cluster results on the reflection probability from the topmost surface layer are in reasonable agreement with OCB results (fig. A.5) confirming the reliability of both approaches.

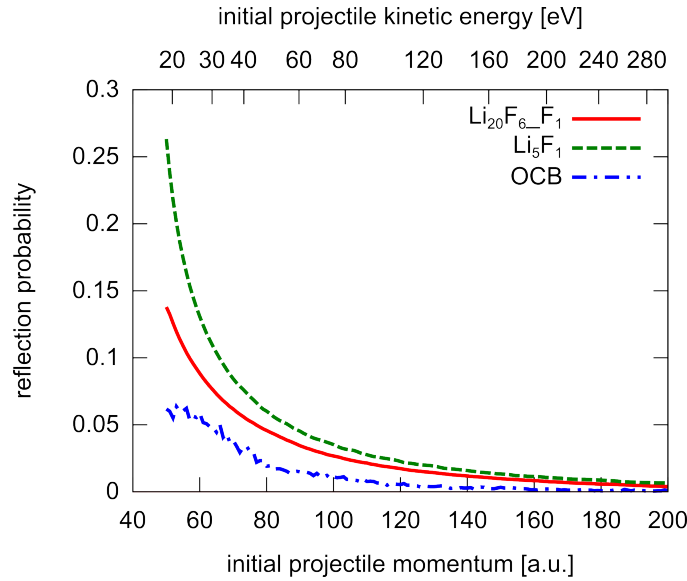


Figure A.5.: Fractions of initially H^+ (embedded cluster approach) or H (OCB approach) projectiles reflected from the topmost surface layer of an embedded $\text{Li}_{20}\text{F}_6\text{F}_1$ cluster (solid red line), an Li_5F_1 cluster (dashed green line), and a surface approximated by OCB binary potentials (dash dotted blue line).

A.7. Extrapolation of the MS-CASPT2 work function

We estimate the converged MS-CASPT2 work function, converged with cluster size, by extrapolating $W_{\text{LiF}}^{\text{MS-CASPT2}}$ to an infinite number of active F^- ions ($\#F^-$). In fig. A.6 the MS-CASPT2 work function is plotted as a function of $(\#F^-)^{-1/2}$ and $(\#F^-)^{-1/3}$ which are measures for the inverse of the linear dimension of the surface covered by the cluster and its volume, respectively. For infinitely large clusters, $(\#F^-)^{-1/2} \rightarrow 0$ and $(\#F^-)^{-1/3} \rightarrow 0$, we find by linear regression values of 10.8 eV and 10.2 eV, respectively.

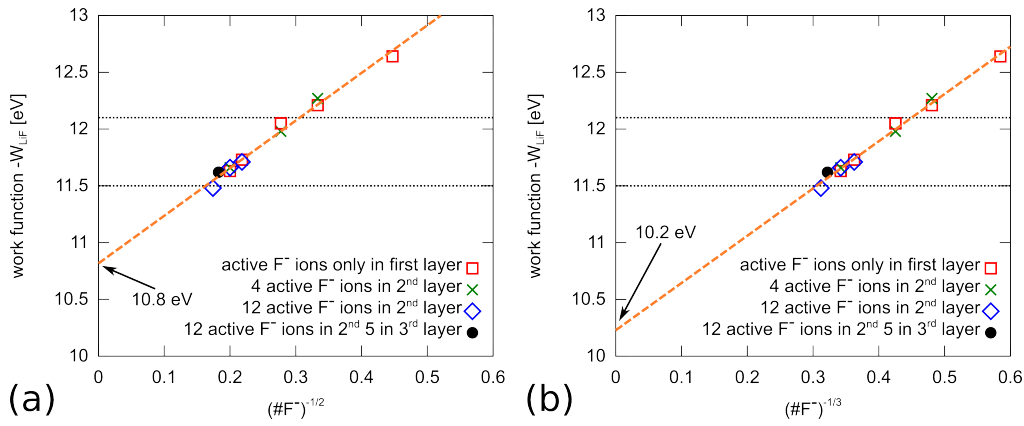


Figure A.6.: MS-CASPT2 work functions of embedded clusters as function of (a) $(\#F^-)^{-1/2}$ and (b) $(\#F^-)^{-1/3}$, where $\#F^-$ is the number of active F^- ions.

A.8. Definition of top-F and top-Li contributions

Consider initial trajectories started at $R_z = 14$ a.u. within a lateral circle with radius 1 a.u. ($R_x^2 + R_y^2 \leq 1$ a.u.) around the F^- and the Li^+ ion (fig. 6.13 (a)) which are denoted by top-F and top Li-trajectories in the following. For initial momenta larger than 90 a.u. top-F and top-Li initial trajectories account for all trajectories that are reflected from the surface. Trajectories started at $R_z = 14$ a.u. outside of the top-F or top-Li region penetrate the surface and are neglected in our analysis. For $P_{\text{init}} \gtrsim 90$ a.u., the total number of reflected hydrogen atoms $Y^0(\text{total})$ or protons $Y^+(\text{total})$ can then be splitted into these two contributions:

$$\begin{aligned} Y^0(\text{total}) &= Y^0(\text{topF}) + Y^0(\text{topLi}) \\ Y^+(\text{total}) &= Y^+(\text{topF}) + Y^+(\text{topLi}). \end{aligned} \quad (\text{A.15})$$

The total neutralization probability (for $P_{\text{init}} \gtrsim 90$ a.u.) reads then

$$\begin{aligned} N^0(\text{total}) &= \frac{Y^0(\text{total})}{Y^0(\text{total}) + Y^+(\text{total})} \\ &= \frac{Y^0(\text{topF})}{Y^0(\text{total}) + Y^+(\text{total})} + \frac{Y^0(\text{topLi})}{Y^0(\text{total}) + Y^+(\text{total})}, \end{aligned} \quad (\text{A.16})$$

with the top F and top Li contributions

$$\begin{aligned} N^0(\text{topF}) &= \frac{Y^0(\text{topF})}{Y^0(\text{total}) + Y^+(\text{total})} \\ N^0(\text{topLi}) &= \frac{Y^0(\text{topLi})}{Y^0(\text{total}) + Y^+(\text{total})}. \end{aligned} \quad (\text{A.17})$$

Both contributions are weights normalized to the *total* number of rescattered particles. The variation of the top-F contribution with the initial momentum, therefore, implicitly depends on the neutralization probability and the reflection yield of top Li since

$$N^0(\text{topF}) + N^0(\text{topLi}) = N^0(\text{total}). \quad (\text{A.18})$$

In contrast, the “local” neutralization probability of a particle started in top F and rescattered from F can behave quite differently. It needs to be said that particles started in the top F or the top Li region are always reflected at the particle they are started above. The local F^- neutralization probability completely neglects the top-Li trajectories (and the Li^+ surface ion) and reads

$$N^0(\text{localF}) = \frac{Y^0(\text{F})}{Y^0(\text{F}) + Y^+(\text{F})}. \quad (\text{A.19})$$

Acknowledgments

What has always fascinated me about physics is its predictive power. As my high-school teacher strongly promoted, one can derive, with as simple tools as pencil and paper, the response of nature to a certain question. Not surprisingly, I am finishing my PhD in the field of ab-initio simulations which represent, in some sense, the highest level of prediction making since they only rely on basic and established laws of nature without additional assumption or models. During the long and sometimes tedious way from high school to PhD many people supported me. Now it is time to say thank you.

Already since working on my master's thesis I am a member of the group of *Joachim Burgdörfer*, my thesis adviser. Throughout all this time he impressed me with his profound knowledge of physics and his seemingly infinite passion for science. After every single discussion with him I was motivated to become a better physicist and scientist. I am very grateful for all I could learn from him. Co-adviser of this thesis is *Ludger Wirtz*, professor at the University of Luxembourg. During my many visits in France and Luxembourg we did not only successfully work together but became friends. With his positive attitude he gave me a lot of strength and endurance during the last years for which I am deeply thankful. I also want to thank Ludger's family for their warm hospitality and kindness during my stays in their home. Hopefully, I could "repay" their hospitality during their trips to Burgenland. *Steffi Gräfe*, now professor in Jena, helped me a lot in solving quantum-chemistry related problems during her post-doc time in Vienna. She always strongly supported and backed me when things did not go the way I wanted them. After Steffi left and *Florian Libisch* returned from the US, Florian became a very valuable discussion partner in quantum-chemistry topics. I thank my former "office mate" *Georg Wachter* with whom I spent a great time in talking about physics, computers, music and many other things. I hope he soon can join again *Larisa Chizhova*, *Florian Aigner*, *Shuhei Yoshida*, *Markus Oswald*, and me in our joint music project, the Acoustic Phonon Band. I also want to thank all the other (former) group members for discussions, their friendship and the pleasant working environment they have created: *Renate Pazourek*, *Iva Hunger Brezinova*, *Katharina Doblhoff-Dier*, *Isabella Floss*, *Wei-Chao Jiang*, *Stefan Donsa*, *Stefan Nagele*, *Christoph Lemell*, and *Fabian Lackner*. I am also delighted to acknowledge the administrative staff at the institute *Heike Höller* and *Sylvia Riedler*. They keep the administrative work load of all institute members at a minimum and always provided valuable information on Joachim's whereabouts.

Apart from group members I had the pleasure to interact with other great scientists. I would like to thank *Thorsten Klüner* for reviewing this thesis and for his inspiring talk at the Cecam workshop in Zaragoza in 2012. I am very much indebted to *Francesco Aquillante*. He is MOLCAS developer and always answered my bothersome questions with patience. We collaborated for a long time with *Peter Blaha* and *Ferenc Karsai* from the chemistry department of the TU Wien. I would like to thank both for the large effort they put in the work on the color centers. As a result we were able to publish two interesting papers. I also would like to thank *Peter Bauer* and *Dominik Göbel* from the university in Linz who provided the experimental data in the last chapter of this thesis. We have had many interesting discussions and spent beautiful times on several conferences. Being member of the doctoral college *Solids4Fun* I met many motivated and skilled young scientists from different research fields. During the student seminars and the summer schools they introduced me to their fields and I learned to see my own work from other perspectives.

One of my passions besides science is music. Apart from the Acoustic Phonon Band I would like to thank Larisa and *Sandro Miori* co-founders of Big Peter's band. Everyday I am looking forward to the next rehearsal because of the great music and the lovely people of Big Peter's Band. I am deeply grateful to *Christian Schulte* and all the other members of the Musikverein Großpetersdorf for all I could learn from them and all the beautiful time we spent together.

I owe a very deep "thank you" to *Hannes Zetter* and his family, representative for all my friends. Hannes and I are friends since we are six and I am very sad we have so few chances to spend time together. A big "thank you" is also due for the warmth *Людмила* and *Александр Чижов* offered during all the marvelous new year's eves I spent in cold *Нижний Новгород*. I am very grateful for all the support of my family: Katharina, Martin, Edith, Franz, Helene, and Josef. They never stopped showering me with their love. For her support I would like to thank Larisa. She consistently pushes me out of my comfort zone which helped me to develop various new skills and which makes us experience great moments together. I hope there are many more such moments to come.

I gratefully acknowledge the financial support of the Austrian Science Fund (FWF) in SFB-041 ViCoM and W1243 Solids4Fun.

Bibliography

- [1] F. Watt, A. A. Bettiol, J. A. Van Kan, E. J. Teo, and M. B. H. Breese. *ION BEAM LITHOGRAPHY AND NANOFABRICATION: A REVIEW*. Int. J. Nanosci. **04**, 269 (2005).
- [2] Z. Hameiri, T. Puzzer, L. Mai, A. B. Sproul, and S. R. Wenham. *Laser induced defects in laser doped solar cells*. Progress in Photovoltaics: Research and Applications **19**, 391 (2011).
- [3] K. Nemoto, M. Trupke, S. J. Devitt, A. M. Stephens, B. Scharfenberger, K. Buczak, T. Nöbauer, M. S. Everitt, J. Schmiedmayer, and W. J. Munro. *Photonic Architecture for Scalable Quantum Information Processing in Diamond*. Physical Review X **4**, 031022 (2014).
- [4] E. Goldstein. *Die Thätigkeit (sic!) der Physikalisch-Technischen Reichsanstalt in der Zeit vom 1. April 1895 bis 1. Februar 1896*. Zeitschrift für Instrumentenkunde **16**, 211 (1896).
- [5] F. Seitz. *Color Centers in Alkali Halide Crystals*. Reviews of Modern Physics **18**, 384 (1946).
- [6] F. Seitz. *Color Centers in Alkali Halide Crystals. II*. Reviews of Modern Physics **26**, 7 (1954).
- [7] W. B. Fowler. *The Physics of Colour Centers*. Academic, New York (1968).
- [8] A. M. Stoneham. *Theory of Defects in Solids*. Clarendon Press, Oxford (1975).
- [9] E. Mollwo. *Über die Absorptionsspektren photochemisch verfärbter Alkalihalogenid-Kristalle*. Nachr. Ges. Wiss. Göttingen p. 97 (1931).
- [10] H. F. Ivey. *Spectral Location of the Absorption Due to Color Centers in Alkali Halide Crystals*. Physical Review **72**, 341 (1947).
- [11] R. F. Wood. *The theoretical basis of the Mollwo-Ivey relationship in alkali halide color centers*. Journal of Physics and Chemistry of Solids **26**, 615 (1965).

- [12] M. Malghani and D. Smith. *Physical basis of the Mollwo-Ivey relation between lattice constant and optical absorption of defects in ionic crystals*. Physical Review Letters **69**, 184 (1992).
- [13] C. Auth, A. G. Borisov, and H. Winter. *High Fractions of Negative Ions in Grazing Scattering of Fast Oxygen Atoms from a LiF(100) Surface*. Physical Review Letters **75**, 2292 (1995).
- [14] A. Borisov, V. Sidis, and H. Winter. *Diabatic Energy Level Confluence: The Mechanism of Negative Ion Conversion of Neutral Atoms in Grazing Scattering from Insulator Surfaces*. Physical Review Letters **77**, 1893 (1996).
- [15] A. Arnau, F. Aumayr, P. M. Echenique, M. Grether, W. Heiland, J. Limburg, R. Morgenstern, P. Roncin, S. Schippers, R. Schuch, N. Stolterfoht, P. Varga, T. J. M. Zouros, and H. P. Winter. *Interaction of slow multicharged ions with solid surfaces*. Surface Science Reports **27**, 113 (1997).
- [16] L. Wirtz, J. Burgdörfer, M. Dallos, T. Müller, and H. Lischka. *Potential-energy surfaces for charge exchange between singly charged ions and a LiF surface*. Physical Review A **68**, 032902 (2003).
- [17] J. P. Perdew. *Density functional theory and the band gap problem*. International Journal of Quantum Chemistry **28**, 497 (2009).
- [18] S. N. Steinmann, C. Piemontesi, A. Delachat, and C. Corminboeuf. *Why are the Interaction Energies of Charge-Transfer Complexes Challenging for DFT?* J. Chem. Theory Comput. **8**, 1629 (2012).
- [19] Z.-L. Cai, M. J. Crossley, J. R. Reimers, R. Kobayashi, and R. D. Amos. *Density Functional Theory for Charge Transfer: The Nature of the N-Bands of Porphyrins and Chlorophylls Revealed through CAM-B3LYP, CASPT2, and SAC-CI Calculations*. J. Phys. Chem. B **110**, 15624 (2006).
- [20] A. Dreuw and M. Head-Gordon. *Failure of Time-Dependent Density Functional Theory for Long-Range Charge-Transfer Excited States: The Zinbacteriochlorin-Bacteriochlorin and Bacteriochlorophyll-Spheroidene Complexes*. J. Am. Chem. Soc. **126**, 4007 (2004).
- [21] J. Autschbach. *Charge-Transfer Excitations and Time-Dependent Density Functional Theory: Problems and Some Proposed Solutions*. ChemPhysChem **10**, 1757 (2009).
- [22] G. H. Booth, A. Gruneis, G. Kresse, and A. Alavi. *Towards an exact description of electronic wavefunctions in real solids*. Nature **493**, 365 (2012).

- [23] F. Libisch, C. Huang, P. Liao, M. Pavone, and E. A. Carter. *Origin of the Energy Barrier to Chemical Reactions of O₂ on Al(111): Evidence for Charge Transfer, Not Spin Selection*. Physical Review Letters **109**, 198303 (2012).
- [24] A. Severo Pereira Gomes and C. R. Jacob. *Quantum-chemical embedding methods for treating local electronic excitations in complex chemical systems*. Annual Reports Section "C" (Physical Chemistry) **108**, 222 (2012).
- [25] C. Sousa, S. Tosoni, and F. Illas. *Theoretical Approaches to Excited-State-Related Phenomena in Oxide Surfaces*. Chem. Rev. **113**, 4456 (2013).
- [26] F. Libisch, J. Cheng, and E. A. Carter. *Electron-Transfer-Induced Dissociation of H₂ on Gold Nanoparticles: Excited-State Potential Energy Surfaces via Embedded Correlated Wavefunction Theory*. Zeitschrift für Physikalische Chemie **227**, 1455 (2013).
- [27] F. Libisch, C. Huang, and E. A. Carter. *Embedded Correlated Wavefunction Schemes: Theory and Applications*. Acc. Chem. Res. **47**, 2768 (2014).
- [28] T. Klüner, H. J. Freund, V. Staemmler, and R. Kosloff. *Theoretical Investigation of Laser Induced Desorption of Small Molecules from Oxide Surfaces: A First Principles Study*. Physical Review Letters **80**, 5208 (1998).
- [29] C. Carbogno, A. Groß, and M. Rohlfing. *Ab initio investigation of the laser induced desorption of iodine from KI(100)*. Applied Physics A **88**, 579 (2007).
- [30] T. Klüner. *Photodesorption of diatomic molecules from surfaces: A theoretical approach based on first principles*. Progress in Surface Science **85**, 279 (2010).
- [31] M. Mehring and T. Klüner. *Understanding surface photochemistry from first principles: The case of CO-TiO₂(110)*. Chemical Physics Letters **513**, 212 (2011).
- [32] A. Szabo and N. S. Ostlund. *Modern Quantum Chemistry: Introduction to Advanced Electronic Structure Theory*. Dover (1996).
- [33] F. Jensen. *Introduction to Computational Chemistry*. John Wiley & Sons, Ltd, 2 edition (2009).
- [34] T. Helgaker, P. Jorgensen, and J. Olsen. *Molecular Electronic-Structure Theory*. Wiley (2000).
- [35] T. D. Crawford, H. F. Schaefer, and T. J. Lee. *On the energy invariance of open-shell perturbation theory with respect to unitary transformations of molecular orbitals*. The Journal of Chemical Physics **105**, 1060 (1996).

- [36] M. Hanrath. *On the concepts of connectivity, separability, and consistency: An illustration by partitioned diagrams and numerical probing*. Chemical Physics **356**, 31 (2009).
- [37] O. Christiansen. *Coupled Cluster Theory with Emphasis on Selected New Developments*. Theoretical Chemistry Accounts **116**, 106 (2006).
- [38] M. Head-Gordon. *Quantum Chemistry and Molecular Processes*. J. Phys. Chem. **100**, 13213 (1996).
- [39] K. Andersson, P. A. Malmqvist, B. O. Roos, A. J. Sadlej, and K. Wolinski. *Second-order perturbation theory with a CASSCF reference function*. J. Phys. Chem. **94**, 5483 (1990).
- [40] K. Andersson, P. Malmqvist, and B. O. Roos. *Second-order perturbation theory with a complete active space self-consistent field reference function*. The Journal of Chemical Physics **96**, 1218 (1992).
- [41] J. Finley, P.-A. Malmqvist, B. O. Roos, and L. Serrano-Andrés. *The multi-state CASPT2 method*. Chemical Physics Letters **288**, 299 (1998).
- [42] G. Chiarotti. *1.6 Crystal structures and bulk lattice parameters of materials quoted in the volume*, volume 24c of *Landolt-Börnstein - Group III Condensed Matter*, chapter 6, pp. 21–26. Springer-Verlag, Berlin/Heidelberg (1995).
- [43] M. Piacentini, D. Lynch, and C. Olson. *Thermoreflectance of LiF between 12 and 30 eV*. Physical Review B **13**, 5530 (1976).
- [44] R. Hilsch and R. W. Pohl. *Über die Lichtabsorption in einfachen Ionengittern und den elektrischen Nachweis des latenten Bildes*. Zeitschrift für Physik **68**, 721 (1931).
- [45] G. Baldacchini. *Relaxed Excited States of Color Centers*. In B. Bartolo and C. Beckwith (eds.), *Optical Properties of Excited States in Solids*, volume 301 of *NATO ASI Series*, pp. 255–303. Springer US (1992).
- [46] M. Fox. *Optical Properties of Solids*, pp. 186–203. Oxford University Press, first edition (2001).
- [47] F. Karsai, P. Tiwald, R. Laskowski, F. Tran, D. Koller, S. Gräfe, J. Burgdörfer, L. Wirtz, and P. Blaha. *F center in lithium fluoride revisited: Comparison of solid-state physics and quantum-chemistry approaches*. Physical Review B **89**, 125429 (2014).

- [48] F. Karsai. *Improved ground and excited states using MBPT and DFT methods within the APW framework*. Ph.D. thesis, Institute of Materials Chemistry, TU Wien (2015).
- [49] T. Inui and Y. Uemura. *Untitled*. *Prog. Theor. Phys.* **5**, 252 (1950).
- [50] J. N. Murrell and J. Tennyson. *Molecular SCF calculations on the F centre of LiF*. *Chemical Physics Letters* **69**, 212 (1980).
- [51] A. Y. S. Kung, A. B. Kunz, and J. M. Vail. *Unrestricted-Hartree-Fock cluster analysis of F and F_A centers in some alkali halides*. *Phys. Rev. B* **26**, 3352 (1982).
- [52] R. Pandey, M. Seel, and A. B. Kunz. *Ab initio study of localization and excitation of an excess electron in alkali halide clusters*. *Phys. Rev. B* **41**, 7955 (1990).
- [53] R. F. W. Bader and J. A. Platts. *Characterization of an F-center in an alkali halide cluster*. *Journal of Chemical Physics* **107**, 8545 (1997).
- [54] C. S. Ewig, J. Tellinghuisen, and M. H. Mendenhall. *Ab initio F-center electron topology in LiF*. *Chemical Physics Letters* **188**, 501 (1992).
- [55] C. Kölmel and C. S. Ewig. *Ab Initio Embedded Cluster Study of F and M Centers in LiF*. *J. Phys. Chem. B* **105**, 8538 (2001).
- [56] B. Gourary and F. Adrian. *Approximate Wave Functions for the F Center, and Their Application to the Electron Spin Resonance Problem*. *Physical Review* **105**, 1180 (1957).
- [57] R. H. Bartram, A. M. Stoneham, and P. Gash. *Ion-Size Effects in Color Centers*. *Phys. Rev.* **176**, 1014 (1968).
- [58] S. Huzinaga, L. Seijo, Z. Barandiarán, and M. Klobukowski. *The ab initio model potential method. Main group elements*. *Journal of Chemical Physics* **86**, 2132 (1986).
- [59] L. Seijo and Z. Barandiarán. *The textitAb Initio Model Potential Method: A Common Strategy for Effective Core Potential and Embedded Cluster Calculations*, chapter 2, pp. 55–152. World Scientific, Singapur (1999).
- [60] H. M. Evjen. *On the Stability of Certain Heteropolar Crystals*. *Phys. Rev.* **39**, 675 (1932).

- [61] T. H. Dunning. *Gaussian basis sets for use in correlated molecular calculations. I. The atoms boron through neon and hydrogen*. Journal of Chemical Physics **90**, 1007 (1989).
- [62] A. A. Leitão, R. B. Capaz, N. V. Vugman, and C. E. Bielschowsky. *Hyperfine interactions and lattice distortion of the F center in KCl, NaCl and LiCl crystals*. Journal of Molecular Structure: THEOCHEM **580**, 65 (2002).
- [63] J.-i. Adachi and N. Kosugi. *An Ab Initio Molecular Orbital Approach to Electronic Structures of the F Center in NaCl. Effects of Basis Set and Cluster Size*. Bulletin of the Chemical Society of Japan **66**, 3314 (1993).
- [64] F. Aquilante, L. De Vico, N. Ferré, G. Ghigo, P.-A. Malmqvist, P. Neogrády, T. B. Pedersen, M. Pitonák, M. Reiher, B. O. Roos, L. Serrano-Andrés, M. Urban, V. Veryazov, and R. Lindh. *MOLCAS 7: The Next Generation*. Journal of Computational Chemistry **31**, 224 (2010).
- [65] P. W. Atkins and R. S. Friedman. *Molecular Quantum Mechanics*. University Press, New York, 3 edition (1997).
- [66] E. Miyoshi, Y. Miyake, S. Katsuki, and Y. Sakai. *Theoretical study on the electronic structures of various F centers in MgO crystals*. J. Mol. Struct-Theochem. **451**, 81 (1998).
- [67] D. G. Truhlar. *Basis-set extrapolation*. Chemical Physics Letters **294**, 45 (1999).
- [68] C. Sousa and F. Illas. *On the accurate prediction of the optical absorption energy of F-centers in MgO from explicitly correlated ab initio cluster model calculations*. The Journal of Chemical Physics **115**, 1435 (2001).
- [69] P. L. Fast, M. L. Sanchez, and D. G. Truhlar. *Infinite basis limits in electronic structure theory*. Journal of Chemical Physics **111**, 2921 (1999).
- [70] A. J. C. Varandas. *Basis-set extrapolation of the correlation energy*. Journal of Chemical Physics **113**, 8880 (2000).
- [71] R. K. Dawson and D. Pooley. *F Band Absorption in Alkali Halides as a Function of Temperature*. physica status solidi (b) **35**, 95 (1969).
- [72] G. Feher. *Electronic Structure of F Centers in KCl by the Electron Spin Double-Resonance Technique*. Physical Review **105**, 1122 (1957).
- [73] M. Bucher. *The electron inside the nucleus: an almost classical derivation of the isotropic hyperfine interaction*. European Journal of Physics **21**, 19 (2000).

- [74] W. C. Holton and H. Blum. *Paramagnetic Resonance of F Centers in Alkali Halides*. Physical Review **125**, 89 (1962).
- [75] G. Mallia, R. Orlando, C. Roetti, P. Ugliengo, and R. Dovesi. *F center in LiF: A quantum mechanical ab initio investigation of the hyperfine interaction between the unpaired electron at the vacancy and its first seven neighbors*. Physical Review B **63**, 235102 (2001).
- [76] M. Nisoli, S. De Silvestri, O. Svelto, R. Scholz, R. Fanciulli, V. Pellegrini, F. Beltram, and F. Bassani. *Single-Electron Subpicosecond Coherent Dynamics in KBr F Centers*. Phys. Rev. Lett. **77**, 3463 (1996).
- [77] H. Bilz and W. Kress. *Phonon Dispersion Relations in Insulators*. Springer-Verlag, Berlin Heidelberg (1979).
- [78] A. Schüller, S. Wethekam, D. Blauth, H. Winter, F. Aigner, N. Simonović, B. Solleder, J. Burgdörfer, and L. Wirtz. *Rumpling of LiF(001) surface from fast atom diffraction*. Physical Review A **82**, 062902 (2010).
- [79] G. Russell and C. Klick. *Configuration Coordinate Curves for F-Centers in Alkali Halide Crystals*. Physical Review **101**, 1473 (1956).
- [80] A. Alkauskas, B. B. Buckley, D. D. Awschalom, and C. G. Van de Walle. *First-principles theory of the luminescence lineshape for the triplet transition in diamond NV centres*. New Journal of Physics **16**, 073026 (2014).
- [81] R. Feynman. *Slow Electrons in a Polar Crystal*. Physical Review **97**, 660 (1955).
- [82] H. Fröhlich. *Electrons in lattice fields*. Advances in Physics **3**, 325 (1954).
- [83] T. Koyama and T. Suemoto. *Dynamics of nuclear wave packets at the F center in alkali halides*. Reports on Progress in Physics **74**, 076502 (2011).
- [84] G. Baldacchini. *Radiative and Nonradiative Processes in Color Centers*. In B. Di Bartolo (ed.), *Advances in Nonradiative Processes in Solids*, volume 249 of *NATO ASI Series*, pp. 219–259. Springer US (1991).
- [85] G. Baldacchini. *Colored LiF: an optical material for all seasons*. Journal of Luminescence **100**, 333 (2002).
- [86] L. Bosi, P. Podini, and G. Spinolo. *Data and Speculations on the Electronic Problem for the Relaxed Excited F Center*. Physical Review **175**, 1133 (1968).

- [87] G. Baldacchini, M. Cremona, R. M. Montereali, U. M. Grassano, and V. Kalinov. *Emission properties of γ irradiated LiF crystals excited in the F absorption band by an excimer laser*. In O. Kanert and J. M. Spaeth (eds.), *Proceedings of the XII international conference on defects in insulating materials*, volume 2, p. 1103 (1993).
- [88] G. Baldacchini. *Radiationless Processes in Color Centers*, p. 23. Nova Science Publishers Inc. (1992).
- [89] L. Hedin. *New Method for Calculating the One-Particle Green's Function with Application to the Electron-Gas Problem*. *Physical Review* **139**, A796 (1965).
- [90] S. Albrecht, L. Reining, R. Del Sole, and G. Onida. *Ab Initio Calculation of Excitonic Effects in the Optical Spectra of Semiconductors*. *Physical Review Letters* **80**, 4510 (1998).
- [91] F. Tran and P. Blaha. *Accurate Band Gaps of Semiconductors and Insulators with a Semilocal Exchange-Correlation Potential*. *Physical Review Letters* **102**, 226401 (2009).
- [92] P. Rinke, A. Schleife, E. Kioupakis, A. Janotti, C. Rödl, F. Bechstedt, M. Scheffler, and C. G. Van de Walle. *First-Principles Optical Spectra for F Centers in MgO*. *Physical Review Letters* **108**, 126404 (2012).
- [93] D. Domínguez-Ariza, C. Sousa, F. Illas, D. Ricci, and G. Pacchioni. *Ground- and excited-state properties of M-center oxygen vacancy aggregates in the bulk and surface of MgO*. *Physical Review B* **68**, 054101 (2003).
- [94] H. Fröhlich. *Über die Lage der Absorptionsspektren photochemisch verfärbter Alkalihalogenidkristalle*. *Zeitschrift für Physik* **80**, 819 (1933).
- [95] F. Stöckmann. *Untitled*. *Zeitschrift für Physikalische Chemie* **198**, 215 (1951).
- [96] F. Stöckmann. *Zur Physik der Kristallphosphore*. *Naturwissenschaften* **39**, 226 (1952).
- [97] F. Stöckmann. *Zur Physik der Kristallphosphore. (Fortsetzung)*. *Naturwissenschaften* **39**, 246 (1952).
- [98] D. Y. Smith and M. Inokuti. *Ion-size effects and the spatial extent of defects*. *Radiation Effects and Defects in Solids* **155**, 43 (2001).
- [99] C. Buchenauer and D. Fitchen. *Pressure Shift of the F Band in Alkali Halides: Ion-Size Effects*. *Physical Review* **167**, 846 (1968).

- [100] P. Tiwald, F. Karsai, R. Laskowski, S. Gräfe, P. Blaha, J. Burgdörfer, and L. Wirtz. *Ab initio perspective on the Mollwo-Ivey relation for F centers in alkali halides*. Physical Review B **92**, 144107 (2015).
- [101] M. S. Malghani and D. Y. Smith. *Calculation of the Mollwo-Ivey parameters in the point-ion approximation*. Radiation Effects and Defects in Solids **134**, 101 (1995).
- [102] D. Y. Smith. *Pauli-principle effects in the analysis of optical spectra*. Radiation Effects and Defects in Solids **149**, 209 (1999).
- [103] D. Y. Smith and M. S. Malghani. *Optical determination of the spatial extent of defects in insulators*. Nuclear Instruments and Methods in Physics Research Section B: Beam Interactions with Materials and Atoms **141**, 42 (1998).
- [104] J. Vinti. *Sum Rules for Atomic Transition Probabilities*. Physical Review **41**, 432 (1932).
- [105] M. Brauwers, R. Evrard, and E. Kartheuser. *Sum rules for F centers in alkali halides*. Physical Review B **12**, 5864 (1975).
- [106] F. Lüty. *Höhere Anregungszustände von Farbzentren*. Zeitschrift für Physik **160**, 1 (1960).
- [107] P. W. Fowler and P. A. Madden. *In-crystal polarizabilities of alkali and halide ions*. Physical Review B **29**, 1035 (1984).
- [108] R. D. Shannon. *Revised effective ionic radii and systematic studies of interatomic distances in halides and chalcogenides*. Acta Crystallographica Section A **32**, 751 (1976).
- [109] A. Smakula, N. Maynard, and A. Repucci. *Color Centers in Mixed Crystals of Alkali Halides*. Physical Review **130**, 113 (1963).
- [110] P. Haas, F. Tran, and P. Blaha. *Calculation of the lattice constant of solids with semilocal functionals*. Physical Review B **79**, 085104 (2009).
- [111] G. Sandrone and D. A. Dixon. *A Periodic Density Functional Theory and Hartree-Fock Study of Alkali Halides with Gaussian Orbitals*. J. Phys. Chem. A **102**, 10310 (1998).
- [112] W. Domcke, D. R. Yarkony, and H. Köppel (eds.). *Conical Intersections*, volume 15. World Scientific (2004).
- [113] N. Hiroki. *Nonadiabatic Transitions*. World Scientific (2002).

- [114] E. Nikitin. *Adiabatic and Diabatic Collision Processes at Low Energies*. In G. Drake (ed.), *Springer Handbook of Atomic, Molecular, and Optical Physics*, pp. 741–752. Springer New York (2006).
- [115] W. Pauli. *Über das Modell des Wasserstoff-Molekülions. (German) [On the model of the hydrogen molecular ion]*. Ph.D. thesis, Ludwig-Maximilians-Universität München, Munich, Germany (1921).
- [116] F. Aigner, N. Simonović, B. Solleder, L. Wirtz, and J. Burgdörfer. *Suppression of Decoherence in Fast-Atom Diffraction at Surfaces*. *Physical Review Letters* **101**, 253201 (2008).
- [117] P. Tiwald, A. Schüller, H. Winter, K. Tökesi, F. Aigner, S. Gräfe, C. Lemell, and J. Burgdörfer. *Interaction potentials for fast atoms in front of Al surfaces probed by rainbow scattering*. *Physical Review B* **82**, 125453 (2010).
- [118] S. L. Baliunas and S. E. Butler. *Silicon lines as spectral diagnostics - The effect of charge transfer*. *The Astrophysical Journal* **235**, L45 (1980).
- [119] S. E. Butler and J. C. Raymond. *Charge transfer in astrophysical shocks*. *The Astrophysical Journal* **240**, 680 (1980).
- [120] Z. Fang and V. H. S. Kwong. *Charge Transfer between Ground-State Si^{3+} and He at Electron-Volt Energies*. *The Astrophysical Journal* **483**, 527 (1997).
- [121] S. E. Butler and A. Dalgarno. *Charge transfer of multiply charged ions with hydrogen and helium: Landau-Zener calculations*. *Astrophys. J.* **241**, 838 (1980).
- [122] P. Honvault, M. C. Bacchus-Montabonel, M. Gargaud, and R. McCarroll. *Charge transfer between Si^{3+} and helium at thermal and low energies*. *Chemical Physics* **238**, 401 (1998).
- [123] P. C. Stancil, N. J. Clarke, B. Zygelman, and D. L. Cooper. *Ab initio study of charge transfer in low-energy collisions with helium*. *Journal of Physics B: Atomic, Molecular and Optical Physics* **32**, 1523 (1999).
- [124] D. Rabli, M. Gargaud, and R. McCarroll. *Electron capture in low-energy collisions of Si^{3+} with He*. *Journal of Physics B: Atomic, Molecular and Optical Physics* **34**, 1395 (2001).
- [125] H. Tawara, K. Okuno, C. Fehrenbach, C. Verzani, M. Stockli, B. Depaola, P. Richard, and P. Stancil. *Electron-capture processes of low-energy Si^{3+} , Si^{4+} , and Si^{5+} ions in collisions with helium atoms*. *Physical Review A* **63**, 062701 (2001).

- [126] D. R. Yarkony. *Diabolical conical intersections*. Reviews of Modern Physics **68**, 985 (1996).
- [127] F. Smith. *Diabatic and Adiabatic Representations for Atomic Collision Problems*. Physical Review **179**, 111 (1969).
- [128] M. Baer. *Adiabatic and diabatic representations for atom-molecule collisions: Treatment of the collinear arrangement*. Chemical Physics Letters **35**, 112 (1975).
- [129] Z. H. Top and M. Baer. *Incorporation of electronically nonadiabatic effects into bimolecular reactive systems. I. Theory*. The Journal of Chemical Physics **66**, 1363 (1977).
- [130] M. Baer. *Electronic non-adiabatic transitions derivation of the general adiabatic-diabatic transformation matrix*. Molecular Physics **40**, 1011 (1980).
- [131] F. Plasser, G. Granucci, J. Pittner, M. Barbatti, M. Persico, and H. Lischka. *Surface hopping dynamics using a locally diabatic formalism: Charge transfer in the ethylene dimer cation and excited state dynamics in the 2-pyridone dimer*. The Journal of Chemical Physics **137**, 22A514 (2012).
- [132] B. Esry and H. Sadeghpour. *Split diabatic representation*. Physical Review A **68**, 042706 (2003).
- [133] H. Nakamura. *Nonadiabatic Transition, Concepts, Basic Theories and Applications*. World Scientific (2002).
- [134] L. D. Landau. *On the theory of transfer of energy at collisions I*. Phys. Z. Sowjetunion **1**, 88 (1932).
- [135] L. D. Landau. *On the theory of transfer of energy at collisions II*. Phys. Z. Sowjetunion **2**, 46 (1932).
- [136] C. Zener. *Non-Adiabatic Crossing of Energy Levels*. Proceedings of the Royal Society of London A: Mathematical, Physical and Engineering Sciences **137**, 696 (1932).
- [137] E. C. G. Stueckelberg. *Theorie der unelastischen Stösse zwischen Atomen*. Helv. Phys. Acta **5**, 369 (1932).
- [138] N. Rosen and C. Zener. *Double Stern-Gerlach Experiment and Related Collision Phenomena*. Physical Review **40**, 502 (1932).
- [139] Y. N. Demkov. *Charge Transfer at Small Resonance Defects*. Journal of Experimental and Theoretical Physics (USSR) **18**, 138 (1964).

- [140] Y. Demkov and V. N. Ostrovskii. *Zero-Range Potentials and Their Applications in Atomic Physics*. Springer US, Boston, MA (1988).
- [141] J. C. Tully. *Molecular dynamics with electronic transitions*. The Journal of Chemical Physics **93**, 1061 (1990).
- [142] M. Barbatti. *Nonadiabatic dynamics with trajectory surface hopping method*. Wiley Interdisciplinary Reviews: Computational Molecular Science **1**, 620 (2011).
- [143] M. Barbatti, R. Shepard, and H. Lischka. *Computational and Methodological Elements for Nonadiabatic Trajectory Dynamics Simulations of Molecules*, volume 17. World Scientific (2011).
- [144] N. Shenvi, J. E. Subotnik, and W. Yang. *Phase-corrected surface hopping: Correcting the phase evolution of the electronic wavefunction*. The Journal of Chemical Physics **135**, 024101 (2011).
- [145] B. Zygelman, D. Cooper, M. Ford, A. Dalgarno, J. Gerratt, and M. Raimondi. *Charge transfer of N^{4+} with atomic hydrogen*. Physical Review A **46**, 3846 (1992).
- [146] B. H. Bransden and M. R. C. McDowell. *Charge Exchange and the Theory of Ion-Atom Collisions*, volume 82 of *International Series of Monographs on Physics*. Oxford Science Publication (1992).
- [147] R. Díez Muiño and H. F. Busnengo (eds.). *Dynamics of Gas-Surface Interactions*, volume 50. Springer Berlin Heidelberg, Berlin, Heidelberg (2013).
- [148] J. I. Juaristi, M. Alducin, R. D. Muiño, H. F. Busnengo, and A. Salin. *Role of Electron-Hole Pair Excitations in the Dissociative Adsorption of Diatomic Molecules on Metal Surfaces*. Physical Review Letters **100**, 116102 (2008).
- [149] G. Füchsel, S. Schimka, and P. Saalfrank. *On the Role of Electronic Friction for Dissociative Adsorption and Scattering of Hydrogen Molecules at a Ru(0001) Surface*. J. Phys. Chem. A **117**, 8761 (2013).
- [150] M. Blanco-Rey, J. I. Juaristi, R. Díez Muiño, H. F. Busnengo, G. J. Kroes, and M. Alducin. *Electronic Friction Dominates Hydrogen Hot-Atom Relaxation on Pd(100)*. Physical Review Letters **112**, 103203 (2014).
- [151] S. P. Rittmeyer, J. Meyer, J. I. Juaristi, and K. Reuter. *Electronic Friction-Based Vibrational Lifetimes of Molecular Adsorbates: Beyond the Independent-Atom Approximation*. Physical Review Letters **115**, 046102 (2015).

- [152] T. Klüner, H. J. Freund, J. Freitag, and V. Staemmler. *Laser-induced desorption of NO from NiO(100): Abinitio calculations of potential surfaces for intermediate excited states*. The Journal of Chemical Physics **104**, 10030 (1996).
- [153] R. Brako and D. M. Newns. *Theory of electronic processes in atom scattering from surfaces*. Reports on Progress in Physics **52**, 655 (1989).
- [154] J. Los and J. J. C. Geerlings. *Charge exchange in atom-surface collisions*. Physics Reports **190**, 133 (1990).
- [155] J. Burgdörfer. *Atomic Collisions with Surfaces*, chapter 11, p. 517. World Scientific (1993).
- [156] A. R. Canario, L. Guillemot, O. Grizzi, Y. Bandurin, and V. A. Esaulov. *Scattering of F atoms and anions on a TiO₂(110) surface*. Surface Science **603**, 1099 (2009).
- [157] C. A. Monreal. *Auger neutralization and ionization processes for charge exchange between slow noble gas atoms and solid surfaces*. Progress in Surface Science **89**, 80 (2014).
- [158] N. D. Lang and W. Kohn. *Theory of Metal Surfaces: Induced Surface Charge and Image Potential*. Physical Review B **7**, 3541 (1973).
- [159] J. Burgdörfer and E. Kupfer. *Distance of Excited-State Formation in Ion-Surface Collisions*. Physical Review Letters **57**, 2649 (1986).
- [160] J. Burgdörfer, E. Kupfer, and H. Gabriel. *Theory of resonant charge transfer in ion-surface collisions at grazing incidence at intermediate velocities*. Physical Review A **35**, 4963 (1987).
- [161] P. Nordlander and J. C. Tully. *Energy Shifts and Broadening of Excited Hydrogen-Atom Levels in the Vicinity of a Metal Surface*. Physical Review Letters **61**, 990 (1988).
- [162] P. Kürpick and U. Thumm. *Hybridization of ionic levels at metal surfaces*. Physical Review A **58**, 2174 (1998).
- [163] C. C. Hsu, H. Bu, A. Bousetta, J. W. Rabalais, and P. Nordlander. *Angular dependence of charge-transfer probabilities between O⁻ and a Ni{100}-c(2x2)-O surface*. Physical Review Letters **69**, 188 (1992).
- [164] A. G. Borisov, A. K. Kazansky, and J. P. Gauyacq. *Stabilisation of alkali-adsorbate-induced states on Cu(111) surfaces*. Surface Science **430**, 165 (1999).

- [165] K. Niedfeldt, E. A. Carter, and P. Nordlander. *First principles resonance widths for Li near an Al(001) surface: Predictions of scattered ion neutralization probabilities*. The Journal of Chemical Physics **121**, 3751 (2004).
- [166] X. Li and J. C. Tully. *Ab initio time-resolved density functional theory for lifetimes of excited adsorbate states at metal surfaces*. Chemical Physics Letters **439**, 199 (2007).
- [167] C. Moss, C. Isborn, and X. Li. *Ehrenfest dynamics with a time-dependent density-functional-theory calculation of lifetimes and resonant widths of charge-transfer states of Li^+ near an aluminum cluster surface*. Physical Review A **80**, 024503 (2009).
- [168] B. Obreshkov and U. Thumm. *H^- formation in collisions of hydrogen atoms with Al(100) surfaces*. Physical Review A **87**, 022903 (2013).
- [169] H. Winter. *Scattering of atoms and ions from insulator surfaces*. Progress in Surface Science **63**, 177 (2000).
- [170] H. Winter. *Collisions of atoms and ions with surfaces under grazing incidence*. Physics Reports **367**, 387 (2002).
- [171] R. Souda, K. Yamamoto, W. Hayami, B. Tilley, T. Aizawa, and Y. Ishizawa. *Neutralization and negative-ion formation by impact of low-energy H^+ on ionic compound surfaces*. Surface Science **324**, L349 (1995).
- [172] R. Souda, T. Suzuki, and K. Yamamoto. *Neutralization and electronic excitation during low-energy H and He scattering from LiF*. Surface Science **397**, 63 (1998).
- [173] E. A. Garcia, P. G. Bolcatto, M. C. G. Passeggi, and E. C. Goldberg. *Hydrogen scattering from a LiF ionic surface: Madelung potential and local environment effects*. Physical Review B **59**, 13370 (1999).
- [174] M. Torralba, C. Slutzky, E. García, and E. Goldberg. *Elastic and inelastic processes in the scattering of positive ions of hydrogen and helium from a LiF surface*. Physical Review B **63**, 195411 (2001).
- [175] P. Zeijlmans van Emmichoven, A. Niehaus, P. Stracke, F. Wieggershaus, S. Krischok, V. Kempter, A. Arnau, F. García de Abajo, and M. Peñalba. *Electron promotion in collisions of protons with a LiF surface*. Physical Review B **59**, 10950 (1999).
- [176] A. Borisov and V. Sidis. *Theory of negative-ion conversion of neutral atoms in grazing scattering from alkali halide surfaces*. Physical Review B **56**, 10628 (1997).

- [177] A. Borisov, J. Gauyacq, V. Sidis, and A. Kazansky. *Negative-ion conversion of fluorine atoms in grazing scattering from a LiF(001) surface: A coupled cluster approach*. Physical Review B **63**, 045407 (2001).
- [178] A. Borisov, V. Sidis, P. Roncin, A. Momeni, H. Khemliche, A. Mertens, and H. Winter. *F⁻ formation via simultaneous two-electron capture during grazing scattering of F⁺ ions from a LiF(001) surface*. Physical Review B **67**, 115403 (2003).
- [179] G. R. Darling, Y. Zeiri, and R. Kosloff. *Charge-transfer reactions in atom scattering from ionic surfaces: A time-dependent wavepacket approach*. Faraday Disc. **117**, 41 (2000).
- [180] G. R. Darling, R. Kosloff, and Y. Zeiri. *Time-dependent quantum calculations of negative ion formation in scattering of atoms from alkali-halide surfaces*. Surface Science **528**, 84 (2003).
- [181] L. Wirtz. *Interaction of Singly and Multiply Charged Ions with a Lithium-Fluoride Surface*. Ph.D. thesis, Institute for Theoretical Physics, Vienna University of Technology (2001).
- [182] L. Wirtz, M. Dallos, H. Lischka, and J. Burgdörfer. *Ab-initio calculations of charge exchange in ion-surface collisions: an embedded-cluster approach*. In J. Berakdar and J. Kirschner (eds.), *Correlation Spectroscopy of Surfaces, Thin Films, and Nanostructures*, p. 130. John Wiley & Sons, Ltd (2004).
- [183] W. Pong and C. S. Inouye. *Ultraviolet photoemission study of LiF*. Journal of Electron Spectroscopy and Related Phenomena **11**, 165 (1977).
- [184] F. Himpsel, L. Terminello, D. Lapiano-Smith, E. Eklund, and J. Barton. *Band Dispersion of Localized Valence States in LiF(100)*. Physical Review Letters **68**, 3611 (1992).
- [185] A. Schäfer, H. Horn, and R. Ahlrichs. *Fully optimized contracted Gaussian basis sets for atoms Li to Kr*. The Journal of Chemical Physics **97**, 2571 (1992).
- [186] A. D. Gaus, W. T. Htwe, J. A. Brand, T. J. Gay, and M. Schulz. *Energy spread and ion current measurements of several ion sources*. Review of Scientific Instruments **65**, 3739 (1994).
- [187] D. J. O'Connor and J. P. Biersack. *Comparison of theoretical and empirical interatomic potentials*. Nuclear Instruments and Methods in Physics Research Section B: Beam Interactions with Materials and Atoms **15**, 14 (1986).

- [188] B. O. Roos and K. Andersson. *Multiconfigurational perturbation theory with level shift - the Cr2 potential revisited*. Chemical Physics Letters **245**, 215 (1995).
- [189] B. O. Roos, K. Andersson, M. P. Fülcher, L. Serrano-Andrés, K. Pierloot, M. Merchán, and V. Molina. *Applications of level shift corrected perturbation theory in electronic spectroscopy*. Journal of Molecular Structure: THEOCHEM **388**, 257 (1996).
- [190] N. Forsberg and P.-A. Malmqvist. *Multiconfiguration perturbation theory with imaginary level shift*. Chemical Physics Letters **274**, 196 (1997).
- [191] M. Draxler, S. N. Markin, S. N. Ermolov, K. Schmid, C. Hesch, A. Poschacher, R. Gruber, M. Bergsmann, and P. Bauer. *ACOLISSA: a powerful set-up for ion beam analysis of surfaces and multilayer structures*. Vacuum **73**, 39 (2004).
- [192] G. Hayderer, M. Schmid, P. Varga, H. P. Winter, F. Aumayr, L. Wirtz, C. Lemell, J. Burgdörfer, L. Hägg, and C. O. Reinhold. *Threshold for Potential Sputtering of LiF*. Physical Review Letters **83**, 3948 (1999).
- [193] Q. Li, R. T. Williams, and D. Åberg. *First principles calculations and experiment predictions for iodine vacancy centers in SrI 2*. physica status solidi (b) **250**, 233 (2013).
- [194] L. F. Da Silva. *Mollow-Ivey relation for absorption and emission*. Radiation Effects and Defects in Solids **160**, 117 (2005).
- [195] A. G. Borisov and V. A. Esaulov. *Negative ion formation in the scattering of atoms and ions from dielectric surfaces*. Journal of Physics: Condensed Matter **12**, R177 (2000).
- [196] R. Erickson and D. Smith. *Oscillatory Cross Sections in Low-Energy Ion Scattering from Surfaces*. Physical Review Letters **34**, 297 (1975).
- [197] D. Goebel, D. Roth, D. Primetzhofer, R. C. Monreal, E. Abad, A. Putz, and P. Bauer. *Quasi-resonant neutralization of He ions at a germanium surface*. Journal of Physics: Condensed Matter **25**, 485006 (2013).
- [198] N. Tolk, J. Tully, J. Kraus, C. White, and S. Neff. *Angular Dependence of Oscillatory Structure in Low-Energy Ion-Surface Scattering*. Physical Review Letters **36**, 747 (1976).
- [199] K. Prabhakaran and T. Ogino. *Oxidation of Ge(100) and Ge(111) surfaces: an UPS and XPS study*. Surface Science **325**, 263 (1995).

-
- [200] B. Solleder, L. Wirtz, and J. Burgdörfer. *Excitation energy and pair correlation function of trions near an LiF surface*. Physical Review B **78**, 155432 (2008).
- [201] S. Markin, D. Primetzhofer, and P. Bauer. *Vanishing Electronic Energy Loss of Very Slow Light Ions in Insulators with Large Band Gaps*. Physical Review Letters **103**, 113201+ (2009).
- [202] J. Pruneda, D. Sánchez-Portal, A. Arnau, J. Juaristi, and E. Artacho. *Electronic Stopping Power in LiF from First Principles*. Physical Review Letters **99**, 235501 (2007).